Total and preferential CO oxidation over solid-solution and supported gold catalysts

By

Thandanani Cwele

August 2015

Total and preferential CO oxidation over solid-solution and supported gold catalysts

By

Thandanani Cwele

Submitted in the fulfilment of the academic requirements for the degree of Doctor of Philosophy
at the

School of Chemistry and Physics

University of KwaZulu-Natal

Durban

South Africa

August 2015

Note: This thesis has been written according to Format 3, as outlined in the guidelines from the Faculty of Science and Agriculture, University of KwaZulu-Natal, which states:

This is a thesis in which the chapters are written as a set of discrete research papers, with an overall Introduction and a Final Discussion. These research papers would not be published yet, but at least one paper would have already been submitted for publication. The references are reformatted to a uniform standard.

As the candidate's supervisor I have approved this thesis for submission

Name: Prof. H. B. Friedrich **Signature** _____ **Date** _____

ABSTRACT

In view of a very low CO tolerance of the polymer electrolyte membrane fuel cells (PEMFCs), the removal of trace amounts of CO contained in the reformate (from water gas shift) is necessary in order to achieve optimum power output of the fuel cell. Generally, conventional PEMFCs that use platinum electrocatalysts can only tolerate CO levels of 10 ppmv and below. Carbon monoxide (CO) is also one of the major pollutants released from internal combustion engines. Because the presence of CO, even in trace amounts, raises environmental and health concerns, the regulations governing auto emissions are becoming increasingly stringent. In addressing environmental fears and power output of PEMFCs, catalytic CO oxidation has been intensively studied and well established. However, there is still a need to develop new, efficient and relatively cost effective catalysts.

This project entails the development of catalytic materials that are both highly active and highly selective towards the oxidation of carbon monoxide to carbon dioxide. Transition metal substituted ceria and titania solid-solution materials ($Ce_{1-x}M_x\ O_{2-\delta}$ and $Ti_{1-x}M_xO_{2-\delta}$ where M = Co, Cu, Pd, Fe and x varies from 0.01 to 0.1) have been developed and used as catalysts as well as support materials for gold nanoparticles. Deposition of gold onto these solid-solutions was achieved by the deposition-precipitation method. The properties of the catalysts have been studied by TEM, BET, powder XRD and XPS. Solid-solution materials show good catalytic performance as total and preferential CO oxidation catalysts, compared to pure CeO_2 and TiO_2. On the other hand, supported gold catalysts show superior catalytic performance at temperatures as low as 25 °C.

Although CO-PROX studies conducted with only CO, H_2 and O_2 provide valuable understanding of the catalyst performance, it is necessary to evaluate catalytic behaviour in the presence of H_2O and CO_2, since these components are contained in H_2-rich gas obtained from steam reforming. Hence, the stability of the catalysts was also investigated in the presence of H_2O and CO_2. Cu-containing solid-solution materials and $Au/Ti_{1-x}M_xO_{2-\delta}$ catalysts have been found to be robust in the presence of H_2O and CO_2.

PREFACE

The experimental work described in this thesis was carried out in the School of Chemistry and Physics,
University of KwaZulu-Natal, Durban, from March 2010 to June 2014 under the supervision of Prof H. B. Friedrich and Dr S. Singh.

These studies present original work by the author and have not otherwise been submitted in any form for any degree or diploma to any tertiary institution. Where use has been made of the work of others it is duly acknowledged in the text.

_____

Thandanani Cwele

On this 18th day of August 2015

DECLARATION 1

Plagiarism

I, Thandanani Cwele, declare that:

1 The research reported in this thesis, except where otherwise indicated, and is my original research.

2 This thesis has not been submitted for any degree or examination at any other university.

3 This thesis does not contain other persons' data, pictures, graphs or other information, unless specifically acknowledged as being sourced from other persons.

4 This thesis does not contain other person's writing unless specifically acknowledged as being sourced from other researchers. Where other written sources have been quoted, then:

(a) Their words have been re-written but the general information attributed to them has been referenced.

(b) Where their exact words have been used, then their writing has been placed in italics and inside quotation marks, and referenced.

5 This thesis does not contain text, graphics or tables copied and pasted from the internet, unless specifically acknowledged, and the source being detailed in the thesis and in the Reference sections.

_____

Thandanani Cwele

On this 18th day of August 2015

DECLARATION 2

Publications and conference contributions

DETAILS OF CONTRIBUTION TO PUBLICATIONS that form part and/or include research presented in this thesis.

Publications

1.

Authors: Thandanani Cwele, Mahadevaiah Narayanappa, Sooboo Singh and Holger B. Friedrich.

Title: CO oxidation activity enhancement of $Ce_{0.95}Cu_{0.05}O_{2-\delta}$ induced by Pd co-substitution. **Status:** Submitted for publication**.**

Contributions: All experimental work and manuscript preparation was carried out by me, under the supervision of Prof H. B. Friedrich, Dr S. Singh and Dr M. Narayanappa.

2.

Authors: Thandanani Cwele, Mahadevaiah Narayanappa, Sooboo Singh and Holger B. Friedrich.

Title: Effect of Cu additives on the performance of a cobalt substituted ceria ($Ce_{0.90}Co_{0.10}O_{2-\delta}$) catalyst in total and preferential CO oxidation.

Status: Accepted for publication in Applied Catalysis B: Environmental

Contributions: All experimental work and manuscript preparation was carried out by me, under the supervision of Prof H. B. Friedrich, Dr S. Singh and Dr M. Narayanappa.

3.

Authors: Thandanani Cwele, Mahadevaiah Narayanappa, Sooboo Singh and Holger B. Friedrich.

Title: Au supported on substituted titania catalysts for CO oxidation and preferential CO oxidation in H_2-rich stream: Effects of the support, H_2O and CO_2.

Status: Submitted for publication**.**

Contributions: All experimental work and manuscript preparation was carried out by me, under the supervision of Prof H. B. Friedrich, Dr S. Singh and Dr M. Narayanappa.

Conference contributions

Oral presentation, *Gold catalysts for low temperature CO oxidation,* New Metals Development Network, 2011, Johannesburg, South Africa.

Poster presentation, *Gold catalysts for low temperature CO oxidation,* CATSA conference, 2011, Johannesburg, South Africa.

Poster presentation, *Preferential Oxidation of CO in Excess H_2 over Gold Catalysts Supported on Ceria and Transition Metal Substituted Ceria,* 23rd NAM, 2013, Louisville, USA.

Oral presentation, *Preferential CO oxidation in excess H_2 over gold supported on metal ion substituted CeO_2 and TiO_2,* The Precious Metals Development Network, 2013, Cape Town, South Africa.

Oral presentation, *Preferential CO oxidation in excess H_2 over gold supported on metal ion substituted CeO_2 and TiO_2,* CATSA conference, 2013, Wild Coast, South Africa.

_____

Thandanani Cwele

On this 18th day of August 2015

ACKNOWLEDGEMENTS

Saying thank you seems so inadequate, but I offer my sincerest gratitude to everyone who assisted or contributed in any way towards the completion of this research work. Thank you to the following people and institutions for their assistance:

* My supervisors, Professor Holger. B. Friedrich and Dr Sooboo Singh for their supervision, professional guidance and encouragement.
* My mentor, Dr Mahadevaiah Narayanappa for his never-ending enthusiasm and helpful discussions while conducting this research.
* Dr James Wesley-Smith and Ms Rhandzu Rikhotso of the National Centre for Nano-structured Materials (CSIR) for assistance with HRTEM analysis.
* Phillip Christopher and Vishal Bharath for their help with TEM and FEG-SEM studies.
* The Solid State and Structural Chemistry Unit at the Indian Institute of Science (Bangalore) and Dr P. B. Khoza (Rhodes University) for their help with XPS recording.
* The Atomic & Molecular Physics Division (A.K. Yadav, S.N. Jha, D. Bhattacharyya and N. K. Sahoo) at the Bhabha Atomic Research Centre (Mumbai) for helping with XANES and EXAFS experiments.
* Mfanafuthi Radebe who worked on the project as a trainee.
* The main sponsors, Mintek and the Department of Science and Technology (Advanced Metals Initiative program) for financial support.
* Catalysis Research Group (UKZN) members for valuable discussions.
* Dr M. Raphulu (Mintek), Dr Venkata Dasireddy, Dr M. L. Shozi and Dr M. N. Cele (UKZN) for scientific and general help.
* Dr Samuel Jali, Mr Lindelani Qwabe and Janine Kasavel for proof-reading.
* Technical staff of the School of Chemistry and Physics (UKZN) for their services.
* Above all, my parents and Sithembile for their support and encouragement. This work is dedicated to you. *Inkosi inibusise.*

TABLE OF CONTENTS

LIST OF FIGURES

LIST OF TABLES

ABBREVIATIONS

at%	Atomic percent
β_{hkl}	Peak broadening at half the maximum intensity
BET	Brunauer-Emmett-Teller
D	Average crystallite size
DMFC	Direct methanol fuel cells
DP	Deposition-precipitation
e-	Electron
EDS	Energy dispersive spectroscopy
EDX	Energy dispersive x-ray spectroscopy
eV	Electron volts
EXAFS	Extended X-ray absorption fine structure
FEG-SEM	Field emission gun-scanning electron microscope
GC	Gas chromatography
GHSV	Gas hourly space velocities
H_2-TPR	Hydrogen temperature-programmed reduction
HR-TEM	High resolution transmission electron microscopy
ICP-OES	Inductively coupled plasma optical emission spectrometry
IEP	Isoelectric point
IUPAC	International Union of Pure and Applied Chemistry
JCPDS	Joint committee on powder diffraction standards
K	Shape factor (0.891)
MCFC	Molten carbonate fuel cells
MvK	Mars-van Krevelen
OSC	Oxygen storage capacity

O_v	Oxygen vacancies
PAFC	Phosphoric acid fuel cells
PEMFC	Proton exchange membrane fuel cells
PGM	Platinum group metals
PROX	Preferential CO oxidation
rt	Room temperature
R-WGS	Reverse water gas shift reaction
Sel Meth	Selective Methanation
SEM	Scanning electron microscope
SOFC	Solid oxide fuel cells
SR	Steam reforming
T_{100}	Temperature of complete conversion
T_{50}	Temperature of 50% conversion
TCD	Thermal conductivity detector
TEM	Transmission electron microscopy
TOX	Total CO oxidation
TPR	Temperature-programmed reduction
viz.	Namely
vol%	Volume percent
WGS	Water gas shift reaction
wt%	Weight percent
XANES	X-ray absorption near edge structure
XPS	X-ray photoelectron spectroscopy
XRD	X-ray powder diffraction
λ	Amount of O_2 relative CO in PROX

CHAPTER 1

Hydrogen and fuel cells: moving towards greener pastures

1.1 Energy transitions: past, present and future

The history of energy, spanning for over more than 200 years, is the outcome of continuous technological innovations [1]. Before the industrial revolution, energy demand was limited and most economies were essentially dependent on agricultural activities. Energy needs were exclusively met by renewable sources. Windmills and ships depended on wind, homes were warmed by wood and waterwheels used running water [2, 3]. Before the advent of coal, biomass was the largest contributor to the world's energy demand up to the end of the 19th century. At the beginning of the 20th century, coal came to the fore and usurped 50% of the global energy requirements. The energy triangle shown in Figure 1.1 depicts the historical changes in the global primary energy system over nearly two centuries [4]. It also shows projected changes in the system. Constant market shares of the three primary energy sources are shown as isoshare lines of the triangle: the bottom side of the triangle is for carbon-free, the left side for coal and the right side represents oil/gas energies. The dark line inside the triangle denotes history.

When petroleum emerged as a "cleaner" and versatile energy alternative, it took more than 50 years for it to replace coal as the world's largest contributor in the energy mix. However, coal consumption continued to rise in the 20th century due to demand for electricity generation. The use of coal as an energy source, the discovery of internal combustion engines and the use of petroleum fuelled the industrial revolution and transformed the automobile sector [1].

Today, the world still depends on hydrocarbons, mainly oil, coal and natural gas as primary energy sources. As can be seen from the energy mix data in Figure 1.2, almost 90% of today's world energy appetite is met by hydrocarbons [5]. The dominance of these fuels can be attributed to their relatively easy accessibility and the relatively less energy-consuming efforts needed to extract and process the sources. In short, the unprecedented global economic growth over the past century can be partly attributed to the use of fossil fuels. However, there are several problems associated with the current world energy mix. Although fossil fuels have the capacity

to generate huge amounts of energy, their main disadvantage is that the technologies related to the extraction, processing and final use of these fuels have a harmful environmental impact. The environmental concerns range from air to water and soil pollution due to emissions, spills and leaks [6]. These problems can be destructive to the global economy. It is a widely held view in the scientific community that most of the pollutants in the atmosphere are a direct consequence of the combustion of fossil fuels. Crude oil has enjoyed dominance in the automobile sector and coal has been the largest contributor in the electricity generation. Therefore, it is not surprising that the automobile sector is one of the major contributors to a harmful environment.

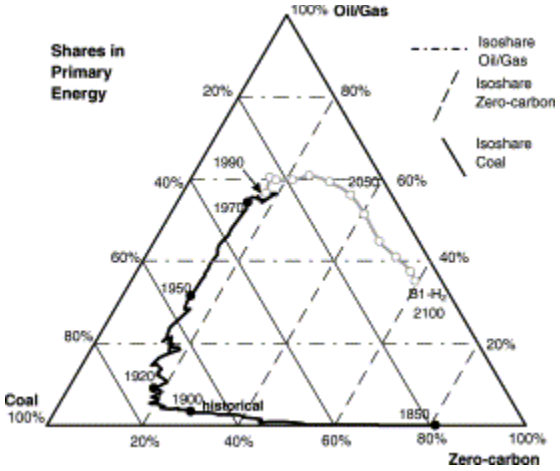

Figure 1.1 *The energy triangle, showing global shares in primary energy use. Reprinted from [4] with permission from Elsevier.*

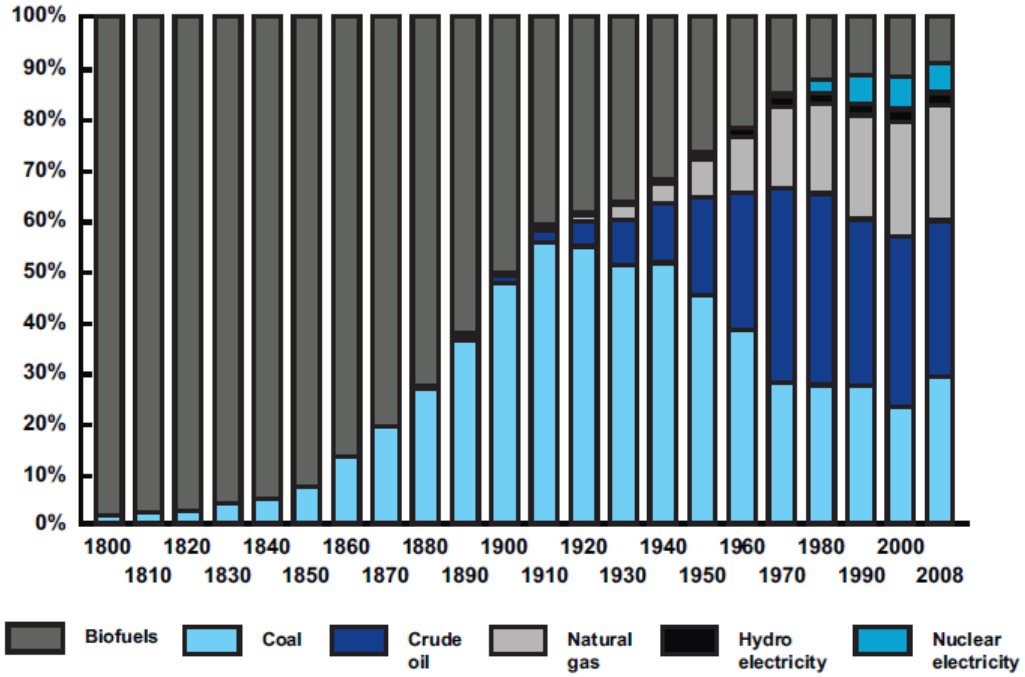

Figure 1.2 *Share of fuels in the energy mix from 1800-2008 [1, 5].*

Because of stringent environmental regulations, any new energy sources and technology advancements that ignore environmental concerns cannot be considered as groundbreaking achievements. Even without consideration of climate change, there is a greater need for the development of alternative clean, reliable and efficient energy conversion processes. Although the world will not run out of oil, natural gas or coal in the near future, these energy sources are non-renewable and will run out at some point. Hence, the need for alternative energy technologies is greater today, than before. Because of the continued population growth of all nations, the demand for energy supply will inevitably increase. This is also related to the fact that the world's appetite for energy is intrinsically linked to the standard of living of nations, which is dependent on the per capita energy consumption. According to a study reported by the World Economic Forum and IHS Cambridge energy research associates (IHS CERA), primary energy consumption is expected to increase, in proportion with global population growth [5].

A closer look at historical transformation or developments in the global energy system reveals two noticeable trends. Firstly, as the dominant fuel shifted from biomass to coal and then to oil, the newly discovered and dominant fuel has always been more versatile and multipurpose,

compared to fuels that came before it. Most notably, energy transitions in the past century have been accompanied by a slow decarbonisation/hydrogenation of energy carriers. Research has shown that the carbon tonnage per unit of energy [tons C/kilowatt-years] decreased by 35% over the past 120 years [7, 8]. This is in agreement with what is postulated by the energy triangle: the path started with the zero-carbon energy of the first solar civilization and proceeded via low carbon biomass to high carbon coal and then to low carbon oil and natural gas. This has kept researchers optimistic that this route is leading to a lower carbon future dominated by renewable energy and hydrogen as an energy carrier (grey line in the energy triangle Figure 1.1). Table 1.1 summarizes the relative hydrogen-to-carbon ratios and the state of aggregation in different energy carriers [9].

Table 1.1 *Energy carriers [9]*

Type	**H/C ratio**	**State of aggregation**
Coal	0.6	Solid
Oil	1.8	Liquid
Natural gas	4.0	Gas
Hydrogen	∞	Gas

The position enjoyed by hydrocarbons is gradually being challenged as more alternatives are being explored to address energy demands. Research has shown that cleaner energy alternatives can be harnessed to sustain the needs of mankind with less impact on the environment. As energy carriers are becoming more hydrogen-rich, hydrogen as a fuel has received a great deal of attention. Hydrogen-based technologies, mainly fuel cell technologies, are considered as viable options for transforming the energy system into a more flexible, efficient and environmentally friendly system [10, 11]. Fuel cell powered vehicles offer another option for the transportation sector [12]. This chapter gives an overview on the use of hydrogen as an energy carrier and its use in fuel cells. The topics covered include the following aspects of research endeavours: Hydrogen as an energy carrier, fuel cells, hydrogen production and fuel processing for fuel cells. There will not be an in-depth discussion of the fuel cell design itself, but rather a brief description of the fuel cell is included to highlight the relevance of fuel processing technologies.

Although hydrogen production is possible from non-carbon sources, it is not the focus of this research. Hence, such technologies will not be dealt with in detail.

1.1.1 Fuel cell technology

The scientific foundations of fuel cells can be traced from Humphry Davy's research on electrolysis by voltaic pile [13]. However, the first scientific argument about the possibility of producing current by combining hydrogen and oxygen was reported by Christian Friedrich Schönbein in *Philosophical Magazine* in the January issue of 1839 [14]. In the scientific community, Sir William Robert Grove is widely credited for inventing the fuel cell in 183 [15-17]. The development of fuel cell technology is based on his understanding that electrolysis of water to produce hydrogen and oxygen consumes electricity. Therefore, the reverse reaction would produce energy. Grove proved this hypothesis by conducting a series of experiments with what he referred to as a "gaseous voltaic battery" [18, 19]. Indeed, it was proven that an electrochemical reaction between hydrogen and oxygen over a platinum catalyst could produce electrical current. Grove's experimental set-up, a four cell version gas battery, is shown in Figure 1.3 [20]. Grove's research work led to an advanced technology which will later be referred to as fuel cells by Mond and Langer [21]. Since then, continued research efforts have resulted in important advances in fuel cell technology. The 20th century saw the use of fuel cells in space missions, submarines and electric vehicles and in stationary power applications. By the end of the 20th century, custodians in the automotive industry launched fuel cell vehicles (FCVs) to demonstrate the feasibility of the technology.

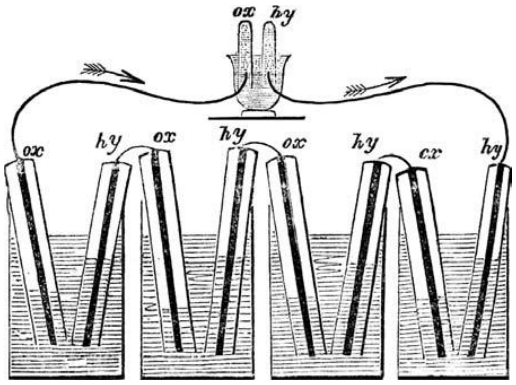

Figure 1.3 *A hydrogen/oxygen gas battery or fuel cell developed by Sir William Robert Grove. (Reprinted with permission from The Taylor and Francis Group) [19, 20].*

By definition, a fuel cell is an electrochemical device that produces energy/electricity from hydrogen and oxygen. The basic electrochemical reactions are illustrated in Equations 1.1 and 1.2.

Anode:	$H_2 \longrightarrow 2\ H^+ + 2e\text{-}$	(1.1)
Cathode:	$½\ O_2 + 2\ H^+ + 2e\text{-} \longrightarrow H_2O$	(1.2)
Overall:	$H_2 + ½\ O_2 \longrightarrow H_2O$	(1.3)

The advantage of this technology over that of batteries is that a fuel cell doesn't require recharging. Theoretically, energy will be produced as long as the device is supplied with a source of hydrogen fuel and a source of oxygen. Water and heat are produced as main by-products. Notably, the products and by-products formed are harmless, which has resulted in fuel cells being coined as *zero-emission engines.* Contrary to the internal combustion engine, the fuel is not burned, instead the chemical energy is directly converted into electrical energy through an electrochemical reaction [17]. According to the exergy concept from engineering thermodynamics, the energy conversion is more efficient in a fuel cell compared to a heat engine [22]. In practice, fuel cell efficiencies can reach as high as 60 % in electrical energy conversion, the difference being heat. The overall efficiency can be over 80% if the heat generated is used for other applications. Such fuel cells are referred to as combined heat and power fuel cells (CHP) and are commonly used in hotels, universities and industries [23]. In short, fuel cell technology is

not only cleaner, but two to three times more efficient compared to conventional combustion technologies.

1.1.2 Types of fuel cells and their main applications

The core building block of most fuel cells is the unit cell, which is the zone where chemical energy is converted into electrical energy. This component consists of a solid or liquid electrolyte in contact with an anode and cathode on either side. A selectively conductive electrolyte transfers charged species between the two electrodes during the operation of the fuel cell [20, 24]. A catalyst is normally used to catalyse the reactions at the electrodes. From the days of Grove's fragile fuel cell, a number of modern fuel cells have been developed. Different types of fuel cells are commonly classified according to the electrolytes and fuels they use. However, the basis of their operation is similar. In the dual chamber fuel cell, a hydrogen-rich fuel is oxidized to protons and electrons at the anode, while oxygen is reduced to oxide ions at the cathode. Figure 1.4 shows a schematic representation of the principles of a fuel cell (based on the reaction of hydrogen and oxygen) [17, 25]. Depending on the electrolyte of that particular fuel cell, specific ions (usually protons or oxide ions) can be conducted either from anode to cathode or *vice versa*. Since each type requires particular materials for its design, they in-turn operate under different conditions and are therefore feasible or suitable for different applications.

There are six classes of fuel cells that are presently receiving attention, being researched and developed viz. direct methanol fuel cells (DMFC), proton exchange membrane fuel cells (PEMFC), alkaline fuel cells (AFC), phosphoric acid fuel cells (PAFC), molten carbonate fuel cells (MCFC) and solid oxide fuel cells (SOFC) [25]. MCFC and SOFC can be categorized as high-temperature fuel cells, operating at 650 °C and 800-1000 °C, respectively. Such operating temperatures result in improved reaction kinetics, hence they do not require noble metals as catalysts [26, 27]. MCFC use a molten salt of lithium carbonate and potassium as an electrolyte, while SOFC uses a solid ceramic oxide electrolyte. Both systems can use a range of fuels such as coal-derived gas, natural gas and hydrocarbons. This is due to their capability to reform the fuel internally [27, 28]. Unlike MCFC which need a carbon dioxide supply at the cathode, SOFC can also be fuelled by pure hydrogen. The electric efficiency of the two can reach as high as 60% and

can be improved if waste heat is used for other applications. They are popularly used for stationary power generation [29]. The properties of the major types of fuel cells and their respective applications are summarized in Table 1.2.

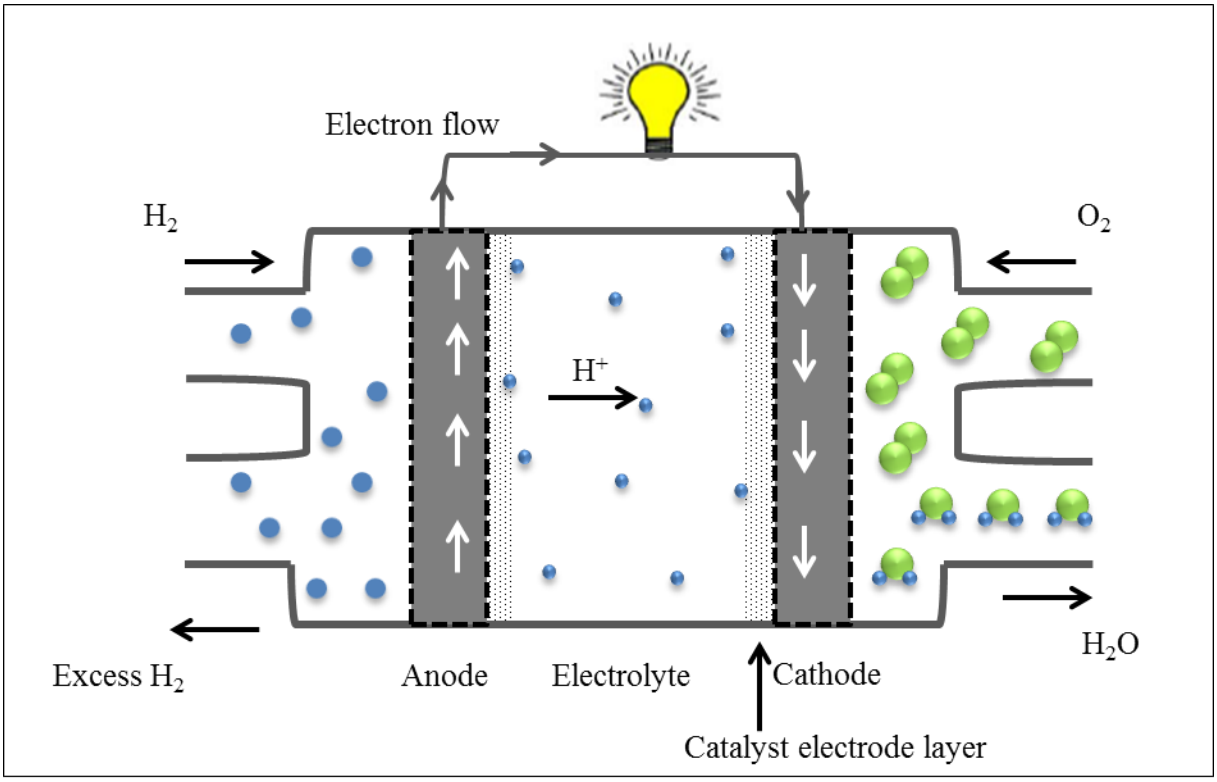

Figure 1.4 *Schematic representation of a fuel cell (PEM). The drawing is adapted from reference [30].*

DMFCs operate at 50-130 °C and are relatively new in the family of fuel cells. Like PEMFC, DMFC uses an acidic polymer membrane as an electrolyte. Liquid methanol is used to indirectly supply hydrogen. The reaction is facilitated by a platinum-ruthenium catalyst at the anode [30]. They are generally viewed as the best candidates to replace batteries in portable devices since they have a longer lifespan compared to lithium ion batteries. Although they have low efficiency (25-40%), they still receive attention due to the easy transportation and handling of methanol fuel.

Table 1.2 *Types of fuel cells and their characteristics and applications [17, 20, 24, 27, 28].*

	DMFC	**PEMFC** [a]	**AFC**	**PAFC**	**MCFC**	**SOFC**
Electrolyte	Proton conducting solid polymer	Proton conducting solid polymer	KOH	H_3PO_4 immobilized on SiC	Molten carbonate [b]	Ceramic [c]
Charge carrier	H^+	H^+	OH^-	H^+	CO_3^{2-}	O^{2-}
Electrodes/ Catalyst	Pt/Ru	Pt on C	Ni (also Pt)	Pt on C	Ni/NiO	Perovskite
Fuel	Methanol	**H_2**	**H_2**	**H_2**	NG, HC [d]	NG, HC [d]
Operating temperature (°C)	50 - 130	50 - 100	~70	150 - 220	~650	800 - 1000
Electric efficiency (%)	25 - 40	35 - 47	35 - 60	35 - 42	44 - 60	45 - 60
Power range (kW)	< 250 W	< 1 MW	< 400 kW	50 kW – 1 MW	300 kW – 2.8 MW	< 3 MW
Applications (examples)	Portable devices	Ideal for FCVs and stationary electricity generation	Military services and space programes	Stationary power and heat generation	Stationary power and heat generation	Stationary power and heat generation

[a] Also known as a solid polymer fuel cell (SPFC), [b] Lithium and potassium carbonate, [c] yttria, zirconia, [d] natural gas and hydrocarbons.

The PEMFC, AFC and PAFC use hydrogen as a fuel and operate in relatively low temperature ranges (50-100 °C, 70 °C and 150-220 °C respectively) [31]. In contrast to high-temperature systems and DMFC, these fuel cells could truly represent a clean energy technology, if the hydrogen used is pure and generated from renewable sources. The AFC and PEMFC are very sensitive to poisoning, while PAFC have a maximum tolerance of 2% CO. The presence of CO is known to be detrimental to the platinum electro-catalyst, consequently shortening the lifespan of the fuel cell. In addition, AFC are also highly intolerant to CO_2 [24]. As a result air from the atmosphere cannot be used as an oxidant. Although they have relatively short lifetimes, they have been used in the space shuttle program by the *National Aeronautics and Space Administration* (NASA) [32]. PAFC use phosphoric acid, immobilized on SiC, as an electrolyte and offer electrical efficiency of 35%-42%. The limitations of these fuel cells are associated with the fact that they are prone to corrosion and are heavy [29].

PEMFCs have been the most popular and widely used of the aforementioned fuel cell technologies. In comparison with other fuel cells, PEMFC have high voltage, current and power density. The solid polymer used to separate the anode and the cathode allows them to operate up to 4 A/cm^2 [33]. The main advantages that come with using a solid electrolyte include simple mechanical design and easy handling, with no possibility of corrosion. These fuel cells are also known for having fast start-up and response times to change of load. Due to their beneficial attributes, they have been demonstrated and tested for a variety of applications, such as power for airplanes and automobiles, portable devices and stationary power generation. To the best of our knowledge, they are the only fuel cells considered for powering fuel cell vehicles (FCV), offering an operational efficiency that is more than two times that of traditional combustion engines [12]. One of the major drawbacks of these systems is their high sensitivity to impurities in the hydrogen fuel. Specifically, the maximum tolerance is 50 ppm of CO. Considering that most of the hydrogen used in fuel cells is generated from reforming of hydrocarbons, the reformate stream normally contains CO [34]. The next section gives an overview of the technologies used to produce hydrogen. The section also attempts to highlight different ways of cleaning hydrogen before it can be used in sensitive fuel cells such as the PEMFC.

It has been demonstrated that PEMFC can be modified into high-temperature PEMFC (HT-PEMFC) by changing an electrolyte into a mineral, acid-based system. HT-PEMFC can operate at temperatures as high as 200 °C and the thinking behind their design is to minimize the CO poisoning by working at temperatures where CO chemisorption is reduced. Nonetheless, HT-PEMFCs are still surpassed by low temperature analogues in terms of performance [35].

1.2 Hydrogen as a versatile energy carrier

Hydrogen is the simplest, lightest and the most abundant of all chemical elements in the universe. However, hydrogen rarely exists in a natural molecular form and thus is almost always found as part of compounds such as water, hydrocarbons and alcohols. It is also available in natural biomass [36, 37]. Hydrogen can be produced from these different sources and can be used as a versatile, clean and efficient fuel in almost all applications where fossil fuels are used. Therefore, hydrogen can be viewed as an energy *carrier* and not as an energy *source* [6, 11, 37]. The availability of almost sulfur and carbon monoxide-free hydrogen fuel is the driving force for the advancement of fuel cell technologies, particularly PEMFCs. Unlike other conventional fuels, hydrogen fuel is non-toxic and its utilization produces no pollutants. Hence, hydrogen is widely accepted as a universal clean fuel that can be produced from both fossils and renewable resources.

Recent reports show that the annual production of hydrogen is approximately 50 million tons [37]. In the face of increasing hydrogen consumption and fast-paced research efforts, this output is expected to increase in the near future. Hydrogen can be produced from a diverse range of sources. Thus, water splitting by photolytic and electrolytic technologies can produce pure hydrogen, clean enough to be used for fuel cell applications. The drawback of these technologies is that they are considered as energy consuming and expensive [36]. In addition, if such methods are to be considered as truly green and renewable, they will have to rely on the electricity produced from nuclear, water, wind and/or solar technology. The research efforts in this regard are still in their early stages and not yet capable of large scale hydrogen production. Biomass processing from plants and animal and municipal waste is still the most viable renewable option for hydrogen production with existing infrastructure [3]. Common options for hydrogen

production and the process steps involved are summarized in Figure 1.5 [38]. An envisaged sustainable and environmental friendly energy system, where electricity and hydrogen complement the renewable energy sources, is depicted in Figure 1.6.

1.2.1 Hydrogen from fossil fuels

Although significant progress is being made in developing different hydrogen production technologies, hydrogen is mainly produced from fossil fuels via steam reforming of hydrocarbons. Steam reforming is currently regarded as the least expensive and most viable method to produce hydrogen [39]. At present, steam reforming of natural gas accounts for almost half of all hydrogen production. Partial oxidation of oil/naphtha from refineries or off-gases from chemical industries contribute nearly 30 %, while coal gasification and water electrolysis contribute 18 % and 3.9 % respectively. Other sources are struggling to make an impact and have a 0.1% share.

Hydrogen can only be the clean fuel of choice if its production is sustainable and nearly emission free. Carbon capture and storage technology is widely considered as one of the methods to reduce emissions during hydrogen production. However, these efforts are still in the early developmental stage and do not solve the world's dependency on fossil fuels for energy needs. Therefore, the justification for producing hydrogen from fossil fuels cannot be limited to environmental concerns, since it also touches on economic borders. While renewable hydrogen production is still considered as an expensive technology and is not operational on a large scale, hydrogen produced from fossil fuels helps to build early markets and infrastructure for hydrogen based technologies such as fuel cells. Generally, fuels from fossil sources contain sulphur. Consequently, before the fuel reaches the reformer and/or used in fuel cells, a desulfurization step is necessary during fuel processing. Sulphur removal is a diverse topic on its own and will not be covered in the current work.

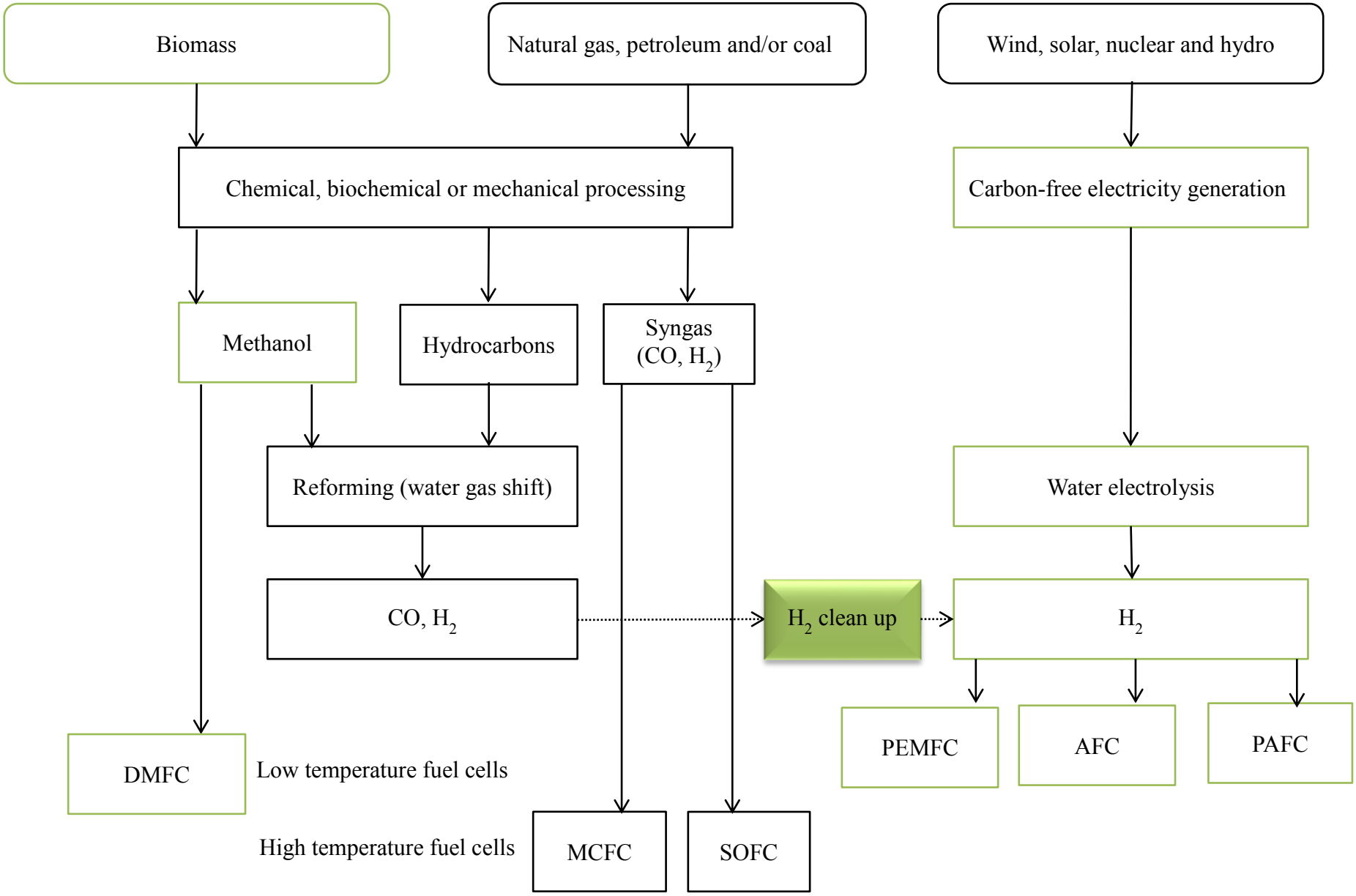

Figure 1.5 *Energy sources and conversion steps involved in hydrogen production. Adapted from Hotza et al.[39]*

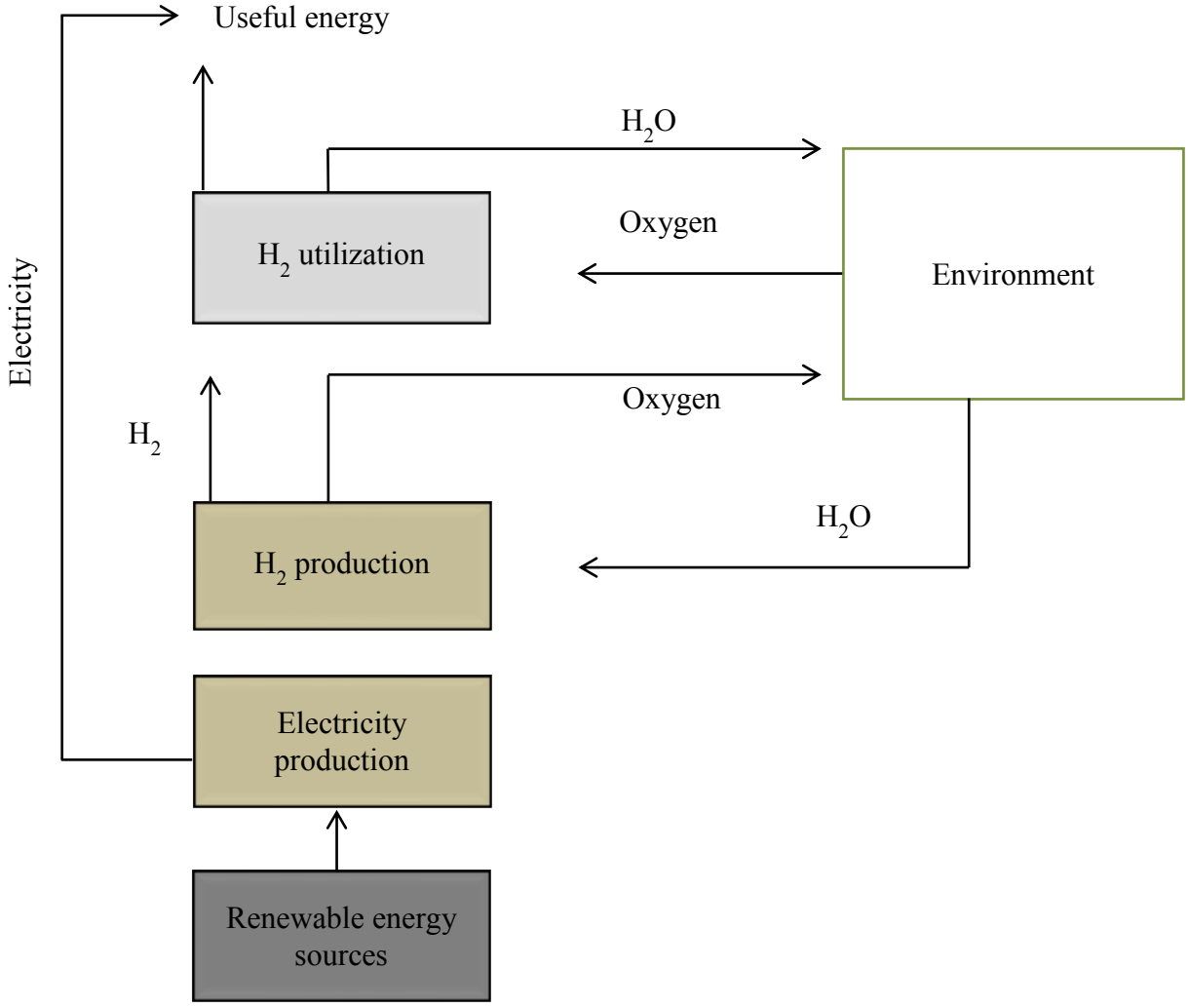

Figure 1.6 *A Scheme of an environmentally compatible energy system. Adapted from Barbir et al.[6, 11]*

1.2.1.1 Hydrocarbon reforming, partial oxidation and gasification

The conversion of hydrocarbon fuels to hydrogen involves complex chemical and engineering steps. In this section, the main steps of reforming and clean-up will be discussed. Steam reforming (SR), partial oxidation (POX) and autothermal reforming (ATR) are the three common methods used to produce hydrogen from hydrocarbons. These techniques are normally referred to as thermal processes, since they require thermal energy to favour the reactions that produce hydrogen directly from hydrocarbons.

Generally, steam reforming can be described as the gas phase conversion of energy carriers into synthesis gas (H_2 + CO). It is an endothermic reaction. The heat supplied is generated by the combustion of additional fuel in a reactor and is separated from the steam reforming section by a thermal conductive wall [40]. Natural gas, light hydrocarbons, methanol and oxygenated hydrocarbons are the preferred fuels for steam reforming. In the case of methanol and oxygenated hydrocarbons, the reaction is performed at ~ 180 °C, whereas the reaction temperature can be as high as 500 °C for other hydrocarbons. Although precious metal catalysts are used to speed-up the reaction, nickel catalysts are the industrially approved catalysts for the reaction [41, 42]. The following reactions represent reforming reactions involving hydrocarbons and methanol as representative fuels:

$$C_mH_n + mH_2O \longrightarrow mCO + (m + 0.5n)\, H_2 \qquad (1.4)$$

$$C_mH_n + 2mH_2O \longrightarrow mCO_2 + (2m + 0.5n)\, H_2 \qquad (1.5)$$

$$CO + H_2O \leftrightarrow CO_2 + H_2 \qquad (1.6)$$

$$CH_3OH + H_2O \leftrightarrow CO_2 + 3H_2 \qquad (1.7)$$

The resulting gas mixture of the steam reforming process is often referred to as the *reformate*. The mixture normally contains other components, such as steam and CO_2, in addition to H_2 and CO. In the second stage of the process, CO in the cooled reformate can be converted to CO_2 via the water gas shift reaction (WGS) (Equation 1.6). The reaction improves the hydrogen content in the reformate, while reducing CO levels. Although this hydrogen rich stream can be employed in high temperature fuel cells, it is still not pure enough to be used in low temperature counterparts, which are highly CO sensitive. Hence, further purification is necessary. The clean-up methods will be discussed in Chapter 2.

Partial oxidation (POX) is another important reaction for producing hydrogen on an industrial scale. The reaction is primarily used for processing heavier hydrocarbons or oil fractions [43]. However, biogas and methane can also be employed as raw materials for the process. It can be viewed as an oxidative conversion of fuels under oxygen deficient conditions. Complete combustion is normally avoided by controlling residence time and keeping the amount of oxygen

lower than the stoichiometric amount required for complete oxidation. In simple terms, POX is a non-catalytic process where fuel is gasified at high temperatures (1300 – 1500 °C) and under pressure (3 – 8 MPa) [44]. The general reaction for POX is shown in equation 1.8. In contrast to steam reforming, the amount of carbon monoxide formed in POX is substantially higher. In addition, coke may be formed from carbon monoxide according to the Boudouard reaction and the reaction with hydrogen (Equations 1.9 and 1.10 respectively) [43]. In cases where the fuel processor is connected to CO-sensitive fuel cells, the clean-up reactions are necessary. The water formed during the combustion is used in the subsequent WGS reaction (Equation 1.6).

$$C_mH_n + 0.5mO_2 \longrightarrow mCO + 0.5nH_2 \qquad (1.8)$$

$$2CO \leftrightarrow CO_2 + C \qquad (1.9)$$

$$CO + H_2 \longrightarrow C + H_2O \qquad (1.10)$$

When hydrocarbon reforming is performed in the presence of both steam and air, the process is called oxidative steam reforming. The general reaction for this process is represented by Equation 1.11. The process is the combination of steam reforming and partial oxidation [37]. The heat generated from the exothermic partial oxidation reaction (POX) is used to promote an energy demanding steam reforming reaction during steady-state operation. Consequently, this combined process requires no external heat and the overall reaction is autothermal. Hence, the process is often referred to as autothermal reforming (ATR). In order for the overall reaction to be self-sustaining and thermally neutral, heat losses are normally compensated by performing the reaction with a high atomic oxygen-to-carbon ratio (O/C). Optimum O/C and steam-to-carbon (S/C) ratios differ from fuel to fuel, ranging between 0.7 - 1.0 and 1.5 – 12.0, respectively [43, 44]. Careful manipulation of the two ratios is of significant importance as they dictate the actual reaction temperature, reformate compositions and coke formation [45]. Different catalysts (Rh, Ru, Pt and Ni based) have been used to speed up the reaction [41, 42, 46]. Generally, the reaction is operated at temperatures between 700 and 800 °C.

$$C_mH_n + 0.25mO_2 + 0.5mH_2O \longrightarrow mCO + (0.5n + 0.5m)H_2 \qquad (1.11)$$

Comparing all three reforming processes, SR has the lowest operating temperature and produces a reformate with the highest H_2/CO ratio (3/1). Despite the advantage of eliminating additional compartments or steps (heat and steam supply) in POX reformers, a drawback is that they operate at very high temperatures which results in soot formation, which adds to the process complexities. Significant advantages of ATR over POX are that its operation temperature is low and it produces a high H_2/CO ratio. Regardless of the compactness and economic viability of ATR technology, it is still not popular in industry [37]. The comparison and relationship between POX, ATR and steam reforming is schematically depicted in Figure 1.7 [37].

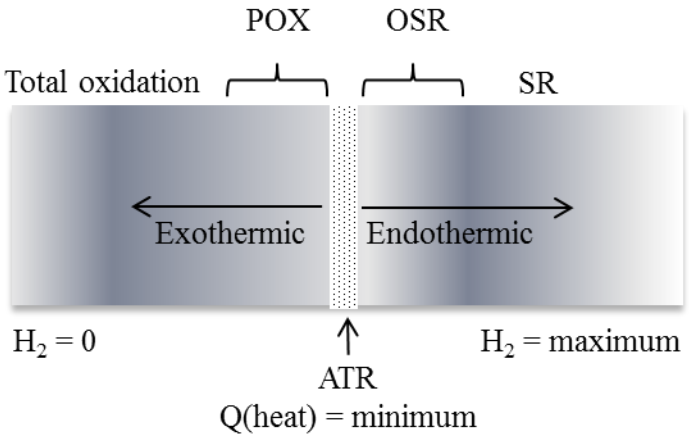

Figure 1.7 *Comparison and relationship between SR, POX and ATR. Adapted from Kalamaras et al. [38].*

All three processes produce a reformate containing mostly H_2, CO and CO_2. In addition to this, the composition also contains N_2, in the cases of POX and ATR where air is used to supply oxygen. Therefore, reforming processes are normally followed by one or two water gas shift reactors to reduce the CO content to lower levels. Fe-Cr based [47, 48] and Cu-Zn-Al_2O_3 [48-50] based catalysts are commonly used for high temperature (HT-WGS) and low temperature water gas shift (LT-WGS), respectively. HT-WGS reactors are usually operated in the temperature range between 320-240 °C, while LT-WGS counterparts are performed at 180- 240 °C to avoid catalyst sintering [51]. Precious metal catalysts have also received great interest for the WGS reaction. In particular, ceria and titania-supported platinum [52, 53] and gold [54] catalysts are among the promising candidates that have been extensively studied [51].

Although the hydrogen-rich stream obtained after WGS usually contains a low CO content (~1 vol%), this is still high enough to poison the Pt electrocatalyst in the PEMFC. Hence, there is a need for further purification of the reformate to ensure maximum PEMFC power output. Methods used for further hydrogen clean-up will be discussed in Chapter 2, as they form an important part of the current research work. Special attention will be given to the recent progress in preferential CO oxidation in a hydrogen rich stream and in total CO oxidation.

References

[1] V. Smil, Energy Transitions: History, Requirements, Prospects, Praeger, Santa Barbara, California, 2010.

[2] C.-J. Winter, Int. J. Hydrogen Energy 34 (2009) S1-S52.

[3] S. Dutta, J. Ind. Eng. Chem. 20 (2014) 1148-1156.

[4] L. Barreto, A. Makihira, K. Riahi, Int. J. Hydrogen Energy 28 (2003) 267-284.

[5] D. Yergin, S. Gross, N. Meyer, L. Tillemann-Dick, Energy transitions: Past and Future, World Economic Forum, The Energy Industry Partnership Programme, 2013.

[6] F. Barbir, Energy 34 (2009) 308-312.

[7] N. Nakicenovic, Hem. Ind. 53 (1999) 434-440.

[8] N. Nakićenović, A. John, Energy 16 (1991) 1347-1377.

[9] K.P. De Jong, H.M.H. Van Wechem, Int. J. Hydrogen Energy 20 (1995) 493-499.

[10] S.A. Sherif, F. Barbir, T.N. Veziroglu, Elec. J. 18 (2005) 62-76.

[11] F. Barbir, Chem. Ind. Chem. Eng. Q. 11 (2005) 105-113.

[12] A. Veziroglu, R. Macario, Int. J. Hydrogen Energy 36 (2011) 25-43.

[13] J. Davy, The Lancet 73 (1859) 134-135.

[14] R. Meldola, Nature 62 (1900) 97-99.

[15] E. Chen, in: G. Hoogers (Ed.), Fuel Cell Technology Handbook, CRC Press LLC, Boca Raton, Florida, 2003, pp. 2/1-2/40.

[16] P.G. Grimes, Aerospace and Electronic Systems Magazine, IEEE 15 (2000) 7-10.

[17] U. Lucia, Renewable and Sustainable Energy Reviews 30 (2014) 164-169.

[18] W.R. Grove, Philosophical Magazine Series 3 13 (1838) 430-431.

[19] W.R. Grove, Philosophical Magazine Series 3 14 (1839) 127-130.

[20] G. Hoogers, Fuel Cell Technology Handbook, CRC Press LLC, Boca Raton, Florida, 2003.

[21] L. Mond, C. Langer, Proceedings of the Royal Society of London 46 (1889) 296-304.

[22] E. Chen, in: G. Hoogers (Ed.), Fuel Cell Technology Handbook, CRC Press LLC, Boca Raton, Florida, 2003, pp. 3/1-3/30.

[23] L. Blum, R. Deja, R. Peters, D. Stolten, Int. J. Hydrogen Energy 36 (2011) 11056-11067.

[24] M.C. Williams, in: D. Shekhawat, J.J. Spivey, D.A. Berry (Eds.), Fuel Cells, Elsevier, Amsterdam, 2011, pp. 11-27.

[25] Fuel Cell Today, Fuel cell basics: Technology Types, www.fuelcelltoday.com, 03 November 2014.

[26] J.M. Andújar, F. Segura, Renewable and Sustainable Energy Reviews 13 (2009) 2309-2322.

[27] IEA, Energy Technology Essentials: Fuel Cells, International Energy Agency 2007.

[28] H.J. Neef, Energy 34 (2009) 327-333.

[29] D. Carter, J. Wing, Fuel Cell Today, The Fuel Cell Industry Review 2013, www.fuelcelltoday.com, 03 November 2014.

[30] X. Li, A. Faghri, J. Power Sources 226 (2013) 223-240.

[31] H.W. Cooper, Chem. Eng. Prog. 103 (2007) 34-43.

[32] National Aeronautics and Space Administration, Hydrogen and Fuel Cells at NASA, http://www.nasa.gov 03 November 2014.

[33] F. Barbir, S. Yazici, Int. J. Energy Res. 32 (2008) 369-378.

[34] G. Hoogers, in: G. Hoogers (Ed.), Fuel Cell Technology Handbook, CRC Press LLC, Boca Raton, Florida, 2003, pp. 4/1-4/27.

[35] J. Zhang, Z. Xie, J. Zhang, Y. Tang, C. Song, T. Navessin, Z. Shi, D. Song, H. Wang, D.P. Wilkinson, Z.-S. Liu, S. Holdcroft, J. Power Sources 160 (2006) 872-891.

[36] C. Acar, I. Dincer, Int. J. Hydrogen Energy 39 (2014) 1-12.

[37] C.M. Kalamaras, A.M. Efstathiou, Conference Papers in Energy 2013 (2013) 1-9.

[38] D. Hotza, J.C. Diniz da Costa, Int. J. Hydrogen Energy 33 (2008) 4915-4935.

[39] O. Veneri, Hydrogen Fuel Cells for Road Vehicles, Springer London, 2011, pp. 33-70.

[40] F. Barbir, in: F. Barbir (Ed.), PEM Fuel Cells, Academic Press, Burlington, 2005, pp. 271-336.

[41] T. Krause, J. Kopasz, C. Rossignol, J.D. Carter, M. Krumpelt, Prepr. Symp. Am. Chem. Soc., Div. Fuel Chem. 47 (2002) 542-544.

[42] K.P. De Jong, R.J. Schoonebeek, K.A. Vonkeman, Contacting feed mixture comprising hydrocarbon, oxygen-containing gas, nitrogen, sulfur compound with oxidation catalyst to produce carbon monoxide and/or hydrogen, Google Patents, US5720901, 1998.

[43] D. Shekhawat, D.A. Berry, J.J. Spivey, Fuel Cells: Technologies for Fuel Processing, 1st ed., Elsevier Ltd., Amsterdam, Netherlands 2011, pp. 1-9.

[44] G. Kolb, Fuel processing for fuel cells, Wiley-VCH Verlag GmbH & Co. KGaA, Weinheim, Germany, 2008.

[45] M. Krumpelt, T.R. Krause, J.D. Carter, J.P. Kopasz, S. Ahmed, Catal. Today 77 (2002) 3-16.

[46] J.J. Krummenacher, K.N. West, L.D. Schmidt, J. Catal. 215 (2003) 332-343.

[47] C. Rhodes, B. Peter Williams, F. King, G.J. Hutchings, Catal. Commun. 3 (2002) 381-384.

[48] W. Ruettinger, O. Ilinich, R.J. Farrauto, J. Power Sources 118 (2003) 61-65.

[49] N. Thouchprasitchai, A. Luengnaruemitchai, S. Pongstabodee, J. Ind. Eng. Chem. 19 (2013) 1483-1492.

[50] F. Huber, J. Walmsley, H. Venvik, A. Holmen, Appl. Catal. A 349 (2008) 46-54.

[51] C. Ratnasamy, J.P. Wagner, Catal. Rev. 51 (2009) 325-440.

[52] A. Faur Ghenciu, Curr. Opin. Solid State Mater. Sci. 6 (2002) 389-399.

[53] W. Ruettinger, X. Liu, R.J. Farrauto, Appl. Catal. B 65 (2006) 135-141.

[54] F. Zane, V. Trevisan, F. Pinna, M. Signoretto, F. Menegazzo, Appl. Catal. B 89 (2009) 303-308.

CHAPTER 2

Recent advances in CO removal in hydrogen-rich stream

In view of a very low CO tolerance of the polymer electrolyte membrane fuel cells (PEMFCs), the removal of trace amounts of CO contained in the reformate after the water gas shift reaction is necessary in order to achieve optimum power output of the fuel cell. Generally, conventional PEMFCs that use platinum electrocatalysts (anode) cannot tolerate CO levels above 50 ppmv. In certain cases where alloys are used as anodes, the CO tolerance may be about ~ 100 ppmv [1]. It has been shown that CO adsorbs strongly on the Pt electrocatalyst at typical operating temperatures (~80 °C) of the membrane electrode assembly (MEA). In a CO-contaminated reformate, the CO binds to the Pt sites according to Equations 2.1 and/or 2.2, resulting in the inhibition of the dissociative adsorption of hydrogen and the subsequent charge transfer (Equations 2.3 and 2.4) [2]. Although this is not a fast process, the performance of the fuel cell can decrease significantly with increasing CO adsorption over time.

$$CO + Pt \rightarrow Pt\text{-}CO \quad (2.1)$$

$$2CO + 2Pt\text{-}H_{ads} \rightarrow 2Pt\text{-}CO + H_2 \quad (2.2)$$

$$H_2 + 2Pt \rightarrow 2Pt\text{-}H_{ads} \quad (2.3)$$

$$2Pt\text{-}H_{ads} \rightarrow 2Pt + 2H^+ + 2e\text{-} \quad (2.4)$$

Figure 2.1 shows the dependence of the calculated equilibrium CO concentration, at the exit of the WGS reactor [3]. The authors based their calculations on a feed containing only H_2O and CO. The technologies used for the final cleanup of the reformate can be broadly classified into four categories: adsorption, membrane separation, scrubbers and selective reactions (CO methanation and preferential oxidation of CO).

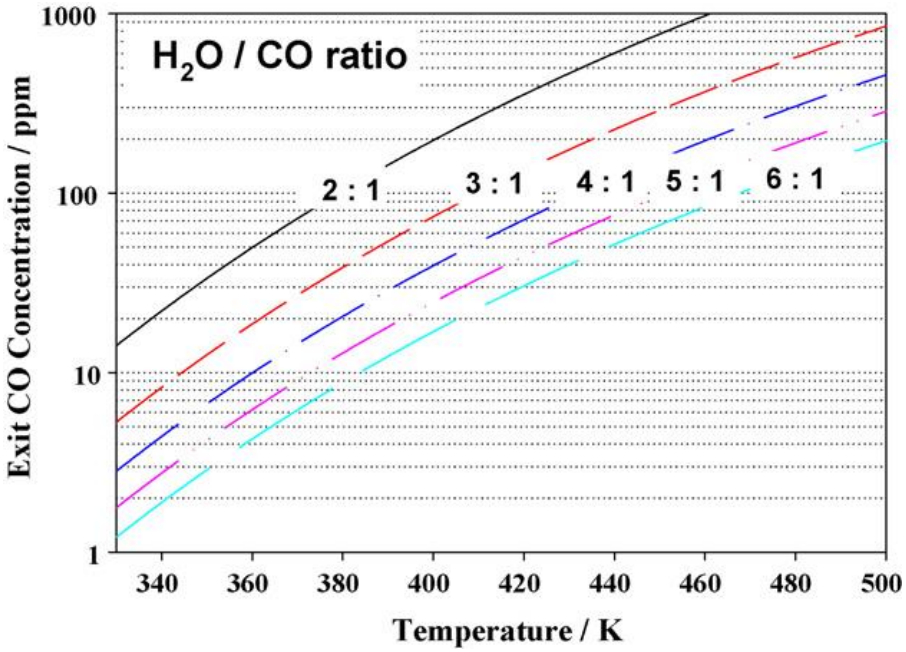

Figure 2.1 *Calculated equilibrium CO concentrations as a function of H_2O/CO ratio and temperature. Reprinted from [3] with permission of Elsevier.*

In adsorption, activated carbon of high surface area is commonly used to adsorb and desorb the contaminant of choice. Once the bed of the activated carbon material is saturated with the adsorbent, the process is stopped and the stream is diverted to another bed. The saturated bed can be removed and regenerated [4, 5]. In order to avoid frequent stops and diversion of the stream, a series of beds can be employed continuously. This is often referred to as pressure swing adsorption (PSA). In a typical PSA system, the adsorbent is pressurized and depressurized to generate a continuous stream of purified reformate [6]. One of the disadvantages of the adsorption technology is that high CO removal efficiencies are achieved only when working at high pressures. Therefore, this results to design complications, as the system contains high proportions of H_2 and energy consuming. Another drawback is that the materials used to trap the contaminants tend to lose their adsorption capacity over time. This forces the replacement of the entire series of beds.

Another alternative for reformate clean-up is the use of hydrogen selective membranes. Polymeric, metallic and inorganic membranes have been used to separate hydrogen from gaseous contaminants such as CO, CH_4 and CO_2. Most hydrogen selective membranes are designed in such a way that they allow only H_2 to penetrate through the membrane [4]. Metallic membranes, particularly palladium-based, exhibit the best hydrogen permeability [7]. However, these membranes undergo embrittlement and form hydrides when exposed to hydrogen at low temperatures [8]. These changes have been associated with the loss of selectivity in palladium membranes [9]. Other disadvantages include the high cost of palladium and deactivation by carbon compounds [10]. Most researchers in this field are exploring the use of palladium alloys to overcome these drawbacks [4, 11, 12].

Scrubbers are also a well know purification technology in the chemical industry. In this technique, liquid-stripping agents are used and the process involves the transfer of contaminants from the gas phase to the liquid phase, then back to the gas phase, before venting [13, 14]. Although this multistep process is viable for very large stationary installations, it is not popular for hydrogen purification.

Selective reactions have been extensively studied and continue to receive tremendous interest as a promising way to achieve reformate clean-up [15, 16]. This chapter will briefly focus on selective methanation (Sel Meth.) and extensively highlight recent advances in preferential CO oxidation (PROX), as clean-up processes. These reactions have the same goal of reducing CO levels before hydrogen fuel is used for energy generation. Hence, they are competing processes and only one would need to be employed, based on its inherent benefits.

2.1 Selective methanation

Selective CO methanation, as another way towards almost complete CO removal, has gained attention and has been widely studied. Since both CO and CO_2 are contained in the reformate mixture after the WGS reaction, *selective* refers to the importance of converting CO to CH_4

without transforming CO_2 to CH_4. Generally, CO methanation in a typical reformate dominates at lower temperatures and CO_2 methanation becomes more pronounced at elevated temperatures. This is associated with stronger adsorption of CO on the catalyst's active sites at lower temperatures. However, at higher temperatures, the CO adsorption strength is weakened and the undesirable CO_2 methanation becomes prevalent. Therefore, it is important to design a catalyst that will selectively convert CO in a selected temperature range. Both these reactions are highly exothermic and are represented in Equations 2.5 and 2.6. The methanation reaction takes place over a hydrogenation catalyst and can be viewed as the reversal of the steam reforming of methane. Methanation requires no additional gas component as it uses the hydrogen that is already present in the reformate. In this way, process complication is avoided and the CH_4 produced does not affect the fuel cell performance, but only acts as a diluent.

$$CO + 3H_2 \rightarrow CH_4 + H_2O \qquad \Delta H^0_{298} = -206 \text{ kJ/mol} \qquad (2.5)$$

$$CO_2 + 4H_2 \rightarrow CH_4 + 2H_2O \qquad \Delta H^0_{298} = -165 \text{ kJ/mol} \qquad (2.6)$$

$$CO_2 + H_2 \rightarrow CO + H_2O \qquad \Delta H^0_{298} = 41 \text{ kJ/mol} \qquad (2.7)$$

Removal of CO by selective methanation in a H_2-rich stream has been studied over different metal catalysts that include Ru, noble metals, Ni, Au and alloys of the aforementioned metals. Ni- and Ru-based catalysts have been the most effective catalysts for selective methanation, hence most of the published research focused on these two catalyst systems. In the early pioneering work by Baker *et al.* [17] and Rehmat and Randhava [18], Ru catalysts were reported to have highest methanation activity, followed by Ni catalysts. Although these catalysts were highly selective for CO hydrogenation in the presence of CO_2, the CO concentration used was relatively lower (0.29%) than the levels found in typical reformate streams. Ru/Al_2O_3 reduced CO levels from 0.29% to 10 – 20 ppm over the temperature range of 150 – 180 °C at relatively low space velocities (500 – 1000 h^{-1}). Rehmat and Randhava [18] further studied the catalytic behaviour of Ru/Al_2O_3 over a wide temperature range (125 – 300 °C) and high space velocities (9000 – 36000 h^{-1}). Their results showed that the catalyst was highly selective at temperatures below 250 °C. Increasing temperature above this point resulted in pronounced CO_2 methanation and the reverse water gas shift reaction (Equation 2.3), which increased the CO concentration. Takenaka and co-workers screened different supported metal catalysts for CO methanation [19]. Once again, Ru- and Ni-based systems were the most promising candidates and the activity was

found to be dependent on the type of the support used. ZrO_2-supported Ni and TiO_2-supported Ru catalysts were the best combinations for Sel Meth. These catalysts reduced CO levels from 0.5% to 20 ppm in a reformate generated from methane steam reforming.

There have been several attempts to develop and improve the performance of Ru-based catalysts. These have ranged from studying the effect of the preparation methods and metal loading, to support effect and particle size [20]. Microchannel reactors [21-24] and different reaction conditions have been studied to improve reactor efficiencies and optimize selectivity over a wide temperature window. Thus, Dangle and co-workers studied the effect of the preparation method, metal loading and particle size on the performance of Ru/γ-Al_2O_3 [25]. It was found that the activity increased with the metal loading, which is in agreement with the results reported by other authors [26]. The catalysts with the loading range of 3 – 7 wt% reduced CO levels from 0.9% to 10 – 20 ppm at temperatures between 215 – 220 °C. However, increasing the metal loading was accompanied by an increase in CO_2 methanation, corroborating the importance of choosing a metal loading that will balance activity and selectivity. In the same work, it was observed that the catalysts prepared by single-step and multi-step impregnation had different catalytic behavior. The single-step impregnation method produced a more active catalyst, reaching maximum CO conversion at 220 °C and showing high H_2 conversion due to CO_2 methanation. In contrast, the multistep catalyst reached maximum conversion at 240 °C. Notably, this catalyst converted less CO_2 even at high temperatures. The difference in the catalytic performance of the two catalysts was related to crystallite size, 10.9 and 34.2 nm for the single-step and multistep syntheses, respectively. Panagiotopoulou *et al.* also suggested that CO and CO_2 methanation reactions are structure sensitive, observing that larger Ru (Al_2O_3 and TiO_2) crystallites are more active[20].

Ruthenium, as the most used metal for Sel Meth, has been supported on different supports in efforts to design the best catalytic materials. Tekenaka *et al.* reported that smaller Ru particles ($\leq$ 5 nm) showed the best catalytic performance [19]. The catalytic activity decreased in order of $Ru/TiO_2 > Ru/Al_2O_3 > Ru/ZrO_2 > Ru/MgO$, while the crystallite sizes decreased in order of $Ru/MgO > Ru/ZrO_2 > Ru/Al_2O_3 > Ru/TiO_2$. Notably, their explanation contradicts the work by Panagiotopoulou and co-workers [20], discussed in the previous paragraph.

Although Ru-based catalysts are the preferred catalysts for methanation, Ni-based catalysts have also been extensively studied. Liu *et al.* [27] investigated the effect of Ni loading and found that the activity decreased with an increase in Ni loading, whereas Men *et al.* [21] reported better catalytic performance for higher metal loading (43 wt.%) in a microchannel reactor. The acid-base nature of the support also influences the methanation reaction. Men *et al.* [21] showed that Ni/Al_2O_3 displayed better activity than Ni/TiO_2. However, Tekenaka *et al.* [19] reported that the CO conversion followed the order of $Ni/MgO < Ni/Al_2O_3 < Ni/SiO_2 < Ni/TiO_2 < Ni/ZrO_2$.
The fact that there are opposing observations among researchers highlights the urgent need for further work on such catalysts in order to understand and perfect catalyst design and activation on different supports. Attempts to improve the methanation technique have involved coupling a Pd-membrane with a selective methanation catalyst [28]. The membrane traps most of the CO and CO_2 present and the catalyst converts trace amounts of CO remaining.

Different groups have proposed the use of multistage methanation by applying two or more kinds of catalysts [29-31]. The process reported by Li *et al.* reduced CO from 1% to levels below 10 ppm after two stages over Ru/Al_2O_3 [29].

In principle, methanation appears to be a viable and relatively simple process, without the need to add oxygen. However, it has some drawbacks. Most literature refers to gas composition containing CO levels below 0.5%. As it can be seen from Table 2.1, even with relatively low CO concentration, most catalytic studies demonstrated that it is difficult to reduce CO to acceptable levels of $\leq$ 10 ppm. When CO concentrations are present in the ~ 1% range, the methanation reaction is conducted with the penalty of fuel efficiency, i.e three molecules of hydrogen are sacrificed for each CO molecule converted to CH_4 (Equation 2.5). This easily escalates, since most methanation catalysts are active at high temperature, where an additional four hydrogen molecules are consumed for each CO_2 converted in undesired CO_2 methanation (Equation 2.6). Thus, it is a general view that methanation is not yet matured for deep CO removal in typical reformates. Hence, preferential CO oxidation has received far greater attention for deep CO clean-up in PEMFC systems.

Table 2.1 *Comparison of the catalytic performance of reported catalysts for CO methanation.*

Catalyst	Inlet CO level (%)	Temperature (°C)	Space velocity	Outlet CO level (ppm)	Reference
0.5%Ru/Al_2O_3	0.29	150 - 180	500-1000 h^{-1}	10 -20	Baker *et al*. [17]
0.5%Ru/α-Al_2O_3	0.3	250	9 000 h^{-1}	50	Rehmat and Randhava [18]
35%Ni/Al_2O_3	0.27	200	9 000 h^{-1}	60	Rehmat and Randhava [18]
5% Ru/TiO_2	0.5	220	2.525 mL g^{-1} min^{-1}	~20	Tekenaka *et al.* [19]
10%Ni/ZrO_2	0.5	280	2.525 mL g^{-1} min^{-1}	~20	Tekenaka *et al.* [19]
3%Ru/γ-Al_2O_3	0.9	220	13 500 h^{-1}	~10	Dangle *et al.* [25]
0.4%Ru/Al_2O_3→ 0.8%Ru/Al_2O_3	1→ 0.1	230 →150	2 500 h^{-1}	0.1% → < 10	Li *et al.* [29]

2.2 Total CO oxidation and preferential CO oxidation (PROX) in H_2-rich streams

Catalytic oxidation of CO is one of the most extensively studied reactions in heterogeneous catalysis. The foundation of the Langmuir theory of catalytic adsorption can be traced to this reaction [32]. Hence, CO oxidation has been widely studied to provide answers that allow researchers to probe surface properties of catalytic materials. During the past few decades, there has been a renewed interest in the reaction due to its relevance in pollution control and fuel cell applications. As one of the major toxic auto emission gases, CO removal is accomplished by catalytic converters using platinum group metal (PGM) catalysts. Due to increasing environmental concerns and auto emission regulations, there is a need for new and relatively cheap catalysts to transform the pollutants released from internal combustion engines. With CO methanation consuming a high amount of H_2, the oxidative removal of CO is regarded as the most effective and cost-efficient process for CO clean-up in fuel cells. Currently, there are tremendous efforts in the design of highly active and selective catalysts for CO oxidation in a H_2-rich stream. The process is referred to as preferential oxidation or PROX. Unfortunately, the incorporation of this process in the reformer, in addition to WGS reactors, increases complexity and adds extra cost to the PEMFC system. Nonetheless, it is widely considered as the most

promising purification method among all other methods. In summary, for the maximum operation and efficiency of a PEMFC, the reformate from steam reforming has to pass through two-staged WGS and PROX reactors to reduce CO content to acceptable levels, before it enters the MEA where electrochemical energy is generated (Figure 2.2).

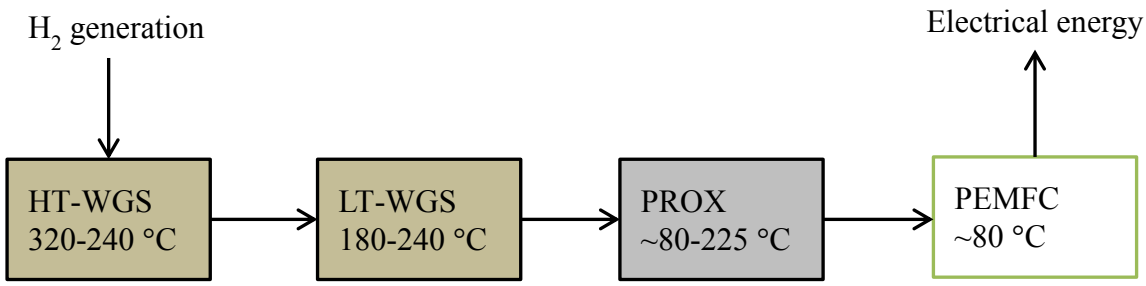

Figure 2.2 *The simplified description of the CO cleanup by water gas shift and PROX*

The key to the application of PROX is the development of a catalyst that meets the following important requirements:

* *The catalyst should be extremely active and highly selective for CO oxidation*. Thus, over the PROX catalyst, CO oxidation (Equation 2.8) should be a preferred reaction, rather than the oxidation of hydrogen (Equation 2.9) present in shifted reformate. For PROX in a reformate consisting of 1 vol% CO, it is important that CO conversion is above 99% before H_2 is used in the PEMFC.

$$CO + ½\ O_2 \rightarrow CO_2 \qquad \Delta H^0_{298} = -283.0\ kJ/mol \qquad (2.8)$$

$$½\ O_2 + H_2 \rightarrow H_2O \qquad \Delta H^0_{298} = -241.8\ kJ/mol \qquad (2.9)$$

* *The catalyst should operate optimally in a wide temperature window*. Because PROX catalysts are positioned between the low temperature WGS unit and the PEM fuel cell, the acceptable temperature range is between 80–225 °C to ensure efficient energy use. Above this range, the CO oxidation reaction might occur concurrently with the reverse WGS reaction (Equation 2.7) and/or the CO methanation reaction. On the other hand, catalysts that are active even at temperatures below that of the fuel cell are beneficial when PEM fuel cells

are used for transportation applications. However, the exact operating temperature is chosen based on two key drivers of the catalyst, the *activity* and *selectivity*.

* *PROX catalysts should be well-suited for conditions of the upstream processes*. Specifically, they should show good resistance to CO_2 and steam from the upstream WGS processes. However, this is not to downplay the importance and validity of the experiments performed in the absence of CO_2 and steam since, they provide scientific knowledge that could not be gained in the presence of CO_2 and steam.

Catalyst formulations for PROX can be classified into three categories, based on the active metal used, viz. platinum group metal catalysts (Pt, Pd, Ru, Rh and Ir), gold catalysts and non-precious metal oxide catalysts. In this section, the recent progress in development of promising PROX catalysts is reviewed. In addition, factors that influence their activity and the mechanisms they adopt will be highlighted. Special attention is given to ceria-based oxides and supported gold catalysts since they are part of the work conducted in our laboratories.

2.3 Supported PGM-based catalysts

PGM-based catalysts have been widely studied and are practically applied for PROX applications. As early as in the 1960s, Pt/Al_2O_3 catalysts were used by the Engelhard Corporation in hydrogen plants to remove CO prior to ammonia synthesis [33]. Since then, different catalyst formulations have been developed to purify hydrogen for PEMFC applications. The commonly studied PGMs are Pt, Pd, Rh and Ru supported on materials such as silica, alumina, zeolites and ceria. Oh and Sinkevitch studied and compared the catalytic performance of different alumina-supported Pt, Pd, Rh and Ru catalysts [34]. They observed that Ru/Al_2O_3 and Rh/Al_2O_3 were better formulations, giving almost complete CO oxidation at 100 °C. On the other hand, the Pt/Al_2O_3 catalyst gave complete CO conversion at 200 °C, while Pd/Al_2O_3 achieved maximum conversion of 85% at 350 °C. The poor catalytic behaviour of Pd/Al_2O_3 has since been confirmed and explained by other researchers [35-37]. At low temperature, this is often attributed to the formation of the β-hydride, preventing the possibility of CO oxidation. At high temperature, palladium is known to selectively adsorb hydrogen rather than CO, leading to hydrogen oxidation instead of the desired CO oxidation [37]. Although the experiments

performed by Oh and Sinkevitch provided valuable information, the gas composition used contained a very low H_2 concentration (0.85%) compared to the H_2 concentration that is present in the reformate gas mixture. It has since become a widely held view that, under ideal PROX conditions, supported PGM (non-promoted monometallic) catalysts are not very active at temperatures below 100 °C, but significant activities have been obtained at temperatures above 150 °C. Manasilp and co-workers have shown that complete CO conversion over 2 wt% Pt/Al_2O_3 is not easily obtained even at temperatures as high as 170 °C [38]. In their work, a 80% conversion was achieved at 170 °C, using 0.5% O_2. Complete conversion was observed at a temperature range of 130 to 150 °C, after increasing O_2 content to 1.35%. The presence of H_2O appeared to improve the activity, while CO_2 had the opposite effect. Avgouropolous *et al*. reported improved activity using a 5wt% $Pt/\gamma\text{-}Al_2O_3$ catalyst [39]. This catalyst showed complete CO conversion at 160 °C and its performance was not significantly affected by the presence of H_2O and CO_2.

Many researchers have used various zeolite materials as supports for Pt catalysts. Such supports include ZSM-5 [40], mordenite [41-43] and, type A, X and Y zeolites [43-46]. Igarashi and co-workers studied the effect of different zeolite materials used to support Pt [43]. The results showed that PROX selectivity over the Pt-zeolite catalysts decreased in the following order: Pt/A-zeolite > Pt/mordenite > Pt/X-zeolite > Pt/Al_2O_3. All examined zeolite-supported catalysts required less O_2 to achieve complete CO conversion, compared to the conventional Pt/Al_2O_3. However, the O_2 content used for all catalysts was above 1% and complete oxidation was observed at high temperatures (>200 °C). Pt/mordenite was the most promising formulation, showing the highest conversion and H_2O resistance.

In order to improve the activity of conventional PGM catalysts at low temperatures, researchers have focused on understanding their mechanisms. To date, it is a widely held view that a Langmuir-Hinshelwood (L-H) mechanism applies during PROX, where O_2, CO and H_2 compete for adsorption on the same active site [47-49]. It has been shown that at low temperatures, CO predominantly adsorbs on the active sites, inhibiting oxygen adsorption [49]. The adsorption of

O_2 and H_2 can only occur at elevated temperatures (> 150 °C) when CO desorption is possible. Thus, the O_2 adsorption or CO desorption has been proposed as the rate determining step for conventional PGM catalysts [47, 49-51]. It is, therefore, necessary to work at high temperatures to achieve reasonable CO conversion, although this comes at the expense of poor selectivity. It appears that an attempt to enhance the activity of these catalysts at low temperatures would require new catalyst formulations to weaken CO adsorption on the metal and/or create O_2 adsorption/activation sites. This modifies the competitive L-H mechanism into a non-competitive dual-site pathway. Considering this view, the performance of PGM catalysts has been improved by implementing the following approaches (Figure 2.3):

* Using reducible oxides as supports for PGMs (route A) or as promoters (route C). The reducible oxide can act as O_2 adsorption/activation sites, while weakening CO adsorption on the PGM.

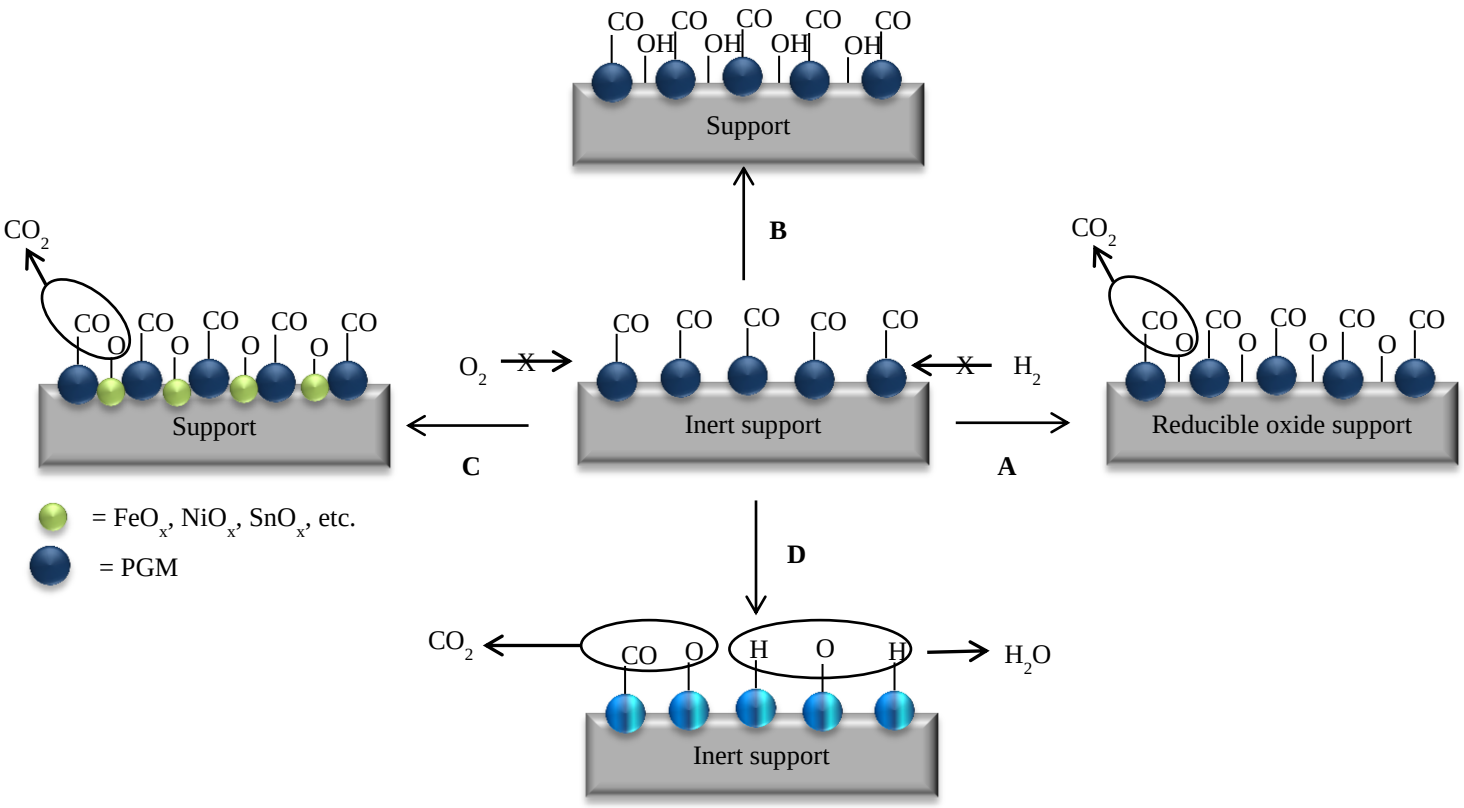

Figure 2.3 *Conceptual representation of reported ways of enhancing the PROX activity of PGM-based catalysts. Adapted from reference [52]with permission from the Royal Society of Chemistry*

* Promoting the catalysts by adding alkali or alkali earth metal cations to weaken the CO adsorption on the PGM. However, it has been proposed that the promotional effect is driven by reactive OH groups that are close to the CO-adsorbing PGM metal (route B).
* Introducing a second transition metal, in addition to the PGM, to form a different bimetallic structure that interacts differently with CO (route D).

Among the reducible metal oxides, ceria and iron oxides have been widely studied as favourable supports or promoters of PGM catalysts. The interest around ceria as a support for these catalysts is due to its oxygen storage capacity (OSC) properties, which in turn influences oxygen supply and subsequent oxidation [53, 54]. The use of CeO_2 [35, 53, 55-58] and $Ce_{1-x}Zr_xO_{2-\delta}$ [35, 59-61], instead of Al_2O_3, significantly improved the activity of the Pt catalyst at low temperatures, 60 to 80 °C. Complete CO conversion over these catalysts was achieved in excess oxygen, but the selectivity was compromised. The involvement of the surface oxygen from the support has been shown by O_2-exchange experiments and the observation of zero order O_2 dependency [62-64]. This confirms the validity of the dual-site non-competitive L-H mechanism where the ceria support adsorbs/activates oxygen atoms before reacting with adsorbed CO at the metal-support interface or via spill-over. In case of $Pt/Ce_{1-x}Zr_xO_{2-\delta}$, where the OSC and oxygen mobility has been enhanced by doping, the catalyst is not only active for CO oxidation but for undesirable hydrogen oxidation as well [60]. The conceptual representation of the dual-site L-H pathway followed by reducible oxide-supported PGM catalysts is represented by route A of Figure 2.3.

The promotional effect of iron or iron oxide was first reported by Korotkikh and co-workers [65]. The FeO_x-promoted catalyst was found to be more active than conventional Pt/Al_2O_3, showing improved CO conversion from 13% to 68%. The iron promotion appears to be dependent on the support. For instance, Fe oxide promoted Pt/zeolites catalysts are known to be more active relative to Fe promoted Pt/Al_2O_3 [42, 66-68]. With regard to Fe oxide promoted Pt/Al_2O_3, the activity has been associated with changes in the electronic states of platinum metal particles [69]. For Pt/zeolite formulations, the addition of Fe promoter results in low CO coverage and Pt-CO bond strength [68]. After being promoted, the activity of Pt/zeolite materials

followed the order, Pt/type-A > Pt/mordenite > Pt/type-X. From a list of Pt-Fe/zeolite catalysts studied by Watanabe's group, it appears that a 4 wt% Pt – 2 wt% Fe/mordenite is the most promising catalyst formulation [68]. This catalyst achieved complete CO conversion in excess O_2 in a temperature range of 80 – 150 °C. No loss in activity was observed, even in the presence of CO_2 and H_2O. One of the best results thus far was obtained using a FeO_x promoted Pt/nano-SiO_2 catalyst [70]. The resulting material is highly active and selective, even at room temperature. It has since been tested on a 1 kW PEMFC system where it proved to be stable for at least 900 h. The superior performance of Pt/SiO_2 catalysts was first reported by Fukuoka and co-workers [52, 71]. They supported Pt nanoparticles on FSM-type mesoporous silica and obtained a highly active and selective catalyst. Based on isotopic tracer and IR experiments, they proposed the involvement of reactive OH groups in CO oxidation (route B in Figure 2.3) [71].

Another option for improving the performance of Pt catalysts is to introduce a second noble metal to form a different bimetallic structure. This approach is inspired by electrocatalysis findings which have shown that alloys have improved CO-tolerance due to reduced CO adsorption [72, 73]. Pt-Ru on SiO_2 [74], Al_2O_3 [75], and mordenite [76] form part of the commonly reported bimetallic systems. Such catalysts have been reported to be more active at low temperatures, compared to their monometallic counterparts, and in some cases they have even wider temperature of operation [74]. Pt-Au/zeolite-A has also shown promising PROX activity, achieving complete CO conversion at a temperature at least 50 °C lower than that of the monometallic catalyst [77]. Eichhorn's group prepared different PGM-Pt core-shell structures, where the core PGM (Ru, Rh, Ir, Pd and Au) nanoparticles are covered by Pt [78, 79]. From these studies, the Ru-Pt catalyst displayed weakened CO adsorption and high PROX activity at temperatures as low as 20 °C. Other reported promoted catalysts include the following combinations, Pt-Mn [80], Pt-Ni [81, 82], Pt-Cu [83], Pt-Co [83-86] and Pt-Sn [87, 88].

Although this section has focused on Pt-based catalysts, other PGM metals, on various supports, are cited in literature as promising candidates for PROX. After Oh and Senkevitch reported Ru and Rh as good metals catalysts for selective CO oxidation, other researchers have considered

these metals, but to a lesser extent compared to Pt. Han *et al*. have compared the activity of a commercial Rh catalyst (Rh/MgO) with those of $Ru/\gamma\text{-}Al_2O_3$ and $Pt/\gamma\text{-}Al_2O_3$ [89]. The Rh catalyst was reported to be effective only at high temperature (250 °C), while $Ru/\gamma\text{-}Al_2O_3$ and $Pt/\gamma\text{-}Al_2O_3$ showed promising results at 150 and 200 °C, respectively. Specchia's group has since supported Rh on type-A zeolites (3A, 4A and 5A), Al_2O_3, TiO_2 and CeO_2 [90, 91]. From the examined catalyst formulations, 1% Rh/3A-zeolite displayed better performance at low temperatures (80 - 140 °C), achieving ~10 ppm exit CO concentration in the presence of excess oxygen.

The catalytic behaviour of supported Ru catalysts, for PROX, has also been explored by different groups [92-104]. The performance of these catalysts is known to be sensitive and dependent on factors such as pretreatment, Ru precursor, and reducing agent used. For instance Echigo *et al*. reported that pre-reduced Ru/Al_2O_3 catalysts are capable of reducing CO concentrations to levels below 10 ppm over a much wider temperature window (85 – 170 °C), compared to unreduced catalysts [96-102]. In addition, the study of Chin *et al*. on Ru/SiO_2 and Ru/Al_2O_3 catalysts revealed that formulations prepared from a nitrate precursor are comparatively more active than those prepared from $RuCl_3$ [103]. Despite poor performance in the presence of CO_2 and deactivation due to metal sintering, these catalysts completely removed CO in reasonable temperature ranges, in the absence of H_2O and CO_2. For Ru/SiO_2 catalyst, complete CO removal was achieved from 120 to 150 °C and for Ru/Al_2O_3, this was achieved in a temperature range from 160 to 180 °C. Han *et al*. have since demonstrated that the presence of surface Ru^0 results in high PROX activity [92]. Ruthenium catalysts are unique from other PGM analogues due to their ability to perform CO/CO_2 methanation (Equation 2.5 and 2.6) and reverse water gas shift reactions (Equation 2.7), in addition to CO oxidation. As mentioned in Section 2.1, the methanation process results in hydrogen consumption, while RWGS counteracts CO reduction. Therefore, regardless of ruthenium's low cost and its promising PROX activity (relative to other PGMs), interest in the application of Ru-based PROX catalysts has stagnated. In literature, there are many PGM-based catalysts that are active and selective for PROX under different conditions. A system also worth-mentioning is that of Ir/CeO_2. This catalyst has been reported to display reasonable PROX activity, but less than that observed for Pt-based catalysts [105, 106]. The selectivity of Ir/CeO_2 has been improved by incorporating Ir into the ceria matrix [106].

2.3.1 Gold catalysts

Over the long history of catalysis, gold was regarded as chemically inert and overlooked as an important component of catalyst formulations. Therefore, its reactivity and practical applications have not been as fully investigated compared to PGMs. This is regardless of the fact that more gold is being mined than the PGMs. It is partly due to the old, widely held, view that bulk gold is one of the most stable and noble substances, which is devoid of any interesting catalytic behaviour. This viewpoint of the nobility of gold relied on the fact that bulk gold adsorbs neither oxygen nor hydrogen to any meaningful degree at room temperature [107]. In spite of this consensus, the first indication that the gold has catalytic properties when dispersed as small particles on the support, surfaced in the 1970s. The work conducted by Bond and Sermon on the hydrogenation of alkenes and alkynes gave the first indication of dissociative chemisorption of hydrogen on supported gold particles at ≈ 100 °C [108, 109]. A little later, the promising and interesting performance of supported gold catalysts on oxygen and hydrogen transfer reactions was reported by Paravano's group [110, 111] and this work was reviewed by Schwank [112].

The seminal works of the 1980s demonstrated that gold, in a suitable form, displays some interesting catalytic properties. These early studies in gold catalysis were steered by Haruta *et al*. [113] and Hutchings and co-workers [114] for their respective discoveries of gold catalyzed low-temperature CO oxidation and ethyne hydrochlorination. Haruta's work on gold catalysis was inspired by the volcano-like plots, drawn between the H_2 oxidation activity of metal oxides and the metal-oxygen bond strength, as shown in Figure 2.4 [115].

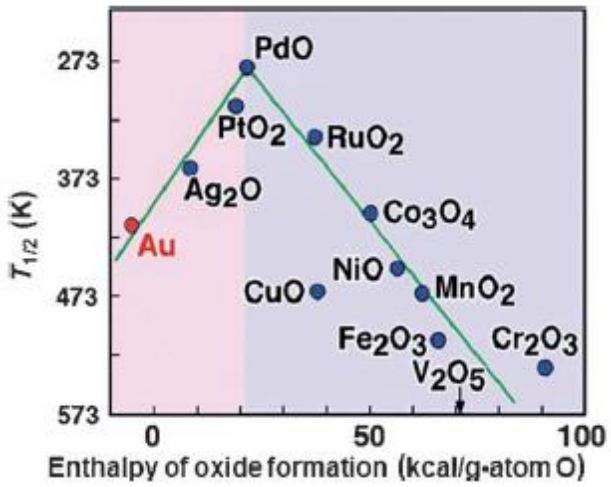

Figure 2.4 *Volcano-like plot based on H_2 oxidation activity and the enthalpy of oxide formation. Reprinted from [115] with permission from Elsevier.*

In the plot (Figure 2.4), the catalytic activities of the metal oxides are plotted based on the temperature at which 50% of H_2 oxidation ($T_{1/2}$) is achieved, and the metal-oxygen bond strengths are inferred from the enthalpy of formation of metal oxides. It was assumed that a combination of the oxides of the metals that are positioned on the left side (Ag and Au) with those on the opposite side (Mn, Fe, Co and Ni) of the volcano plot would result in active composite oxides, matching the performance observed for PtO_2. In the extension of this work, it was found that the catalysts were composed of gold nanoparticles supported on metal oxides. These observations revived the interest of scientists to explore the catalytic behavior of gold in different reactions. The credit for the advancement of gold catalysis is often given to Haruta and co-workers because they have extensively studied the catalytic performance of supported gold catalysts in reactions such as low temperature CO oxidation [113], preferential CO oxidation (PROX), water gas shift [116], hydrogenation [117-119] and oxidation of hydrocarbons [120]. Since then, there has been a tremendous interest in mastering the preparation and understanding of the working of supported gold catalysts in different chemical reactions.

To date, gold-based catalysts are known to catalyze numerous chemical reactions, with potential applications in emission control and fuel cell technology. It has been shown in literature that the catalytic performance of supported gold catalysts is mostly dependent on the preparation method [121-126], particle size [127], choice of the support [127-129] and the effect of water in the feed

[130, 131]. Although there are other factors contributing to the activity of supported gold catalysts, the aforementioned are ranked high in the hierarchy. This section highlights recent advances in gold catalysis, especially in the techniques for preparing active gold catalysts and the factors that influence catalytic performance of gold catalysts in specific oxidation reactions. Although gold catalysis has been reported in homogenous systems, this section will only focus on the heterogeneous applications.

2.3.1.1 Preparation of supported gold catalysts

Various methods have been reported for the preparation of supported gold catalysts. These methods can be classified into two categories [132]:

* Co-precipitation or sol-gel: *the method is based on the formation of both support and gold precursors which can be transformed into gold particles strongly attached onto the metal oxide support upon calcination.*
* Impregnation, deposition-precipitation (DP), ion adsorption or exchange, chemical vapour deposition and deposition of colloidal gold: *the technique involves the application of the gold precursor on the preformed oxide support and subjecting the material to calcination.*

Different research groups have shown that these preparation methods are open to modifications. The published works reflect no consensus on the rationale behind the numerous variations and thermal treatment conditions. The modifications account for the different activities reported, and the importance attached to the preparation method. Although gold chloride ($AuCl_3$) [133] is sometimes used, chloroauric acid ($HAuCl_4.3H_2O$) [127, 128, 134, 135] is commonly used as the Au^{3+} precursor for making supported gold catalysts. Hence, in most cases, gold exists in the +3 oxidation state prior to thermal treatment. Since auric oxide (Au_2O_3) is unstable, the Au^{3+} species can be reduced to Au^0 by thermal treatment at temperatures up to 300 °C [132]. However, it has been reported that some of the ionic species may remain after thermal treatment [136]. The first generation of gold catalysts was prepared by an impregnation method, partly because of its inherent simplicity [119]. Those skilled in the art of designing such catalysts have since realized that this method produces catalysts with Au particle size ($\geq$ 30 nm) that falls outside the boundaries (2-10 nm) that are traditionally associated with high activity [137]. Thus, catalysts

obtained by this method often show poor catalytic performance and have had limited success, in particular, for CO oxidation reactions. This phenomenon is commonly related to the presence of chloride ions which promote mobility and coagulation of gold particles during thermal conditioning [138, 139].

Haruta's group and others have demonstrated that effective metal oxide supported gold catalysts can be produced by the co-precipitation method [140]. Generally, the method involves the formation of co-precipitates from an aqueous mixture of $HAuCl_4.3H_2O$ and a nitrate of the subsequent corresponding metal oxide support in the presence of a neutralizing agent. In order to accelerate the hydrolysis of the $[AuCl_4]^-$ complex, the reaction is often conducted at 70 °C and Na_2CO_3 is preferred as a neutralizing base to maintain a pH of ~ 9. A catalyst with highly dispersed small Au particles is achieved by washing, drying and calcination of the co-precipitates. The drawback of this preparation method is that it is only feasible for base metals that are capable of forming carbonates or hydroxides in the pH range of 6 to10, where $Au(OH)_3$ also co-precipitates [132]. Catalyst formulations that have been generated using this method include Au/Fe_2O_3, Au/Co_3O_4, Au/Al_2O_3, Au/In_2O_3, Au/NiO, Au/MgO, Au/ZnO and Au/La_2O_3. Among these, Au/Fe_2O_3, Au/Co_3O_4 and Au/NiO catalysts are some of the most successful formulations that have been prepared by this method, showing excellent CO oxidation activity at temperatures as low as -70 °C [140]. Nonetheless, this technique is becoming less used, as it has been suggested that some of the gold particles could be embedded in the bulk support during the preparation.

The most effective technique, to date, for the preparation of supported gold catalysts is the deposition-precipitation (DP) method. Geus and co-workers pioneered this method for the synthesis of supported nickel and copper catalysts [141]. It has since been developed for the preparation of gold-based systems. Deposition-precipitation, although seemingly a simple preparation method, requires careful control of variable parameters such as the concentration of $HAuCl_4$ solution, the base used to control the pH, the reaction temperature, and the calcination. Alteration of these parameters can lead to the formation of catalysts with different catalytic behaviour. In this method, gold species are deposited onto the support as the pH (6-10) and temperature (rt – 70 °C) values of the suspension of $HAuCl_4.3H_2O$ (~$1x10^{-3}$ M) and the support

are adjusted to fixed values. Sodium hydroxide and sodium carbonate are often used to control the pH, while urea [142, 143] has been occasionally used when higher metal loadings are targeted. Increasing the pH during the reaction facilitates gold precipitation, as a hydroxide. The precursor must be thoroughly washed, dried and calcined (< 300 °C) to get the final material.

Among other synthesis parameters, pH appears to be a decisive factor that determines the chemical nature, particle size and the activity of the gold species. Several studies have been conducted in order to investigate the importance and influence of the pH during gold deposition. The increase in the pH of a $HAuCl_4$ solution induces changes in the nature of gold species in solution. Nechayev *et al*. calculated the dependence of the concentrations of anionic gold species on the pH [144]. Their thermodynamic calculations showed that three sequential reactions occur as the pH is increased (Table 2.2), viz. displacement of Cl^- ions from the $[AuCl_4]^-$ complex by H_2O (1 and 3), deprotonation of the neutral hydrated species (2 and 4) and (iii) replacement of Cl^- ions by OH^- (5 and 6). The equilibrium constants presented in Table 2.2 have been used to predict probable concentrations of different gold species as the extent of hydrolysis is increased (Figure 2.5) [134, 135].

Table 2. 2 *Gold speciation of the $HAuCl_4$ solution showing hydrolysis progression [134].*

$[AuCl_4]^- + H_2O \leftrightarrow AuCl_3(H_2O) + Cl^-$	$K_1 = 4 \times 10^{-6}$	1
$AuCl_3(H_2O) \leftrightarrow [AuCl_3(OH)]^- + H^+$	$K_2 = 2.6 \times 10^{-1}$	2
$[AuCl_3(OH)]^- + H_2O \leftrightarrow AuCl_2(H_2O)(OH) + Cl^-$	$K_3 = 3.6 \times 10^{-3}$	3
$AuCl_2(H_2O)(OH) \leftrightarrow [AuCl_2(OH)_2]^- + H^+$	$K_4 = 2.8 \times 10^{-5}$	4
$[AuCl_2(OH)_2]^- + H_2O \leftrightarrow [AuCl(OH)_3]^- + Cl^- + H^+$	$K_5 = 9.0 \times 10^{-9}$	5
$[AuCl(OH)_3]^- + H_2O \leftrightarrow [Au(OH)_4]^- + Cl^- + H^+$	$K_6 = 1.0 \times 10^{-10}$	6

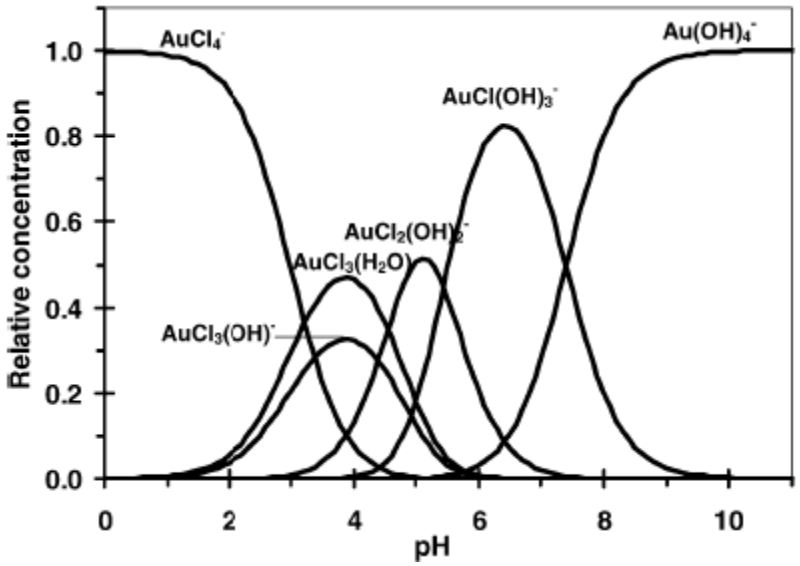

Figure 2.5 *Estimated dependence of the concentrations of gold anionic species on the pH. Reprinted with permission from Elsevier [134, 144].*

Figure 2.5 shows that gold predominantly exits as the neutral $AuCl_3.H_2O$ at the pH interval of 3-4, while there is high probability that $[AuCl(OH)_3]^-$ species dominate at pH 7, which is often the chosen range for gold deposition on many supports. At pH 10, which is often regarded as the utmost permitted pH for deposition precipitation, gold is mostly present as the fully hydrolyzed $[Au(OH)_4]^-$ anion. In the DP method, the adhesion of hydrolyzed species such as $[Au(OH)_nCl_{4-n}]^-$ (n = 1-3) to the support, is guided by the concept of electrostatic interaction between the two components [145]. Figure 2.6 gives a pictorial representation of the DP method.

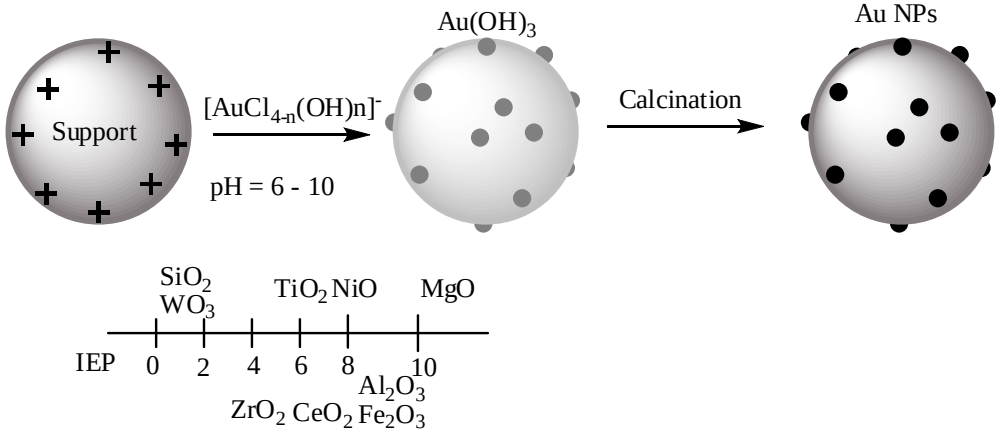

Figure 2.6 *Schematic representation of deposition-precipitation method and isoelectric points of different supports. The scheme is adapted from reference [146], with permission from Wiley.*

At the pH values below the isoelectric point (IEP) of the support, the negatively charged gold species can be adsorbed because the surface is mainly positively charged. However, for most supports, this pH range is within the borders where there is less hydrolysis of the Au-Cl bonds and the presence of the chloride facilitates the mobility of Au on the support, resulting in large gold particles [138, 139]. Systemic and detailed studies have accordingly showed that catalysts prepared below a pH of 6 have poor performance, despite high gold deposition efficiency. Poor catalytic activity could be attributed to large particle size [147]. On the other hand, catalysts prepared in the range of pH 7 to 10 involve the adsorption of highly hydrolyzed gold species (with less chloride content) and have been found to show excellent CO oxidation due to a markedly reduced Au particle size [134, 135, 145, 147]. However, for supports with the IEPs below this preparation pH, low deposition efficiency is expected, impacting on the catalytic activity. Hence, DP is not a feasible preparation method for supporting gold on metal oxides supports with IEP below pH 5. Examples of such materials include acidic supports such as SiO_2 (IEP = 2), SiO_2-Al_2O_3 (IEP = 1), and WO_3 (IEP = 1) [148]. Haruta's group has highlighted the importance of preparing Au/TiO_2 above pH 6 if particle sizes below 4 nm are to be obtained [127]. Moreau and Bond have shown that pH 9 is the optimum value for the preparation of highly active Au/TiO_2 catalysts for CO oxidation [145]. Figure 2.7 shows the comparison of the catalytic performance displayed by catalysts prepared at different pH values [145].

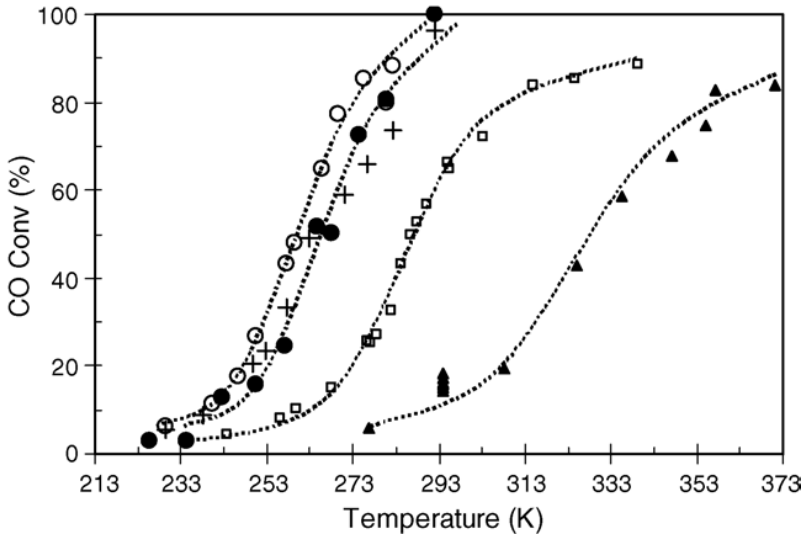

Figure 2.7 *CO conversion as a function of temperature for Au/TiO_2 catalysts prepared at different temperatures; ▲= pH 3,□ = pH 5,○= pH 7, + = pH 8 and ● = pH 9 (reprinted with permission from Elsevier) [145].*

To date, the DP method has been used to deposit gold on a wide range of supports and catalysts obtained have demonstrated very effective CO oxidation and PROX performance. Commercial gold catalysts are also prepared by this technique [148]. Other preparation methods, e.g. direct anion exchange [149, 150], chemical vapour deposition [151, 152] and the co-sputtering method [153-155] have been employed to prepare gold catalysts supported on metal oxides. However, these approaches are still not considered as the methods of choice for the preparation of robust PROX catalysts.

2.3.1.2 The nature of active gold: Influence of the support, oxidation state and mechanism

The most important prerequisite for achieving high activity on supported gold catalysts is the size of the gold nanoparticles. In most catalytic reactions, catalysts composed of Au particles of $\leq$ 5 nm show excellent activity. It has been highlighted in Section 2.3.1.1 that the gold particle size can be controlled by the preparation methods and its related variable parameters. Although a comparison of published catalytic data shows that CO oxidation activity over gold-based catalysts is primarily dictated by particle size (Figure 2.8) [156], the contact structure of Au nanoparticles and the support also plays an important role in ensuring that gold remains as nanoparticles even after calcination [148]. When gold is supported on semiconductive metal oxides such as Co_3O_4, α-Fe_2O_3, NiO and TiO_2, more stable catalysts are formed due to strong Au-support interaction, compared to catalyst formulations that include insulating supports such as Al_2O_3 and SiO_2 [148]. It has been suggested that a better configuration for the contact structure is an epitaxial contact, where gold sits on the support with its densely packed (111) plane exposed [148, 157]. Therefore, it is not surprising that the catalytic behaviour of gold catalysts is also influenced by the chemical nature of the support. In the case of Au/TiO_2, Haruta *et al.* have emphasized that hemispherical gold metal particles are more effective for CO oxidation and epoxidation, compared to spherical ones [148, 158].

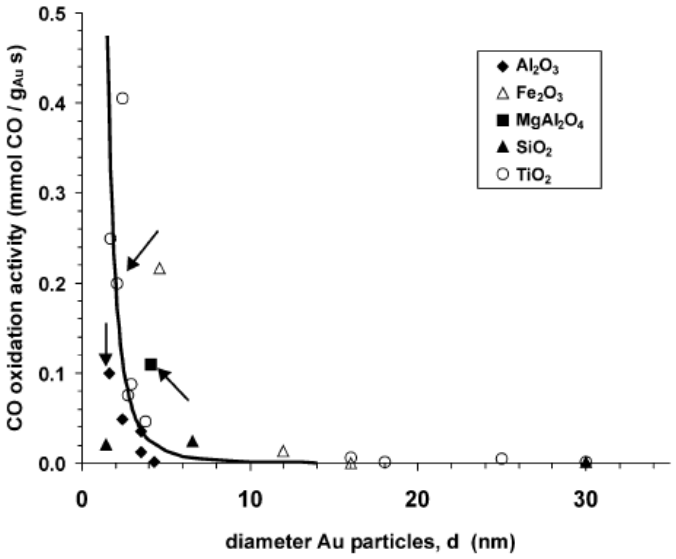

Figure 2.8 *Comparison of measured activities for CO oxidation over different Au catalysts as a function of the average Au particle size (reprinted with permission from Elsevier) [156].*

Au particle size distribution over different supports differs, despite using the same preparation method. For example, Au particle sizes larger than 30 nm have been reported to exist on supports such as CdO, Cr_2O_3 and SiO_2 [129, 159]. Therefore, the support may directly or indirectly affect the reaction by either influencing Au particle size or by electronic interaction with Au nanoparticles. Rousset and co-workers have studied the direct effect of the support by depositing the same loading of gold with comparable diameters (~ 3 nm) on Al_2O_3, ZrO_2 and TiO_2 [160]. In their studies, the CO oxidation activity of the catalysts was found to be dependent on the support and increased in the order: $Au/TiO_2 > Au/ZrO_2 > Au/\gamma\text{-}Al_2O_3$. Based on the X-ray photoemission measurements, the authors concluded that Au was present in the zero oxidation state and the variation of Au ($4f_{7/2}$) binding energies suggested a possible metal-support electronic interaction.

Based on numerous reports, there is a consensus that reducible metal oxides such as Fe_2O_3, TiO_2, CeO_2, ZrO_2, Co_3O_4 and ZnO are the best supports to produce highly active gold catalysts [161]. Because such supports tend to have oxide ion vacancies on their surfaces, they are capable of binding and providing active oxygen species required for catalytic progression. For supported gold catalysts, it is presumed that vacancies are concentrated near gold particles because of the

Schottky junction at the metal-semiconductor interface [162]. Individual reports have revealed that the activity of Au/ZrO_2 [163] and Au/CeO_2 [164] catalysts can be enhanced by employing well-defined nanocrystalline supports (ZrO_2 and CeO_2), rich in anion vacancies. On nanocrystalline CeO_2 supported catalysts, the presence of superoxide (O_2^-) and peroxide (O_2^{2-}) species has been identified by Raman spectroscopy [164]. These species are presumed to be active oxygen species responsible for CO transformation at the metal-support perimeter. The superiority of Iwasawa's Au/FeO_x catalyst has been associated with easy reducibility and the presence of anion vacancies [165]. In contact with ferric oxide and ceria, XPS and Mössbauer measurements often show gold in ionic states (Au^+ and Au^{3+}) [136, 166]. In the latter, it has been suggested that ionic gold may represent gold ions dissolved into the fluorite CeO_2 support [136]. In the case of Fe_2O_3, the highly active Au^{3+} species has been linked to the oxyhydroxide ($AuO(OH).xH_2O$) [166].

A number of CO oxidation studies over gold supported on reducible oxides points to a mechanism that involves "collaboration" between metal particles and the support [148, 161, 167-170]. The general consensus is that CO is largely chemisorbed on metallic gold particles. The active oxygen species is either adsorbed on the surface vacancies of the support, or the lattice oxygen species at the metal-support interface is directly used in a route that can be regarded as a modified Mars-van Krevelen mechanism [170]. In the latter case, O_2 from the feed is used to replenish lattice oxygen and the route is more plausible for more easily reducible oxide supports such as CeO_2 and Fe_2O_3. The two possibilities are depicted in Figure 2.9. Schubert *et al*. reported that the turn over frequency (TOF) of gold catalysts supported on reducible oxide supports is not dependent on the Au particle size, since oxygen dissociation is not a rate limiting step [161]. They classified such supports as *active* supports.

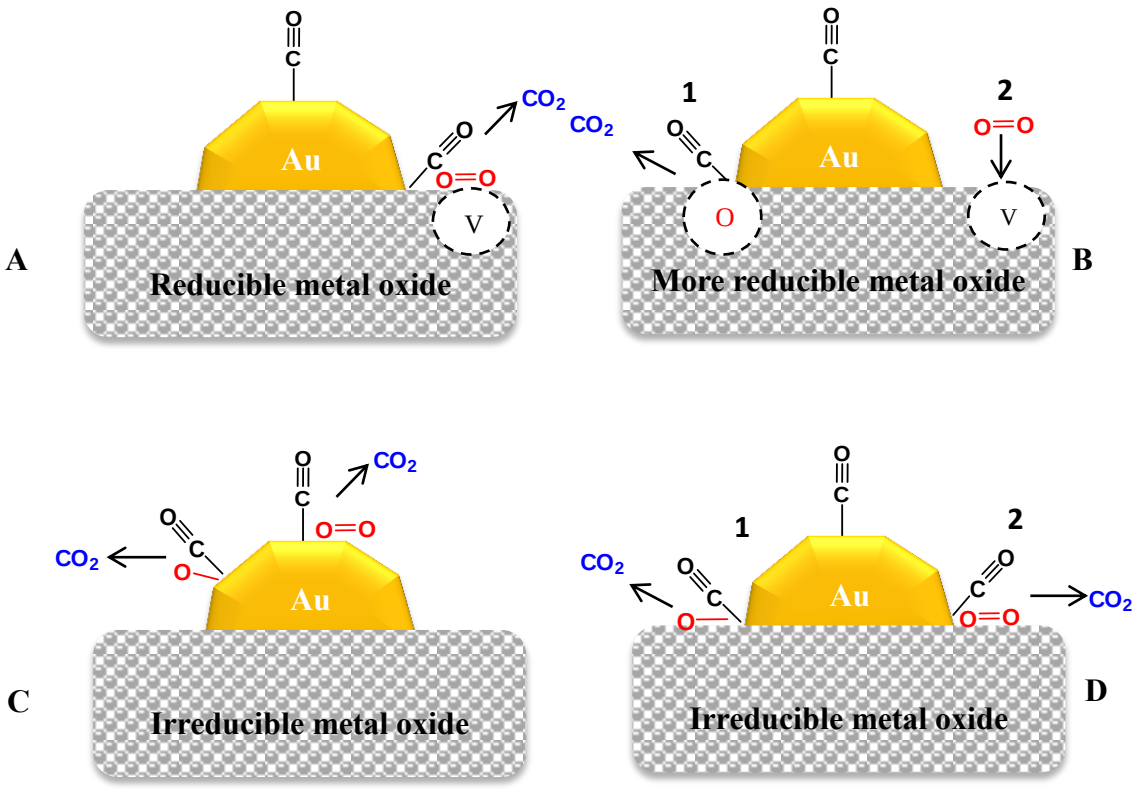

Figure 2.9 *General schematic representation of possible reaction pathways proposed for the CO oxidation over gold catalysts supported on reducible (A), more easily reducible (B) and irreducible oxides (C and D).*

Generally, supporting gold on activated carbon, alumina and acidic support materials, such as Al_2O_3-SiO_2, SiO_2 and WO_3 produces less active catalyst formulations [171]. It is hardly conceivable that such supports can bind, activate and/or supply oxygen required the reaction progression. Hence, there is uncertainty about the nature of the active site for oxygen activation and the active oxygen species, making it difficult to construct a plausible CO oxidation mechanism over such formulations. Schubert's group classified such supports as *inert* supports [161].

Although several theoretical studies have inferred that weakly bound molecular O_2 represents active oxygen, calculated absorption energies are low, suggesting that such species are highly unstable and unlikely to be active oxygen species at room temperature and above [169, 172,

173]. It has been proposed that CO oxidation over Au supported on irreducible oxides proceeds only on metallic gold, where the TOF is strongly dependent on the Au particle size [161]. As shown in Figure 2.9, the active oxygen species is either atomically or molecularly chemisorbed oxygen on the Au nanoparticles (route C) [161, 172]. Alternatively, molecularly or atomically chemisorbed oxygen reacts with CO at the gold-support interface (route D) [168, 172]. The mechanisms highlighted in this section are not the only proposed mechanisms, but they are commonly acceptable. Detailed information about CO oxidation mechanisms associated with gold catalysts can be found in different books [132] and review articles [168, 174, 175].

2.3.1.3 The effect of moisture or water

Several studies have shown that the presence of moisture or water in the reactant gas has a significant influence on the catalytic activity of supported gold catalysts, particularly for CO oxidation. Although an enhancement of the catalytic activity of supported gold catalysts by moisture is considered as a unique feature of such formulations, other authors have reported moisture to have a detrimental or non-beneficial effect. Careful studies have shown that the effect of moisture is dependent on the support material and the quantity of moisture co-fed in the reactant gas [131, 176]. Daté and Haruta have reported that the optimum moisture concentration for CO oxidation over Au/TiO_2 is ~200 ppm [176]. Their findings showed that the reaction was enhanced by at least 10 fold compared to dry conditions. However, further increase in the moisture concentration led to a decrease in activity, attributed to the blockage of active sites. In a separate report, the same group emphasized that the degree of enhancement was dependent on the support. It was high for insulating metal oxides such as Al_2O_3 and SiO_2 and moderate for the semiconducting oxide, TiO_2 [131]. Regardless of the considerable enhancement by moisture, the activation energies calculated for Au/Al_2O_3 and Au/TiO_2 were almost independent of water concentration. Based on these results, the authors concluded that moisture did not significantly affect the structure of these catalysts and the mechanistic pathway. However, for Au/SiO_2, the conversion curves were unusual and significantly changed by the moisture concentration.

A similar picture emerged from the moisture effect studies conducted by Park and Lee using Au/Fe_2O_3, Au/Al_2O_3 and Au/TiO_2 catalysts [177]. Based on XPS measurements, it was established that during the reaction under dry conditions, Au exists in the metallic form, whereas ionic species (Au^{3+}) were identified under wet conditions. Here, water presumably creates active sites for CO oxidation, since oxidized species were more active. Bond and Thompson have suggested that both Au^{3+} and Au^0 species play a collaborative role in CO oxidation, where Au^0 is needed for the chemisorption of CO and Au^{3+} carries OH^- and ensures strong metal-support interaction [175]. According to the proposed mechanism (Figure 2.10), the hydroxyl attached either on the periphery ($Au^{3+}—OH^-$) or on a support cation (OH_s^-), attacks the chemisorbed CO ($Au^0—CO$) to form a hydroxycarbonyl ($Au^{3+}—COOH$).

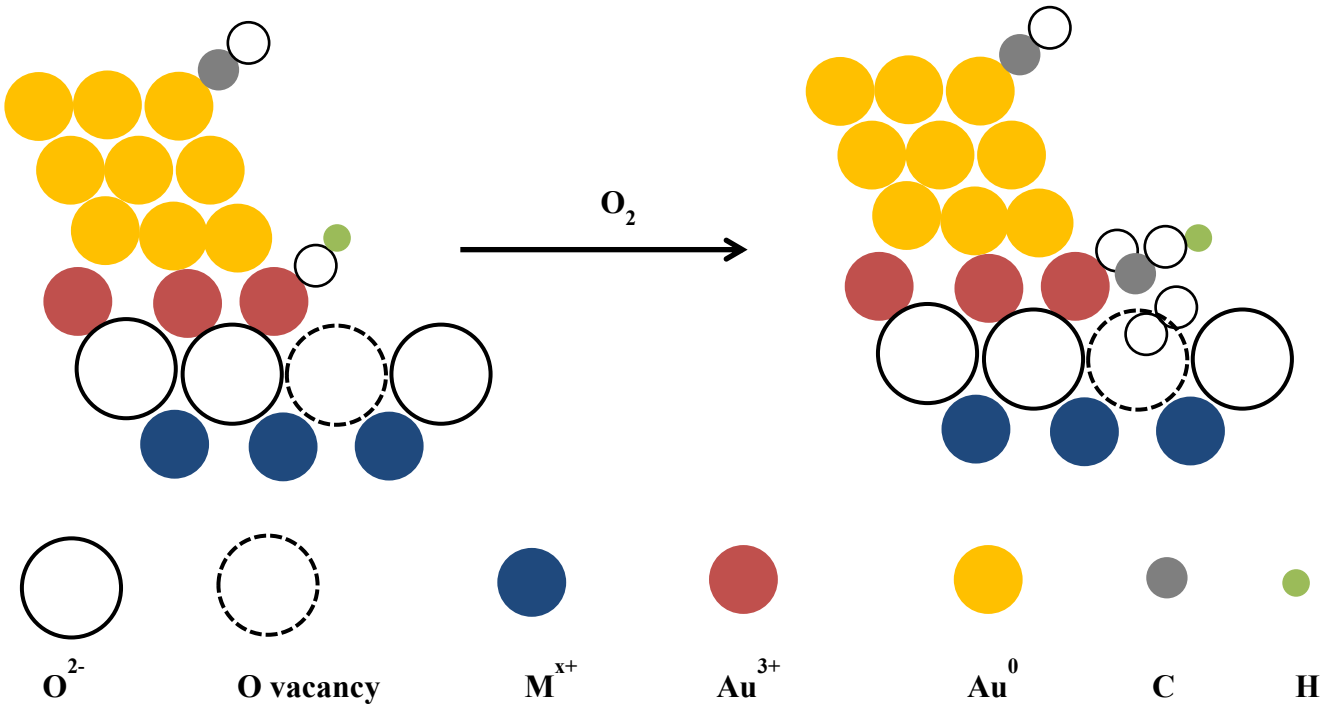

Figure 2.10 *A schematic representation of the initial stages CO oxidation at the periphery of active gold particles, as proposed by Bond and Thompson [175].*

The superoxide ion, O_2^-—$\square_s$, where $\square_s$ represents the vacancy of the support, then successively oxidizes two carboxylate groups to form CO_2 and the hydroxyl group, which then migrates to its original position and enters the next catalytic cycle. The cycle and the proposed mechanism involve the following subsequent reactions [175]:

$$Au^0 + CO \rightarrow Au^0—CO \quad \text{(i)}$$

$$Au^{3+} + OH_s^- \rightarrow Au^{3+}—OH \quad \text{(ii)}$$

$$Au^0—CO + Au^{3+}—OH \rightarrow Au^{3+}—COOH + Au^0 \quad \text{(iii)}$$

$$O_2 + \square_s^- \rightarrow O_2^- —\square_s \quad \text{(iv)}$$

$$Au^{3+}—COOH + O_2^- —\square_s \rightarrow Au^{3+} + CO_2 + HO_2^-—\square_s \quad \text{(v)}$$

$$Au^{3+}—COOH + HO_2^- —\square_s \rightarrow Au^{3+} + CO_2 + 2OH_s^- + \square_s \quad \text{(vi)}$$

$$Au^+ + \square_s \rightarrow Au^{3+} + \square_s^- \quad \text{(vii)}$$

The mechanism proposed by Bond and Thompson is similar to the one reported by Kung's group for Au/Al_2O_3, except that no assistance from the support was suggested, as Al_2O_3 is irreducible (Figure 2.11) [169]. In their study, thermal treatment of the catalyst led to its deactivation, presumably due to dehydration and subsequent modification of the active site (Au^+—OH). The catalyst could be reactivated by exposing it to moisture. In the study of the effect of moisture and calcination temperature on the performance of Au/Fe_2O_3, Daniells *et al*. have proposed a similar mechanism [167]. Notably, there is a disagreement between the mechanisms and conclusions proposed by Kung and those reached by Daté [176], regarding the activity enhancement of Au/Al_2O_3 by moisture.

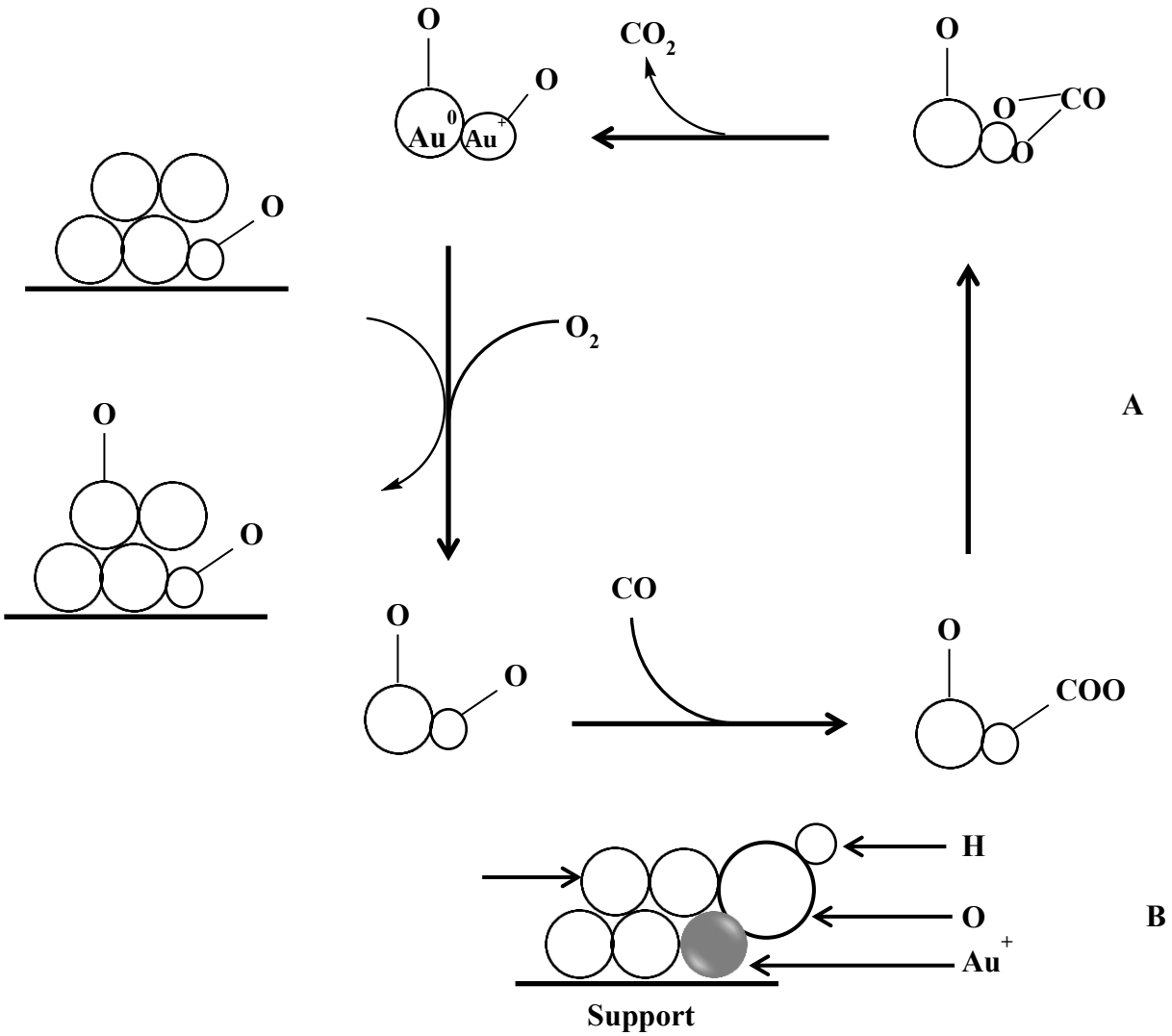

Figure 2.11 *(A) Mechanism proposed by Kung et al. and (B) the associated model assemble of the active site (Au^0 and Au^+—OH)*

2.3.1.4 Performance of some gold catalysts for PROX

The innovative research advances highlighted in the whole of Section 2.3.1 have been used as the basis for the development of efficient gold-based catalysts for the removal of CO from a H_2-rich reformate. One of the most important requirements that a successful PROX catalyst should possess is that the oxidation of CO should not be inhibited by the presence of H_2, H_2O and CO_2. Since the literature cited in Section 2.2.2.3 shows that water promotes CO oxidation for some

gold catalysts, PROX studies of these catalysts are widely explored and continue to be a topic of interest. Also, gold catalysts are active at low temperatures, making them suitable candidates to be employed in processing units coupled to PEMFC. In the past two decades, gold supported on selected metal oxides such as Fe_2O_3, MnOx, CeO_2 and TiO_2, have received tremendous interest as potential catalysts for PROX applications. Generally, Au catalysts show excellent activity and selectivity for CO oxidation at low temperature. However, the selectivity towards CO_2 under PROX conditions decreases sharply with increasing temperature. Hence, at the operation temperature window of the PEMFC (80 -100 °C) or processing unit (200 – 300 °C), competitive H_2 consumption becomes a concern. The stability of gold catalysts in PROX testing has also been considered as a drawback. Reports about the long-term stability of these catalysts under idealistic simulated PROX conditions are very limited. In this section, gold catalyst formulations that show promising PROX activity are discussed.

One of the early PROX studies using supported gold catalysts was reported by Haruta *et al*. for Au/MnO_x prepared by co-precipitation [178]. In the presence of H_2, the catalyst showed CO conversions between 85 – 95% in the respective temperature range of 50 to120 °C. This activity outperforms that achieved over Pt/A-zeolite catalysts, which are active at temperatures above 150 °C [34]. The results obtained by Haruta and co-workers inspired Kahlich *et al*. to conduct detailed kinetic studies for a $Au/\alpha\text{-}Fe_2O_3$ PROX catalyst [179]. The respective activation energies of CO and H_2 oxidation reactions were 31 and 50 kJ/mol, which correlated with the loss of selectivity with increasing temperature. The CO oxidation rate constant for $Au/\alpha\text{-}Fe_2O_3$ at 80 °C was comparable to that of conventional Pt/Al_2O_3 (at 200 °C) [179].

Avgouropoulos *et al*. studied the effect of H_2O and CO_2 in the catalytic performance of $Au/\ \alpha\text{-}Fe_2O_3$ [39]. Compared to $Pt/\gamma\text{-}Al_2O_3$ and $CuO\text{-}CeO_2$, the gold-based catalyst showed superior catalytic performance for PROX at relatively low temperatures (80 – 120 °C). However, $Au/\alpha\text{-}Fe_2O_3$ was sensitive to the presence of H_2O and CO_2, showing significant decrease in activity and selectivity. Later, Schubert and co-workers emphasized that although water enhances the activity of $Au/\alpha\text{-}Fe_2O_3$, it cannot completely counteract the detrimental effect of CO_2 during the PROX process [180]. Similar results and observations have been reported for a comparative study of $Au/\alpha\text{-}Fe_2O_3$ and Au/MnO_x [181]. The performance of these catalysts was very comparable, in the

presence of H_2O and CO_2. The positive effect of water can be explained by the involvement of OH^- groups in the CO oxidation, as explained by in Section 2.2.2.3. It was later shown that the PROX activity of Au/α-Fe_2O_3 formulations could be improved by careful pre-treatment [182]. The Au/Fe_2O_3 catalyst prepared via two-stage calcination has been reported to reduce CO to acceptable levels under realistic PROX conditions. However, optimum results were only observed in a narrow temperature window. To the best of our knowledge, no other supported gold catalyst has since surpassed the results observed for Au/Fe_2O_3.

Several groups have reported promising results for PROX over gold catalysts supported on ceria-based materials [125, 164, 183-186]. It has been reported that the performance of Au/CeO_2 catalysts can be fine-tuned by careful selection of the preparation method [187] and by doping the ceria support or by employing nanostructured CeO_2 [164]. For these catalysts, the chemical and structural nature of the support greatly influences the catalytic performance of the gold catalyst. The chemistry associated with ceria-based materials will be briefly discussed in the next section. In most cases, Au/doped-ceria catalysts are more effective than Au/pure-CeO_2, depending on the dopant. Ilieva *et al*. recently studied the PROX activity of gold catalysts supported on ceria doped with FeO_x, MnO_x and CoO_x [125, 185]. In their study, Mn- and Fe-containing gold catalysts displayed high activity and selectivity compared to Au/pure-ceria and Au/CoO_x-CeO_2 catalysts. However, PROX activity of these materials decreased drastically in the presence of CO_2 and H_2O. Wang and co-workers have systematically studied the effect of Ce/Co atomic ratio in the PROX activity of Au/Co_3O_4-CeO_2 catalysts [188]. A Au/Co_3O_4-CeO_2 catalyst with a Ce/Co ratio of 0.2 displayed promising PROX results, achieving CO conversion of 91% and selectivity of 51% at 80 °C. In a similar study for gold catalysts supported on iron-modified ceria, catalysts containing 10 mol% of Fe were reported to be more active and stable under PROX conditions, compared to Au/CeO_2 [189].

Gold has also been supported on ceria doped with zinc oxide [184, 186] and rare earth metals such as La, Sm, Gd and Y [184-186]. Amongst the investigated combinations, doping ceria with Zn, Sm and Y resulted in an improvement of the activity and stability. Generally, for Au/ceria and Au/MO_x-CeO_2 catalysts, promising activity and selectivity are achieved in the temperature window of 30 – 130 °C [183]. Although both Au/pure-ceria and Au/doped-CeO_2 formulations

are often negatively affected by the presence of CO_2 and H_2O, the degree of deactivation is less pronounced for gold catalysts supported on Fe_2O_3, ZnO and Y_2O_3-doped under similar conditions.

PROX activity of gold catalysts supported on other oxides and mixed oxides also has been studied. However, most of these catalysts appear to have very little potential for further applications [190]. Au/TiO_2 catalysts prepared by deposition-precipitation show good catalytic activity for PROX at temperatures between 25 and 50 °C [190-193]. However, increasing temperature often leads to substantial decrease in selectivity and promotes deactivation. Deactivation has been associated with the accumulation of carbonate species and complete transformation of Au^{x+} to Au^0 [190, 193]. Different reports have showed that Fe_2O_3 [194], Co_3O_4 [195] and CeO_2 [196] are suitable promoters for Au/TiO_2 catalysts for PROX applications. Au/Al_2O_3 catalysts are generally less active and tend to deactivate over a period of time [132]. However, their activity can be restored by treatment with H_2 or moisture [132].

2.3.2 Transition metal oxide catalysts

Major concerns involving the use of PGM and gold-based catalysts are the high cost and limited resources. As a result, greater emphasis now is placed on developing cost effective catalysts. Alternate metal oxide catalyst systems have been studied and have captured the attention of scientists as cost effective candidates for future applications in PROX. Some of the catalyst formulations that have been studied for PROX include oxides of transition metals such as Co, Cr, Cu, Ni, and Zn, supported on MgO, La_2O_3, SiO_2-Al_2O_3, CeO_2 and CeO_2-ZrO_2 [197]. For these types of catalysts, supporting Co, Cu or combinations of Co and Cu on fluorite structured oxides such as CeO_2 and CeO_2–ZrO_2 often generate active catalysts. The most studied catalysts of this type are ceria supported copper catalysts. In comparison with Au/α-Fe_2O_3 and Pt/γ-Al_2O_3, Avgouropoulos *et al*. found the CuO/CeO_2 catalyst to be the most selective, maintaining 100% selectivity at temperatures up to 120 °C, with ~ 80% CO conversion [39]. However, to obtain 99% CO conversion, a temperature of 200 °C and excess oxygen were required. When H_2O and CO_2 were added to the feed, the temperature required for the catalyst to nearly achieved complete CO conversion increased. Liu and Flytzani-Stephanopoulos have attributed the notable

activity of CuO/CeO_2 catalysts to a synergistic interaction between copper and CeO_2, as represented by a proposed redox equilibrium: $Ce^{4+}— Cu^{1+} \leftrightarrow Ce^{3+}— Cu^{2+}$ [198, 199]. It was suggested that CuO is easily reduced and adsorbs CO better when finely dispersed on CeO_2.

It has been reported that the catalytic performance of CuO/CeO_2 catalysts is strongly influenced by the preparation method [200, 201]. Avgouropoulos and co-workers found that the catalyst prepared by the urea-nitrate combustion method displayed superior activity compared to those prepared by co-precipitation, impregnation or the citrate-hydrothermal method [201]. The activity followed the order: urea-nitrate combustion > citrate-hydrothermal > co-precipitation > impregnation. A chelating method has also been reported to be an effective preparation method for these catalysts, promoting the formation of defects in the ceria structure and catalytic progression [202]. There is a vast literature discussing different preparation methods and varied PROX activities over CuO/CeO_2. Some reports contradict earlier studies, claiming that impregnation and co-precipitation can also produce effective catalysts [200, 201]. Therefore, it is not clear as to the effect of the preparation method on the structure and activity of the catalyst. However, there is consensus that the optimal Cu loading is ~ 5 wt% and that bulk CuO on CeO_2 is not effective [202-206]. A detailed discussion on the factors affecting the activity of these catalysts has been presented by Bion *et al*. [207]. Based on temperature programmed reduction experiments and comparative studies of CuO catalysts on different acidic and basic supports, most researchers agree that good activity is dependent on the promotion of synergistic redox features as a result of strong interaction between CuO and CeO_2 [197, 208, 209]. Therefore, tuning the redox properties and improving interaction between the two components can result in improved performance. The following section highlights ways of inducing redox and catalytic properties of ceria.

Cobalt oxide based catalysts have been widely studied for CO oxidation in the absence of H_2 [210-212]. For cobalt oxide, optimum CO oxidation activity is associated with Co_3O_4, in which cobalt exists in a mixed valence state of +2 and +3. Different authors have emphasized that Co_3O_4 is more active than CoO [211, 213]. Both bulk and supported Co_3O_4 are reported to display high CO oxidation activities in the absence of H_2. In a H_2-rich stream, the Co species, in bulk Co_3O_4, are reduced to Co^{2+} and Co^0 which are not active for CO oxidation [214, 215]. It has

been shown that when supported on suitable oxides, Co_3O_4 catalysts can maintain their efficient CO oxidation activity due to the enhancement of Co^{2+}— Co^{3+} redox couple efficiency [216]. In this context, the choice of the support is of paramount importance in order to ensure optimum activity. Zhao *et al*. investigated the effect of the support by studying the performance of cobalt catalysts supported on different metal oxides such as ZrO_2, CeO_2, SiO_2, Al_2O_3, and TiO_2 [217]. Among these catalysts, Co/ZrO_2 was the most active under PROX conditions. It was claimed that the cobalt is in a Co_3O_4 phase and the performance of Co/ZrO_2 was linked to a high dispersion of the active species. In an extension to this work, Woods *et al.* and Gawade *et al.* reported that supporting CoO_x on high-surface area ceria nanoparticles improved the dispersion of the active component from 0.1% to 3.4%, resulting in an in increase in the activity of the catalyst [218, 219]. However, this catalyst showed a decrease in PROX activity in the presence of water and CO_2 and it consumed H_2 via the methanation reaction at temperatures above 220 °C. Although the presence of H_2 led to a decrease in CO oxidation rate, the activation energy of H_2 oxidation was always higher than that of CO oxidation, regardless of cobalt loading. There is a growing number of reports suggesting that supported cobalt catalysts can be promising candidates for PROX applications [217, 220-225].

In the work published involving the use of metal oxide catalysts for PROX studies, limited literature is available detailing the stability of these catalysts in the presence of water and CO_2. In most of these studies, a decrease in CO conversion is observed in the presence of CO_2 and water. For CuO/CeO_2 catalysts, deactivation has been related to an accumulation of hydroxyl and carbonate species on the active sites, sintering of copper species [220] and copper redistribution [226]. The stability of the Co-based catalysts has been cited as a concern in a reducing environment due to reduction of Co to a lower valence state which is not active for CO oxidation [227]. Also, the formation of CO-H_2O "complex" has also been suggested as the possible explanation for loss of activity [228, 229]. It has been shown by Operando-DRIFTS studies that the surface CO-H_2O complexes are the hydroxylated carbonate-type species [229]. Their presence can lead to the impediment re-oxidation during PROX.

2.3.2.1 Insight into ceria properties and their modification

Ceria-based materials are well known for their applications as oxygen storage materials in automotive three-way catalytic converters (TWC) [230]. Recently, ceria-based catalysts have gained recognition in a wide range of applications, most notably, in the field of alternative energy and fuel cells [230]. The attractive catalytic behaviour demonstrated by ceria-based materials is often attributed to their good ionic conduction, temperature stability and most importantly, the facile redox cycle between Ce^{3+} and Ce^{4+} [231]. This reversible redox transition results from the release of lattice oxygen, which leads to structural defects and the formation of oxygen vacancies in ceria. Therefore, the single electron defects of Ce^{3+} ions can serve as vacant sites for active oxygen species required for catalytic reactions. In this way the oxygen storage capacity (OSC) and oxygen mobility become the important features in catalysis by ceria-based systems. Defects that are induced by thermal disorder or redox processes are referred to as intrinsic defects [230]. These changes can be represented by Equation 10 or by the Kröger–Vink notation (Equation 11) [232]. In the following equations, Ce'_{Ce}, $V_O^{\bullet\bullet}$ and $O_O^{\times}$ represents Ce^{3+}, a doubly charged vacancy and the oxide ion in the lattice, respectively.

$$O^{2-} + 2Ce^{4+} \leftrightarrow 2Ce^{3+} + \tfrac{1}{2} O_2\,(g) \qquad (2.10)$$

$$O_O^{\times} \quad 2Ce_{Ce}^{\times} \leftrightarrow 2V_O^{\bullet\bullet} + 2Ce'_{Ce} + \tfrac{1}{2} O_2\,(g) \qquad (2.11)$$

Fluorite structured oxides such as ceria are known to tolerate high atomic disorder which may be induced by reduction or introducing a dopant [230]. A high concentration of oxygen vacancies can be created by incorporating foreign metal ions with a lower valence (M^{3+}/M^{2+}) into the lattice structure of ceria [233]. The formation of oxygen vacancy defects ($V_O^{\bullet\bullet}$) occurs in order to compensate for charge imbalance after the incorporation of dopants with lower valence. In addition, the formation of vacancies is also driven by structural strain effects, where larger or smaller dopant cations may prefer a different coordination than the 8-fold coordination of the fluorite structure [234]. Hence, substituting Ce^{4+} by isovalent metal ions (M^{4+}) still allows modification of the electronic properties and the catalytic properties of ceria. Based on this, zirconium-doped ceria materials are common components of three way catalysts (TWC) and are well-known as oxygen storage materials [235]. Oxygen vacancy defects that are invoked by the incorporation of foreign metal ions into the lattice are termed extrinsic defects [230]. In a class of

ceria mixed oxides, ceria-based materials that have foreign metal ions dissolved into the ceria lattice structure are commonly referred to as *solid solutions*. The representation of non-substituted CeO_2 is shown on the right, while substituted ceria on the left of the cube as shown in Figure 2.12 [236].

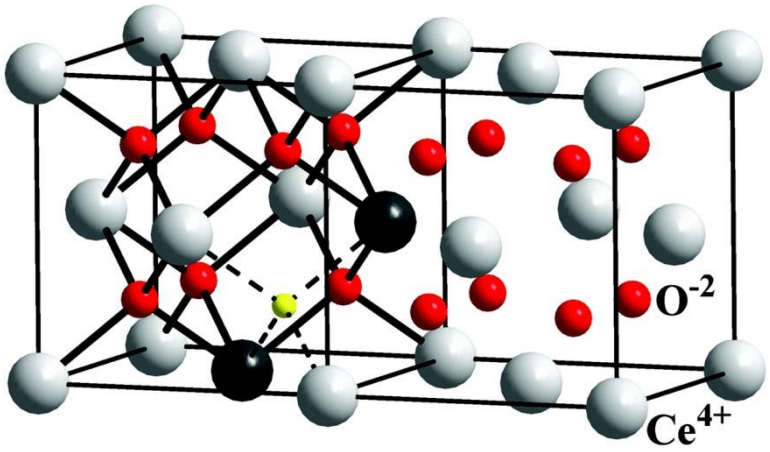

Figure 2.12 *Representation of the fluorite structure, showing non-substituted (right of the cube) and substituted ceria (left of the cube). Dark spheres represent the dopant and the oxygen vacancy is shown as a small sphere. Reprinted from [236] with the permission of the National Academy of Science, USA*

Since the formation of oxygen vacancies is linked to oxygen deficiency in the structure of CeO_2, ceria that is rich in oxygen vacancy defects tend to have increased proportions of Ce^{3+} in order to maintain charge balance. It has been shown that high surface area nanoparticulate ceria has improved redox properties, shown by reduction at low temperatures compared to bulk ceria [237-240]. These observations were found to be related to the presence of intrinsic oxygen vacancy defects. Therefore, catalytic properties of ceria can also be modified without introducing dopant metals into the lattice. In this context, careful design of the synthesis method is important. Preparation methods that have been reported to be effective in producing high surface area nanoparticulate ceria include sol-gel [241], combustion [233] and the surfactant-assisted methods [237, 242]. For catalytic CO oxidation, ceria-based materials that are rich in oxygen vacancies and in turn enhanced oxygen storage capacity often show better activity [233, 241]. In the case of CuO/CeO_2, it has been proposed that the presence of copper improves the reducibility, the thermal stability and enhances the oxygen storage capacity of ceria [197]. Accordingly, studies

have shown that the redox transition during CO oxidation involves the reduction and oxidation of both the ceria and copper species [208, 243]. Several researchers have attributed the notable activity of CuO/CeO_2 catalysts to a synergistic interaction between Cu and CeO_2, as represented by a proposed redox equilibrium: $Ce^{4+}— Cu^{1+} \leftrightarrow Ce^{3+}— Cu^{2+}$ [199, 203, 205]. The redox mechanism and catalytic activity of CuO/CeO_2 catalysts has been associated with the possible incorporation of some of the copper ions into the ceria lattice, forming a solid solution with Ce—O—Cu phases [202, 203, 205]. In other studies, Jung *et al.* [203] and Liu and Flytzani-Stephanopoulos [205] have demonstrated that the calcination of ~5 wt% CuO/CeO_2 catalysts at temperatures between 600 to 700 °C produces stable solid solution catalysts with enhanced activity. Calcination of the catalysts above this temperature window led to a decrease in activity, which was linked to phase separation due to the migration of copper species to the surface.

In recent years, several groups have shown that introducing a third metal such as Pt, Ni, Sn, Zr, Fe or Co to CuO/CeO_2 systems improved the activity [244-250]. However, the addition of Pt, Ni and Co additives showed no improvement on the selectivity. Comparative studies of CuO/CeO_2 and CuO/CeO_2-ZrO_2 catalysts showed that the latter formulation performed better than the former under PROX conditions [244]. Superior catalytic performance displayed by CuO/CeO_2-ZrO_2 was attributed to the enhanced oxygen mobility, induced by incorporation of zirconium. In the same study, the CuO/CeO_2-ZrO_2 catalyst was reported to be as active as the more expensive Pt/Al_2O_3 catalyst, but showed even better selectivity. Incorporating an appropriate amount of Al_2O_3 (20%) into this formulation improved the dispersion of CuO and, consequently, the activity of this catalyst [251]. Li and co-workers doped the CuO/CeO_2 catalyst with different metals such as Mn, Fe, Ni, Co and Cr [204]. The PROX activity of the catalysts followed the order: $CuO/Mn\text{-}CeO_2 \approx CuO/Fe\text{-}CeO_2 > CuO/Ti\text{-}CeO_2 > CuO/Ni\text{-}CeO_2 > CuO/CeO_2 > CuO/Co\text{-}CeO_2 > CuO/Cr\text{-}CeO_2$. The superiority of Mn and Fe-doped catalysts was linked to the formation of a solid solution network, with a high concentration of oxygen vacancies. Recently, Chen *et al.* reported high PROX activity for CuO catalysts supported on cobalt-doped ceria materials (CuO/Co_3O_4-CeO_2) [249]. Depositing 7 wt% CuO on a support which comprised a Ce/(Ce + Co) atomic ratio of 0.1 was reported to be the most promising formulation, where complete CO conversion was maintained over a broad temperature window, 98 – 173 °C.

In an attempt to improve the dispersion of Cu species, Moretti *et al*. prepared a mesoporous and high surface area $CuO/CeO_2/Al_2O_3$ catalyst, using a surfactant-assisted synthesis [206]. The high activity, selectivity and prolonged stability of the catalyst under PROX conditions were associated with high surface area. In another study with $CuO\text{-}CeO_2/\gamma\text{-}Al_2O_3$, addition of a small amount of Co (0.2 wt%) promoted the activity of the catalyst [252]. Supporting CuO on high surface area (HAS) ceria prepared by the surfactant-assisted [242, 253] or sol-gel method [241] has been reported to produce formulations that display high activity due to high dispersion, enhanced redox properties and high OSC.

2.3.2.2 Active entities and mechanistic aspects of metal oxide catalysts

In CuO/CeO_2 catalysts, copper can exist as three different species, viz. finely dispersed CuO, Cu^{2+} incorporated into the ceria lattice and bulk CuO species [207, 241, 254]. It was suggested that CuO is easily reducible and much more efficient in CO adsorption when finely dispersed on CeO_2. Cu^{2+} in the lattice ensures redox synergism between the cerium and copper species and facilitates the formation of defects, which are an incentive for the enhancement of the catalytic activity CuO/CeO_2. Bulk CuO is known to play the least role in CO oxidation. Under PROX conditions, the synergistic effect between the copper and ceria species has been reported to facilitate the reducibility of Cu^{2+} and subsequently lead to the formation of Cu^{+}— CO species. Based on *in situ* diffuse reflectance infrared spectroscopy studies (DRIFTS), it has been demonstrated that, during PROX progression, CO adsorbs on Cu^{+} mainly as carbonyl, forming Cu^{+}— CO species [241, 249, 254]. It is generally accepted that CO oxidation over CuO/CeO_2 and many other ceria supported metal oxide catalysts proceeds according to the Mars-van Krevelen (MvK) redox pathway, in which the metal cations serve as anchoring sites for CO and there is a dynamic equilibrium between solid gaseous oxygen [199, 210, 226, 247, 255-257]. As discussed earlier, the redox and OSC properties of ceria favour oxygen adsorption, which can be transformed to lattice oxygen species according to the following steps [226, 255, 256]:

$$O_2\,(ad) \rightarrow O_2^{-}\,(ad) \rightarrow O_2^{2-}\,(ad) \rightarrow 2O^{-}\,(ad) \rightarrow 2O^{2-}\,(latt) \qquad (2.12)$$

Equilibrium between solid and gaseous oxygen has been proven by means of isotopic exchange experiments [258]:

$$Ce^{16}O^{16}O + {}^{18}O^{18}O \leftrightarrow Ce^{18}O^{16}O + {}^{18}O^{16}O \qquad (2.13)$$

The involvement of lattice oxygen in CO oxidation has been verified by the use of the temporal product analysis (TPA) reactor technique [199]. In these studies, passing CO through the oxidized CuO/CeO_2 led to a spike of CO conversion, which then decreased after the consumption of all active oxygen species. Figure 2.13 shows a general MvK catalytic pathway employed to describe CO oxidation over ceria supported metal oxide, including CuO/CeO_2 and Co_3O_4/CeO_2 catalysts.

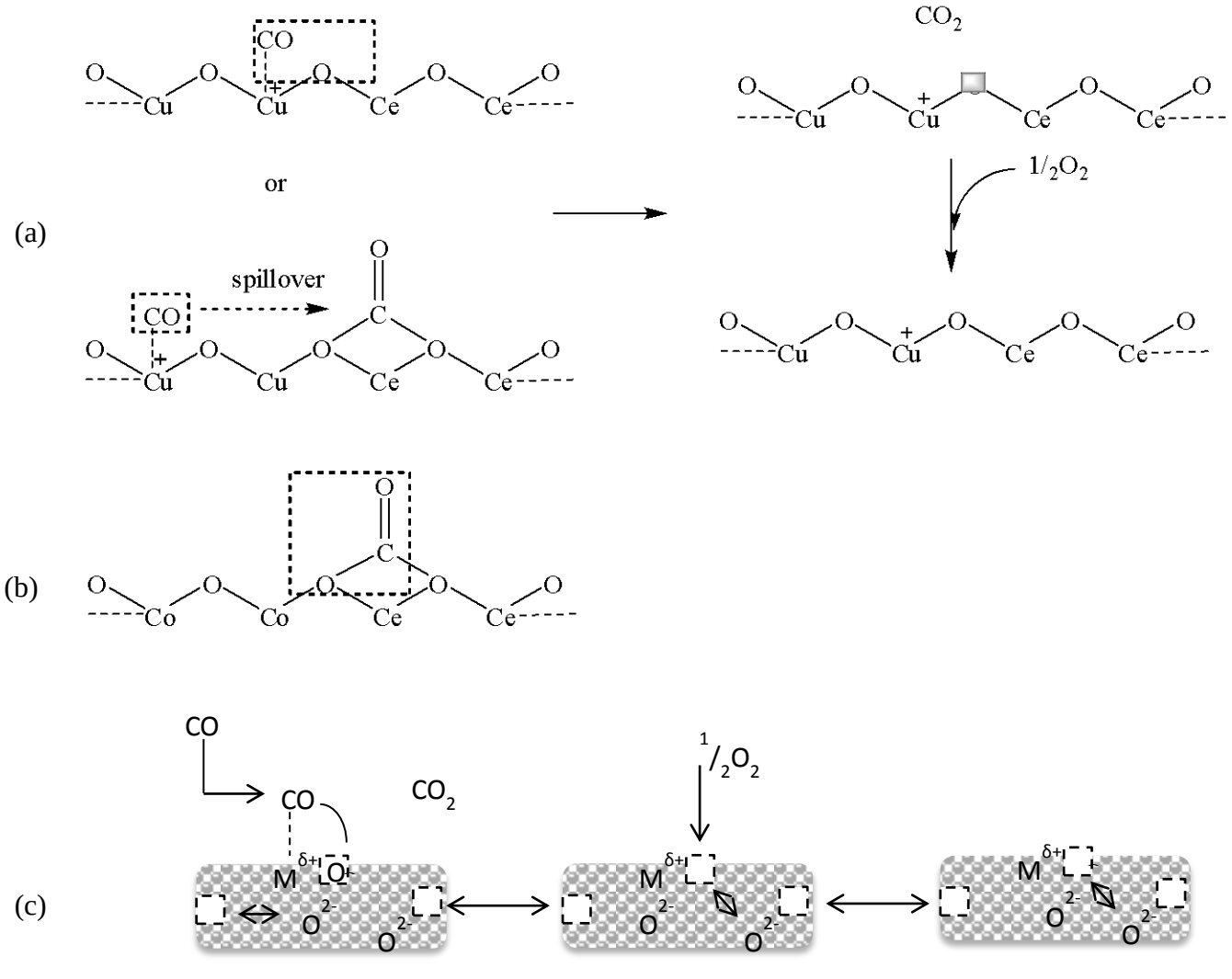

Figure 2.13 *Schematic representation of CO oxidation over supported metal oxide catalysts: (a) CuO/CeO_2, (b) Co_3O_4/CeO_2 and (c) general simplification for general metal oxides[252, 254]*

Different authors have reported that Co_3O_4 is more active than CoO [211, 213]. The high activity of Co_3O_4 has been associated with the co-existence of Co^{2+}— Co^{3+} pairs [211, 213]. Royer and Duprez suggested that Co^{3+} may be the anchoring site for CO and could be reduced to Co^{2+} upon CO adsorption [210]. This proposal is supported by the density functional theory (DFT) calculation results reported elsewhere [259]. Xie *et al*. emphasized that the superior performance of Co_3O_4 depends on the balance of Co^{3+}/Co^{2+} ratio of the spinel structure [211]. It was suggested that CO and O_2 adsorb at Co^{2+} sites and Co^{2+}—□—Co^{3+} specific sites, respectively. Adsorption of CO on Co^{2+} has been confirmed by infrared experiments [212]. With respect to Co_3O_4 catalysts supported on ceria-based materials, DRIFTS studies have indicated that bidentate carbonate species are the intermediates for CO oxidation [254].

2.4 Summary and outlook

It is a necessary requirement to reduce the CO concentration in the reformate in order to achieve maximum power output and ensure prolonged lifespan of the PEMFC. Different process technologies have been discussed and compared as H_2 purification methods for PEMFC applications. Selective catalytic reactions appear to be a promising way of achieving reformate clean-up, compared to membrane separation techniques which are limited to large scale applications. Two catalytic processes, Sel Meth and PROX were discussed in detail. Although literature shows that Sel Meth is a promising process and eliminates the need to add oxygen, its drawback is that three molecules of hydrogen are consumed for every CO molecule converted to CH_4.

Based on the literature survey, it can be concluded that PROX is the preferred method that can selectively reduce the CO concentration (≈ 1 vol%) to acceptable levels for PEMFC applications. Catalyst systems that have been demonstrated as candidates for PROX include supported noble metals, metal oxide supported gold nanoparticles and non-precious metal oxides, with the first category being conventionally used. A conceptual comparison of the performance of the catalysts is depicted in Figure 2.14, and Table 2.3 summarises the performance of different catalysts, cited in this chapter, under different PROX conditions.

Table 2.3 *Comparison of the catalytic performance of noble metal, supported gold and non-precious metal oxide catalysts for PROX reported in literature*

Catalyst	Preparation method	Operation parameters	Comments	Reference
Noble metal catalysts				
2 wt% Pt/γ-Al_2O_3	Sol-gel	$H_2/CO/O_2/CO_2/H_2O$ (60/1/1.35/25/10 vol%) in He. Space velocity: 571 mL g^{-1} min^{-1}	~100% CO conversion at 150 -175 °C.	Manasilp and Gulari [38]
5 wt% Pt/γ-Al_2O_3	Impregnation	$H_2/CO/O_2/CO_2/H_2O$ (50/1/1.25/15/10 vol%) in He. *W/F* = 0.144 g .s. ml^{-1}	Stable. 93± 7 % CO conversion at 150 °C	Avgouropoulos *et al*. [39]
6 wt% Pt-mordenite	Ion-exchange	$CO/O_2/H_2O$ (1/1/20 vol%) in H_2. Space velocity: 1 000 mL g^{-1} min^{-1}	Stable. 70% CO conversion at 200 °C	Igarashi *et al*. [43]
0.32 wt% Pt/$Ce_{0.8}Zr_{0.2}O_2$	Impregnation	$H_2/CO/O_2/CO_2/H_2O$ (60/1/1/5/5 vol%) in He. Space velocity: 12 000 h^{-1}	~90% CO conversion at 80 °C	Ayastuy *et al*. [59]
4% Pt-0.5% Fe/mordenite	Ion-exchange	$H_2/CO/O_2/CO_2/H_2O$ (68/1/1/20/20 vol%) in N_2. Space velocity: 50 000 h^{-1}	100% CO conversion at 150 °C	Watanabe *et al*. [68]
4% Pt-0.5% Fe/SiO_2	Sol-gel	$CO/O_2/CO_2/H_2O$ (1/0.5/25/20 vol%) in H_2. Space velocity: 36 000 mL g^{-1} h^{-1}	92% CO conversion at 80 °C	Fu *et al*. [70]
5% Pt/FSM-16	Impregnation	$N_2/CO/O_2/CO_2/H_2O$ (5/1/0.5 vol%) in H_2. Space velocity: 200 mL g^{-1} min^{-1}	Not stable. ~100% CO conversion at 60 -150 °C.	Fukuoka *et al*. [71]
1 wt% (2:1) Pt-Au/A-zeolite	Impregnation	$H_2/CO/O_2/CO_2/H_2O$ (40/1/1/10/10 vol%) in He. Space velocity: n.d	~100% CO conversion at 180 -210 °C.	Naknam *et al*. [77]
0.5% Pt-Co/YSZ (Co/Pt = 10)	Impregnation	$H_2/CO/O_2/CO_2/H_2O$ (64.6/0.9/0.9/17.4/13 vol%) in N_2. Space velocity: 278 mL g^{-1} min^{-1}	Stable. CO reduced to below 10 ppm at 110-150 °C	Ko *et al*. [84]

Gold catalysts				
Au/MnOx (Au/Mn = 1/50)	Co-precipitation	CO/O_2 (1/1 vol%) in H_2. Space velocity: 10 000 h^{-1}	~100% CO conversion at 50 °C	Sanchez *et al.* [178]
2.9 wt% Au/α-Fe_2O_3	Co-precipitation	$H_2/CO/O_2/CO_2/H_2O$ (50/1/1.25/15/10 vol%) in He. *W/F* = 0.144 mL g^{-1} min^{-1}	Not stable ~100% CO conversion at 100 °C	Avgouropoulos *et al.* [39]
5.38% Au/FeOx	Co-precipitation	$H_2/CO/O_2/CO_2/H_2O$ (40/1/1/2/2.6 vol%) in He. Space velocity: 500 mL g^{-1} h^{-1}	Stable ~100% CO conversion at 50 °C	Luengnaruemitchai *et al*. [181]
5% Au/Fe_2O_3	Co-precipitation	$H_2/CO/O_2/CO_2/H_2O$ (50/0.9/0.9/22/4.7 vol%) in N_2. Space velocity: 12 000 h^{-1}	Stable 99.8 % CO conversion at 80 °C	Landon *et al.* [182]
3 wt% Au /10FeCeO_2	Deposition–precipitation	$H_2/CO/O_2/CO_2/H_2O$ (50/1/1/10/10 vol%) in He. Space velocity: 4000 h^{-1}	~70 % CO conversion at 100 °C	Ilieva *et al.* [125]
Au/CeO_2–Co_3O_4	deposition-precipitation	$H_2/CO/O_2$ (50/1/1 vol%) in Ar. Space velocity: 30 000 mL g^{-1} h^{-1}	Not stable. 94% CO conversion at 80 °C	Wang *et al.* [188]
1 wt.% Au/ 10CuOx–CeO_2	deposition-precipitation	$H_2/CO/O_2/CO_2/H_2O$ (50/1/1.25/2/10 vol%) in N_2.	Not stable. ~100% CO conversion at 150 °C	Laguna *et al.* [189]
Non-precious metal oxide catalysts				
1.9 wt.% CuO–CeO_2	sol–gel	$H_2/CO/O_2/CO_2/H_2O$ (50/1/1.25/15/10 vol%) in He. *W/F* = 0.144 g s mL^{-1}	Stable. ~100% CO conversion at 175 °C	Avgouropoulos *et al*. [39]
3 wt% Cu-CeO_2	Impregnation	$H_2/CO/O_2$/ (50/2/1 vol%) in He. Space velocity: 100 N mL min^{-1}	n.d. 76.2 % CO conversion at 136 °C	Mariño *et al*. [197]
25 wt% CuO-CeO_2	Citrate-hydrothermal	$H_2/CO/O_2/CO_2/H_2O$ (50/1/1.25/15/10 vol%) in He. Space velocity: 417 mL g^{-1} min^{-1}	Stable. 99% conversion at 200-210 °C	Avgouropoulos and Ioanides [200]
$Cu_{0.15}Ce_{0.85}$	Urea nitrate combustion	$H_2/CO/O_2/CO_2/H_2O$ (50/1/1.25/15/10 vol%) in He. Space velocity: 417 mL g^{-1} min^{-1}	n.d . 99% conversion at 190 °C	Avgouropoulos *et al*. [201]

5% CuO-CeO_2	Chelating method	$H_2/CO/O_2$ (50/1/1.25/15/10 vol%) in Ar. Space velocity: 12 000 mL g^{-1} h^{-1}	Stable. ~99% conversion at 120 °C	Liu *et al*. [202]
7 wt% CuO/$Ce_{0.9}Zr_{0.1}O_2$	Impregnation	$H_2/CO/O_2/CO_2/H_2O$ (50/1/1/15/10 vol%) in He. Space velocity: 10 000 mL g^{-1} h^{-1}	Stable. ~100% CO conversion at 150 °C	Chen *et al*. [244]
7% CuO/$Ce_{0.9}Zr_{0.1}O_2$-Al_2O_3	Suspension/co-precipitation	$H_2/CO/O_2/CO_2/H_2O$ (50/1/1/15/10 vol%) in He. Space velocity: 167 mL g^{-1} min^{-1}	Stable. ~100% CO conversion at 160 -170 °C.	Chen *et al*. [251]
5 wt% CuO/MnOx-CeO_2	Hydrothermal	$H_2/CO/O_2/CO_2/H_2O$ (50/1/1/15/7.5 vol%) in Ar. Space velocity: 60 000 mL g^{-1} h^{-1}	~100% CO conversion at 140 °C	Li *et al*. [204]
5% CuO/20% CeO_2/γ-Al_2O_3	Impregnation	$H_2/CO/O_2$ (30/0.6/0.6/ vol%) in He. Space velocity: 300 mL g^{-1} min^{-1}	Stable. ~99% CO conversion at 200 °C.	Moretti *et al*. [206]
7 wt% CuO/Co_3O_4-CeO_2	Impregnation	$H_2/CO/O_2/CO_2/H_2O$ (50/1/1/12.5/10 vol%) in N_2. Space velocity: 12 000 mL g^{-1} h^{-1}	~100% CO conversion at 120 °C (Highly selective)	Chen *et al*. [249]
Co-promoted CuOCeO_2/ γ-Al_2O_3	Impregnation	$H_2/CO/O_2/CO_2/H_2O$ (60/1/1/13/10 vol%) in N_2. Space velocity: 60 000 h^{-1}	Not stable. ~99% CO conversion at 200 -235 °C.	Park *et al*. [252]
10 wt% Co/ZrO_2	Impregnation	$H_2/CO/O_2$ (60/1/1/13/10 vol%) in He.	~90% CO conversion at 175 °C	Zhao *et al*. [217]
10%Co/CeO_2 nanoparticles	Impregnation	$H_2/CO/O_2$ (60/1/1 vol%) in He. Space velocity: 30 000 mL g^{-1} min^{-1}	~100% CO conversion at 200 °C.	Woods *et al*. [218]

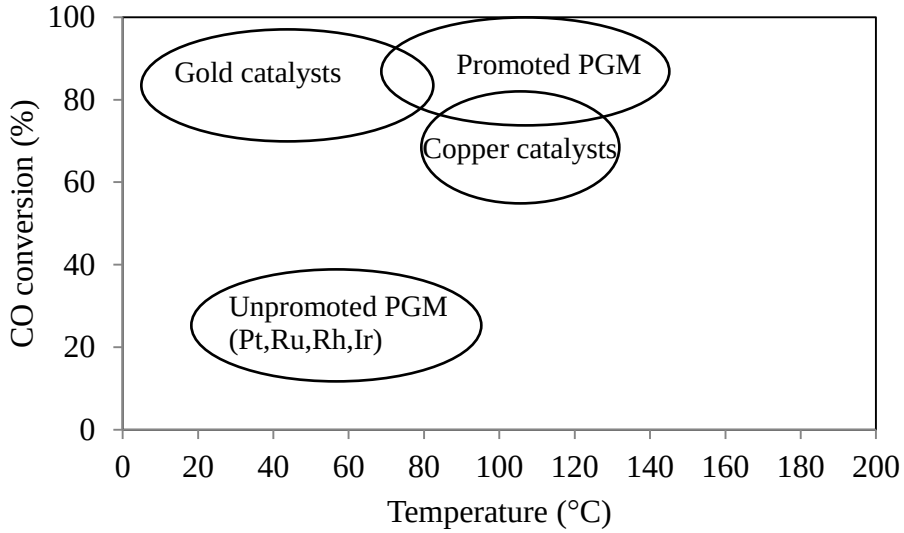

Figure 2.14 *Conceptual depiction of the PROX activity of different classes of catalyst. Adopted from [260]*

2.5 Rationale, aim and objectives of the current study

Catalytic CO oxidation is a preferred method for reducing CO concentration as an auto emission pollutant and/or detrimental poison for the Pt electro-catalyst in PEMFCs. Conventionally, supported PGMs and gold catalysts are used, while CuO/CeO_2 catalysts are an alternative system. Enhanced catalytic activity of these catalysts generally depends on the dispersion of the active component and its strong interaction with the support. However, complete dispersion is difficult to achieve and only 20 to 25% of the active components are normally used in catalytic conversion. In the current study, supported gold and ceria-based catalysts were considered. The aim of this research work was to:

* Synthesize and characterize single-phase metal ion substituted ceria catalysts $Ce_{1-x}M_xO_{2-\delta}$ (solid-solution), where M = Cu, Co, Pd or a combination of either two metals. *Solid-solution formation allows maximum dispersion of the active metal ions, tuning of the redox properties, metal-Ce interaction and consequently the catalytic behaviour.*

* Prepare and characterize titania-based solid-solution materials, $Ti_{1-x}M_xO_{2-\delta}$ where M = Fe or Co, and use them as supports for gold catalysts. *Incorporating metal ions in the TiO_2 matrix*

would be expected to induce the formation of oxygen defect sites and supporting gold on such supports is anticipated to yield catalysts with enhanced performance.

* Investigate the catalytic activity of the prepared materials as total CO oxidation and preferential CO oxidation catalysts.

2.6 Reactor system

Continuous fixed-bed reactors are the easiest, cost effective and commonly used reactor systems for gas-solid catalysed reactions. Therefore, catalytic measurements reported in this thesis were conducted using a continuous fixed-bed reactor, due to its compatibility. A schematic diagram of the reactor unit used in this study is shown in Figure 2.15. The fittings and piping used to build the test unit were made from stainless steel and were supplied by Swagelok®. The reactor is equipped with Brooks mass flow controllers (MFC) for gas flow rate regulation. MFCs were calibrated for standard temperature and pressure (STP, 0 °C and 1 atmospheric pressure) prior use. Additional details about the reactor system are presented in subsequent chapters and Appendix 2. Gases used in the studies were purchased from Afrox or Air Products SA.

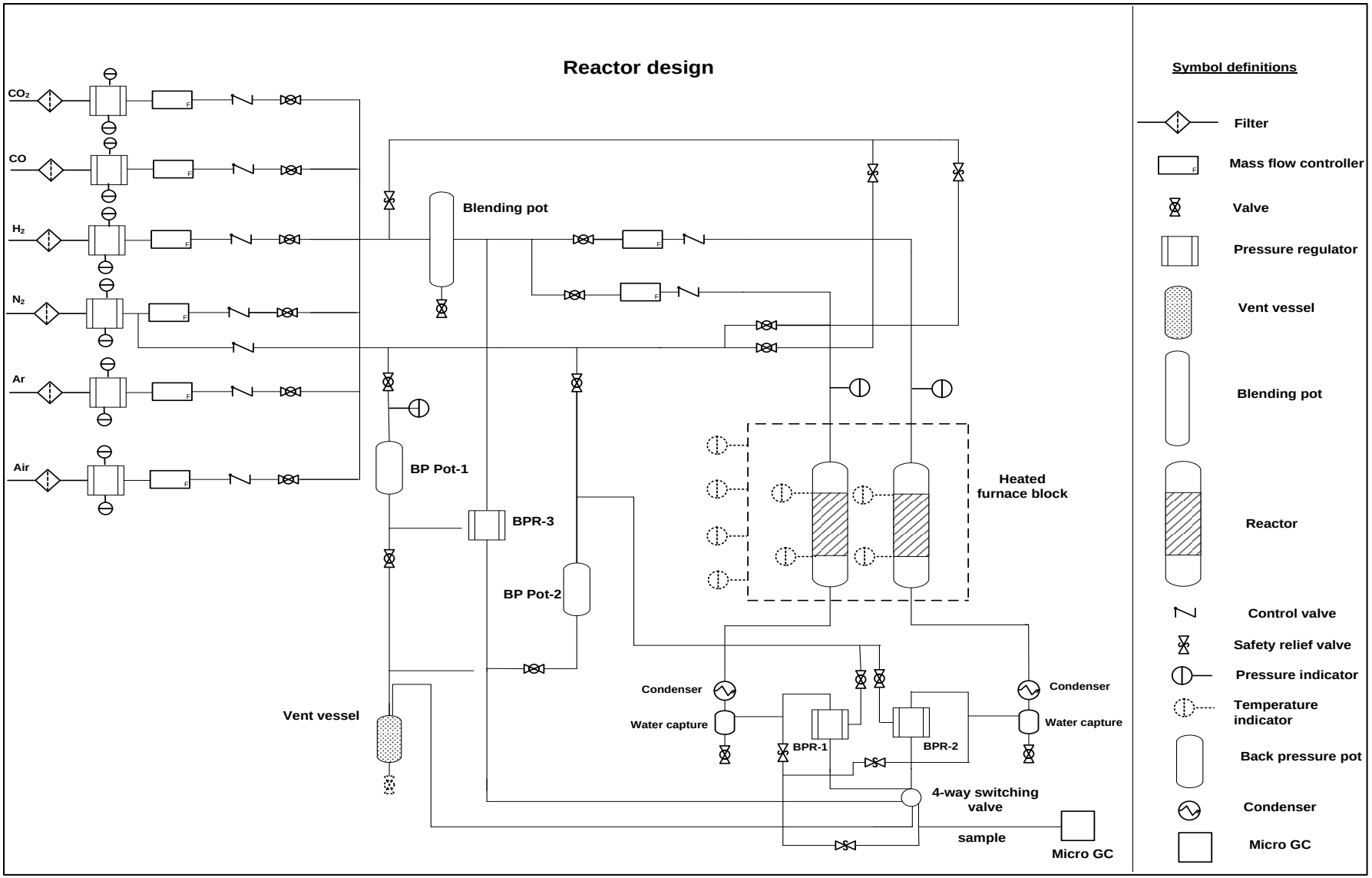

Figure 2.15 *Schematic diagram of the test unit used for catalytic measurements*

References

[1] J.-H. Wee, K.-Y. Lee, J. Power Sources 157 (2006) 128-135.

[2] A. Rodrigues, J.C. Amphlett, R.F. Mann, B.A. Peppley, P.R. Roberge, Carbon monoxide poisoning of proton-exchange membrane fuel cells, Energy Conversion Engineering Conference, 1997. IECEC-97., Proceedings of the 32nd Intersociety, 1997, pp. 768-773 vol.762.

[3] F. Marschner, F.W. Moeller, Methanol synthesis, Academic, 1983, pp. 215-243.

[4] D. Edlund, in: K. Liu, C. Song, V. Subramani (Eds.), Hydrogen and Syngas Production and Purification Technologies, John Wiley & Sons, Inc., Hoboken, New Jersey, 2009, pp. 357-384.

[5] J. Huang, J. Zou, W.S.W. Ho, in: K. Liu, C. Song, V. Subramani (Eds.), Hydrogen and Syngas Production and Purification Technologies, John Wiley & Sons, Inc., Hoboken, New Jersey, 2009, pp. 385-413.

[6] S. Sircar, T.C. Golden, in: K. Liu, C. Song, V. Subramani (Eds.), Hydrogen and Syngas Production and Purification Technologies, John Wiley & Sons, Inc., Hoboken, New Jersey, 2009, pp. 414-450.

[7] A. Basile, A. Iulianelli, T. Longo, S. Liguori, M. Falco, in: M. De Falco, L. Marrelli, G. Iaquaniello (Eds.), Membrane Reactors for Hydrogen Production Processes, Springer London, 2011, pp. 21-55.

[8] T.M. Adams, J. Mickalonis, Mater. Lett. 61 (2007) 817-820.

[9] C. Lemier, J. Weissmüller, Acta Mater. 55 (2007) 1241-1254.

[10] Y. Sakamoto, F.L. Chen, Y. Kinari, F. Sakamoto, Int. J. Hydrogen Energy 21 (1996) 1017-1024.

[11] S.K. Gade, M.K. Keeling, A.P. Davidson, O. Hatlevik, J.D. Way, Int. J. Hydrogen Energy 34 (2009) 6484-6491.

[12] Ø. Hatlevik, S.K. Gade, M.K. Keeling, P.M. Thoen, A.P. Davidson, J.D. Way, Sep. Purif. Technol. 73 (2010) 59-64.

[13] H. Bai, A.C. Yeh, Ind. Eng. Chem. Res. 36 (1997) 2490-2493.

[14] T.E. Rufford, S. Smart, G.C.Y. Watson, B.F. Graham, J. Boxall, J.C. Diniz da Costa, E.F. May, J. Pet. Sci. Eng. 94–95 (2012) 123-154.

[15] D.L. Trimm, Appl. Catal., A 296 (2005) 1-11.

[16] E.D. Park, D. Lee, H.C. Lee, Catal. Today 139 (2009) 280-290.

[17] B.S. Baker, J. Huebler, H.R. Linden, J. Meek, Selective removal by methanation of carbon monoxide from a mixture of gases containing carbon dioxide, Consolidated Natural Gas Service Co., Inc.; Southern California Gas Co.; Southern Counties Gas Co. of California . 1971, p. 8 pp.

[18] A. Rehmat, S.S. Randhava, Ind. Eng. Chem. Prod. Res. Dev. 9 (1970) 512-515.

[19] S. Takenaka, T. Shimizu, K. Otsuka, Int. J. Hydrogen Energy 29 (2004) 1065-1073.

[20] P. Panagiotopoulou, D.I. Kondarides, X.E. Verykios, J. Phys. Chem. C 115 (2010) 1220-1230.

[21] Y. Men, G. Kolb, R. Zapf, V. Hessel, H. Löwe, Catal. Today 125 (2007) 81-87.

[22] Y. Men, G. Kolb, R. Zapf, rsquo, M. Connell, V. Hessel, Chem. Lett. 38 (2009) 824-825.

[23] P. Pfeifer, L. Bohn, O. Görke, K. Haas-Santo, K. Schubert, Chem. Eng. Technol. 28 (2005) 474-476.

[24] J.D. Holladay, Y. Wang, E. Jones, Chem. Rev. 104 (2004) 4767-4790.

[25] R.A. Dagle, Y. Wang, G.-G. Xia, J.J. Strohm, J. Holladay, D.R. Palo, Appl. Catal., A 326 (2007) 213-218.

[26] Z. Kowalczyk, K. Stołecki, W. Raróg-Pilecka, E. Miśkiewicz, E. Wilczkowska, Z. Karpiński, Appl. Catal., A 342 (2008) 35-39.

[27] Q. Liu, X. Dong, X. Mo, W. Lin, J. Nat. Gas. Chem. 17 (2008) 268-272.

[28] N. Mori, T. Nakamura, O. Sakai, Y. Iwamoto, T. Hattori, Ind. Eng. Chem. Res. 47 (2008) 1421-1426.

[29] Z. Li, W. Mi, S. Liu, Q. Su, Int. J. Hydrogen Energy 35 (2010) 2820-2823.

[30] M. Echigo, T. Tabata, J. Chem. Eng. Jpn. 37 (2004) 75-81.

[31] Z. Li, W. Mi, J. Gong, Z. Lu, L. Xu, Q. Su, J. Nat. Gas. Chem. 17 (2008) 359-364.

[32] E. Rideal, C. The, W.A. Bone, G. Ingle-Finch, E.C.C. Baly, W.C. McC. Lewis, E. Edser, E.F. Armstrong, T.P. Hilditch, H.E. Holtorp, I. Langmuir, S. Arrhenius, Transactions of the Faraday Society 17 (1922) 655-675.

[33] J.G.E. Cohn, Carbon monoxide removal from hydrogen-containing gases, Engelhard Industries, Inc. . 1965, p. 3 pp.

[34] S.H. Oh, R.M. Sinkevitch, J. Catal. 142 (1993) 254-262.

[35] F. Mariño, C. Descorme, D. Duprez, Appl. Catal., B 54 (2004) 59-66.

[36] I. Rosso, C. Galletti, G. Saracco, E. Garrone, V. Specchia, Appl. Catal., B 48 (2004) 195-203.

[37] O. Pozdnyakova, D. Teschner, A. Wootsch, J. Kröhnert, B. Steinhauer, H. Sauer, L. Toth, F.C. Jentoft, A. Knop-Gericke, Z. Paál, R. Schlögl, J. Catal. 237 (2006) 17-28.

[38] A. Manasilp, E. Gulari, Appl. Catal., B 37 (2002) 17-25.

[39] G. Avgouropoulos, T. Ioannides, C. Papadopoulou, J. Batista, S. Hocevar, H.K. Matralis, Catal. Today 75 (2002) 157-167.

[40] M. Kotobuki, A. Watanabe, H. Uchida, H. Yamashita, M. Watanabe, Chem. Lett. 34 (2005) 866-867.

[41] S. Ren, X. Hong, Fuel Process. Technol. 88 (2007) 383-386.

[42] M. Kotobuki, A. Watanabe, H. Uchida, H. Yamashita, M. Watanabe, J. Catal. 236 (2005) 262-269.

[43] H. Igarashi, H. Uchida, M. Suzuki, Y. Sasaki, M. Watanabe, Appl. Catal., A 159 (1997) 159-169.

[44] M. Watanabe, H. Uchida, H. Igarashi, M. Suzuki, Chem. Lett. (1995) 21-22.

[45] V. Sebastian, S. Irusta, R. Mallada, J. Santamaría, Appl. Catal., A 366 (2009) 242-251.

[46] R. Andorf, W. Maunz, C. Plog, T. Stengel, The use of zeolites PtNaY as oxidation catalyst for selectively removing CO from hydrogen-rich gas from methanol reformation, Daimler-Benz A.-G., Germany . 1997, p. 10 pp.

[47] D.H. Kim, M.S. Lim, Appl. Catal., A 224 (2002) 27-38.

[48] M.M. Schubert, M.J. Kahlich, H.A. Gasteiger, R.J. Behm, J. Power Sources 84 (1999) 175-182.

[49] M.J. Kahlich, H.A. Gasteiger, R.J. Behm, J. Catal. 171 (1997) 93-105.

[50] A. Sirijaruphan, J.G. Goodwin Jr, R.W. Rice, J. Catal. 227 (2004) 547-551.

[51] Y.F. Han, M.J. Kahlich, M. Kinne, R.J. Behm, PCCP 4 (2002) 389-397.

[52] S. Huang, K. Hara, A. Fukuoka, Energy Environ. Sci. 2 (2009) 1060-1068.

[53] D. Tibiletti, E.A.B. de Graaf, S. Pheng Teh, G. Rothenberg, D. Farrusseng, C. Mirodatos, J. Catal. 225 (2004) 489-497.

[54] I. Son, A. Lane, Catal. Lett. 76 (2001) 151-154.

[55] O. Pozdnyakova-Tellinger, D. Teschner, J. Kröhnert, F.C. Jentoft, A. Knop-Gericke, R. Schlögl, A. Wootsch, J. Phys. Chem. C 111 (2007) 5426-5431.

[56] J.L. Ayastuy, A. Gil-Rodríguez, M.P. González-Marcos, M.A. Gutiérrez-Ortiz, Int. J. Hydrogen Energy 31 (2006) 2231-2242.

[57] D. Teschner, A. Wootsch, O. Pozdnyakova-Tellinger, J. Kröhnert, E.M. Vass, M. Hävecker, S. Zafeiratos, P. Schnörch, P.C. Jentoft, A. Knop-Gericke, R. Schlögl, J. Catal. 249 (2007) 318-327.

[58] D. Teschner, A. Wootsch, O. Pozdnyakova, H. Sauer, A. Knop-Gericke, R. Schlögl, React. Kinet. Catal. Lett. 87 (2006) 235-247.

[59] J.L. Ayastuy, M.P. González-Marcos, A. Gil-Rodríguez, J.R. González-Velasco, M.A. Gutiérrez-Ortiz, Catal. Today 116 (2006) 391-399.

[60] A. Wootsch, C. Descorme, D. Duprez, J. Catal. 225 (2004) 259-266.

[61] H.-S. Roh, H.S. Potdar, K.-W. Jun, S. Han, J.-W. Kim, Catal. Lett. 93 (2004) 203-207.

[62] C. Descorme, Y. Madier, D. Duprez, J. Catal. 196 (2000) 167-173.

[63] A. Holmgren, D. Duprez, B. Andersson, J. Catal. 182 (1999) 441-448.

[64] E. Bekyarova, P. Fornasiero, J. Kašpar, M. Graziani, Catal. Today 45 (1998) 179-183.

[65] O. Korotkikh, R. Farrauto, Catal. Today 62 (2000) 249-254.

[66] M. Kotobuki, A. Watanabe, H. Uchida, H. Yamashita, M. Watanabe, Appl. Catal., A 307 (2006) 275-283.

[67] M. Kotobuki, T. Shido, M. Tada, H. Uchida, H. Yamashita, Y. Iwasawa, M. Watanabe, Catal. Lett. 103 (2005) 263-269.

[68] M. Watanabe, H. Uchida, K. Ohkubo, H. Igarashi, Appl. Catal., B 46 (2003) 595-600.

[69] X. Liu, O. Korotkikh, R. Farrauto, Appl. Catal., A 226 (2002) 293-303.

[70] Q. Fu, W.-X. Li, Y. Yao, H. Liu, H.-Y. Su, D. Ma, X.-K. Gu, L. Chen, Z. Wang, H. Zhang, B. Wang, X. Bao, Science 328 (2010) 1141-1144.

[71] A. Fukuoka, J.-i. Kimura, T. Oshio, Y. Sakamoto, M. Ichikawa, J. Am. Chem. Soc. 129 (2007) 10120-10125.

[72] M. Watanabe, S. Motoo, J. Electroanal. Chem. Interfacial Electrochem. 60 (1975) 259-266.

[73] M. Watanabe, S. Motoo, J. Electroanal. Chem. Interfacial Electrochem. 60 (1975) 275-283.

[74] S.Y. Chin, O.S. Alexeev, M.D. Amiridis, J. Catal. 243 (2006) 329-339.

[75] S. Lee, J. Han, K.-Y. Lee, Korean J. Chem. Eng. 19 (2002) 431-433.

[76] H. Igarashi, H. Uchida, M. Watanabe, Chem. Lett. 29 (2000) 1262-1263.

[77] P. Naknam, A. Luengnaruemitchai, S. Wongkasemjit, S. Osuwan, J. Power Sources 165 (2007) 353-358.

[78] A.U. Nilekar, S. Alayoglu, B. Eichhorn, M. Mavrikakis, J. Am. Chem. Soc. 132 (2010) 7418-7428.

[79] S. Alayoglu, A.U. Nilekar, M. Mavrikakis, B. Eichhorn, Nat. Mater. 7 (2008) 333-338.

[80] J.L. Ayastuy, M.P. González-Marcos, J.R. González-Velasco, M.A. Gutiérrez-Ortiz, Appl. Catal., B 70 (2007) 532-541.

[81] R. Mu, Q. Fu, H. Xu, H. Zhang, Y. Huang, Z. Jiang, S. Zhang, D. Tan, X. Bao, J. Am. Chem. Soc. 133 (2011) 1978-1986.

[82] S. Lu, C. Zhang, Y. Liu, Int. J. Hydrogen Energy 36 (2011) 1939-1948.

[83] T. Komatsu, A. Tamura, J. Catal. 258 (2008) 306-314.

[84] E.Y. Ko, E.D. Park, H.C. Lee, D. Lee, S. Kim, Angew. Chem. Int. Ed. 46 (2007) 734-737.

[85] P.V. Snytnikov, K.V. Yusenko, S.V. Korenev, Y.V. Shubin, V.A. Sobyanin, Kinet. Catal. 48 (2007) 276-281.

[86] W.S. Epling, P.K. Cheekatamarla, A.M. Lane, Chem. Eng. J. 93 (2003) 61-68.

[87] M.M. Schubert, M.J. Kahlich, G. Feldmeyer, M. Huttner, S. Hackenberg, H.A. Gasteiger, R.J. Behm, PCCP 3 (2001) 1123-1131.

[88] G. Uysal, A.N. Akın, Z.İ. Önsan, R. Yıldırım, Catal. Lett. 111 (2006) 173-176.

[89] Y.F. Han, M.J. Kahlich, M. Kinne, R.J. Behm, Appl. Catal., B 50 (2004) 209-218.

[90] C. Galletti, S. Fiorot, S. Specchia, G. Saracco, V. Specchia, Top. Catal. 45 (2007) 15-19.

[91] C. Galletti, S. Specchia, G. Saracco, V. Specchia, Ind. Eng. Chem. Res. 47 (2008) 5304-5312.

[92] Y.F. Han, M. Kinne, R.J. Behm, Appl. Catal., B 52 (2004) 123-134.

[93] Y.H. Kim, E.D. Park, H.C. Lee, D. Lee, Appl. Catal., A 366 (2009) 363-369.

[94] Y.H. Kim, E.D. Park, Appl. Catal., B 96 (2010) 41-50.

[95] I. Rosso, M. Antonini, C. Galletti, G. Saracco, V. Specchia, Top. Catal. 30-31 (2004) 475-480.

[96] M. Echigo, T. Tabata, J. Chem. Eng. Jpn. 37 (2004) 558-562.
[97] M. Echigo, N. Shinke, S. Takami, S. Higashiguchi, K. Hirai, T. Tabata, Catal. Today 84 (2003) 209-215.
[98] M. Echigo, N. Shinke, S. Takami, T. Tabata, J. Power Sources 132 (2004) 29-35.
[99] M. Echigo, T. Tabata, Catal. Today 90 (2004) 269-275.
[100] M. Echigo, T. Tabata, Catal. Lett. 98 (2004) 37-42.
[101] M. Echigo, T. Tabata, Appl. Catal., A 251 (2003) 157-166.
[102] M. Echigo, T. Tabata, Top. Catal. 52 (2009) 739-742.
[103] S.Y. Chin, O.S. Alexeev, M.D. Amiridis, Appl. Catal., A 286 (2005) 157-166.
[104] Y.H. Kim, E.D. Park, H.C. Lee, D. Lee, K.H. Lee, Catal. Today 146 (2009) 253-259.
[105] Y. Huang, A. Wang, X. Wang, T. Zhang, Int. J. Hydrogen Energy 32 (2007) 3880-3886.
[106] Y. Huang, A. Wang, L. Li, X. Wang, T. Zhang, Catal. Commun. 11 (2010) 1090-1093.
[107] U. Heiz, U. Landman, Nanocatalysis, Springer - Verlag, Berlin, 2007.
[108] G. Bond, Gold Bulletin 5 (1972) 11-13.
[109] G.C. Bond, P.A. Sermon, Gold Bulletin 6 (1973) 102.
[110] D.Y. Cha, G. Parravano, J. Catal. 18 (1970) 200-211.
[111] S. Galvagno, G. Parravano, J. Catal. 55 (1978) 178-190.
[112] J. Schwank, Gold Bulletin 16 (1983) 103-110.
[113] M. Haruta, T. Kobayashi, H. Sano, N. Yamada, Chem. Lett. 16 (1987) 405-408.
[114] B. Nkosi, N.J. Coville, G.J. Hutchings, J. Chem. Soc., Chem. Commun. (1988) 71-72.
[115] M. Haruta, H. Sano, in: P.G. G. Poncelet, P.A. Jacobs (Eds.), Stud. Surf. Sci. Catal., Elsevier, 1983, pp. 225-236.
[116] H. Sakurai, A. Ueda, T. Kobayashi, M. Haruta, Chem. Commun. (1997) 271-272.
[117] Y. Iizuka, T. Tamai, T. Hayashi, I. Okuda, M. Haruta, Preparation of cycloolefins by partial hydrogenation of monocyclic aromatic hydrocarbons with gold catalysts, Kyoto Institute of Technology, Japan; Tokyo Metropolitan University . 2010, p. 24pp.
[118] M. Okumura, T. Akita, M. Haruta, Catal. Today 74 (2002) 265-269.
[119] K. Tanaka, T. Hayashi, M. Haruta, Nippon Kinzoku Gakkaishi 60 (1996) 693-694.
[120] M. Haruta, Catal. Surv. Jpn. 1 (1997) 61-73.
[121] M. Haruta, Gold Bulletin 37 (2004) 27-36.

[122] S. Scirè, C. Crisafulli, P.M. Riccobene, G. Patanè, A. Pistone, Appl. Catal., A 417–418 (2012) 66-75.

[123] P. Sangeetha, L.-H. Chang, Y.-W. Chen, Ind. Eng. Chem. Res. 48 (2009) 5666-5670.

[124] K.M. Parida, P. Mohapatra, J. Moma, W.A. Jordaan, M.S. Scurrell, J. Mol. Catal. A: Chem. 288 (2008) 125-130.

[125] L. Ilieva, T. Tabakova, G. Pantaleo, I. Ivanov, R. Zanella, D. Paneva, N. Velinov, J.W. Sobczak, W. Lisowski, G. Avdeev, A.M. Venezia, Appl. Catal., A 467 (2013) 76-90.

[126] S. Shimada, T. Takei, T. Akita, S. Takeda, M. Haruta, Stud. Surf. Sci. Catal. 175 (2010) 843-847.

[127] M. Haruta, Catal. Today 36 (1997) 153-166.

[128] S. Ivanova, V. Pitchon, C. Petit, V. Caps, ChemCatChem 2 (2010) 556-563.

[129] M. Haruta, S. Tsubota, T. Kobayashi, H. Kageyama, M.J. Genet, B. Delmon, J. Catal. 144 (1993) 175-192.

[130] T. Fujitani, I. Nakamura, M. Haruta, Catal. Lett. 144 (2014) 1475-1486.

[131] M. Date, M. Okumura, S. Tsubota, M. Haruta, Angew. Chem., Int. Ed. 43 (2004) 2129-2132.

[132] G.C. Bond, C. Louis, D.T. Thompson, Catalysis by Gold, Imperial College Press ; Distributed by World Scientific, London, 2006.

[133] S.D. Lin, M. Bollinger, M.A. Vannice, Catal. Lett. 17 (1993) 245-262.

[134] F. Moreau, G.C. Bond, Catal. Today 122 (2007) 260-265.

[135] F. Moreau, G.C. Bond, A.O. Taylor, J. Catal. 231 (2005) 105-114.

[136] A.M. Venezia, G. Pantaleo, A. Longo, G. Di Carlo, M.P. Casaletto, F.L. Liotta, G. Deganello, J. Phys. Chem. B 109 (2005) 2821-2827.

[137] M. Haruta, Cattech 6 (2002) 102-115.

[138] H.S. Oh, J.H. Yang, C.K. Costello, Y.M. Wang, S.R. Bare, H.H. Kung, M.C. Kung, J. Catal. 210 (2002) 375-386.

[139] H.H. Kung, M.C. Kung, C.K. Costello, J. Catal. 216 (2003) 425-432.

[140] M. Haruta, N. Yamada, T. Kobayashi, S. Iijima, J. Catal. 115 (1989) 301-309.

[141] L.A.M. Hermans, J.W. Geus, in: P.G.P.J. B. Delmon, G. Poncelet (Eds.), Stud. Surf. Sci. Catal., Elsevier, 1979, pp. 113-130.

[142] R. Zanella, L. Delannoy, C. Louis, Appl. Catal., A 291 (2005) 62-72.

[143] R. Zanella, S. Giorgio, C.R. Henry, C. Louis, J. Phys. Chem. B 106 (2002) 7634-7642.

[144] Y.A. Nechayev, N.V. Nikolenko, Geochem. Int. 23 (1986) 32-37.

[145] F. Moreau, G.C. Bond, Appl. Catal., A 302 (2006) 110-117.

[146] T. Takei, T. Ishida, M. Haruta, Novel Concepts in Catalysis and Chemical Reactors, Wiley-Blackwell, Weinheim, Germany, 2010, pp. 51-71.

[147] A. Wolf, F. Schüth, Appl. Catal., A 226 (2002) 1-13.

[148] M. Haruta, The Chemical Record 3 (2003) 75-87.

[149] S. Ivanova, C. Petit, V. Pitchon, Appl. Catal., A 267 (2004) 191-201.

[150] S. Ivanova, V. Pitchon, C. Petit, H. Herschbach, A.V. Dorsselaer, E. Leize, Appl. Catal., A 298 (2006) 203-210.

[151] K. Chan, Z. Aspanut, B. Goh, M.R. Muhamad, S.A. Rahman, Thin Solid Films 519 (2011) 4952-4957.

[152] M. Okumura, K. Tanaka, A. Ueda, M. Haruta, Solid State Ionics 95 (1997) 143-149.

[153] G.M. Veith, A.R. Lupini, S.J. Pennycook, A. Villa, L. Prati, N.J. Dudney, Catal. Today 122 (2007) 248-253.

[154] G.M. Veith, A.R. Lupini, S.J. Pennycook, G.W. Ownby, N.J. Dudney, J. Catal. 231 (2005) 151-158.

[155] T. Kobayashi, M. Haruta, S. Tsubota, H. Sano, B. Delmon, Sensors and Actuators B: Chemical 1 (1990) 222-225.

[156] N. Lopez, T.V.W. Janssens, B.S. Clausen, Y. Xu, M. Mavrikakis, T. Bligaard, J.K. Nørskov, J. Catal. 223 (2004) 232-235.

[157] T. Akita, K. Tanaka, S. Tsubota, M. Haruta, J. Electron Microsc. 49 (2000) 657-662.

[158] G.R. Bamwenda, S. Tsubota, T. Nakamura, M. Haruta, Catal. Lett. 44 (1997) 83-87.

[159] M. Haruta, H. Kageyama, N. Kamijo, T. Kobayashi, F. Delannay, in: T. Inui (Ed.), Stud. Surf. Sci. Catal., Elsevier, Amsterdam, Netherlands, 1989, pp. 33-42.

[160] S. Arrii, F. Morfin, A.J. Renouprez, J.L. Rousset, J. Am. Chem. Soc. 126 (2004) 1199-1205.

[161] M.M. Schubert, S. Hackenberg, A.C. van Veen, M. Muhler, V. Plzak, R.J. Behm, J. Catal. 197 (2001) 113-122.

[162] J.C. Frost, Nature 334 (1988) 577-580.

[163] X. Zhang, H. Wang, B.-Q. Xu, J. Phys. Chem. B 109 (2005) 9678-9683.

[164] S. Carrettin, P. Concepcion, A. Corma, J.M.L. Nieto, V.F. Puntes, Angew. Chem. Int. Ed. 43 (2004) 2538-2540.

[165] A.I. Kozlov, A.P. Kozlova, H. Liu, Y. Iwasawa, Appl. Catal., A 182 (1999) 9-28.

[166] R. M. Finch, N. A. Hodge, G. J. Hutchings, A. Meagher, Q. A. Pankhurst, M. Rafiq H. Siddiqui, F. E. Wagner, R. Whyman, PCCP 1 (1999) 485-489.

[167] S.T. Daniells, A.R. Overweg, M. Makkee, J.A. Moulijn, J. Catal. 230 (2005) 52-65.

[168] D. Widmann, R.J. Behm, Acc. Chem. Res. 47 (2014) 740-749.

[169] C.K. Costello, J.H. Yang, H.Y. Law, Y. Wang, J.N. Lin, L.D. Marks, M.C. Kung, H.H. Kung, Appl. Catal., A 243 (2003) 15-24.

[170] H. Liu, A.I. Kozlov, A.P. Kozlova, T. Shido, K. Asakura, Y. Iwasawa, J. Catal. 185 (1999) 252-264.

[171] M. Okumura, S. Nakamura, S. Tsubota, T. Nakamura, M. Azuma, M. Haruta, Catal. Lett. 51 (1998) 53-58.

[172] I.N. Remediakis, N. Lopez, J.K. Nørskov, Angew. Chem. 117 (2005) 1858-1860.

[173] Z.-P. Liu, X.-Q. Gong, J. Kohanoff, C. Sanchez, P. Hu, Phys. Rev. Lett. 91 (2003) 266102.

[174] G. Bond, D. Thompson, Gold Bulletin 42 (2009) 247-259.

[175] G. Bond, D. Thompson, Gold Bulletin 33 (2000) 41-50.

[176] M. Date, M. Haruta, J. Catal. 201 (2001) 221-224.

[177] E.D. Park, J.S. Lee, J. Catal. 186 (1999) 1-11.

[178] T.R.M. Sanchez, A. Ueda, K. Tanaka, M. Haruta, J. Catal. 168 (1997) 125-127.

[179] M.J. Kahlich, H.A. Gasteiger, R.J. Behm, J. Catal. 182 (1999) 430-440.

[180] M.M. Schubert, A. Venugopal, M.J. Kahlich, V. Plzak, R.J. Behm, J. Catal. 222 (2004) 32-40.

[181] A. Luengnaruemitchai, D. Thi Kim Thoa, S. Osuwan, E. Gulari, Int. J. Hydrogen Energy 30 (2005) 981-987.

[182] P. Landon, J. Ferguson, B.E. Solsona, T. Garcia, S. Al-Sayari, A.F. Carley, A.A. Herzing, C.J. Kiely, M. Makkee, J.A. Moulijn, A. Overweg, S.E. Golunski, G.J. Hutchings, J. Mater. Chem. 16 (2006) 199-208.

[183] G. Avgouropoulos, in: G. Avgouropoulos, T. Tabakova (Eds.), Environmental Catalysis over Gold-Based Materials, The Royal Society of Chemistry, Cambridge, 2013, pp. 96-122.

[184] G. Avgouropoulos, M. Manzoli, F. Boccuzzi, T. Tabakova, J. Papavasiliou, T. Ioannides, V. Idakiev, J. Catal. 256 (2008) 237-247.

[185] L. Ilieva, G. Pantaleo, I. Ivanov, R. Zanella, A.M. Venezia, D. Andreeva, Int. J. Hydrogen Energy 34 (2009) 6505-6515.

[186] M. Manzoli, G. Avgouropoulos, T. Tabakova, J. Papavasiliou, T. Ioannides, F. Boccuzzi, Catal. Today 138 (2008) 239-243.

[187] A. Luengnaruemitchai, S. Osuwan, E. Gulari, Int. J. Hydrogen Energy 29 (2004) 429-435.

[188] H. Wang, H. Zhu, Z. Qin, F. Liang, G. Wang, J. Wang, J. Catal. 264 (2009) 154-162.

[189] O.H. Laguna, W.Y. Hernández, G. Arzamendi, L.M. Gandía, M.A. Centeno, J.A. Odriozola, Fuel 118 (2014) 176-185.

[190] J. Steyn, G. Pattrick, M.S. Scurrell, D. Hildebrandt, M.C. Raphulu, E. van der Lingen, Catal. Today 122 (2007) 254-259.

[191] L.F. Liotta, G. Di Carlo, G. Pantaleo, A.M. Venezia, Catal. Today 158 (2010) 56-62.

[192] C. Galletti, S. Fiorot, S. Specchia, G. Saracco, V. Specchia, Chem. Eng. J. 134 (2007) 45-50.

[193] Y. Denkwitz, B. Schumacher, G. Kučerová, R.J. Behm, J. Catal. 267 (2009) 78-88.

[194] Y.-F. Yang, P. Sangeetha, Y.-W. Chen, Ind. Eng. Chem. Res. 48 (2009) 10402-10407.

[195] Y.-W. Chen, H.-J. Chen, D.-S. Lee, J. Mol. Catal. A: Chem. 363–364 (2012) 470-480.

[196] P. Sangeetha, Y.-W. Chen, Int. J. Hydrogen Energy 34 (2009) 7342-7347.

[197] F. Mariño, C. Descorme, D. Duprez, Appl. Catal., B 58 (2005) 175-183.

[198] W. Liu, M. Flytzanistephanopoulos, J. Catal. 153 (1995) 304-316.

[199] G. Sedmak, S. Hočevar, J. Levec, J. Catal. 222 (2004) 87-99.

[200] G. Avgouropoulos, T. Ioannides, Appl. Catal., B 67 (2006) 1-11.

[201] G. Avgouropoulos, T. Ioannides, H. Matralis, Appl. Catal., B 56 (2005) 87-93.

[202] Z. Liu, R. Zhou, X. Zheng, J. Mol. Catal. A: Chem. 267 (2007) 137-142.

[203] C.R. Jung, J. Han, S.W. Nam, T.H. Lim, S.A. Hong, H.I. Lee, Catal. Today 93-95 (2004) 183-190.

[204] J. Li, Y. Han, Y. Zhu, R. Zhou, Appl. Catal., B 108–109 (2011) 72-80.

[205] Y. Liu, Q. Fu, M.F. Stephanopoulos, Catal. Today 93–95 (2004) 241-246.

[206] E. Moretti, M. Lenarda, L. Storaro, A. Talon, T. Montanari, G. Busca, E. Rodríguez-Castellón, A. Jiménez-López, M. Turco, G. Bagnasco, R. Frattini, Appl. Catal., A 335 (2008) 46-55.

[207] N. Bion, F. Epron, M. Moreno, F. Mariño, D. Duprez, Top. Catal. 51 (2008) 76-88.

[208] M.-F. Luo, Y.-J. Zhong, X.-X. Yuan, X.-M. Zheng, Appl. Catal., A 162 (1997) 121-131.

[209] F. Giordano, A. Trovarelli, C. de Leitenburg, M. Giona, J. Catal. 193 (2000) 273-282.

[210] S. Royer, D. Duprez, ChemCatChem 3 (2011) 24-65.

[211] Y. Xie, F. Dong, S. Heinbuch, J.J. Rocca, E.R. Bernstein, PCCP 12 (2010) 947-959.

[212] M.J. Pollard, B.A. Weinstock, T.E. Bitterwolf, P.R. Griffiths, A. Piers Newbery, J.B. Paine Iii, J. Catal. 254 (2008) 218-225.

[213] H.-K. Lin, H.-C. Chiu, H.-C. Tsai, S.-H. Chien, C.-B. Wang, Catal. Lett. 88 (2003) 169-174.

[214] K. Omata, Y. Kobayashi, M. Yamada, Catal. Commun. 6 (2005) 563-567.

[215] W.-H. Yang, M.H. Kim, S.-W. Ham, Catal. Today 123 (2007) 94-103.

[216] L.F. Liotta, G. Di Carlo, G. Pantaleo, A.M. Venezia, G. Deganello, Appl. Catal., B 66 (2006) 217-227.

[217] Z. Zhao, M.M. Yung, U.S. Ozkan, Catal. Commun. 9 (2008) 1465-1471.

[218] M.P. Woods, P. Gawade, B. Tan, U.S. Ozkan, Appl. Catal., B 97 (2010) 28-35.

[219] P. Gawade, B. Bayram, A.-M.C. Alexander, U.S. Ozkan, Appl. Catal., B 128 (2012) 21-30.

[220] A. Martínez-Arias, A.B. Hungría, G. Munuera, D. Gamarra, Appl. Catal., B 65 (2006) 207-216.

[221] Z. Zhao, R. Jin, T. Bao, X. Lin, G. Wang, Appl. Catal., B 110 (2011) 154-163.

[222] Z. Zhao, R. Jin, T. Bao, H. Yang, X. Lin, G. Wang, Int. J. Hydrogen Energy 37 (2012) 4774-4786.

[223] Z. Zhao, X. Lin, R. Jin, Y. Dai, G. Wang, Catal. Commun. 12 (2011) 1448-1451.

[224] Z. Zhao, X. Lin, R. Jin, Y. Dai, G. Wang, Catal. Sci. Technol. 2 (2012) 554-563.

[225] Z. Zhao, X. Lin, R. Jin, G. Wang, M. Qiu, Curr. Top. Catal. 9 (2010) 1-14.

[226] G. Sedmak, S. Hočevar, J. Levec, J. Catal. 213 (2003) 135-150.

[227] M.M. Yung, Z. Zhao, M.P. Woods, U.S. Ozkan, J. Mol. Catal. A: Chem. 279 (2008) 1-9.

[228] Q. Guo, S. Chen, Y. Liu, Y. Wang, Chem. Eng. J. 165 (2010) 846-850.

[229] D. Gamarra, A. Martínez-Arias, J. Catal. 263 (2009) 189-195.

[230] A. Trovarelli, P. Fornasiero, Editors, Catalysis by Ceria and Related Materials, 2nd Edition, Imperial College Press ; Distributed by World Scientific, London, 2013.

[231] R.J. Gorte, AlChE J. 56 1126-1135.

[232] F.A. Kroger, H.J. Vink, Solid State Physics 3 (1956) 307-435.

[233] K.C. Patil, M.S. Hegde, T. Rattan, S.T. Aruna, Chemistry of Nanocrystalline Oxide Materials, World Scientific Publishing, Singapore, 2008, pp. 117-153.

[234] A. Gupta, U.V. Waghmare, M.S. Hegde, Chem. Mater. 22 (2010) 5184-5198.

[235] J. Kaspar, P. Fornasiero, Catal. Sci. Ser. 2 (2002) 217-241.

[236] K. Schwarz, Proceedings of the National Academy of Sciences of the United States of America 103 (2006) 3497.

[237] D. Terribile, A. Trovarelli, J. Llorca, C. de Leitenburg, G. Dolcetti, Catal. Today 43 (1998) 79-88.

[238] D. Terribile, A. Trovarelli, J. Llorca, C. De Leitenburg, G. Dolcetti, J. Catal. 178 (1998) 299-308.

[239] D. Terribile, A. Trovarelli, C. de Leitenburg, A. Primavera, G. Dolcetti, Catal. Today 47 (1999) 133-140.

[240] K. Zhou, Z. Yang, S. Yang, Chem. Mater. 19 (2007) 1215-1217.

[241] M.-F. Luo, Y.-P. Song, J.-Q. Lu, X.-Y. Wang, Z.-Y. Pu, J. Phys. Chem. C 111 (2007) 12686-12692.

[242] D. Terribile, A. Trovarelli, C. de Leitenburg, G. Dolcetti, J. Llorca, Chemistry of Materials 9 (1997) 2676-2678.

[243] A. Martínez-Arias, M. Fernández-García, O. Gálvez, J.M. Coronado, J.A. Anderson, J.C. Conesa, J. Soria, G. Munuera, J. Catal. 195 (2000) 207-216.

[244] Y.-Z. Chen, B.-J. Liaw, H.-C. Chen, Int. J. Hydrogen Energy 31 (2006) 427-435.

[245] C.R. Jung, A. Kundu, S.W. Nam, H.-I. Lee, Appl. Catal., A 331 (2007) 112-120.

[246] E.-Y. Ko, E.D. Park, K.W. Seo, H.C. Lee, D. Lee, S. Kim, Catal. Today 116 (2006) 377-383.

[247] Y.-Z. Chen, B.-J. Liaw, C.-W. Huang, Appl. Catal., A 302 (2006) 168-176.

[248] A. Arango-Díaz, J.A. Cecilia, E. Moretti, A. Talon, P. Núñez, J. Marrero-Jerez, J. Jiménez-Jiménez, A. Jiménez-López, E. Rodríguez-Castellón, Int. J. Hydrogen Energy 39 (2014) 4102-4108.

[249] Y. Chen, D. Liu, L. Yang, M. Meng, J. Zhang, L. Zheng, S. Chu, T. Hu, Chem. Eng. J. 234 (2013) 88-98.

[250] S. Lang, M. Türk, B. Kraushaar-Czarnetzki, J. Catal. 286 (2012) 78-87.

[251] Y.-Z. Chen, B.-J. Liaw, W.-C. Chang, C.-T. Huang, Int. J. Hydrogen Energy 32 (2007) 4550-4558.

[252] J. Won Park, J. Hyeok Jeong, W.L. Yoon, C.S. Kim, D.K. Lee, Y.-K. Park, Y.W. Rhee, Int. J. Hydrogen Energy 30 (2005) 209-220.

[253] M.-F. Luo, J.-M. Ma, J.-Q. Lu, Y.-P. Song, Y.-J. Wang, J. Catal. 246 (2007) 52-59.

[254] J.-Y. Luo, M. Meng, Y.-Q. Zha, L.-H. Guo, J. Phys. Chem. C 112 (2008) 8694-8701.

[255] J. Cortes, E. Valencia, P. Araya, Catal. Lett. 143 (2013) 176-183.

[256] Z. Guo, B. Liu, Q. Zhang, W. Deng, Y. Wang, Y. Yang, Chem. Soc. Rev. 43 (2014) 3480-3524.

[257] M. Moreno, L. Bergamini, G.T. Baronetti, M.A. Laborde, F.J. Marino, Int. J. Hydrogen Energy 35 (2010) 5918-5924.

[258] D. Duprez, Catal. Today 112 (2006) 17-22.

[259] X.-L. Xu, E. Yang, J.-Q. Li, Y. Li, W.-K. Chen, ChemCatChem 1 (2009) 384-392.

[260] K. Liu, A. Wang, T. Zhang, ACS Catalysis 2 (2012) 1165-1178.

CHAPTER 3

CO oxidation activity enhancement of $Ce_{0.95}Cu_{0.05}O_{2-\delta}$ induced by Pd co-substitution

Keywords: Ceria, bimetallic, solid solution, CO oxidation

Abstract

A bimetallic, ionic, $Ce_{0.93}Pd_{0.02}Cu_{0.05}O_{2-\delta}$ catalyst was synthesized in one-step using a urea-assisted solution combustion method. The structural and electronic properties of the catalyst were studied by different techniques, together with those of mono-metallic analogues. The catalytic performance of the materials was investigated using CO oxidation as the model exhaust reaction. X-ray diffraction (XRD), Raman spectroscopy, XPS, XANES, EXAFS and high resolution transmission electron microscopy (HR-TEM) revealed that the prepared materials are single-phase, solid-solution oxides with a fluorite structure. The correlation of the characterization and catalytic results indicates that catalytic performance is influenced by the presence of oxygen vacancies and the existence of synergism between Pd^{2+}, Cu^{2+} and cerium ions. The activation energy for CO oxidation over $Ce_{0.93}Pd_{0.02}Cu_{0.05}O_{2-\delta}$ was found to be 45.8 kJ/mol, compared to 72.2 kJ/mol over $Ce_{0.95}Cu_{0.05}O_{2-\delta}$.

3.1 Introduction

Ceria-based materials are regarded as materials of technological importance due to their various applications in automotive catalysis [1], solar cells [2] and hydrogen production reactions for fuel cell technology [3-5]. The catalytic activity of ceria-related materials mainly originates from their ability to be reduced and oxidized, switching between the redox couple $Ce^{4+} \leftrightarrow Ce^{3+}$ [3]. This redox transition results from the release of lattice oxygen, creating vacant sites [6]. Therefore, the single electron defects of Ce^{3+} ions can serve as vacant sites for active oxygen species required for catalytic reactions. In this way, the oxygen storage capacity (OSC) and oxygen mobility become the important features at the core of catalysis by ceria-based systems.

Ceria has been used as a support for different metals and metal oxides in order to produce catalyst formulations with enhanced performance. To date, the properties and performance of ceria-related catalytic systems such as CuO/CeO_2 [7-9], Pd/CeO_2 [8], Pt/CeO_2 [8], Rh/CeO_2 [8] and Au/CeO_2 [10] have been investigated for different reactions. In most cases, CeO_2 as a support, has been associated with improved metal dispersion and better metal-support interaction, which in turn translate to enhanced catalytic activity. However, complete dispersion is difficult to achieve and only 20 to 25% of the active components are normally used in catalytic conversion [11]. An approach that has been proposed as a solution to the dispersion problem involves incorporating foreign metal ions into the lattice structure of the support (CeO_2), forming a solid-solution material [11]. With this method, the active metal can be fully dispersed as ions within the $Ce_{1-x}M_xO_{2-\delta}$ single-phase material. Importantly, this approach allows tuning of the redox properties, oxygen storage capacity, metal-Ce interaction and consequently the catalytic behaviour. Moreover, the incorporation of foreign metal ions creates oxygen vacancies which act as local sites for active oxygen needed during catalytic progression. It has been shown that the insertion of metals such as Pt, Pd, Rh, Cu, Fe and Co leads to materials with enhanced OSC and improved catalytic performance [5, 11-15].

Carbon monoxide (CO) is one of the major pollutants released from internal combustion engines. Because the presence of CO, even in trace amounts, raises environmental and health concerns, the regulations governing auto emissions are becoming increasingly stringent. In the course of addressing environmental fears, catalytic CO oxidation has been intensively studied and well established [16, 17]. However, there is still a need to develop new efficient and cost effective catalysts. Traditionally, supported platinum group metals (PGMs) and gold catalysts are used to achieve this goal. In particular, Pd supported on ceria-based materials has been included in the three-way catalyst formulations [8, 18]. Alternate CuO/CeO_2 catalyst systems have also been studied and may be promising candidates for future applications in auto-emission control, due to their high activity towards CO oxidation [9, 19].

In recent years, several groups have shown that introducing a third metal such as Pt, Zr or Co to CuO/CeO_2 systems improved the activity [7, 10, 20]. The improved catalytic performance in bimetallic catalysts is often linked to the presence of synergism between the corresponding metals. Based on this, we have synthesized ceria-based solid-solution mono-metallic and

bimetallic ionic catalysts, viz. $Ce_{0.98}Pd_{0.02}O_{2-\delta}$, $Ce_{0.95}Cu_{0.05}O_{2-\delta}$ and $Ce_{0.93}Pd_{0.02}Cu_{0.05}O_{2-\delta}$. The intention was to explore the combined effect of Cu^{2+} and Pd^{2+} ions within the matrix of CeO_2. To understand this, the structure, redox features and CO oxidation activity of the $Ce_{0.93}Pd_{0.02}Cu_{0.05}O_{2-\delta}$ bimetal ionic catalyst were studied and compared with those of the mono-metallic ionic catalysts, $Ce_{0.98}Pd_{0.02}O_{2-\delta}$ and $Ce_{0.95}Cu_{0.05}O_{2-\delta}$. Simultaneous incorporation of Cu^{2+} (0.73 Å) and Pd^{2+} (0.86 Å) appears to be a viable combination due to their small ionic radii, compared to Ce^{4+} (0.97 Å). More importantly, the substitution of Ce with small valence ions has been reported to result in materials with improved OSC [5, 11, 13]. The presence of Pd in the catalyst is expected to be beneficial for CO adsorption and the use of low Pd atomic loading, relative to Cu, would be economically justifiable.

3.2 Experimental

3.2.1 Catalyst synthesis

Single-phase solid-solution mono-metallic ($Ce_{0.98}Pd_{0.02}O_{2-\delta}$ and $Ce_{0.95}Cu_{0.05}O_{2-\delta}$) and bimetallic ($Ce_{0.93}Pd_{0.02}Cu_{0.05}O_{2-\delta}$) ionic catalysts were prepared using a single-step urea-assisted combustion method [21]. Ceric ammonium nitrate [$(NH_4)_2Ce(NO_3)_6$, 99.9%], copper nitrate [$Cu(NO_3)_2.3H_2O$, 99.9%], palladium chloride [$PdCl_2$, 99%] and urea [NH_2CONH_2, 99.9%] were obtained from Sigma-Aldrich and used without further purification. A typical preparation method involves making a redox combustion mixture composed of stoichiometric amounts the metal precursors and urea fuel in the ratio of 1.0 : 3.77 respectively. Specifically, for the synthesis of $Ce_{0.93}Pd_{0.02}Cu_{0.05}O_{2-\delta}$, 10.197 g of ceric ammonium nitrate, 0.242 g of copper nitrate, 0.107 g of palladium chloride and 4.529 g of urea were dissolved in 50 mL of water in a borosilicate dish. The solution was mixed and reduced to ~ 20 mL at 150 °C on a hotplate for 10 minutes. The boiling solution was then transferred into a muffle furnace which was preheated to 400 °C. After nearly complete dehydration, the solution boiled with foaming and dried before igniting. The resulting dark-brown solid product was kept in the furnace overnight at 400 °C. Mono-metallic, ionic analogues were prepared using a similar combustion method. Detailed calculations for the preparation of solid solution materials are presented in Appendix 2.

3.2.2 Catalyst characterization

Surface area, pore volume and pore size distribution were measured by nitrogen adsorption-desorption at -196 °C using a Micromeritics TriStar 3000 multipoint analyser. The samples were degassed under a flow of nitrogen at 200 °C for 12 h before being analysed. The linear part of the adsorption curve was used to determine the specific surface area (S_{BET}). The pore size distribution was deduced from the desorption curve applying the Barret-Joyner-Halenda (BJH) theory.

Powder X-ray diffraction (XRD) patterns of the samples were recorded on a Bruker D8 Advance diffractometer, equipped with an Anton Paar XRK900 *in situ* cell and a Cu Kα source (λ = 1.5406 Å). The XRD patterns of 2θ from 10 to 90 degrees were recorded at a scan rate of 0.5 °/min. The structures were refined by the Rietveld method using the Full Prof Suite-2000 program. The average crystallite size (*D*) and lattice strain (ε) values of the substituted ceria materials were determined from Williamson-Hall (W-H) plots and equation (3.1).

$$\beta_{hkl}\cos\theta = \frac{K\lambda}{D} + 4\varepsilon\sin\theta \qquad (3.1)$$

Raman spectra were recorded at room temperature using an Advantage 532 series spectrometer, employing the visible laser line of 514 nm. High resolution transmission electron microscopy (HR-TEM) images were recorded on a JEM-2100 electron microscope and the images obtained were further analysed using ImageJ software. The samples were dispersed in ethanol via sonication prior to deposition on the holey carbon-coated grids. A ZEISS FEG-SEM Ultra Plus instrument was used to acquire the field emission scanning electron microscope (FEG-SEM) images.

X-ray photoelectron spectra (XPS) were recorded with a Thermo Scientific Multilab 2000 spectrometer equipped with the Al Kα radiation source (1486.6 eV). All the binding energies were referenced to the C(1s) peak (284.5 eV). Temperature programmed reduction by hydrogen (H_2-TPR) was conducted on an AutoChem II 2920 chemisorption instrument, with

a thermal conductivity detector (TCD). The gases were purified by a solid trap of molecular sieves. The powder catalyst was placed in a quartz reactor tube and held by the quartz wool beds on either side. Before the analysis, the sample was preheated at 400 °C for 30 minutes and cooled to 80 °C. The temperature of the sample was raised from 80 to 900 °C at a rate of 10 °C/min under a flow of 5% H_2/Ar (30 mL/min) as the hydrogen consumption was monitored.

The EXAFS measurements were carried out at the Energy-Scanning EXAFS beamline (BL-9) in transmission mode at the INDUS-2 Synchrotron Source (2.5 GeV, 100 mA) at Raja Ramanna Centre for Advanced Technology (RRCAT), Indore, India [22, 23]. This beamline operates in the energy range of 4 KeV to 25 KeV. The beamline optics consist of a Rh/Pt coated collimating meridional cylindrical mirror and the collimated beam reflected by the mirror is monochromatized by a Si(111) (2d=6.2709) based double crystal monochromator (DCM). The second crystal of the DCM is a sagittal cylindrical crystal which is used for horizontal focusing of the beam, while another Rh/Pt coated bendable post mirror facing down is used for vertical focusing of the beam at the sample position. Three ionization chambers (300 mm length each) were used for data collection in transmission mode, one ionization chamber for measuring incident flux (I_0), the second one for measuring transmitted flux (I_t) and the third ionization chamber for measuring the EXAFS spectrum of a reference metal foil for energy calibration. Appropriate gas pressure and gas mixture were chosen to achieve 10-20% absorption in the first ionization chamber and 70-90% absorption in the second ionization chamber to obtain better signal to noise ratio. The Si drift detector was used in standard 45 degree geometry for fluorescence mode. Rejection of the higher harmonics content in the X-ray beam was performed by detuning the second crystal of DCM. The absorption coefficient μ was obtained using the relation:

$$I_T = I_o e^{-\mu x} \qquad (3.2)$$

In this equation, x is the thickness of the absorber. Ce edge measurements were done in transmission mode and Cu edge measurements were done in fluorescence mode. For transmission measurements, powder samples of appropriate weight, estimated to obtain a reasonable edge jump, were mixed thoroughly with cellulose powder to

obtain a total weight of 100 mg, and homogenous pellets of 15 mm diameter were prepared using an electrically operated hydraulic press.

3.2.3 Catalytic activity measurements

CO oxidation activity measurements were performed in a continuous flow fixed-bed reactor (L = 500 mm, internal diameter D = 18 mm) at atmospheric pressure. The temperature of the catalyst bed was measured by an insulated *unitemp* thermocouple wire. Feed and effluent gases were analysed online with a three-channel Agilent CP-4900 micro gas chromatograph, each channel equipped with a TCD and column. The GC is fitted with Molsieve 5Å and CP-Sil5 CB columns, with 1.0 µL back-flushing to discharge residual components after analysis. The catalysts were pelletized and sieved into small granules (300-600 µm mesh). The catalyst pellets was diluted with inert carborundum beads (24-grit, ~ 600 µm) to a volume of 3 mL and loaded at the centre of the reactor. The empty spaces on the either side of the catalyst bed were filled with carborundum and the ends of the reactor were plugged with glass wool.

CO oxidation experiments were performed at gas hourly space velocities (GHSV) of 12 000, 24 000 and 48 000 h^{-1}, using respective catalyst volumes of 0.70, 0.35 and 0.175 mL. The reactant gas composition contained 1 vol% CO, 1 vol% O_2 and the balance was nitrogen gas. Before the reaction, the catalyst was conditioned at 150 °C for 4 h under a continuous flow of air and cooled to room temperature under nitrogen flow. CO conversions and specific rates were calculated based on equations (3.2) and (3.3). In the latter, X_{CO} represents CO conversion, F_{CO} is the molar flow rate of CO in mol/s and m_{cat} is the mass of the catalyst in g. Data points were collected within 30 minutes in triplicates at steady state (1 h) and all carbon and oxygen balances were within ± 5%.

$$\text{CO conversion (Xco)} = \frac{[CO]in - [CO]out}{[CO]in} \times 100 \qquad (3.3)$$

$$\text{rate (r)} = \frac{X_{CO} \times F_{CO}}{m_{cat}} \qquad (3.4)$$

3.3 Results and discussion

3.3.1 Structural and morphological properties

The XRD patterns of $Ce_{0.93}Pd_{0.02}Cu_{0.05}O_{2-\delta}$ and the two mono-metallic, ionic catalysts are displayed in Figure 3.1 A. The diffraction peaks of all the catalysts can be indexed to the fluorite structure of ceria (JCPDS 34-0394). Diffraction lines corresponding to either the metallic components or pure oxides, namely PdO and CuO, were not detected. This observation suggests the formation of single-phase solid-solution materials with a fluorite structure. However, the presence of pure oxides on the surface cannot be ruled out completely, since oxides may be undetectable by XRD if they are well dispersed as small crystals on CeO_2. The magnification of the (111) peak in the 2θ range of 26-32° is shown as an insert in Figure 3.1. It can be seen that this peak slightly shifts to lower 2θ values when foreign metal ions are incorporated into the ceria lattice. Such changes are often associated with an alteration in lattice parameters [13].

A typical refined XRD pattern is shown for $Ce_{0.98}Pd_{0.02}O_{2-\delta,}$ in Figure 3.1 B, and the rest of the patterns are included as supplementary information in Appendix 1. The results obtained from the Rietveld refinement show that the lattice parameter, *a*, decreases slightly upon the incorporation of Cu and Pd ions. Lattice contraction would be expected since the ionic radii for Pd^{2+} (0.86 Å) and Cu^{2+} (0.73 Å) are smaller than the radius of the host Ce^{4+} (0.97 Å). On the other hand, introduction of foreign metal ions of lower valence in the CeO_2 lattice can result in solid-solution materials enriched with single electron defects of Ce^{3+} ions and oxide ion vacancies. Ceria-based materials with high concentrations of oxide ions have been found to have increased lattice parameters [13]. Therefore, a slight change in the lattice parameter is a reflection of counteractive effects, due to the incorporation of foreign metal ions with small ionic radii and the presence of oxide ion vacancies. The structural properties and crystallite sizes of the studied materials are summarised in Table 3.1.

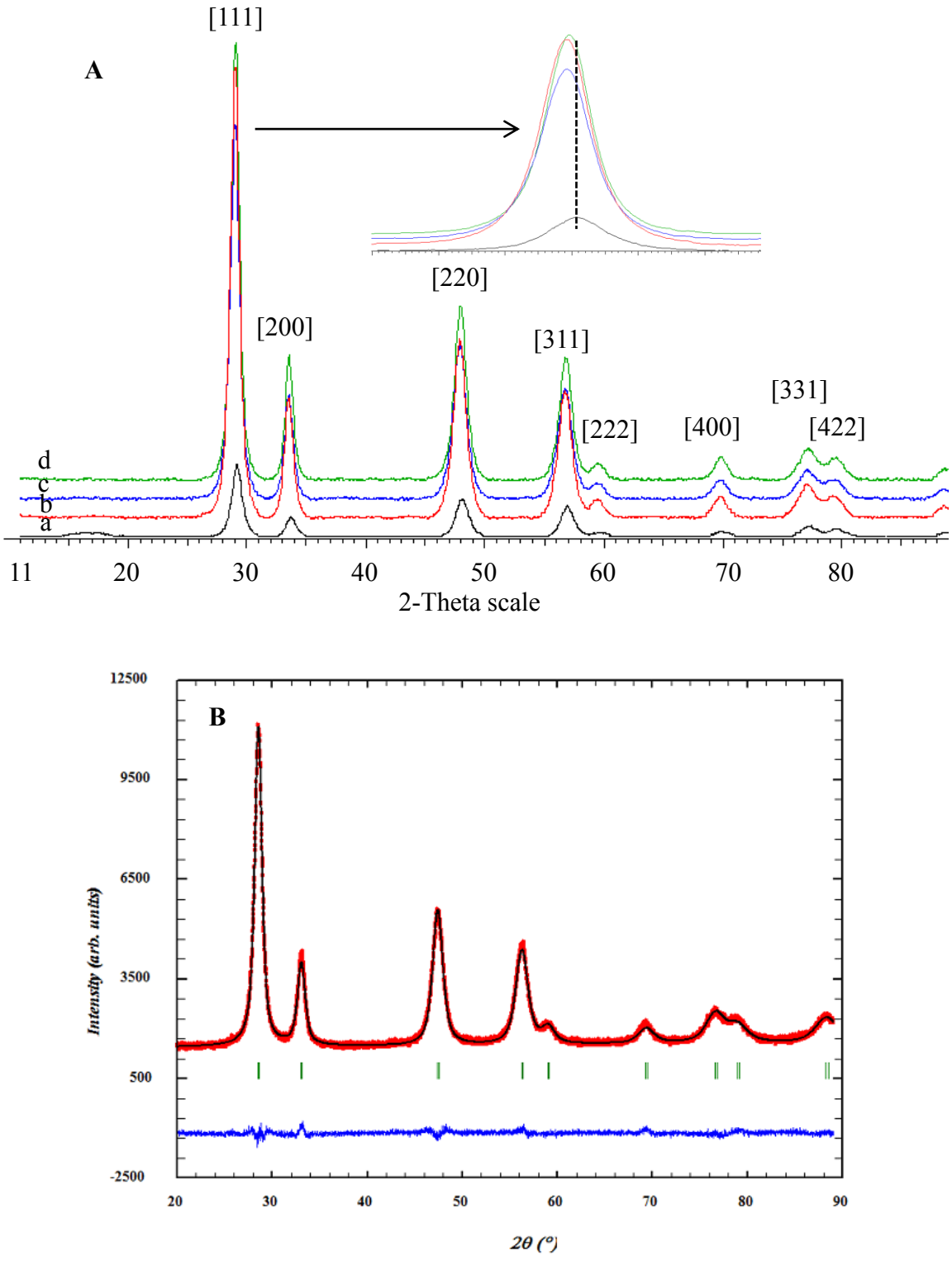

Figure 3.1 A *X-ray diffraction patterns of (a) CeO_2, (b) $Ce_{0.98}Pd_{0.02}O_{2-\delta}$, (c) $Ce_{0.95}Cu_{0.05}O_{2-\delta}$ and (d) $Ce_{0.93}Cu_{0.05}Pd_{0.02}O_{2-\delta}$.* ***B*** *Rietveld refined XRD pattern of $Ce_{0.93}Cu_{0.05}Pd_{0.02}O_{2-\delta}$*

Table 3.1 *Structural parameters of investigated catalysts*

Catalyst	Lattice parameter *a* (Å)	Structure factor (R_f)	Bragg factor (R_B)	χ^2	Lattice strain (10^{-3})	Crystallite size (nm)	d-spacing[a] (nm)
CeO_2	5.4221	1.95	3.06	1.24	1.10	8	0.307
$Ce_{0.95}Cu_{0.05}O_{2-\delta}$	5.4185	1.12	1.76	1.87	3.80	14	0.308 (0.30)
$Ce_{0.98}Pd_{0.02}O_{2-\delta}$	5.4200	1.27	2.28	1.54	4.20	13	0.309
$Ce_{0.93}Cu_{0.05}Pd_{0.02}O_{2-\delta}$	5.4197	1.06	1.79	1.85	5.10	14	0.309 (0.32)

[a] Values show in parenthesis were estimated from HR-TEM

XRD patterns were further analysed by the Williamson-Hall (W-H) method. The W-H plot corresponding to the XRD data of $Ce_{0.93}Pd_{0.02}Cu_{0.05}O_{2-\delta}$ is shown in Figure 3.2, as an example of the linear fits used to deduce the lattice strains and crystallite sizes. The rest of the plots are given in Appendix 1. As expected, there is a minimal lattice strain on non-substituted ceria (Table 3.1). For the studied substituted ceria materials, this value increases in the following order: $Ce_{0.95}Cu_{0.05}O_{2-\delta} < Ce_{0.98}Pd_{0.02}O_{2-\delta} < Ce_{0.93}Pd_{0.02}Cu_{0.05}O_{2-\delta}$. The results are a good indication of distortion of the structure of CeO_2, as a consequence of introducing Cu and/or Pd ions. The average crystallite size of substituted ceria samples, calculated by the W-H equation, is comparable (~ 14 nm) and higher than that of pure ceria (8 nm).

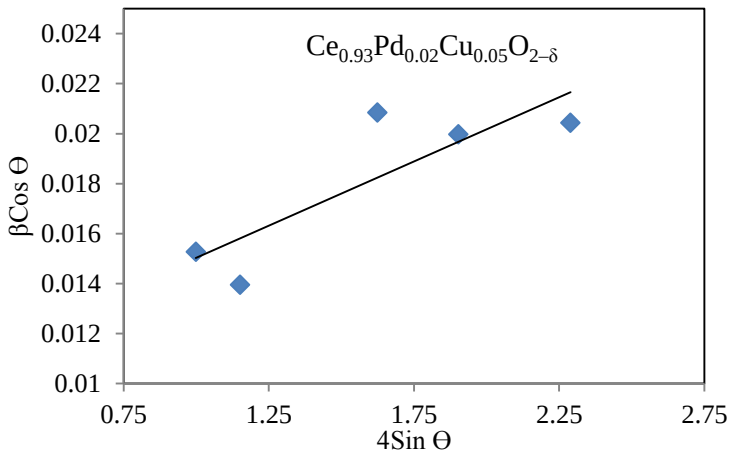

Figure 3.2 *Classical Williamson-Hall plot used to determine the lattice strain and crystallite size for* $Ce_{0.93}Pd_{0.02}Cu_{0.05}O_{2-\delta}$

Local structures of the solid-solution materials were also studied by Raman spectroscopy and the spectra are compared in Figure 3.3. The Raman spectrum of non-substituted CeO_2 shows one strong peak positioned at 461 cm^{-1}. This peak is associated with the triply degenerate F_{2g} Raman-active mode of the CeO_2 fluorite structure [24]. It is indicative of the symmetrical stretching mode of the Ce-O_8 vibrational unit, where oxygen atoms surround the Ce^{4+} cations. The F_{2g} Raman peak marginally shifts to 459, 458 and 457 cm^{-1} for $Ce_{0.95}Cu_{0.05}O_{2-\delta}$, $Ce_{0.98}Pd_{0.02}O_{2-\delta}$ and $Ce_{0.93}Pd_{0.02}Cu_{0.05}O_{2-\delta}$, respectively. The blue shift of this Raman peak confirms the insertion of the substitute foreign metal ions into the fluorite structure. Gamarra *et al*. have reported a similar phenomenon for Cu/CeO_2 catalyst formulations [25, 26]. Notably, the incorporation of Cu^{2+} and/or Pd^{2+} is accompanied by the broadening of the main band (F_{2g}). Such characteristics have been related to the existence of an inhomogeneous strain, due to the generation of oxygen vacancies or charge balance compensation in the fluorite structure [26-28]. In the case of $Ce_{0.95}Cu_{0.05}O_{2-\delta}$ and $Ce_{0.93}Pd_{0.02}Cu_{0.05}O_{2-\delta}$, peak broadening is more pronounced, possibly due to a relatively higher concentration of oxygen vacancies. Consequently, the spectra of the two samples show broad peaks between 550 and 650 cm^{-1}, confirming the presence of oxygen vacancies (O_v) [29]. The absence of the O_v band in non-substituted ceria correlates with minimal lattice strain, as seen from W-H analysis of the XRD data (Table 3.1). From this observation, it can be inferred that the oxygen vacancies are not of intrinsic nature due to inherent Ce^{3+} components [30]. Hence, they evolve as a direct result of incorporating foreign metal ions. In summary, Raman data reconciles with data obtained from XRD and points to the possible likely formation of single-phase solid-solution materials.

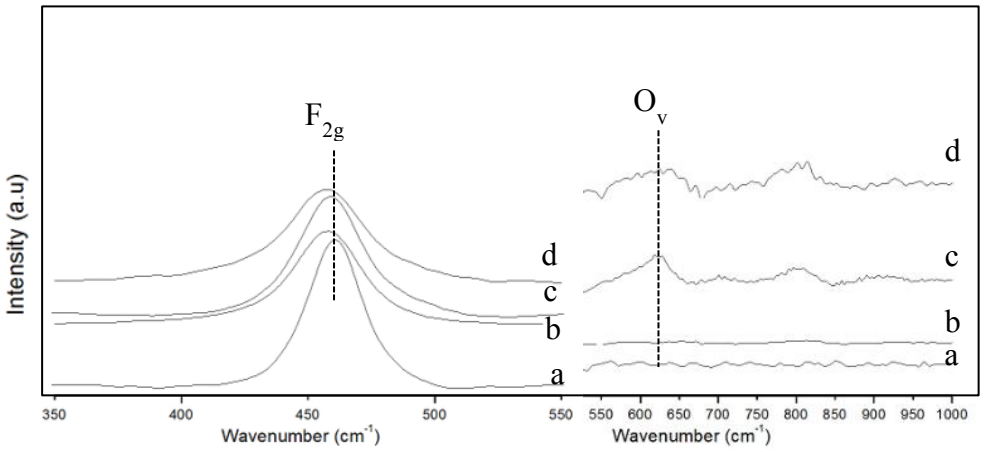

Figure 3.3 *Raman spectra of the prepared (a) CeO_2, (b) $Ce_{0.98}Pd_{0.02}O_{2-\delta}$, (c) $Ce_{0.95}Cu_{0.05}O_{2-\delta}$ and (d) $Ce_{0.93}Cu_{0.05}Pd_{0.02}O_{2-\delta}$*

HR-TEM and SEM were used to investigate the structure and morphology of the samples. Figure 3.4(a) and (b) show characteristic HR-TEM images of $Ce_{0.95}Cu_{0.05}O_{2-\delta}$ and $Ce_{0.93}Pd_{0.02}Cu_{0.05}O_{2-\delta}$. The particle size distribution of the materials, estimated from images given in Appendix 1, is in the range of 10 – 16 nm, which is comparable to the average crystallite size determined by W-H analysis of the XRD data (Table 3.1). The respective interplanar spacings between the adjacent fringes were measured to be 0.30 nm for both $Ce_{0.95}Cu_{0.05}O_{2-\delta}$ and $Ce_{0.93}Pd_{0.02}Cu_{0.05}O_{2-\delta}$, which are related to the d_{111} lattice planes of the CeO_2 structure. These values are consistent with the d-spacing values obtained from XRD, applying the Bragg equation at the (111) peak (Table 3.1).

The FEG-SEM images of the catalysts, depicted as inserts in Figure 3.5(a) and (b), show that the catalysts are uniform nanomaterials of nearly spherical morphology. The spheres are agglomerates of small nanocrystals. The corresponding EDX profiles of the $Ce_{0.95}Cu_{0.05}O_{2-\delta}$ and $Ce_{0.93}Pd_{0.02}Cu_{0.05}O_{2-\delta}$ samples are shown in Figure 3.5(a) and (b), respectively. In the latter, the molar ratio of Ce, Pd and Cu was found to be 0.93:0.01:0.06 and the molar ratio of Ce:Cu is 0.92:0.08 was obtained in the former material.

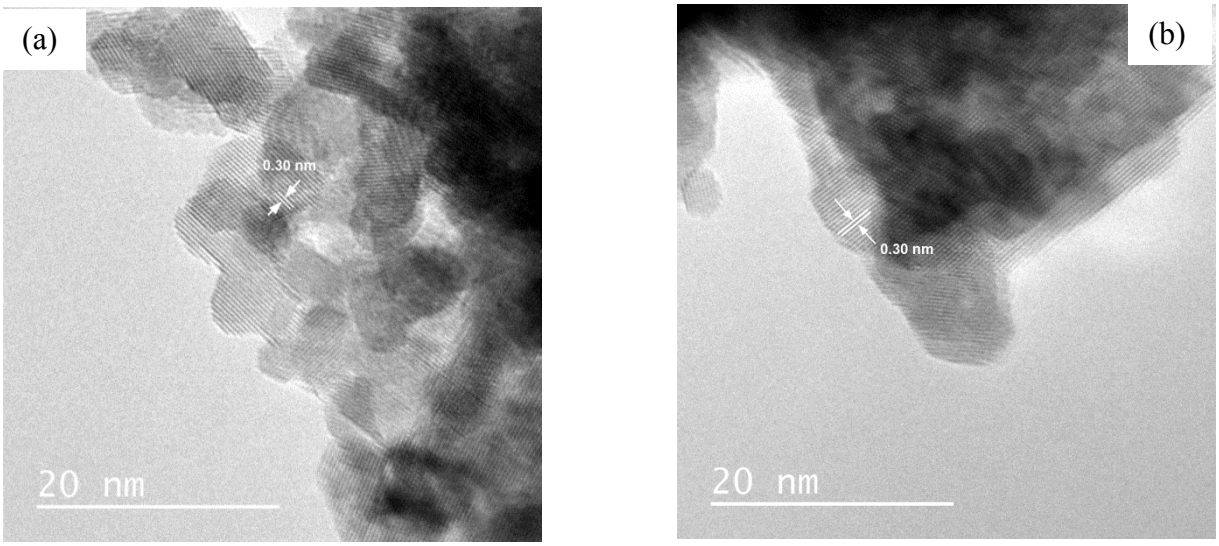

Figure 3.4 *HRTEM images of (a) $Ce_{0.93}Cu_{0.05}Pd_{0.02}O_{2-\delta}$ and (b) $Ce_{0.95}Cu_{0.05}O_{2-\delta}$*

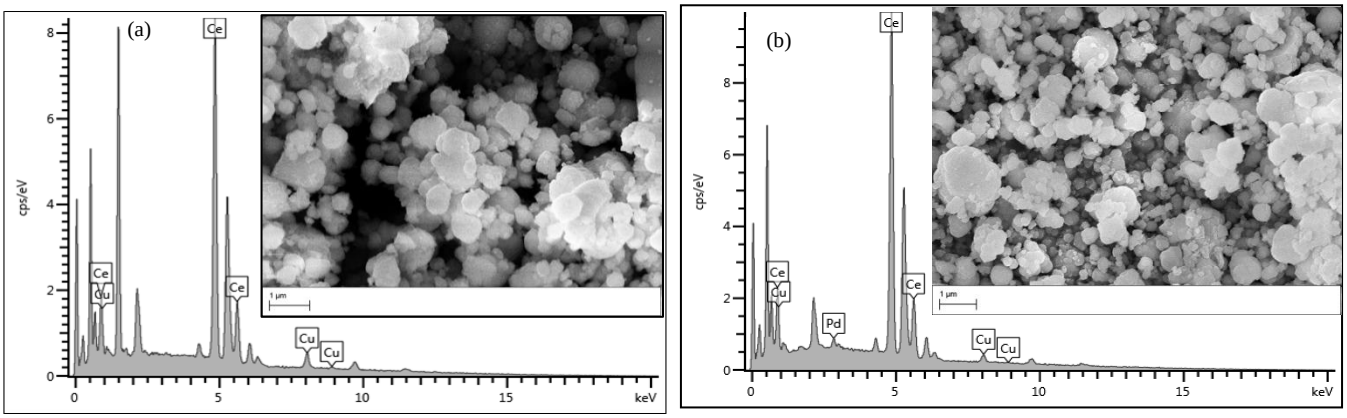

Figure 3.5 *SEM micrographs and corresponding EDS of (a) $Ce_{0.95}Cu_{0.05}O_{2-\delta}$ and (b) $Ce_{0.93}Cu_{0.05}Pd_{0.02}O_{2-\delta}$*

The nitrogen adsorption/desorption isotherms and the corresponding pore size distributions of pure CeO_2 and solid-solutions are depicted in Figure 3.6. It can be seen that the isotherms are characteristic of type II isotherms, with a sharp increase in relative pressure (P/P_0) at ~ 0.8. This suggests the existence of mesopores (2-50 nm) [31]. The absence of an adsorption plateau at (P/P_0) ~ 1 indicates the presence of some macropores [32]. According to the IUPAC classification, it can be inferred that the materials are mesoporous with a slight contribution of macroporosity [33]. Pore size distribution of non-substituted CeO_2 crossed the mesoporous/macroporous border, with two distribution peaks centered at 7-15 nm and 15-60 nm. After incorporating metal ions, only a fraction of narrow pores can be seen, centred at 2.5-10 nm and 6-12 nm for $Ce_{0.93}Pd_{0.02}Cu_{0.05}O_{2-\delta}$ (or $Ce_{0.95}Cu_{0.05}O_{2-\delta}$) and $Ce_{0.98}Pd_{0.02}O_{2-\delta}$, respectively. Pd-containing (69 m^2/g) and $Ce_{0.95}Cu_{0.05}O_{2-\delta}$ (58 m^2/g) mono-metallic catalysts have surface areas that are slightly higher than that of pure CeO_2 (51 m^2/g), whereas the bimetallic material has the lowest surface area (21 m^2/g). The textural properties of the materials are summarized in the Table 3.2.

Table 3.2 *Chemical composition and surface properties of prepared catalysts.*

Catalyst	**Ce (at%)**	**Pd (at%)**	**Cu (at%)**	**S_{BET} (m^2/g)**	**Average pore size (nm)**	**Pore volume (cm^3/g)**
CeO_2	100	-	-	51	3.2	0.041
$Ce_{0.98}Pd_{0.02}O_{2-\delta}$	99.0	1.0		69	2.7	0.048
$Ce_{0.95}Cu_{0.05}O_{2-\delta}$	94.8	-	5.2	58	4.7	0.021
$Ce_{0.93}Cu_{0.05}Pd_{0.02}O_{2-\delta}$	93.0	1.5	5.5	21	2.9	0.047

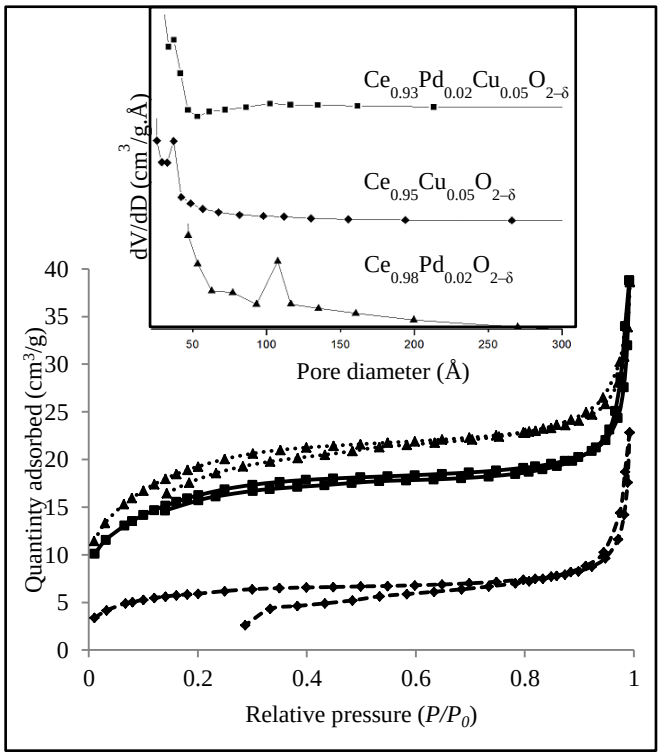

Figure 3.6 *Nitrogen adsorption/desorption isotherms and pore size distribution curves of* $Ce_{0.98}Pd_{0.02}O_{2-\delta}$, $Ce_{0.95}Cu_{0.05}O_{2-\delta}$ *and* $Ce_{0.93}Cu_{0.05}Pd_{0.02}O_{2-\delta}$

3.3.2 Electronic and redox properties

X-ray photoelectron spectroscopy was used to explain the electronic states of Ce, Cu, Pd and oxygen on the prepared solid-solution catalysts. Figure 3.7A shows the comparison of the core level XP spectra of Pd (3d) in $Ce_{0.93}Pd_{0.02}Cu_{0.05}O_{2-\delta}$ and $Ce_{0.98}Pd_{0.02}O_{2-\delta}$. The XP spectra of the two Pd-containing samples show two peaks with a spin-orbit coupling energy of 5 eV. The peaks are positioned at 337.5 and 342.5 eV and are assigned to Pd ($3d_{5/2}$) and ($3d_{3/2}$), respectively. The binding energy of Pd ($3d_{5/2}$) in the prepared materials is higher than the literature values for Pd in PdO (336.8 eV) [34-36] and Pd^0 (335.0 eV) [36, 37]. Instead, it is in good agreement with the reported values for palladium ions in $PdCl_2$ (338.0 eV) and the $Ce_{1-x}Pd_xO_{2-\delta}$ solid-solutions [13, 37, 38]. The results give an indication that palladium is dispersed as individual Pd^{2+} ions in the ceria lattice.

Figure 3.7B depicts the Cu (2p) spectra of $Ce_{0.93}Pd_{0.02}Cu_{0.05}O_{2-\delta}$ and $Ce_{0.95}Cu_{0.05}O_{2-\delta}$. The spectra of the two samples show a shake-up peak at ~ 940 eV and a Cu ($2p_{3/2}$) peak appears at 933 eV. The presence of these peaks suggests that the oxidation state of the Cu species in the

catalysts is +2 [9, 19]. The Ce (3d) spectra of all the catalysts are shown in Figure 3.7C. The Ce (3d) spectra were deconvoluted in order to show the presence of Ce^{3+} components. The peaks can be labelled as U (U-U´´´) for $3d_{3/2}$ spin-orbit and V (V-V´´´) for $3d_{5/2}$ components, according to Burrough's nomenclature [39]. The V peak at ~ 882 eV and its corresponding satellite V´´ peak at ~ 889 eV is indicative of the Ce^{4+} in CeO_2. The crescent between these two peaks is partially filled-up and is not well-defined because the V´ peak of the Ce^{3+}component appears in this region. Based on this, the Ce (3d) spectra of all prepared materials confirm that Ce is predominantly present as Ce^{4+}, with some contribution of Ce^{3+} [39].

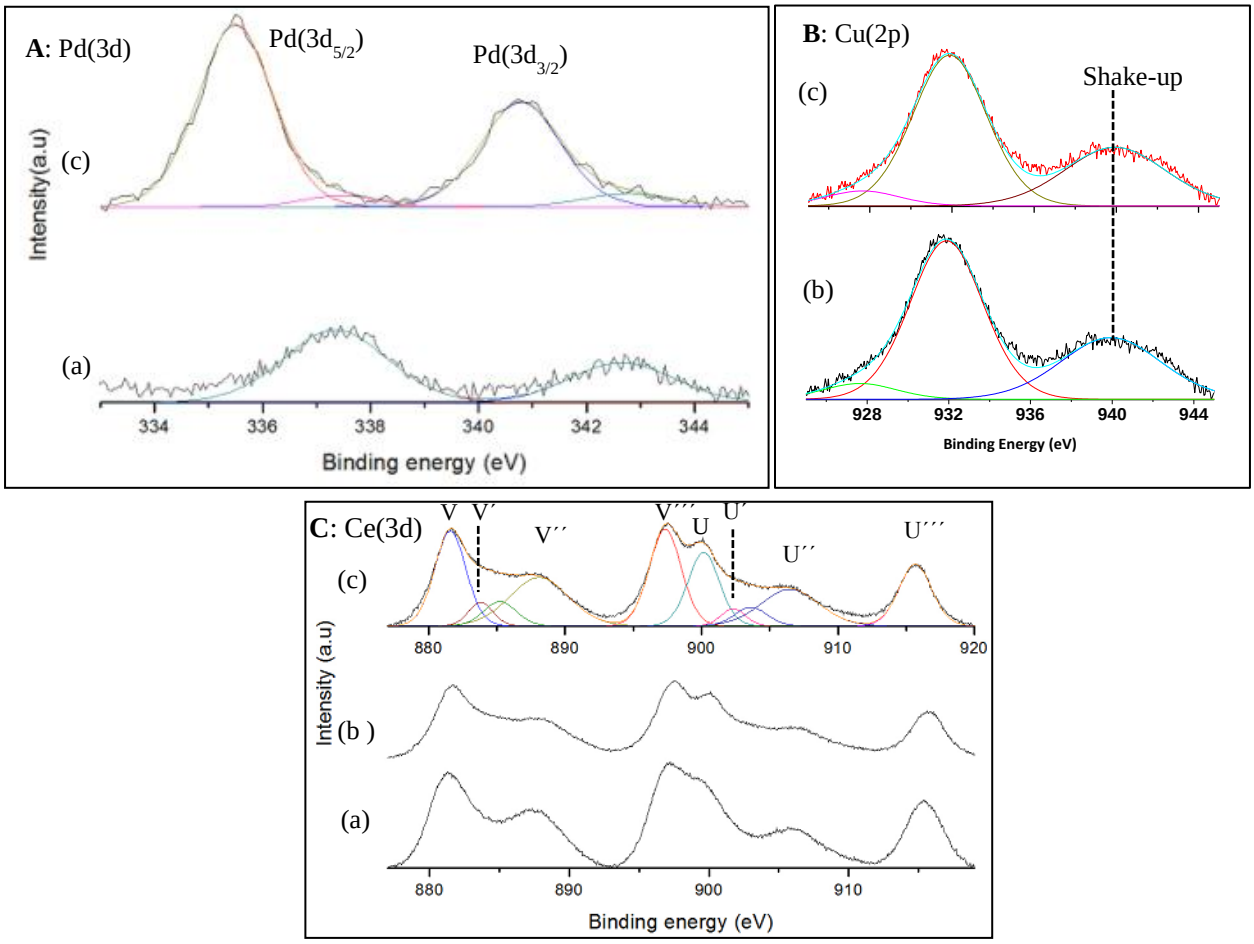

Figure 3.7 *A: Pd (3d), B: Cu(2p) and C: Ce(3d) XP spectra of the catalysts: (a) $Ce_{0.98}Pd_{0.02}O_{2-\delta}$, (b) $Ce_{0.95}Cu_{0.05}O_{2-\delta}$ and (c) $Ce_{0.93}Cu_{0.05}Pd_{0.02}O_{2-\delta}$.*

The redox behaviour of the catalysts was studied by H_2-TPR measurements. The H_2-TPR profiles of the catalysts are compared in Figure 3.8. The H_2-TPR profile of Cu-containing mono-metallic ionic catalyst shows two reduction peaks located at 186 °C and 211 °C. Notably, these peaks are lower than the reduction peaks reported for pure CeO_2 (≥400 °C and ≥ 700 °C) [40], pure CuO (≥ 300 °C) [9] and other CuO/CeO_2 formulations [19]. Two reduction peaks, for CuO/CeO_2 catalysts, have been reported by Liu and Flytzani-Stephanopoulos [41], Wrobel *et al*. [42] and Avgouropoulos *et al*. [9]. Based on these reports, a low temperature reduction peak can be attributed to the reduction of copper ions strongly interacting with cerium ions, possibly acting as substitute ions in the ceria lattice. A high temperature peak is possibly related to the reduction of copper species weakly interacting with ceria. A single hydrogen uptake peak at 138 °C is observed for $Ce_{0.93}Pd_{0.02}Cu0_{.05}O_{2-\delta}$. The absence of separate reduction peaks at 180-211 °C suggests that the Cu^{2+} ions are reduced together with Pd^{2+} ions in $Ce_{0.93}Pd_{0.02}Cu0_{.05}O_{2-\delta}$. Accordingly, the hydrogen consumption increases from 9.4 cm^3/g for $Ce_{0.95}Cu_{0.05}O_{2-\delta}$ to 10.3 cm^3/g for $Ce_{0.93}Pd_{0.02}Cu0_{.05}O_{2-\delta}$. Hence, the addition of Pd^{2+} to $Ce_{0.95}Cu_{0.05}O_{2-\delta}$ improves the reducibility of the catalyst and thus lowers the reduction temperature of copper species. This redox behaviour possibly arises as a consequence of synergistic interaction between Pd, Cu and Ce ions.

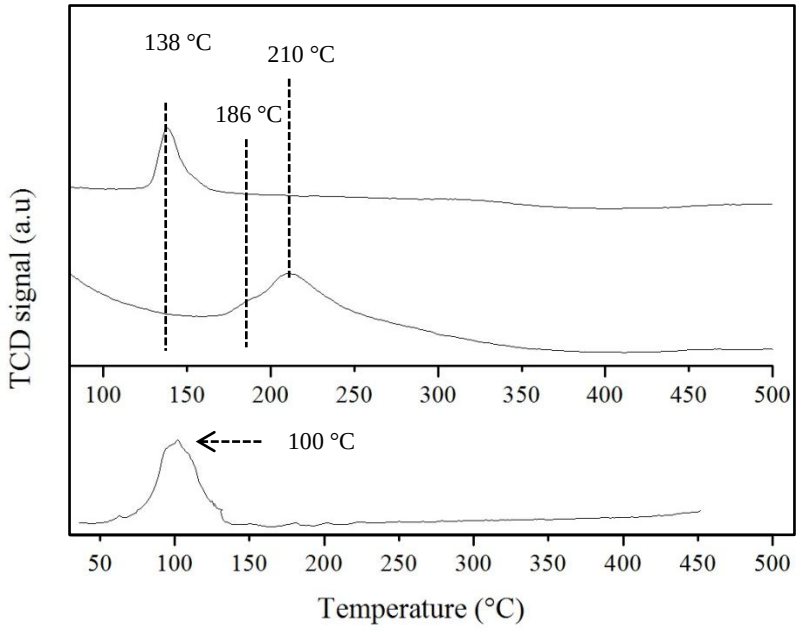

Figure 3.8 *H_2-TPR profiles of (a) $Ce_{0.98}Pd_{0.02}O_{2-\delta}$ Co(2p), (b) $Ce_{0.95}Cu_{0.05}O_{2-\delta}$ and (c) $Ce_{0.93}Cu_{0.05}Pd_{0.02}O_{2-\delta}$ catalysts.*

3.3.3 XANES and EXAFS studies

The XANES spectra of $Ce_{0.93}Pd_{0.02}Cu_{0.05}O_{2-\delta}$, $Ce_{0.95}Cu_{0.05}O_{2-\delta}$ and $Ce_{0.98}Pd_{0.02}O_{2-\delta}$ samples are shown in the inset of Figure 3.9 along with that of the CeO_2 standard. The calibration of experimental spectra was done using Cr metal foil and the third ionisation chamber was used to measure reference spectra to align the edge position. The four main features are depicted as A, B, C and D by the dashed line in Figure 3.9 inset. The pre-edge structure, labelled A, is assigned to final states with delocalized *d* character at the bottom of the conduction band and corresponding to 2s to 5d transition. Due to the cubic crystal-field splitting of Ce *5d* states, features B and C are associated to the transitions of Ce *2p* to the Ce $4f^1 5de_g\ L$ and Ce $4f^1 5dt_{2g}\ L$ states, where, *L* denotes an oxygen ligand *2p* hole; $4f^1$ refers to an electron from an oxygen *2p* orbital to a cerium *4f* one (charge transfer-like). The energy separation between peaks B and C is about 3.6 eV and between C and D is 7.1 eV, which is in agreement with previous works [43, 44]. The feature D is attributed to the contribution of a different final state configuration $4f^0 5d$. It has been experimentally shown by other researchers that the peak at B would increase if Ce were present in the sample in the +3 oxidation state [45, 46]. No such change is observed in the three samples studied here, and from the resemblance of the XANES spectra of the samples with that of the CeO_2 standard, it can be concluded that in all the samples Ce is present in the +4 oxidation state. The presence of Ce^{+3} states in the samples as observed from XPS studies might be confined to the surface states only.

The XANES spectra of the $Ce_{0.93}Pd_{0.02}Cu_{0.05}O_{2-\delta}$ and $Ce_{0.95}Cu_{0.05}O_{2-\delta}$ samples measured at the Cu K edge are shown in the inset of Figure 3.10 along with those of standard samples of CuBr and CuO in which Cu is present in +1 and +2 oxidation states respectively. The Cu K edge positions for both the samples are significantly shifted to the higher energy side compared to the Cu K edge position in CuBr and matches with the Cu K edge position of CuO. The edge position conclusively indicates that Cu is present in the +2 oxidation state in the samples.

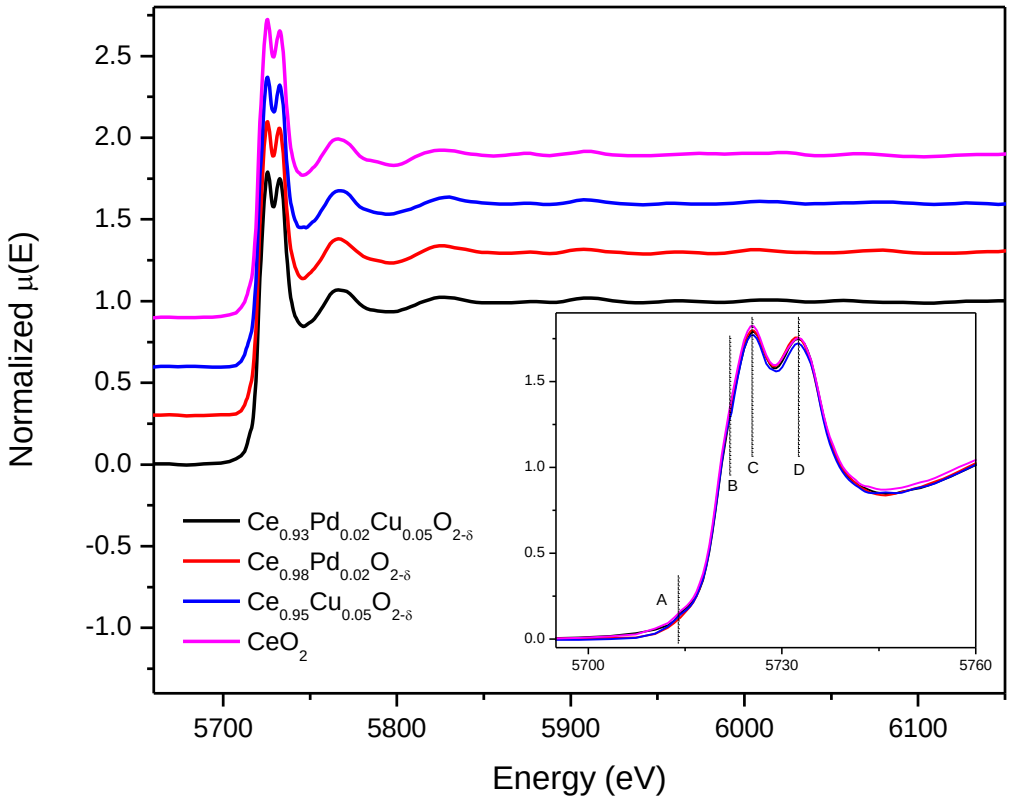

Figure 3. 9 *Normalised EXAFS spectra of CeO_2, $Ce_{0.93}Pd_{0.02}Cu_{0.05}O_{2-\delta}$, $Ce_{0.95}Cu_{0.05}O_{2-\delta}$ and $Ce_{0.98}Pd_{0.02}O_{2-\delta}$ at the Ce L3 edge. The XANES spectra are shown in inset.*

Figures 3.9 and 3.10 show the normalised EXAFS spectra of the $Ce_{0.93}Pd_{0.02}Cu_{0.05}O_{2-\delta}$, $Ce_{0.95}Cu_{0.05}O_{2-\delta}$ and $Ce_{0.98}Pd_{0.02}O_{2-\delta}$ samples measured at Ce L3 and Cu K-edges. In order to take care of the oscillations in the absorption spectra, $\mu(E)$ has been converted to absorption function $\chi(E)$ defined as follows [47]:

$$\chi(E) = \frac{\mu(E) - \mu_0(E)}{\Delta\mu_0(E_0)} \qquad (3.5)$$

In this equation, E_0 is absorption edge energy, $\mu_0(E_0)$ is the bare atom background and $\Delta\mu_0(E_0)$ is the step in the $\mu(E)$ value at the absorption edge. The energy dependent absorption coefficient $\chi(E)$ has been converted to the wave number dependent absorption coefficient $\chi(k)$ using the relation:

$$K = \sqrt{\frac{2m(E - E_o)}{\hbar^2}} \qquad (3.6)$$

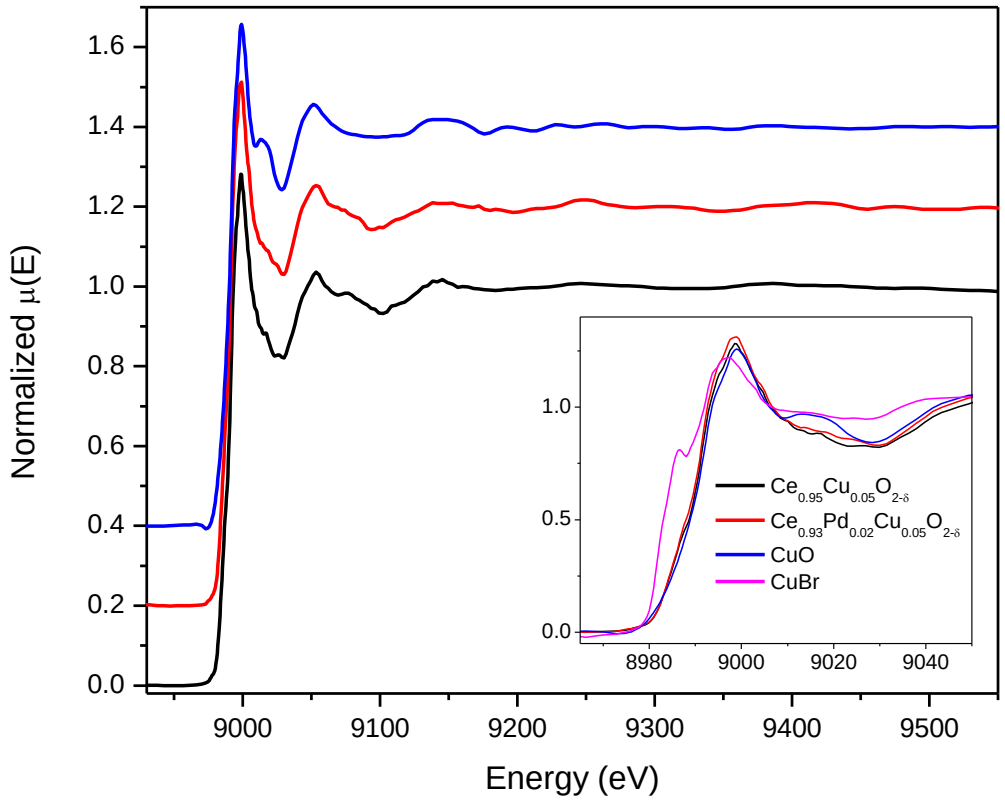

Figure 3. 10 *Normalised EXAFS spectra of CuO, $Ce_{0.93}Pd_{0.02}Cu_{0.05}O_{2-\delta}$ and $Ce_{0.95}Cu_{0.05}O_{2-\delta}$ at the Cu K edge. The XANES spectra are shown in inset along with those of CuBr and CuO.*

In equation 3.6, m is the electron mass. $\chi(k)$ is weighted by k^3 to amplify the oscillation at high k and the k^3 weighted $\chi(k)$ versus k plots for the $Ce_{0.93}Pd_{0.02}Cu_{0.05}O_{2-\delta}$, $Ce_{0.95}Cu_{0.05}O_{2-\delta}$ and $Ce_{0.98}Pd_{0.02}O_{2-\delta}$ samples are shown in Figures 3.11 (a)-(c) for Ce the L3 edge and Figure 3.11 (d)-(e) for the Cu K edge respectively. The $\chi(k)k^3$ functions are Fourier transformed in R space to generate the $\chi(R)$ versus R spectra in terms of the real distances from the centre of the absorbing atom. The set of EXAFS data analysis programmes available within the IFEFFIT software package has been used for the EXAFS data analysis [48]. This includes background reduction and Fourier transform to derive the $\chi(R)$ versus R plots from the absorption spectra (using

ATHENA software), generation of the theoretical EXAFS spectra starting from an assumed crystallographic structure and finally fitting of experimental data with the theoretical spectra using ARTEMIS software.

The $\chi(R)$ versus R plots generated (Fourier transform range is k =3.0-10.0 Å^{-1} for the Ce L3 edge and k =3.0-11.0 Å^{-1} for the Cu K edge) for all the samples from $\mu(E)$ versus E spectra, following the methodology described above, are shown in Figure 3.11 at Ce L3 and Cu K-edges. The goodness of fit has been determined by the value of the R_{factor} defined by:

$$R_{factor} = \sum \frac{[\mathrm{Im}(\chi_{dat}(r_i) - \chi_{th}(r_i)]^2 + [\mathrm{Re}(\chi_{dat}(r_i) - \chi_{th}(r_i)]^2}{[\mathrm{Im}(\chi_{dat}(r_i)]^2 + [\mathrm{Re}(\chi_{dat}(r_i)]^2} \qquad (3.7)$$

In this expression, χ_{dat} and χ_{th} refer to the experimental and theoretical $\chi(r)$ values respectively and Im and Re refer to the imaginary and real parts of the respective quantities. Other than the single scattering paths, multiple scattering paths are also used for fitting purposes.

The structural parameters (atomic coordination and lattice parameters) of CeO_2 have been used for simulation of theoretical FT-EXAFS spectra of the samples at the Ce L3 edge and the best fit $\chi(R)$ versus R plots of the samples are shown in Figure 3.11 (a)-(c) along with the experimental data. The bond distances, co-ordination numbers (including scattering amplitudes) and disorder (Debye-Waller) factors (σ^2), which give the mean square fluctuations in the distances, have been used as fitting parameters and the EXAFS fitting results are shown in Table 3.3.

Table 3.3 *Bond lengths, coordination number and disorder obtained by EXAFS fitting at the Ce L3 edge.*

Path	Parameters	CeO_2	$Ce_{0.93}Pd_{0.02}Cu_{0.05}O_{2-\delta}$	$Ce_{0.95}Cu_{0.05}O_{2-\delta}$	$Ce_{0.98}Pd_{0.02}O_{2-\delta}$
Ce-O	**R (Å)**	2.33	2.27(2)	2.29(1)	2.29(5)
	N	8	8.0(2)	8.0(3)	8.0(2)
	σ^2	0.0095	0.0089(1)	0.0073(9)	0.0071(7)
Ce-Ce	**R (Å)**	3.78	3.70(2)	3.82(1)	3.83(3)
	N	12	12.0(4)	12.0(5)	12.0(4)
	σ^2	0.0052	0.0094(6)	0.0044(9)	0.0032(6)
Ce-O	**R (Å)**	4.33	4.29(3)	4.40(9)	4.39(6)
	N	24	26.0(7)	24.0(9)	24.0(7)
	σ^2	0.0132	0.0012(8)	0.0127(44)	0.0073(9)

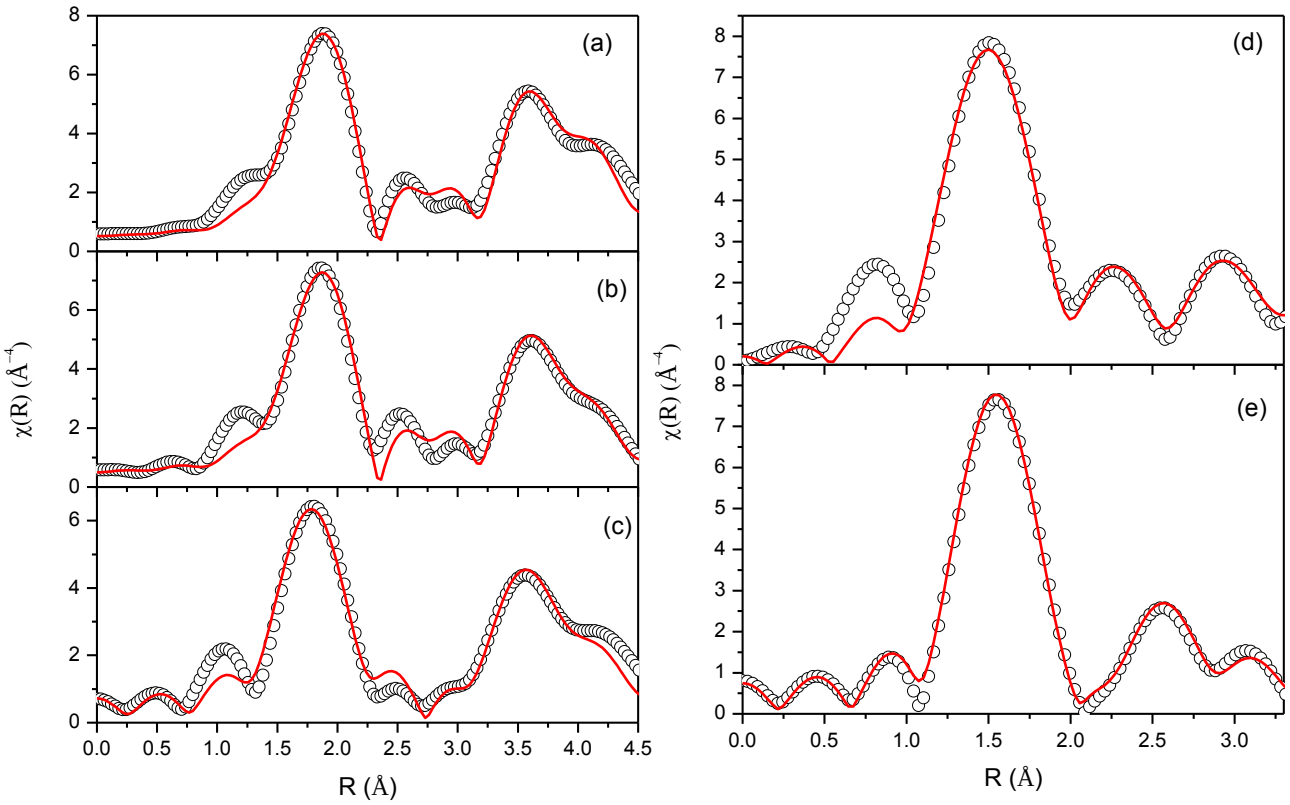

Figure 3.11 *Fourier transformed EXAFS spectra of (a) $Ce_{0.98}Pd_{0.02}O_{2-\delta}$ (b) $Ce_{0.95}Cu_{0.05}O_{2-\delta}$ and (c) $Ce0_{.93}Pd_{0.02}Cu_{0.05}O_{2-\delta}$ (scatter points) and theoretical fit (solid line) at the Ce L3 edge. Fourier transformed EXAFS spectra of (d) $Ce_{0.93}Pd_{0.02}Cu_{0.05}O_{2-\delta}$ and (e) $Ce_{0.95}Cu_{0.05}O_{2-\delta}$ (Scatter points) and theoretical fit (Solid line) at the Cu K edge.*

The first peak in $Ce_{0.95}Cu_{0.05}O_{2-\delta}$ is a contribution of 8 oxygen atoms around Ce at a distance of ~2.29 Å (without phase correction it appears at lower bond length). This bond length is slightly lower than the Ce-O bond length (2.33 Å) in CeO_2. The second peak around 3.5 Å is a contribution of 12 Ce-Ce bonds and the peak at 4 Å is due to a longer Ce-O bond with 24 coordination number. Coordination numbers are found to be the same for all three samples, however the disorder factors of the Ce-O as well as Ce-Ce shells are higher for the sample $Ce_{0.93}Pd_{0.02}Cu_{0.05}O_{2-\delta}$ in comparison to the samples $Ce_{0.95}Cu_{0.05}O_{2-\delta}$ and $Ce_{0.98}Pd_{0.02}O_{2-\delta}$. One also observes a shorter Ce-Ce bond length for the sample $Ce_{0.93}Pd_{0.02}Cu_{0.05}O_{2-\delta}$ in comparison to the samples $Ce_{0.95}Cu_{0.05}O_{2-\delta}$ and $Ce_{0.98}Pd_{0.02}O_{2-\delta}$.

The Fourier transform EXAFS spectra at the Cu K edge for the samples $Ce_{0.95}Cu_{0.05}O_{2-\delta}$ and $Ce_{0.93}Pd_{0.02}Cu_{0.05}O_{2-\delta}$ are shown in Figure 3.11 (d)-(e) along with best fit theoretical spectra. The initial parameters for generating the theoretical spectra are obtained using the CuO structure due to similarity in the XANES spectra. The bond distances, co-ordination numbers and disorder have been used as fitting parameters and the EXAFS fitting results are shown in Table 3.4 The first peak in $Ce_{0.95}Cu_{0.05}O_{2-\delta}$ is a contribution of the Cu-O bond at 1.96 Å with coordination number ~3.2. It is the same as the Cu-O bond length in copper oxide, but oxygen coordination in this shell is found to be lower than that in CuO (4 oxygens at 1.96 Å). The next coordination peak (2.6 Å) is due to Cu-Cu shells at distances of 2.94 Å and 3.13 Å respectively. The third peak at 3.1 Å is a contribution of a Cu-Ce shell at a distance of 3.35 Å. This Cu-Ce bond length obtained here is slightly longer than obtained by Bera et al. for Cu/CeO_2 [45]. Thus, comparison of the EXAFS results of CuO and the Cu doped CeO_2 samples, as shown in Table 3.4, shows that the environment of Cu in the samples, is significantly different from that of CuO after the first coordination peak and, hence, it suggests that Cu^{2+} goes to Ce^{4+} sites in CeO_2. Similar behaviour is also observed by Bera et al. [45] and they concluded that Cu^{2+} is largely occupying Ce^{4+} sites in Cu doped CeO catalysts. However, less oxygen coordination in Cu sites manifests the presence of oxygen vacancies at Cu sites, which has also been observed by Bera et al. [45].

Table 3.4 *Bond length, coordination number and disorder factors obtain by EXAFS fitting at the Cu K edge.*

Path	**Parameters**	**CuO**	**$Ce_{0.93}Pd_{0.02}Cu_{0.05}O_{2-\delta}$**	**$Ce_{0.95}Cu_{0.05}O_{2-\delta}$**
Cu-O	**R (Å)**	1.95	1.94(1)	1.96(2)
	N	4	3.6(7)	3.25(6)
	σ^2		0.0010(5)	0.0010(5)
Cu-O	**R (Å)**	2.78		
	N	2		
	σ^2			
Cu-Cu	**R (Å)**	2.90	3.29(3)	2.94(1)
	N	4	3.6(11)	4.0(4)
	σ^2		0.0227(18)	0.0069(1)
Cu-Cu	**R (Å)**	3.07		3.13(1)
	N	4		4.0(4)
	σ^2			0.0069(1)
Cu-Ce	**R (Å)**		3.21(1)	3.35(6)
	N		3.6(11)	2.0(2)
	σ^2		0.0038(8)	0.0182(23)
Cu-Cu	**R (Å)**	3.15		
	N	2		
	σ^2			

3.3.4 Catalytic studies

Having studied the characteristics of the materials, CO oxidation was used as the model exhaust reaction to evaluate the catalytic performance. The activity of the bimetallic, ionic catalyst was compared with those of the mono-metallic analogues in order to highlight the benefit of incorporating two foreign metal ions in the CeO_2 lattice. Figure 3.9 shows the light-off curves of CO oxidation of the prepared solid-solution catalysts. Based on the temperatures at which 50% and complete CO conversions were achieved (T_{50} and T_{100}), it is observed that the bimetallic, ionic catalyst displays better catalytic performance compared to the mono-metallic analogues and pure CeO_2. The respective T_{50} and T_{100} values are marked on the light-off curves. The $Ce_{0.93}Pd_{0.02}Cu_{0.05}O_{2-\delta}$ catalyst has the lowest T_{50} (75 °C) and T_{100} (150 °C) values amongst the studied catalysts and is thus the most active. The T_{50} value of this catalyst is lower by 15 °C compared to that of $Ce_{0.95}Cu_{0.05}O_{2-\delta}$ and 45 °C lower than that of $Ce_{0.98}Pd_{0.02}O_{2-\delta}$. The temperature of complete CO conversion follows the same trend: $Ce_{0.93}Pd_{0.02}Cu_{0.05}O_{2-\delta}$ (150 °C) < $Ce_{0.95}Cu_{0.05}O_{2-\delta}$ (180 °C) < $Ce_{0.98}Pd_{0.02}O_{2-\delta}$ (200 °C).

The activity trend of Cu-containing catalysts correlates with the H_2-TPR profiles of the materials. The considerable enhancement of the CO oxidation activity of copper-ceria is due to the improved reducibility upon the addition of palladium ions. The results suggest that there is a synergistic interaction between Pd^{2+}, Cu^{2+} and the parent Ce ions. The catalytic behaviour of the prepared materials can also be explained by the presence of oxygen vacancies or defects.

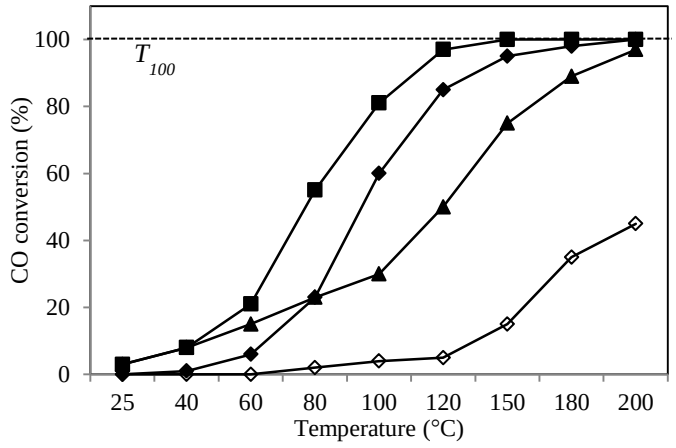

Figure 3.12 *CO conversion as a function of temperature over ◊ CeO_2, ▲ $Ce_{0.98}Pd_{0.02}O_{2-\delta}$, ♦ $Ce_{0.95}Cu_{0.05}O_{2-\delta}$ and ■ $Ce_{0.93}Cu_{0.05}Pd_{0.02}O_{2-\delta}$ catalysts.*

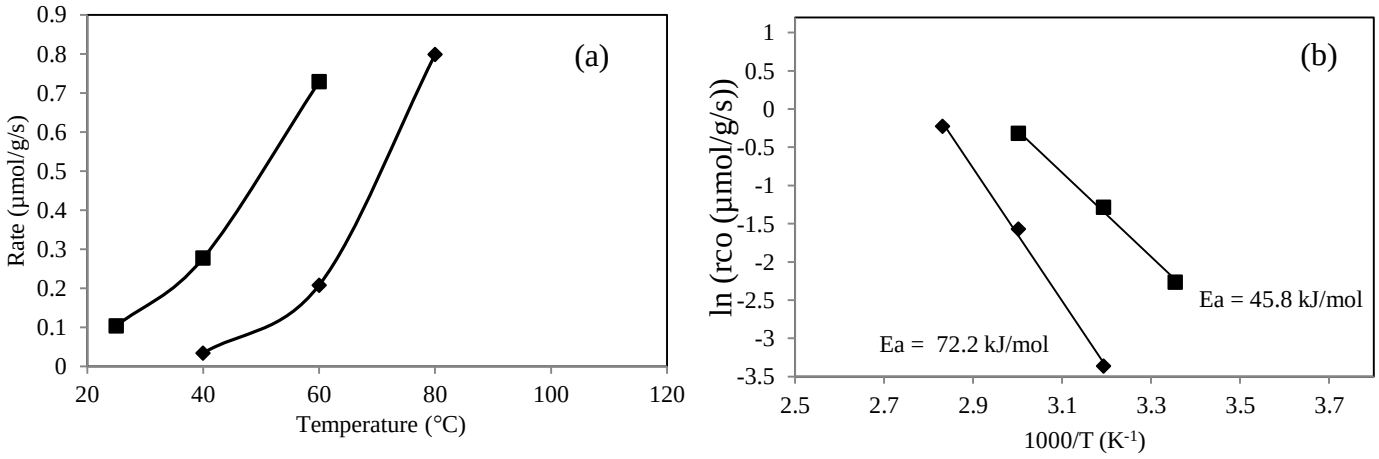

Figure 3.13 *(a) Rate of the reaction as the function of temperature and corresponding (b) Arrhenius plots for* ♦ $Ce_{0.95}Cu_{0.05}O_{2-\delta}$ *and* ■ $Ce_{0.93}Cu_{0.05}Pd_{0.02}O_{2-\delta}$ *catalysts.*

Since the Raman spectra showed no clear presence of oxygen vacancy defects in $Ce_{0.98}Pd_{0.02}O_{2-\delta}$ and CeO_2, it is not surprising that $Ce_{0.98}Pd_{0.02}O_{2-\delta}$ is the least active among the studied substituted ceria materials. Yang *et al*. have indicated that the presence of oxygen vacancies promotes the reducibility of ceria-based materials [19]. Hence, it may be concluded that the oxygen vacancies in $Ce_{0.93}Pd_{0.02}Cu_{0.05}O_{2-\delta}$ and $Ce_{0.95}Cu_{0.05}O_{2-\delta}$ promote the CO oxidation reaction.

The specific reaction rates over $Ce_{0.93}Pd_{0.02}Cu_{0.05}O_{2-\delta}$ and $Ce_{0.95}Cu_{0.05}O_{2-\delta}$ were calculated using the three lowest CO conversion data points. The plots of specific rates with temperature are shown in Figure 10(a), while the corresponding Arrhenius plots for the CO oxidation are depicted in Fig 10(b). The activation energy values extracted from the Arrhenius plots were found to be 72.2 and 45.8 kJ/mol for $Ce_{0.95}Cu_{0.05}O_{2-\delta}$ and $Ce_{0.93}Pd_{0.02}Cu_{0.05}O_{2-\delta}$, respectively. The results are within the range reported for similar catalyst formulations and also highlight appreciable enhancement of the activity of $Ce_{0.95}Cu_{0.05}O_{2-\delta}$ by Pd addition [19, 49]. The adsorption and desorption of gas molecules on the catalyst are the key steps in the CO oxidation reaction [50] and, since Pd is well-known for CO adsorption, the superior performance by the bimetallic ionic catalyst also may be due to enhanced CO adsorption.

The steady-state activity of the bimetallic ionic catalyst was further studied at gas hourly space velocities of 12 000, 24 000 and 48 000 h^{-1}. As shown in Figure 11, decreasing the

GHSV at a given temperature increases the CO conversion. Upon decreasing the GHSV from 48 000 h^{-1} to 24 000 and then to 12 000 h^{-1}, the temperature at which 50% CO conversion is obtained shifts from 75 °C to 70 and then 60 °C, respectively. At 24 000 and 12 000 h^{-1}, complete CO conversion is achieved at respective temperatures of 120 and 100 °C. These results demonstrate that the prepared catalyst, $Ce_{0.93}Pd_{0.02}Cu_{0.05}O_{2-\delta}$, is highly active and capable of achieving complete CO conversion over a wide temperature window, if the contact time is extended.

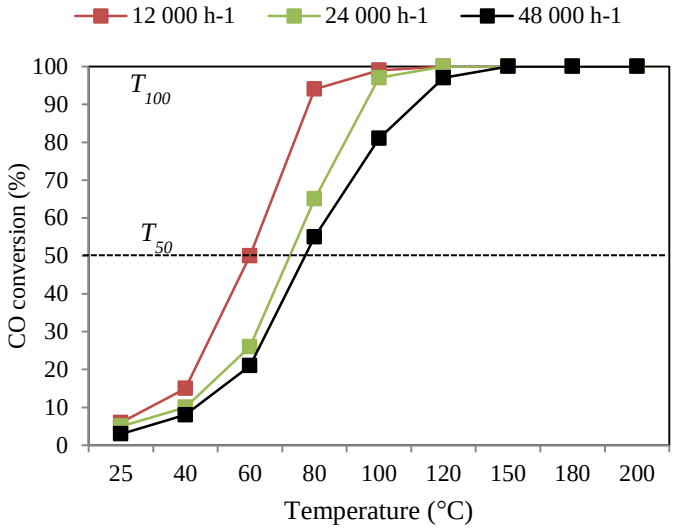

Figure 3.14 *CO conversion as a function of temperature at different GHSVs (12 000 – 48 000 h^{-1}) over $Ce_{0.93}Pd_{0.02}Cu_{0.05}O_{2-\delta}$.*

3.4 Conclusion

In this study, three substituted ceria catalysts ($Ce_{0.98}Pd_{0.02}O_{2-\delta}$, $Ce_{0.95}Cu_{0.05}O_{2-\delta}$ and $Ce_{0.93}Pd_{0.02}Cu0_{.05}O_{2-\delta}$) were prepared using one-step solution combustion. Their structural and electronic characteristics were established by multiple techniques (XRD, Raman, HR-TEM, XPS and H_2-TPR). The CO oxidation activity of $Ce_{0.95}Cu_{0.05}O_{2-\delta}$ was considerably enhanced by the incorporation of palladium as the second substitute metal in the lattice structure. The synergetic effect between palladium, copper and cerium ions in $Ce_{0.93}Pd_{0.02}Cu0_{.05}O_{2-\delta}$ resulted in improved reducibility and superior performance. The catalytic behaviour of the studied catalysts was found to be directly associated with the enhancement of the reducibility and the presence of oxygen vacancies.

3.5Acknowledgements

The financial support provided by Mintek and the Department of Science and Technology (Advanced Metals Initiative Program) is gratefully acknowledged. The authors are also thankful to the Solid State and Structural Chemistry Unit at the Indian Institute of Science (Bangalore) for their help with XPS recording. We are thankful to the Atomic & Molecular Physics Division (A.K. Yadav, S.N. Jha, D. Bhattacharyya and N. K. Sahoo) at the Bhabha Atomic Research Centre (Mumbai) for helping with XANES and EXAFS experiments. Thanks are due to Mfanafuthi Radebe who worked on the project as a trainee.

References

[1] M. Shelef, G.W. Graham, R.W. McCabe, in: A. Trovarelli (Ed.), Catalysis by Ceria and Related Materials, Imperial College Press ; Distributed by World Scientific, Landon, 2013, pp. 343-375.

[2] A. Corma, P. Atienzar, H. Garcia, J.-Y. Chane-Ching, Nat Mater 3 (2004) 394-397.

[3] C. Sun, H. Li, L. Chen, Energy & Environmental Science 5 (2012) 8475-8505.

[4] V.M. Shinde, G. Madras, Appl. Catal., B 123–124 (2012) 367-378.

[5] V.M. Shinde, G. Madras, Appl. Catal., B 138-139 (2013) 51-61.

[6] A. Trovarelli, P. Fornasiero, Editors, Catalysis by Ceria and Related Materials, 2nd Edition, Imperial College Press ; Distributed by World Scientific, London, 2013.

[7] C.R. Jung, A. Kundu, S.W. Nam, H.-I. Lee, Appl. Catal., A 331 (2007) 112-120.

[8] N. Luong, E. Yamasue, H. Okumura, K. Ishihara, in: T. Yao (Ed.), Zero-Carbon Energy Kyoto 2012, Springer Japan, 2013, pp. 167-177.

[9] G. Avgouropoulos, T. Ioannides, Appl. Catal., A 244 (2003) 155-167.

[10] E.-Y. Ko, E.D. Park, K.W. Seo, H.C. Lee, D. Lee, S. Kim, Catal. Today 116 (2006) 377-383.

[11] M.S. Hegde, G. Madras, K.C. Patil, Acc. Chem. Res. 42 (2009) 704-712.

[12] P. Singh, M.S. Hegde, Dalton Trans. 39 (2010) 10768-10780.

[13] A. Gupta, U.V. Waghmare, M.S. Hegde, Chem. Mater. 22 (2010) 5184-5198.

[14] A. Gayen, K.R. Priolkar, P.R. Sarode, V. Jayaram, M.S. Hegde, G.N. Subbanna, S. Emura, Chem. Mater. 16 (2004) 2317-2328.

[15] P. Bera, S. Malwadkar, A. Gayen, C.V.V. Satyanarayana, B.S. Rao, M.S. Hegde, Catal. Lett. 96 (2004) 213-219.

[16] S. Royer, D. Duprez, ChemCatChem 3 (2011) 24-65.

[17] H.J. Freund, G. Meijer, M. Scheffler, R. Schlögl, M. Wolf, Angew. Chem. Int. Ed. 50 (2011) 10064-10094.

[18] A. Iglesias-Juez, A.B. Hungria, A. Martinez-Arias, J.A. Anderson, M. Fernandez-Garcia, Catal. Today 143 (2009) 195-202.

[19] F. Yang, J. Wei, W. Liu, J. Guo, Y. Yang, Journal of Materials Chemistry A 2 (2014) 5662-5667.

[20] Y.-Z. Chen, B.-J. Liaw, H.-C. Chen, Int. J. Hydrogen Energy 31 (2006) 427-435.

[21] M. Narayanappa, V.D.B.C. Dasireddy, H.B. Friedrich, Appl. Catal., A 447–448 (2012) 135-143.

[22] A.K. Poswal, A. Agrawal, A.K. Yadav, C. Nayak, S. Basu, S.R. Kane, C.K. Garg, D. Bhattachryya, S.N. Jha, N.K. Sahoo, AIP Conf. Proc. 1591 (2014) 649-651.

[23] S. Basu, C. Nayak, A.K. Yadav, A. Agrawal, A.K. Poswal, D. Bhattacharyya, S.N. Jha, N.K. Sahoo, J. Phys: Conf. Ser. 493 (2014) 012032.

[24] S. Saitzek, J.F. Blach, S. Villain, J.R. Gavarri, Physica Status Solidi A 205 (2008) 1534-1539.

[25] D. Gamarra, A.L. Cámara, M. Monte, S.B. Rasmussen, L.E. Chinchilla, A.B. Hungría, G. Munuera, N. Gyorffy, Z. Schay, V.C. Corberán, J.C. Conesa, A. Martínez-Arias, Appl. Catal., B 130–131 (2013) 224-238.

[26] D. Gamarra, G. Munuera, A.B. Hungría, M. Fernández-García, J.C. Conesa, P.A. Midgley, X.Q. Wang, J.C. Hanson, J.A. Rodríguez, A. Martínez-Arias, J. Phys. Chem. C 111 (2007) 11026-11038.

[27] M. Fernandez-Garcia, A. Martinez-Arias, J.C. Hanson, J.A. Rodriguez, Chem. Rev. (Washington, DC, U. S.) 104 (2004) 4063-4104.

[28] J.E. Spanier, R.D. Robinson, F. Zhang, S.W. Chan, I.P. Herman, Phys. Rev. B 64 (2001) 245407.

[29] T. Taniguchi, T. Watanabe, N. Sugiyama, A.K. Subramani, H. Wagata, N. Matsushita, M. Yoshimura, J. Phys. Chem. C 113 (2009) 19789-19793.

[30] P. Sudarsanam, B. Mallesham, P.S. Reddy, D. Großmann, W. Grünert, B.M. Reddy, Appl. Catal., B 144 (2014) 900-908.

[31] B. Holland, J. Porous Mater. 10 (2003) 17-22.

[32] P.Y. Peng, I. Jin, T.C.K. Yang, C.-M. Huang, Chem. Eng. J. 251 (2014) 228-235.

[33] K.S.W. Sing, D.H. Everett, R.A.W. Haul, L. Moscou, R.A. Pierotti, J. Rouquerol, T. Siemieniewska, in: G. Ertl, H. Knözinger, F. Schüth, J. Weitkamp (Eds.), Handbook of Heterogeneous Catalysis, 2nd ed., Wiley-VCH Verlag GmbH & Co. KGaA, Weinheim, Germany, 2008, pp. 1217-1230.

[34] J.-Y. Luo, M. Meng, J.-S. Yao, X.-G. Li, Y.-Q. Zha, X. Wang, T.-Y. Zhang, Appl. Catal., B 87 (2009) 92-103.

[35] I. Twagirashema, M. Engelmann-Pirez, M. Frere, L. Burylo, L. Gengembre, C. Dujardin, P. Granger, Catal. Today 119 (2007) 100-105.

[36] S. Sharma, M.S. Hegde, R.N. Das, M. Pandey, Appl. Catal., A 337 (2008) 130-137.

[37] K.R. Priolkar, P. Bera, P.R. Sarode, M.S. Hegde, S. Emura, R. Kumashiro, N.P. Lalla, Chem. Mater. 14 (2002) 2120-2128.

[38] R.V. Gulyaev, E.M. Slavinskaya, S.A. Novopashin, D.V. Smovzh, A.V. Zaikovskii, D.Y. Osadchii, O.A. Bulavchenko, S.V. Korenev, A.I. Boronin, Appl. Catal., B 147 (2014) 132-143.
[39] P. Burroughs, A. Hamnett, A.F. Orchard, G. Thornton, J. Chem. Soc., Dalton Trans. (1976) 1686-1698.
[40] J.M. Gatica, D.M. Gómez, J.C. Hernández-Garrido, J.J. Calvino, G.A. Cifredo, H. Vidal, Appl. Catal., A 479 (2014) 35-44.
[41] W. Liu, M. Flytzani-Stephanopoulos, Chem. Eng. J. Biochem. Eng. J. 64 (1996) 283-294.
[42] G. Wrobel, C. Lamonier, A. Bennani, A. D'Huysser, A. Aboukais, J. Chem. Soc., Faraday Trans. 92 (1996) 2001-2009.
[43] J. Zhang, Z. Wu, T. Liu, T. Hu, Z. Wu, J. Xin, J. Synchrotron Radiat. 8 (2001) 531-532.
[44] A.V. Soldatov, T.S. Ivanchenko, S.D. Longa, A. Kotani, Y. Iwamoto, A. Bianconi, Phys. Rev. B: Condens. Matter 50 (1994) 5074-5080.
[45] P. Bera, K.R. Priolkar, P.R. Sarode, M.S. Hegde, S. Emura, R. Kumashiro, N.P. Lalla, Chem. Mater. 14 (2002) 3591-3601.
[46] J.A. Rodriguez, J.C. Hanson, D. Stacchiola, S.D. Senanayake, PCCP 15 (2013) 12004-12025.
[47] D.C. Koningsberger, R. Prins, Editors, Chemical Analysis, Vol. 91: X-ray Absorption: Principles, Applications, Techniques of EXAFS SEXAFS, and XANES, John Wiley & Sons, 1988.
[48] M. Newville, B. Ravel, D. Haskel, J.J. Rehr, E.A. Stern, Y. Yacoby, Physica B: Condens. Matter 208–209 (1995) 154-156.
[49] H.C. Lee, D.H. Kim, Catal. Today 132 (2008) 109-116.
[50] S. Carrettin, P. Concepcion, A. Corma, J.M.L. Nieto, V.F. Puntes, Angew. Chem. Int. Ed. 43 (2004) 2538-2540.

CHAPTER 4

Effect of Cu additives on the performance of a cobalt substituted ceria ($Ce_{0.90}Co_{0.10}O_{2-\delta}$) catalyst in total and preferential CO oxidation

Keywords: PROX, CO oxidation, ceria, solid-solution, Cu-containing catalysts, Co-containing catalysts

Abstract

The study reports the modification of the developed $Ce_{0.90}Co_{0.10}O_{2-\delta}$ catalyst by incorporating copper ions in order to improve the catalytic activity for total and preferential CO oxidation (TOX and PROX). A series of metal ion substituted ceria catalysts, $Ce_{0.90}Co_{0.10}O_{2-\delta}$ and $Ce_{0.90-x}Cu_xCo_{0.10}O_{2-\delta}$ (x = 0.01, 0.03 and 0.05) were synthesized in a single step by the urea-assisted solution combustion method. The compositions, textural and structural properties of the catalysts were characterized by XRD, XPS, Raman, H_2-TPR and ICP-OES. The insertion of Cu ions in $Ce_{0.90}Co_{0.10}O_{2-\delta}$ greatly enhanced the reducibility and improved the activity, with $Ce_{0.85}Cu_{0.05}Co_{0.10}O_{2-\delta}$ showing superior catalytic performance compared to other bimetallic catalysts. When the gas hourly space velocity was varied between 12 000 and 48 000 h^{-1}, the catalyst achieved complete CO conversion below 200 °C under total and preferential CO oxidation conditions. Analysis of the reaction profiles and rate calculations suggest that H_2 and CO oxidation over $Ce_{0.90}Co_{0.10}O_{2-\delta}$ may be occurring on the same active sites while the two reactions seem to be taking place on independent sites over Cu-containing catalysts. In addition, the effect of H_2O and CO_2 in PROX has been studied. The presence of H_2O and/or CO_2 caused a decrease in the activity of the catalysts. However, the degree of deactivation by H_2O and CO_2 decreased with increasing the Cu content in the catalysts. Removing the two components from the feed leads to full restoration of the activity. The present catalysts are highly active, selective and stable in TOX and PROX (in the absence of H_2O and CO_2).

4.1 Introduction

One of the important challenges faced by researchers is the development of clean and alternative energy conversion processes. Polymer electrolyte membrane fuel cells (PEMFCs) have become an important subject of research for sustainable energy development technologies. This is due to their low temperature of operation, reasonably high power density and zero emission of pollutants [1]. Most of the hydrogen required as fuel for PEMFCs is produced by steam reforming of hydrocarbon fuels, followed by the water gas shift (WGS) reaction, in order to improve hydrogen yield. The hydrogen produced after this step co-exists with 1% of carbon monoxide (CO) and other gaseous products [2]. This amount of CO in the hydrogen stream drastically decreases the efficiency of the Pt anode catalyst in converting hydrogen fuel to energy [3, 4]. Therefore, the removal of CO from the reformate gas is necessary in order to ensure maximum PEMFC power output. To date, CO preferential oxidation is one of the most effective ways for the purification of the reformate stream, with minimal hydrogen consumption [5].

Different types of catalyst formulations have been explored and studied for the total CO oxidation (TOX) and preferential CO oxidation (PROX) [6-9]. Among other transition metals, platinum group metal (PGM) based catalysts have been widely studied and applied for PROX. As early as the 1960s, Pt/Al_2O_3 catalysts were used by the Engelhard Corporation in hydrogen plants to remove CO prior to ammonia synthesis [10]. Since then, more catalysts have been developed to purify hydrogen for PEMFCs applications. The most studied PGMs are Pt and Pd and to a lesser extent Rh and Ru, supported on materials such as silica, alumina, zeolites and ceria [11]. A major concern involving the use of PGMs is the high cost and limited supply. As a result greater emphasis is placed on developing cost effective catalysts.

Ceria-based materials are well known for their applications as oxygen storage materials in automotive three-way catalytic converters (TWC) [12]. Recently, ceria-based catalysts have gained recognition in a wide range of applications, most notably, in the field of alternative energy and fuel cells [13, 14]. The attractive catalytic behaviour demonstrated by ceria-based materials is often attributed to their good ionic conduction, temperature stability and the facile redox cycle between Ce^{3+} and Ce^{4+} [15, 16]. In the past decade, selective oxidation has

been the focal point of the work published on ceria-based materials [17-20]. In particular, total CO oxidation and preferential CO oxidation have received more attention due to their applications in emission control and fuel cell technologies [21-24]. In most cases, ceria has been used as a support for active precious metals, such as Pt, Au or Pd [24-27]. Despite good CO oxidation activity shown by these catalysts, the drawback is that they are also active for the undesirable H_2 oxidation reaction.

Many researchers have investigated the catalytic performance of non-precious transition metal oxide catalysts for TOX and PROX [28-30]. Among the explored metal oxides, copper and cobalt based oxides (especially CuO and Co_3O_4) are the most promising catalysts for TOX and PROX [31, 32]. Ceria-supported copper catalysts have also been widely used as alternative catalyst formulations for these reactions [33, 34]. The outstanding activity of CuO-CeO_2 catalysts has been attributed to the synergistic interaction between Cu and Ce, as represented by a proposed redox equilibrium, $Ce^{4+}— Cu^{1+} \leftrightarrow Ce^{3+}— Cu^{2+}$ [28, 29, 35]. The importance of the alternating between Cu(I) and Cu(II) oxidation states has been emphasized by Jernigan and Somorjai [36]. On the other hand, in the case of unsupported Co_3O_4, its activity has been associated with the co-existence of $Co^{2+}— Co^{3+}$ pairs [32]. Unfortunately, pure Co_3O_4 deactivates easily, especially in the presence of moisture and is only efficient for low-temperature total CO oxidation [37]. In a H_2-rich stream, the Co species, in bulk Co_3O_4, can be reduced to Co^{2+} and Co^0 which are not active for CO oxidation [38, 39]. Motivated by the performance of the CuO-CeO_2 system, several researchers have studied the activity of Co_3O_4-CeO_2 catalysts [7, 40-43]. It has been shown that, when supported on oxides, Co_3O_4 catalysts can maintain their good PROX activity due to the enhancement of the $Co^{2+}— Co^{3+}$ redox potential [44]. PROX studies of Co_3O_4-CeO_2 catalysts have shown that the activation energy of CO oxidation is always lower than that of H_2 oxidation [42]. Hence, although CO, H_2 and O_2 may adsorb non-competitively on non-precious metal oxides during CO oxidation, higher temperatures are required for H_2 oxidation to light-off.

Regardless of better stability, compared to pure Co_3O_4, supported Co_3O_4 catalysts suffer from deactivation in excess H_2 due to the formation of CoO and have low tolerance for CO_2 and H_2O [45, 46]. Although the catalytic behaviour of supported metal oxide catalysts is positively influenced by a strong interaction between the support and the active phase, one of

their pitfalls is that the entirety of the supported component is not involved in catalytic conversion. This drawback is often associated with incomplete dispersion of the active phase, which is important for strong interaction and enhanced activity [44, 47-49]. A recent approach to improve interaction involves doping active metals into the matrix of the support, ceria [16]. The resulting material is a uniform solid-solution catalyst with modified redox properties and contains defects, which are significant for oxidation reactions. In some cases, such catalysts have shown improved activity compared to metal supported catalysts [50-52].

With the intention to ensure maximum dispersion of active cobalt ions and strong interaction of Co with Ce, a nanocrystalline $Ce_{0.90}Co_{0.10}O_{2-\delta}$ catalyst has been synthesised, where the cobalt ions are incorporated into the ceria lattice. To improve the robustness of the catalyst in the presence of CO_2 and H_2O, the promotional effect of Cu was investigated by employing new $Ce_{0.90-x}Cu_xCo_{0.10}O_{2-\delta}$ (where x = 0.01, 0.03 and 0.05) catalysts. In the present work, structural studies of the prepared catalysts and their catalytic performance in CO oxidation and PROX are reported for the first time.

4.2 Experimental

4.2.1 Catalyst synthesis

The nanocrystalline solid solution catalyst, $Ce_{0.90}Co_{0.10}O_{2-\delta}$ was prepared using a single-step combustion method, which is the same as described previously [53]. In the preparation of the catalyst, a redox combustion mixture was composed of $(NH_4)_2Ce(NO_3)_6$ (Sigma-Aldrich, 99.9%), $Co(NO_3)_2.6H_2O$ (Sigma-Aldrich, 99.9%) and NH_2CONH_2 (Sigma-Aldrich, 99.9%) in the ratio of 0.90: 0.1: 3.77, respectively. Typically, a mixture of 9.869 g of $(NH_4)_2Ce(NO_3)_6$, 0.582 g of $Co(NO_3)_2.5H_2O$ and 4.529 g of NH_2CONH_2 was dissolved in 50 cm^3 of water in a borosilicate dish. The resulting solution was heated at 150 °C on a hotplate for 10 minutes. The boiling solution was then transferred into a muffle furnace, preheated to 400 °C. After almost complete dehydration, the slurry ignited, resulting in the formation of a brown solid product. The product was maintained at 400 °C in the furnace for an extra 1 h. A similar one-step combustion method was used to prepare the $Ce_{0.90-x}Cu_xCo_{0.10}O_{2-\delta}$ (where x = 0.01, 0.03 and 0.05) bimetallic solid solutions, using $Cu(NO_3)_2.3H_2O$ (Sigma-Aldrich, 99.9%) as a precursor, in addition to the other starting materials mentioned in the preparation of

$Ce_{0.90}Co_{0.10}O_{2-\delta}$. Pure ceria nanopowder was also prepared by the solution combustion method, using a cerium ammonium nitrate-urea redox mixture. The Co_3O_4 used for the preparation of a physical mixture, $10\%Co_3O_4/CeO_2$, was prepared by precipitation and calcined at. 400 °C for 4 h [54]. The physical mixture was prepared by dry-grinding the two pure oxides, followed by calcining at 400 °C for 4 h.

4.2.2 Catalyst characterization

The textural properties; i.e. BET surface area, total pore volume and pore size of the catalysts were determined from the adsorption and desorption isotherms of nitrogen at -196 °C using a micromeritics TriStar 3000 multipoint analyser. Prior to the analysis, the samples were degassed at 200 °C overnight, under nitrogen. X-ray powder diffraction (XRD) experiments were performed on a Bruker D8 Advance diffractometer equipped with an XRK900 *in situ* cell and a Cu Kα source (λ = 1.5406 Å). The XRD patterns were recorded in the 2θ range of 10 to 90 ^{o} at a scan rate of 0.5°/min, with a step width of 0.02 °. The XRD patterns were refined by the Rietveld method using the Full Prof Suite-2000 program. Transmission electron microscopy (TEM) was performed on a Jeol JEM-1010 electron microscope and the images obtained were further analysed using iTEM software. High resolution TEM (HR-TEM) was carried out on a JEM-2100 electron microscope. Samples were prepared by dispersing them in ethanol before they were deposited onto holey carbon-coated grids. The field emission scanning electron microscope (FEG-SEM) images were captured using a ZEISS FEG-SEM Ultra Plus instrument. Raman spectroscopy analysis was conducted using an Advantage 532 series spectrometer, equipped with the visible laser line of 514 nm. X-ray photoelectron measurements were performed with a Thermo Scientific Multilab 2000 apparatus using the Al Kα radiation (1486.6 eV) and the C (1s) spectra as the reference (284.5 eV) for all binding energies. For a pre-reduced sample, the sample was pre-treated at 600 °C for 4 h under a flow of hydrogen. The sample was then cooled to room temperature under hydrogen and immediately sample prepared for analysis in secluded chamber. Inductively coupled plasma (ICP) was carried out using a Perkin Elmer Optical Emission Spectrometer Optima 5,300 DV and standards (1,000 ppm Ce, Cu and Co) were obtained from Fluka. Hydrogen temperature-programmed reduction (H_2-TPR) experiments were carried out on the Micromeritics AutoChem II 2920 Chemisorption analyzer equipped with a thermal conductivity detector (TCD). In these experiments, the sample (~30 mg) was pre-treated under a flow of argon 400 °C for 30 min, followed by cooling to room temperature

before any runs were carried out. The OSC of all the catalysts were studied by H_2-TPR or hydrogen uptake measurements. H_2 uptake measurements were performed repeatedly by reducing the compound in H_2 up to 550 ºC followed by oxidation in O_2 at 400 ºC over several cycles and no changes in the structure of the material during this redox process was observed.

4.2.3 Catalytic activity measurements

The catalytic behaviour of the catalysts was evaluated in the gas phase at atmospheric pressure and a temperature range from ambient to 250 °C. All gases used were analytical grade and were received from Afrox or Air Products. The gases were purified by a solid trap of molecular sieves to ensure that no water passed to the mass flow controllers (MFC) and subsequently to the reactor. The reactions were conducted in a stainless steel, fixed bed continuous flow reactor. The catalysts were crushed and collected through 300-600 µm sieves to obtain granules. For each experiment, a desired volume (0.70, 0.35 and 0.175 mL) of the catalyst was diluted with carborundum granules (24-grit, ~ 600 µm) to a volume of 3 mL. The catalyst was placed in the isothermal zone, near the centre of the reactor tube. Empty spaces on either side of the catalyst bed were filled carborundum and the ends plugged with glass wool. Prior to each reaction, the catalyst was pre-treated *in situ* in air flow at 150 °C for 4 h and then cooled to room temperature in nitrogen flow. For both total CO oxidation and PROX, the total flow rate was fixed at 140 mL/min while the mass of the catalyst was varied between 0.3 and 1.2 g to achieve a gas hourly space velocity (GHSV) ranging from 12 000 to 48 000 h^{-1}. The catalytic behaviour of the catalysts was compared under different reaction feed composition, as reflected in Table 4.1. For total CO oxidation, the feed composition was composed of 1 vol% CO and varied amounts of O_2; viz. 0.5, 1 and 2 vol%, corresponding to the λ values of 1, 2 and 4 respectively. In all experiments, N_2 was used as a balance gas. The factor λ is defined as the amount O_2 in the experiment relative to CO:

$$\lambda = \frac{2\,[O_2]_{in}}{[CO]_{in}} \qquad (4.1)$$

In the case of PROX experiments, 50 vol% H_2 was included in the feed that was used for total CO oxidation. In addition, PROX experiments were also conducted in the presence of 7 vol% H_2O and 15 vol% CO_2. Water was introduced by passing the dry gas through a bubbler kept at 38 °C. Gas compositions are summarized in Table 4.1. The bubbler system is explained in details in Appendix 2, Section A2.1.

Table 4.1 *Feed compositions (in vol.%) used for catalyst evaluation.*

Composition	CO	O_2	H_2	N_2	CO_2	H_2O	λ
1	1	0.5	-	98.5	-	-	1
2	1	1	-	98	-	-	2
3	1	2	-	97	-	-	4
4	1	-	-	99	-	-	0
5	1	0.5	50	48.5	-	-	1
6	1	1	50	48	-	-	2
7	1	2	50	47	-	-	4
8	1	-	50	49	-	-	0
9	1	1	50	33	15	-	2
10	1	1	50	41	-	7	2
11	1	1	50	26	15	7	2

The stability of the catalysts was evaluated at 180 °C by performing PROX experiments as a function of time-on-stream (24 h). The time-on-stream studies were conducted employing a reformate of 1 vol% CO, 1 vol% O_2, 50 vol% H_2 and 48 vol% N_2. A GHSV of 48 000 h^{-1} was used for all catalysts except for $Ce_{0.90}Co_{0.10}O_{2-\delta}$ where 12 000 h^{-1} was used to obtain comparable CO conversion. The effluent gases were analysed using a three-channel online Varian CP-4900 micro-GC, each equipped with separate thermal conductivity detectors (TCD) and columns. The GC has Mol Sieve 5A and CP-Sil5 CB columns with a 1.0 μL back-flushing system, which ensures the discharge of the residual components and simultaneous analysis of the gas mixtures. The percentage of the converted CO and the selectivity to CO_2 were calculated using Equations (4.2) and (4.3), respectively. The oxygen conversion was calculated using Equation (4.4).

$$\text{CO conversion } (X_{co}) = \frac{([CO]_{in}-[CO]_{out})}{[CO]_{in}} \times 100 \qquad (4.2)$$

$$\text{Selectivity to } CO_2 \left(S_{CO_2}\right) = \frac{[CO]_{in}-[CO]_{out}}{2([O_2]_{in}-[O_2]_{out})} \times 100 \qquad (4.3)$$

$$O_2 \text{ conversion } \left(X_{O_2}\right) = \frac{([O_2]_{in}-[O_2]_{out})}{[O_2]_{in}} \times 100 \qquad (4.4)$$

In some instances, the activities are expressed in terms of specific rates (r), determined using Equation (4.5), where X_{CO} stands for CO conversion, F_{CO} is the molar flow rate of CO (mol/s) and m_{cat} (g) is the mass of the catalyst.

$$r = \frac{X_{CO} * F_{CO}}{m_{cat}} \qquad (4.5)$$

4.3 Results and discussion

4.3.1 Structural and morphology studies

XRD studies were conducted to establish if the metal ions have been incorporated into the ceria lattice in the $Ce_{0.90}Co_{0.10}O_{2-\delta}$ catalyst. The XRD diffractograms of $Ce_{0.90}Co_{0.10}O_{2-\delta}$, together with those of the copper containing analogues, $Ce_{0.90}Cu_xCo_{0.10}O_{2-\delta}$ (where x = 0.01, 0.03 and 0.05), are shown in Figure 4.1. The XRD profiles of all catalysts show diffraction peaks that can be indexed to the fluorite structure of CeO_2. No Co_3O_4 diffraction peaks are identified in the X-ray diffractograms, except for those of $Ce_{0.87}Cu_{0.03}Co_{0.10}O_{2-\delta}$ and $Ce_{0.85}Cu_{0.05}Co_{0.10}O_{2-\delta,}$ which showed a small peak at 37.5 °. This peak is characteristic of the (311) reflection of the Co_3O_4 spinel structure [55]. When the pure Co_3O_4 is predominantly on the surface of ceria, as seen from the XRD profiles of the physical mixture (10% Co_3O_4/CeO_2), it could unambiguously be detected (Figure 4.1). For 10% Co_3O_4/CeO_2, the respective (220) and (400) reflections appeared as small peaks at 31° and 45°, while the peak corresponding to the (511) reflection overlaps with that for the (222) of CeO_2. These diffraction peaks are typical of the Co_3O_4 spinel structure. On the other hand, the diffraction peaks corresponding to CuO were not observed. The absence of these diffraction peaks suggests that copper ions have been successfully incorporated into the CeO_2 lattice. However, the existence of CuO finely dispersed on the surface and not detected by XRD is possible. In the past, it has been demonstrated that the incorporation of cobalt ions into ceria is difficult at atomic loadings exceeding 10%, $Ce_{1-x}Co_xO_{2-\delta}$ (x > 10) [53]. The same phenomenon may apply with $Ce_{0.87}Cu_{0.03}Co_{0.10}O_{2-\delta}$ and $Ce_{0.85}Cu_{0.05}Co_{0.10}O_{2-\delta}$ which contain a total metal loading (Cu + Co) exceeding 10%. All prepared ceria-based materials have broad diffraction peaks, indicative of the existence of small crystallites. Upon the incorporation of foreign metal ions into the ceria matrix, the diffraction lines slightly shifted to higher 2Θ values, which correspond to a slight decrease in the lattice constants. In the inset of Figure 4.1, it is shown that the (111) peak marginally moves when foreign metals are incorporated into the CeO_2 structure. This observation is in good agreement with the lattice parameters obtained from Rietveld analysis. A small decrease in lattice constant can also be associated with an increase in crystal size, as a consequence of size effects [56-59].

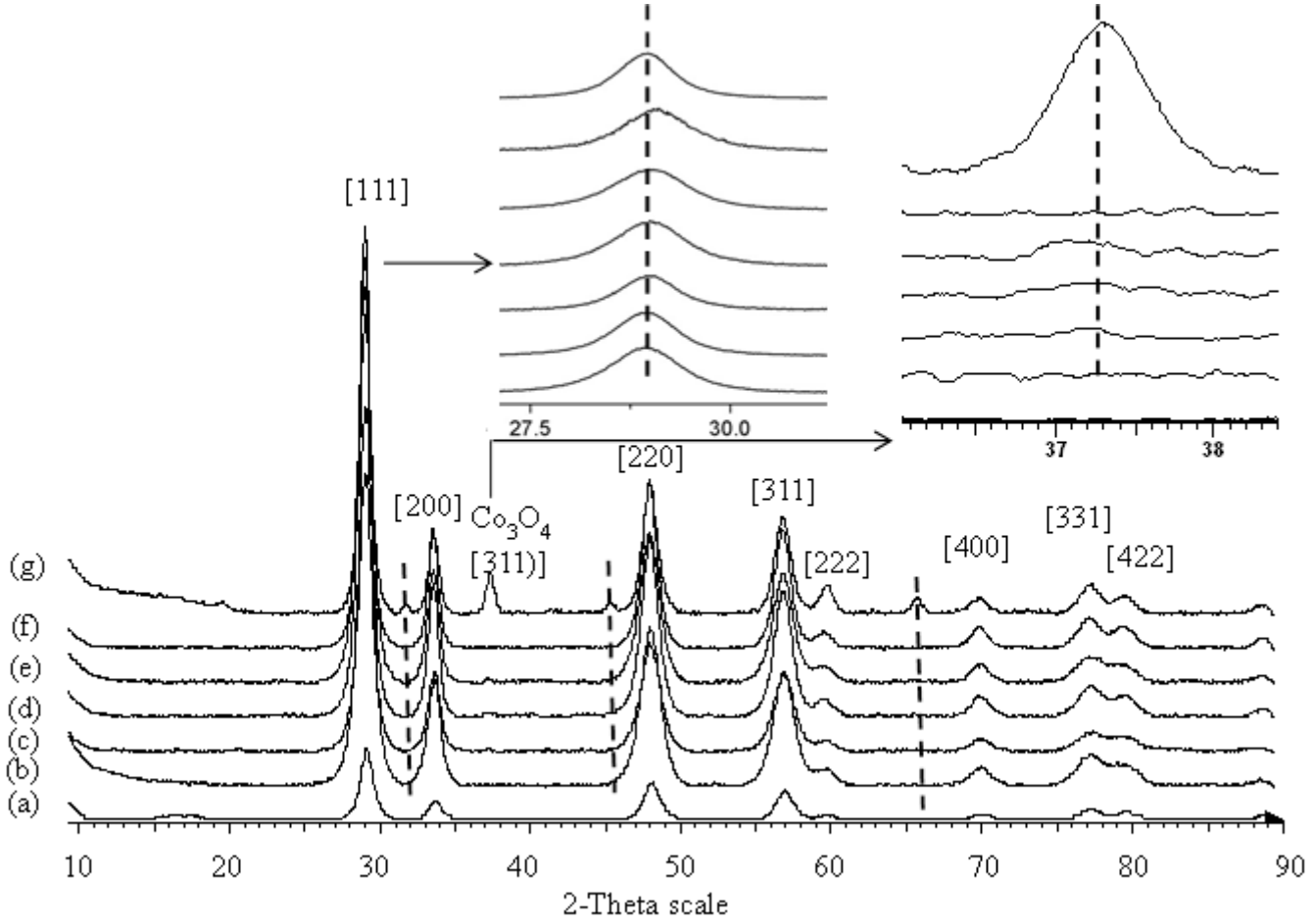

Figure 4.1 *X-ray diffraction patterns of (a) CeO_2, (b) $Ce_{0.9}Co_{0.10}O_{2-\delta}$, (c) $Ce_{0.89}Cu_{0.01}Co_{0.10}O_{2-\delta}$, (d) $Ce_{0.87}Cu_{0.03}Co_{0.10}O_{2-\delta}$, (e) $Ce_{0.85}Cu_{0.05}Co_{0.10}O_{2-\delta}$, (f) $Ce_{0.95}Cu_{0.05}O_{2-\delta}$ and (g)10% Co_3O_4/CeO_2*

Typical Rietveld-refined XRD pattern is shown for $Ce_{0.89}Cu_{0.01}Co_{0.10}O_{2-\delta}$ in Figure 4.2 and the rest of the patterns are given in Appendix 1. The cell parameters obtained from Rietveld refinement are summarized in Table 4.2. Except for $Ce_{0.85}Cu_{0.05}Co_{0.10}O_{2-\delta}$, all difference plots show a good fit, with no surface oxides. This suggests the formation of solid-solution materials. The observed, modelled and the difference (between observed and modelled) XRD patterns are represented in red, black and blue in the refined patterns. The lattice constant of non-substituted ceria was found to be 5.4221 Å, which is in good agreement with results reported elsewhere [53]. Theoretically, the incorporation of dopant ions with smaller ionic radii in the Ce^{4+} (0.97 Å) site are expected to be accompanied by a decrease in lattice parameter. Accordingly, substituted ceria materials, doped with Co^{2+}(0.74 Å) and/or Cu^{2+}(0.73 Å), show this value as being slightly lower than that of pure ceria, except for $Ce_{0.89}Cu_{0.01}Co_{0.10}O_{2-\delta}$. In $Ce_{0.89}Cu_{0.01}Co_{0.10}O_{2-\delta}$, there is a slightly increase in the lattice parameter. This trend has been observed in cases in which the solid-solution materials have a high concentration of Ce^{3+} species [60, 61]. Therefore, this change may be as a result of counteractive contributions induced by the incorporation of foreign metal ions and the

presence of defects of Ce^{3+} ions. As observed with the peak shifts, simultaneous introduction of both metal ions did not lead to significant changes in the lattice parameter. Perhaps, further changes are limited because of the difficulty of incorporating the entirety of both dopant ions at loadings above 10%, as seen for $Ce_{0.87}Cu_{0.03}Co_{0.10}O_{2-\delta}$ and $Ce_{0.85}Cu_{0.05}Co_{0.10}O_{2-\delta}$.

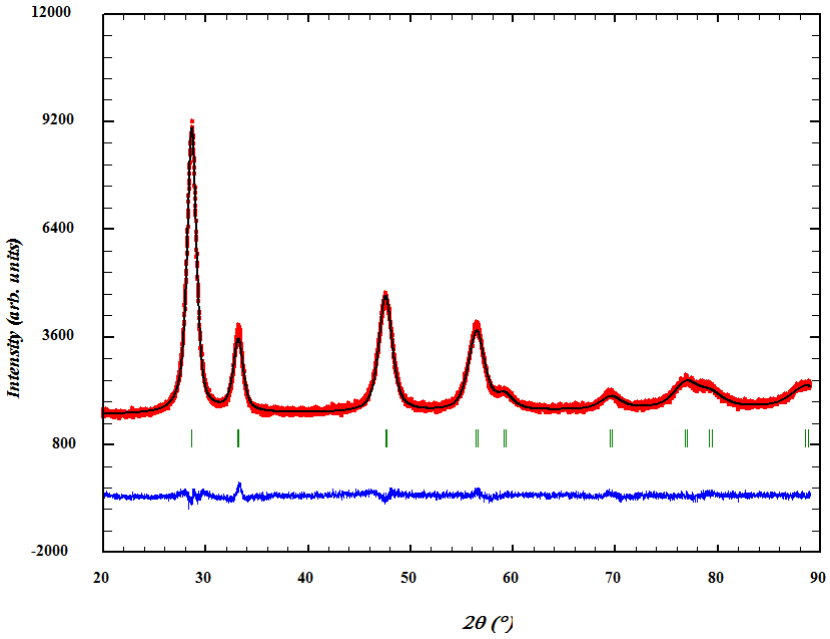

Figure 4.2 *Rietveld-refined XRD pattern of* $Ce_{0.87}Cu_{0.03}Co_{0.1}O_{2-\delta}$

Williamson-Hall (W-H) plots and Equation 4.6 were used to determine the lattice strain (ε) and crystallite size (*D*) for each of the prepared samples. The W-H plots of the catalysts are shown as supplementary information in Appendix 1. A linear fit is drawn with $\beta_{hkl}\cos\theta$ on the *y*-axis and $4\varepsilon\sin\theta$ along the *x*-axis. Pure ceria was found to have the least lattice strain. The lattice strain increases upon the introduction of dopants and it is at its maximum for samples that showed no peaks corresponding to the surface oxides. It is possible that the strain observed for $Ce_{0.85}Cu_{0.05}Co_{0.10}O_{2-\delta}$ is predominantly influenced by the insertion of Cu^{2+}, as it is comparable with that of $Ce_{0.95}Cu_{0.05}O_{2-\delta}$. The strain is possibly induced by lattice contraction, as observed from Rietveld results.

$$\beta_{hkl}\cos\theta = \frac{K\lambda}{D} + 4\varepsilon\sin\theta \qquad (4.6)$$

The average crystallite sizes of CeO_2, $Ce_{0.90}Co_{0.10}O_{2-\delta}$, $Ce_{0.89}Cu_{0.01}Co_{0.10}O_{2-\delta}$, $Ce_{0.87}Cu_{0.03}Co_{0.10}O_{2-\delta}$, $Ce_{0.85}Cu_{0.05}Co_{0.10}O_{2-\delta}$ and $Ce_{0.95}Cu_{0.05}O_{2-\delta}$ are 8, 9, 13, 10, 10 and 14 nm, respectively. These results are summarized in Table 4.2.

Table 4.2 *Structural parameters of investigated catalysts obtained from XRD profiles.*

Catalyst	*Lattice parameter a* (Å)	Structure factor (R_f)	Bragg factor (R_B)	χ^2	Lattice strain (10^{-3})	Crystallite size (nm)[a]	d-spacing (nm)[b]
CeO_2	5.4221	1.95	3.06	1.24	1.10	8 (9)	0.307
$Ce_{0.90}Co_{0.10}O_{2-\delta}$	5.4057	0.68	1.00	1.48	3.90	9 (8)	0.308 (0.31)
$Ce_{0.89}Co_{0.10}\ Cu_{0.01}O_{2-\delta}$	5.4225	0.98	1.60	1.77	4.60	13 (9)	0.308 (0.33)
$Ce_{0.87}Co_{0.10}\ Cu_{0.03}O_{2-\delta}$	5.4060	1.17	1.66	1.83	4.10	10 (8)	0.308 (0.33)
$Ce_{0.85}Co_{0.10}\ Cu_{0.05}O_{2-\delta}$	5.4068	1.25	1.72	1.69	3.60	10 (8)	0.308 (0.34)
$Ce_{0.95}Cu_{0.05}O_{2-\delta}$	5.4185	1.12	1.76	1.87	3.80	14 (10)	0.308 (0.30)

[a] Values shown in parenthesis were estimated using Scherrer equation. [b] Values shown in parenthesis were estimated from HR-TEM

Table 4.3 *Chemical composition and surface properties of prepared catalysts.*

Catalyst	Ce (at%)	Co (at%)	Cu (at%)	S_{BET} (m^2/g)	Average pore size (nm)	Pore volume (cm^3/g)
CeO_2	100	-	-	51	3.2	0.041
$Ce_{0.90}Co_{0.10}O_{2-\delta}$	91.2	8.8	-	27	3.0	0.021
$Ce_{0.89}Co_{0.10}\ Cu_{0.01}O_{2-\delta}$	90.0	9.2	0.8	14	3.7	0.013
$Ce_{0.87}Co_{0.10}\ Cu_{0.03}O_{2-\delta}$	87.8	9.5	2.7	22	3.2	0.017
$Ce_{0.85}Co_{0.10}\ Cu_{0.05}O_{2-\delta}$	86.2	9.0	4.8	27	2.8	0.015
$Ce_{0.95}Cu_{0.05}O_{2-\delta}$	94.8	-	5.2	21	4.7	0.021

The structural properties of ceria-based catalysts were also studied by Raman spectroscopy, employing the laser wavelength of 514 nm. Figure 4.3 depicts the Raman spectra of the metal ion substituted ceria materials together with those of pure CeO_2 and Co_3O_4. All ceria-based materials show an intense main peak at ≈ 460 cm^{-1} which is associated with the triply degenerate (F_{2g}) phonon mode of the cubic fluorite structure [43]. These observations are in agreement with the XRD results, indicating that the fluorite structure is retained upon metal substitution. For substituted ceria samples, an additional broad band is observed between 550 and 650 cm^{-1}. Generally, this peak is ascribed to the presence of oxygen vacancy defects (O_v) which are generated to compensate for charge imbalance after the incorporation of dopants with lower valence [16]. In the case of $Ce_{0.9}Co_{0.10}O_{2-\delta}$, $Ce_{0.85}Cu_{0.05}Co_{0.10}O_{2-\delta}$ and $Ce_{0.95}Cu_{0.05}O_{2-\delta}$, the O_v band was relatively more intense compared to other samples, indicating the presence of substantial oxygen vacancies. The absence of the O_v band in pure CeO_2 suggests that the vacancies present in the doped materials are not mainly intrinsic ones due to the presence of Ce^{3+} [62]. Instead, they are mostly extrinsic vacancies as a consequence of incorporating foreign metal ions in the fluorite lattice [63, 64]. Notably, the F_{2g} bands of substituted ceria materials have an increased width relative to pure ceria. This phenomenon has been associated with the manifestation of inhomogeneous strain, as a result of present oxygen vacancy defects due to metal insertion into the fluorite lattice [65-67].

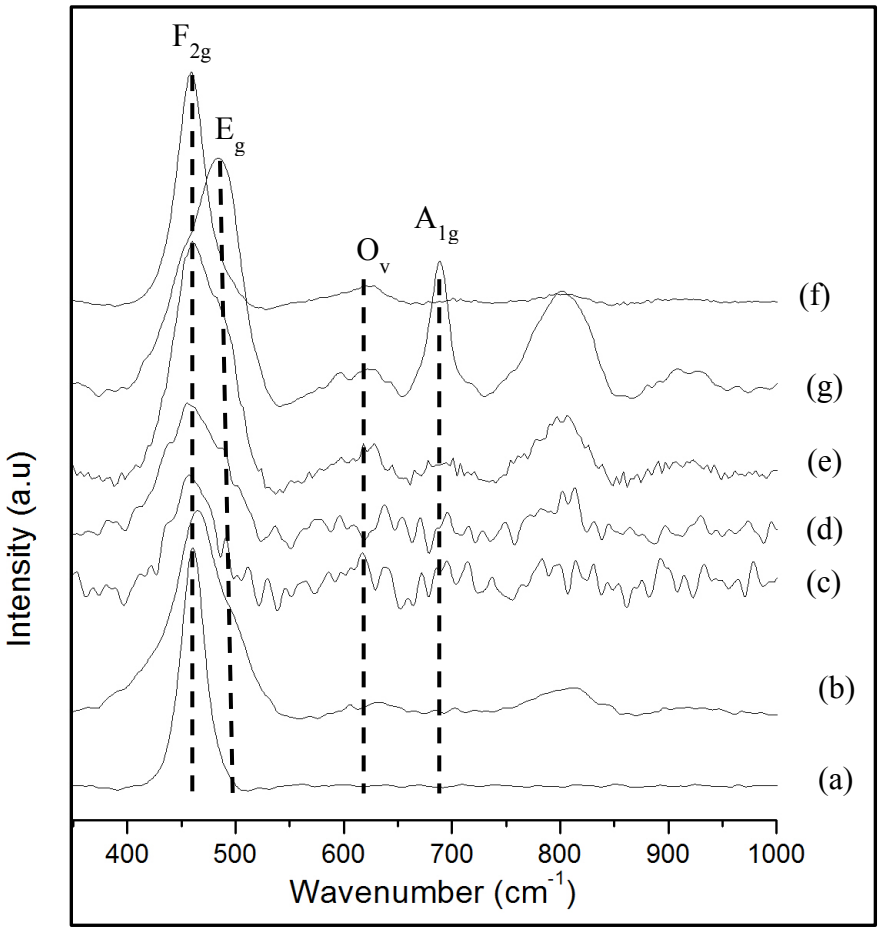

Figure 4.3 *Raman spectra of the prepared (a) CeO_2, (b) $Ce_{0.9}Co_{0.10}O_{2-\delta}$, (c) $Ce_{0.89}Cu_{0.01}Co_{0.10}O_{2-\delta}$, (d) $Ce_{0.87}Cu_{0.03}Co_{0.10}O_{2-\delta}$, (e) $Ce_{0.85}Cu_{0.05}Co_{0.10}O_{2-\delta}$, (f) $Ce_{0.95}Cu_{0.05}O_{2-\delta}$ and (g) Co_3O_4*

The HR-TEM and bright-field images of the catalyst are presented in Figure 4.4. The morphology of the catalysts seems to be comparable, regardless of further doping with Cu. The images show the presence of agglomerates of near-spherical nanoparticles. From image analysis, the materials are composed of nanoparticles of relatively uniform size (6 – 16 nm) which is comparable to the crystallite size deduced from XRD data. In general, the selected area diffraction of images (as seen with $Ce_{0.9}Co_{0.10}O_{2-\delta}$ in Figure 4.4 (a)) show a ring pattern that can be indexed to the fluorite structure [16] and is in agreement with XRD data. Moreover, the HR-TEM images of all the catalysts show lattice fringes with interplanar distances between 0.30 to 0.34 nm, corresponding to the (111) facets of fluorite-structured solid-solutions [16, 19]. These values are comparable with the d-spacing measurements obtained from XRD analyses, by applying the Bragg Equation at the (111) peak (Table 4.2). No diffraction lines associated with pure oxide and/or metallic phases were observed, suggesting the incorporation of metal ions into the CeO_2 matrix.

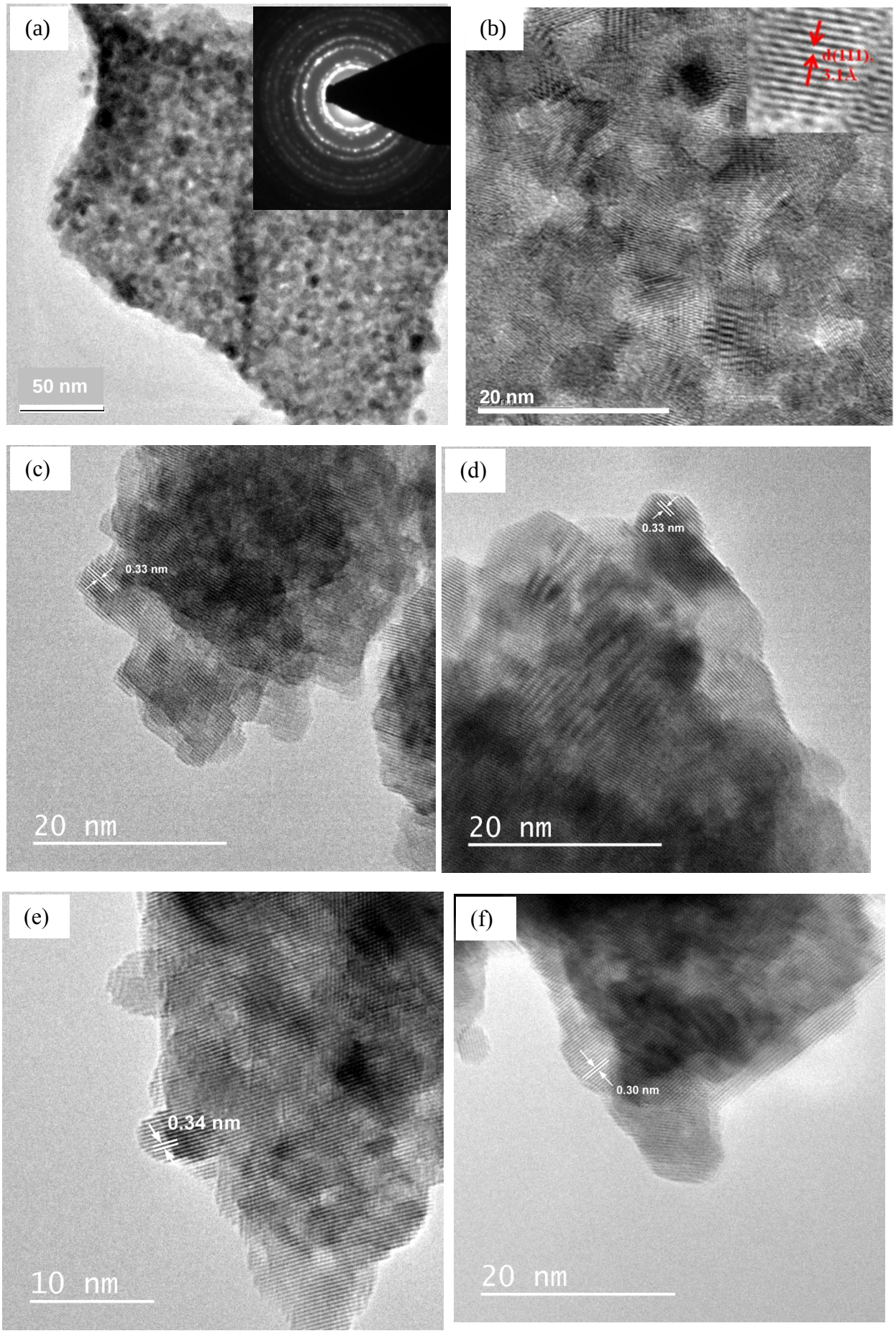

Figure 4.4 *(a) Bright field image and selected area electron diffraction of* $Ce_{0.90}Co_{0.10}O_{2-\delta}$*. HR-TEM images of (b)* $Ce_{0.90}Co_{0.10}O_{2-\delta}$*, (c)* $Ce_{0.89}Cu_{0.01}Co_{0.10}O_{2-\delta}$*, (d)* $Ce_{0.87}Cu_{0.03}Co_{0.10}O_{2-\delta}$*, (e)* $Ce_{0.85}Cu_{0.05}Co_{0.10}O_{2-\delta}$ *and (f)* $Ce_{0.95}Cu_{0.05}O_{2-\delta}$*.*

The FEG-SEM images of the examined catalysts are presented in Figure 4.5. The micrographs reveal that all catalysts possess microspheres which are made up of uniform small nanocrystals. The corresponding EDS results confirmed the presence of Ce, Co and Cu in the catalysts. As further doping does not translate to morphological changes, different catalytic behaviour may not be linked to the differences in morphology. The precise compositions of the catalysts were further established on the basis ICP-OES analysis. The results are summarized in Table 4.3

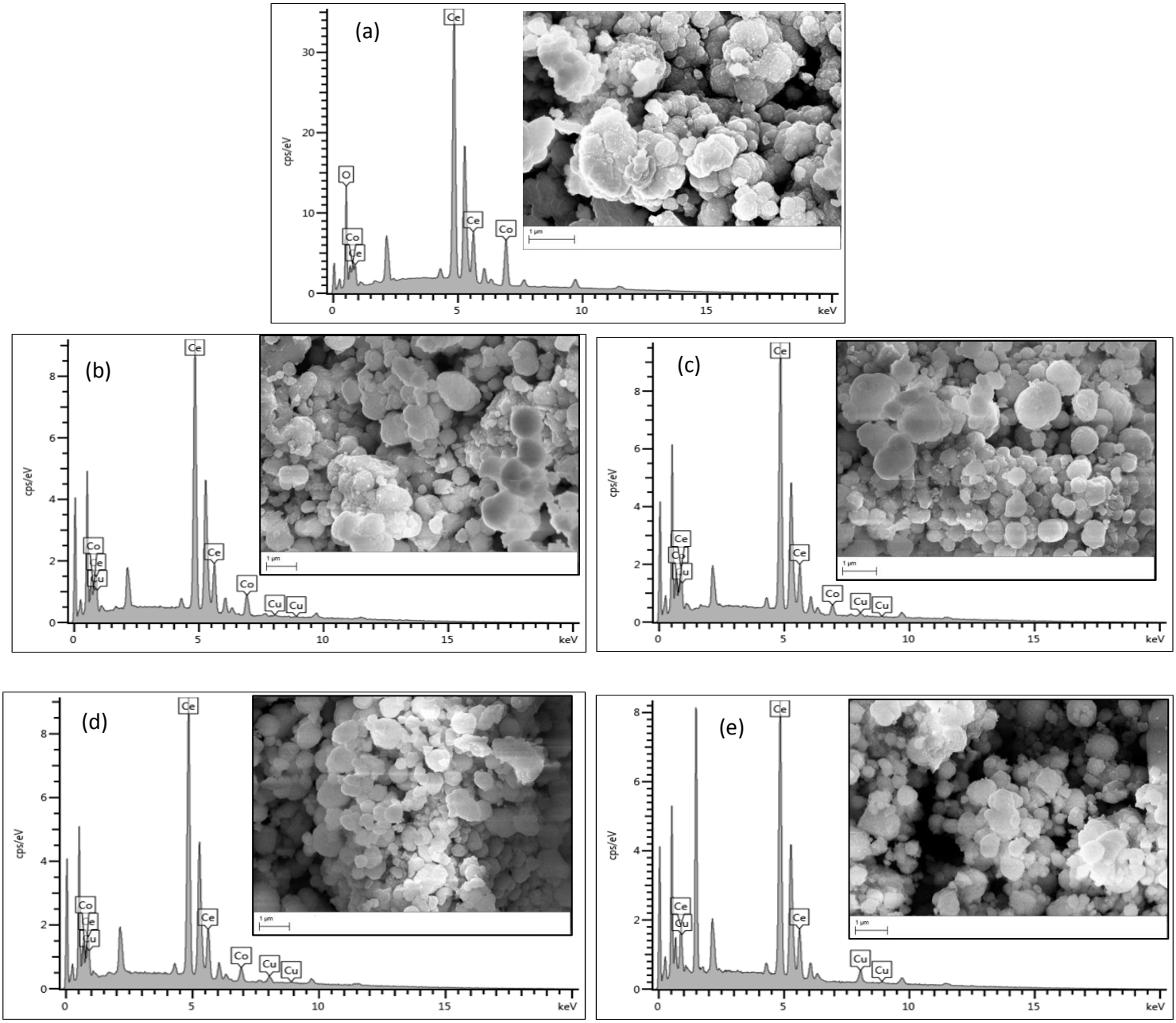

Figure 4. 5 *SEM micrographs and corresponding EDS of (a) $Ce_{0.90}Co_{0.10}O_{2-\delta}$, (b) $Ce_{0.89}Cu_{0.01}Co_{0.10}O_{2-\delta}$, (c) $Ce_{0.87}Cu_{0.03}Co_{0.10}O_{2-\delta}$, (d) $Ce_{0.85}Cu_{0.05}Co_{0.10}O_{2-\delta}$ and (e) $Ce_{0.95}Cu_{0.05}O_{2-\delta}$*

4.3.2 Textural studies

The study of the textural properties of the catalysts suggests that the materials are mesoporous with some involvement of microporosity features. The nitrogen adsorption/desorption isotherms and relative pore size distribution curves (deduced from the desorption curve) of all the catalysts are shown in Figure 4.6 A and B, respectively. Based on the IUPAC classification [68], the $Ce_{0.90}Co_{0.10}O_{2-\delta}$ isotherm is representative of a type IV isotherm, while the rest are characteristic of a type II isotherm. The corresponding hysteresis loops of these isotherms belong to the H1 type which is indicative of mesoporous materials. The isotherms have distinct hysteresis loops, signifying pores with different structural features. The isotherms reveal a sharp increase in adsorption at high relative pressures, which suggests the filling of the mesopores [69]. The pore size distribution curves show a peak in the range of 2.5 to 5 nm, confirming the existence of mesoporous structures. As anticipated, the surface areas and pore volumes of ceria decrease upon the insertion of foreign metals into the matrix structure. The surface areas of the studied solid-solution materials range from 14 to 27 m^2/g, with $Ce_{0.90}Co_{0.10}O_{2-\delta}$ having the largest and $Ce_{0.89}Cu_{0.01}Co_{0.10}O_{2-\delta}$ having the smallest surface area. The textural properties and chemical composition of the catalysts are summarized in Table 4.3.

4.3.3 Electronic and redox properties

In order to investigate the redox properties of the catalysts, H_2-TPR measurements of the catalysts were conducted. Pure ceria showed no H_2 consumption up to 400 °C, indicating that it could not be reduced in this temperature window under current experimental conditions. A comparison of the H_2-TPR profiles of $Ce_{0.90}Co_{0.10}O_{2-\delta}$, $Ce_{0.89}Cu_{0.01}Co_{0.10}O_{2-\delta}$, $Ce_{0.87}Cu_{0.03}Co_{0.10}O_{2-\delta}$, $Ce_{0.85}Cu_{0.05}Co_{0.10}O_{2-\delta}$ and $Ce_{0.95}Cu_{0.05}O_{2-\delta}$ is shown in Figure 4.7. Regarding the reduction profile of $Ce_{0.90}Co_{0.10}O_{2-\delta}$, two reduction peaks can be seen at 280 °C and 343 °C. This suggests that the reduction is a step-wise process where the former peak is due to the reduction of Co^{3+} to Co^{2+} and the latter can be attributed to the reduction of Co^{2+} to Co^0. This reduction pattern is well known for pure Co_3O_4 [42]. In comparison with the reported reduction peaks for pure Co_3O_4, the reduction peaks for the Ce-Co catalysts are lower, suggesting an improved reducibility of cobalt ions as reported elsewhere [61]. In the case of the $Ce_{0.95}Cu_{0.05}O_{2-\delta}$ sample, two overlapping reduction peaks are observed at 186 °C and 211 °C. The mentioned two peaks profile is typical for Cu-Ce samples [70-72]. It has been related to the reduction of two different types of copper oxide entities differing in their degree of interaction with the support. The low temperature peak would correspond to

smaller copper oxide particles subjected to a stronger interaction with the support which would favour their reduction, while the high temperature peak would correspond to larger copper oxide particles [72, 73].

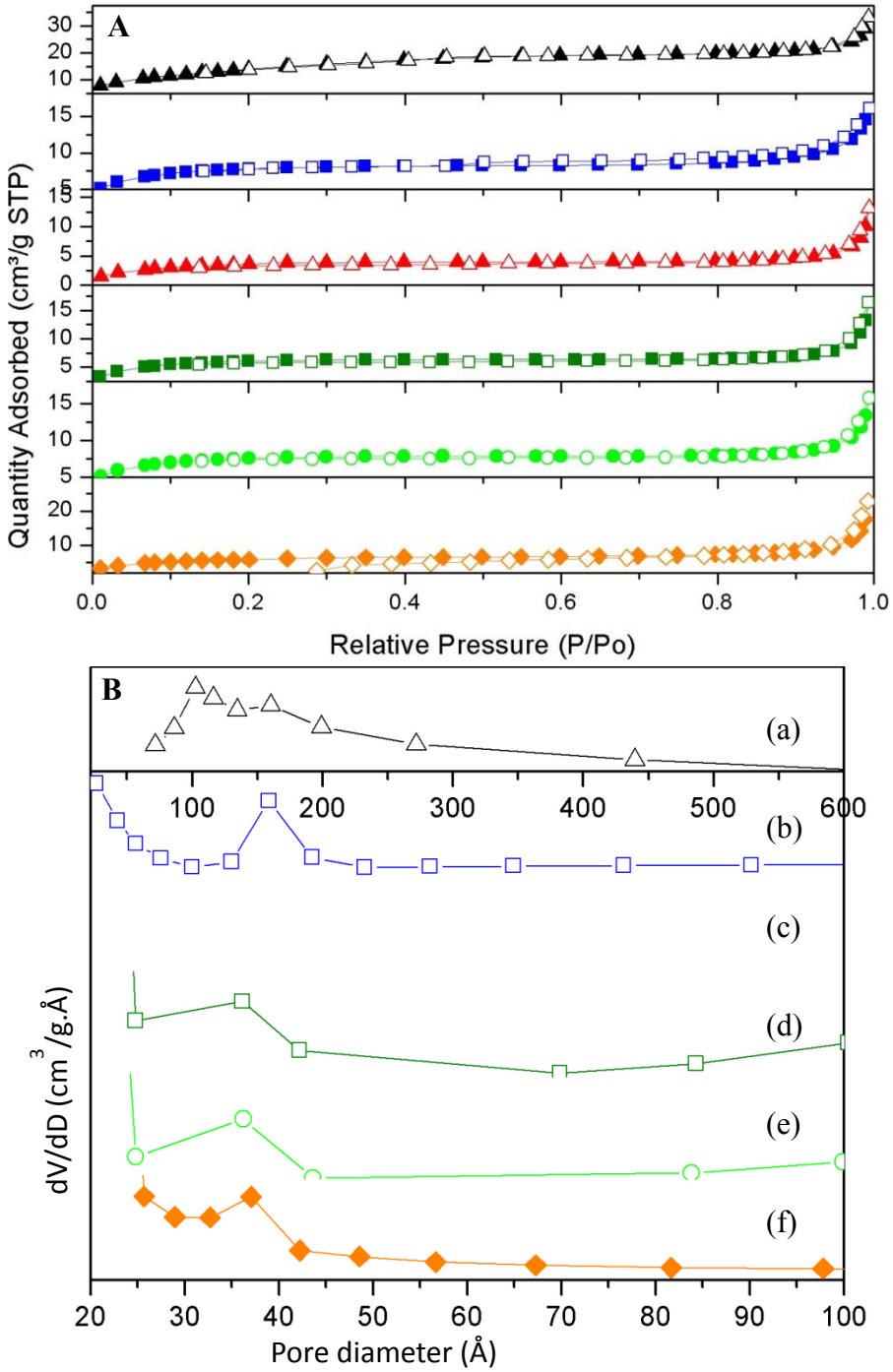

Figure 4.6 **A** *Nitrogen adsorption/desorption isotherms and* **B** *pore size distribution curves of (a) CeO_2, (b) $Ce_{0.9}Co_{0.10}O_{2-\delta}$, (c) $Ce_{0.89}Cu_{0.01}Co_{0.10}O_{2-\delta}$, (d) $Ce_{0.87}Cu_{0.03}Co_{0.10}O_{2-\delta}$, (e) $Ce_{0.85}Cu_{0.05}Co_{0.10}O_{2-\delta}$ and (f) $Ce_{0.95}Cu_{0.05}O_{2-\delta}$.*

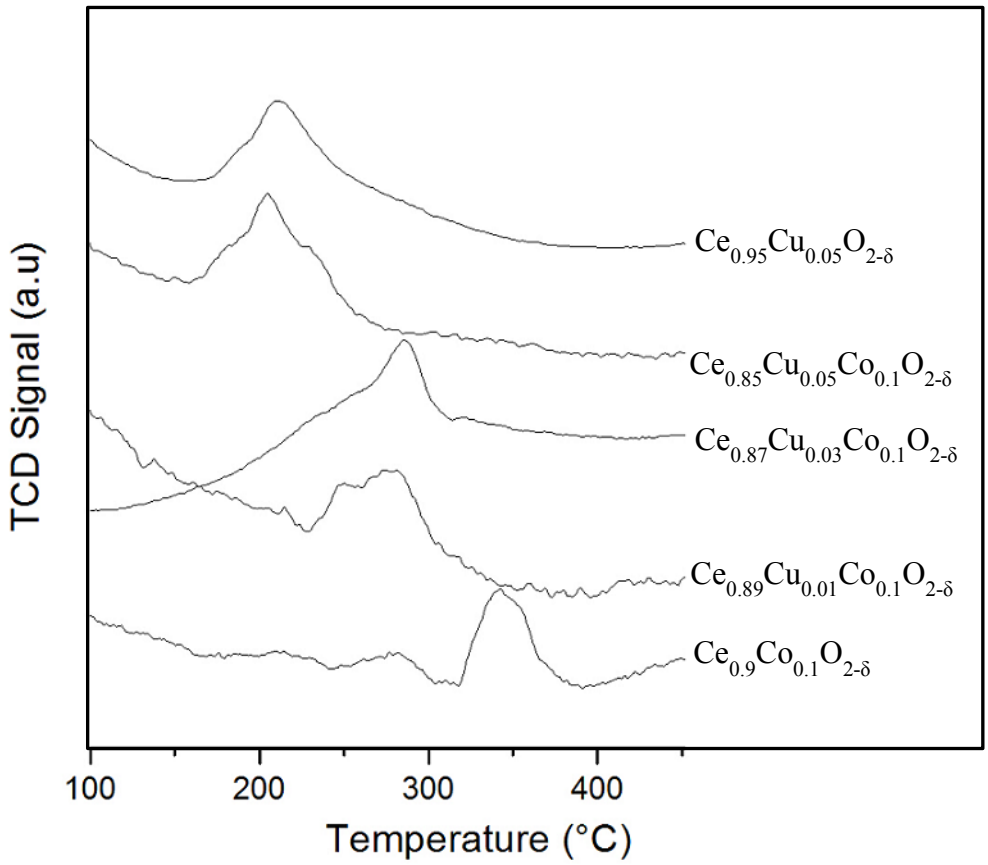

Figure 4.7 *H_2-TPR profiles of monometallic and bimetallic substituted ceria catalysts.*

All the profiles of the catalysts that contain both copper and cobalt species ($Ce_{0.89}Cu_{0.01}Co_{0.10}O_{2-\delta}$, $Ce_{0.87}Cu_{0.03}Co_{0.10}O_{2-\delta}$ and $Ce_{0.85}Cu_{0.05}Co_{0.10}O_{2-\delta}$) show three coinciding peaks located at reduction temperatures relatively lower than those observed in the profile of $Ce_{0.90}Co_{0.10}O_{2-\delta}$. Since the hydrogen consumption related to these peaks is higher than the theoretical consumption, due to the reduction of cobalt oxide species to metallic cobalt, the overlapping peaks also represent the reduction of copper ions to Cu^0. The incorporation of Cu^{2+} ions into the Co-containing catalyst stimulates the reduction of Co ions to a certain degree, depending on the Cu loading. By comparison, temperatures corresponding to cobalt oxide reduction steps decrease in the order of $Ce_{0.9}Co_{0.10}O_{2-\delta}$ > $Ce_{0.89}Cu_{0.01}Co_{0.10}O_{2-\delta}$ ≈ $Ce_{0.87}Cu_{0.03}Co_{0.10}O_{2-\delta}$ > $Ce_{0.85}Cu_{0.05}Co_{0.10}O_{2-\delta}$ ≈ $Ce_{0.95}Cu_{0.05}O_{2-\delta}$. Based on the amount of total hydrogen consumption, calculated up to the temperature of 400 °C, the oxygen storage capacity was estimated [74, 75] to be 78, 196, 210, 257 and 442 µmol/g for $Ce_{0.9}Co_{0.10}O_{2-\delta}$, $Ce_{0.89}Cu_{0.01}Co_{0.10}O_{2-\delta}$, $Ce_{0.95}Cu_{0.05}O_{2-\delta}$, $Ce_{0.87}Cu_{0.03}Co_{0.10}O_{2-\delta}$ and $Ce_{0.85}Cu_{0.05}Co_{0.10}O_{2-\delta}$, respectively. Notably, it increases with the increase of the Cu atomic loading in the Co-containing samples as a consequence of additional reduction of incorporated Cu ions [23]. Among all the studied catalyst formulations, $Ce_{0.95}Cu_{0.05}O_{2-\delta}$ is the

most easily reducible, with the first reduction peak located at 186 °C. This is due to the strong interaction between cerium and copper ions, which is even more enhanced in the absence of cobalt ions.

XPS was used to establish the electronic properties of Co, Cu and Ce in prepared solid-solution materials. Figure 4.8 (a) shows the Co (2p) XP spectra of Co-containing catalysts. For all samples, the main peak at the binding energy of 779 eV is characteristic of Co ($2p_{3/2}$), while the shoulder peak at 795 eV can be attributed to Co ($2p_{1/2}$). In the case of $Ce_{0.90}Co_{0.10}O_{2-\delta}$, the satellite peak can be seen as a broad peak at ~5.5 eV above the main peak. Overall, the spectra unambiguously confirm the presence of Co^{2+} in the high spin state [76]. However, the existence of Co^{3+} species cannot completely be ruled out since the Co($2p_{3/2}$) binding energies of Co^{2+} appear between 780 and 782 eV, which is relatively close to the region (779 - 782 eV) where those of Co^{3+} emerge [77]. Thus, it is often difficult to distinguish the two oxidation states based on their binding energies.

The Ce(3d) and Cu(2p) core level regions of the selected ceria-based catalysts are depicted in Figure 4.8 (b) and (c), respectively. The Ce (3d) XPS spectra of all studied catalysts show eight peaks associated with the pairs of spin-orbit doublets. The peaks are labeled according to the conventional nomenclature established by Burrough *et al*. [78]. The peaks labeled U (U-U′′′) and those assigned as V (V-V′′′) are related to the $3d_{3/2}$ and $3d_{5/2}$ spin-orbit components, respectively. Due to the closeness of U′ and V′ peaks to the main neighboring peaks (U and V), the former peaks are not well resolved. The couple (U′, V′) is characteristic of the Ce^{3+} species and the rest of the peaks correspond to the Ce^{4+} state as in CeO_2. The existence of the Ce^{3+} species was further confirmed by recording the XPS of a pre-reduced sample. For a reduced sample, the crescents formed between (V, V′′) and (U, U′′) are not well-defined as a consequence of increased Ce^{3+} components, V′ and U′ (Figure 4.9 (a)). Although all catalysts contain Ce predominantly in the +4 oxidation state, some degree of Ce^{3+} species is also present.

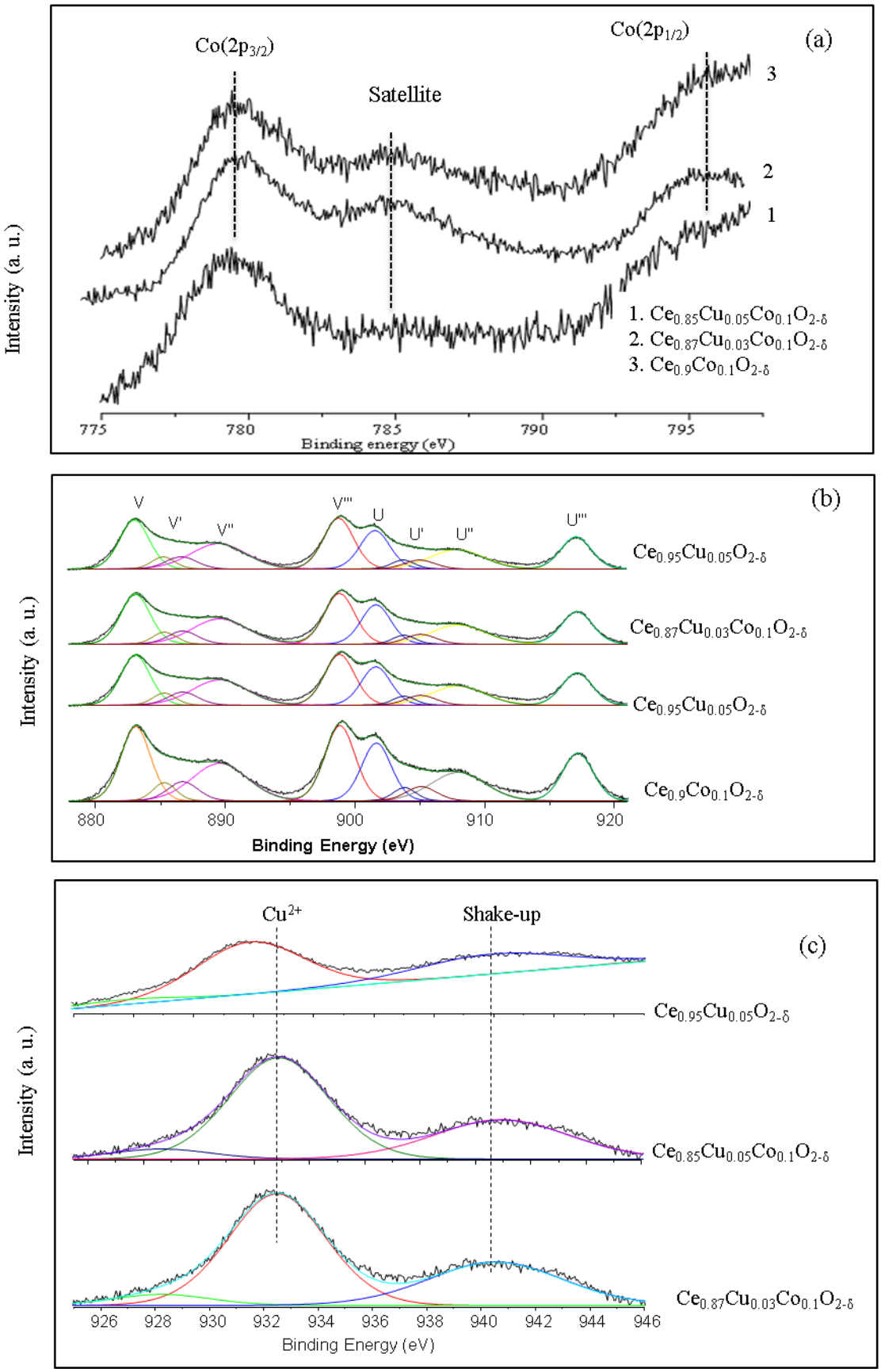

Figure 4.8 *XP spectra of the catalysts: (a) Co(2p), (b) Ce(3d) and (c) Cu(2p).*

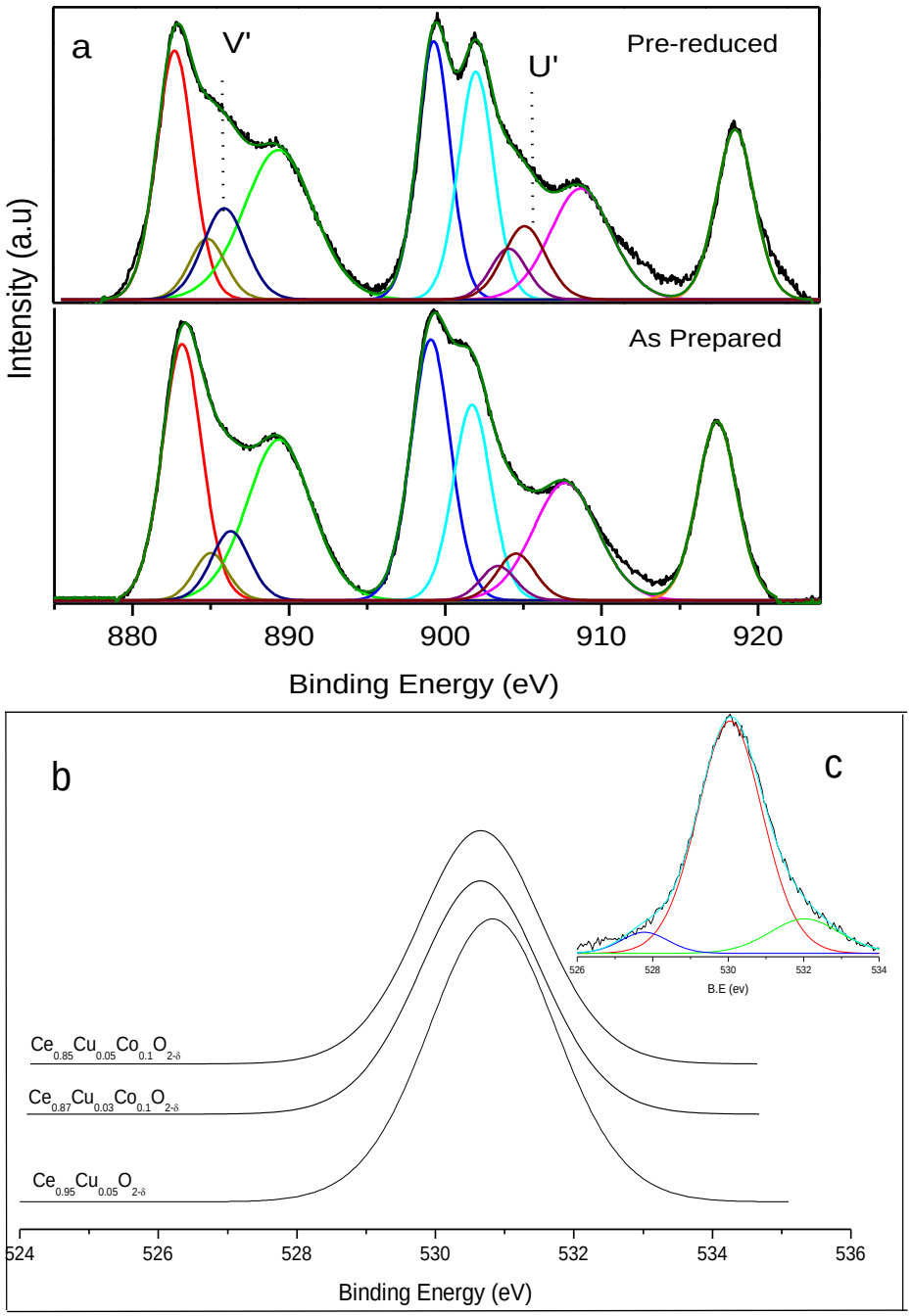

Figure 4.9 *Ce(3d) XP spectra of (a) pre-reduced and (b) as-prepared catalyst. (c) O(1s) XP spectra of the catalysts*

The Cu-containing catalysts ($Ce_{0.87}Cu_{0.03}Co_{0.10}O_{2-\delta}$, $Ce_{0.85}Cu_{0.05}Co_{0.10}O_{2-\delta}$ and $Ce_{0.95}Cu_{0.05}O_{2-\delta}$) show weak shake-up and Cu ($2p_{3/2}$) peaks at the binding energies of 940.5 eV and 932.5 eV, respectively. The weak intensity of the shake-up peak has been associated with the presence of reduced copper species, particularly Cu^{+}, in CuO-CeO_2 catalysts [6, 29]. The formation of Cu^{+} entities can be explained in two ways. Taking into account the similarity of

the Ce^{4+} (0.97 Å) and Cu^{+} (0.96 Å) ionic radii, Cu^{+} formation might be induced during substitution [6]. On the other hand, the copper species, in CuO-CeO_2, may be reduced during XPS measurements due to the desorption of surface oxygen under vacuum [29]. Summarily, the observations reported here suggest the presence of Cu^{2+} and Cu^{+} species and are in good agreement with the TPR profiles. The O(1s) XP spectra of the catalysts with different Cu loadings were also examined (Figure 4.9 (c)). The peaks that are associated with the lattice oxygen of $Ce_{0.87}Cu_{0.03}Co_{0.10}O_{2-\delta}$ and $Ce_{0.85}Cu_{0.05}Co_{0.10}O_{2-\delta}$ are centered at a binding energy of nearly 527 eV. In the case of $Ce_{0.95}Cu_{0.05}O_{2-\delta}$, the lattice oxygen peak appears at a slightly higher binding energy (529 eV) and is accompanied by a shoulder peak at 531.5 eV. The latter peak can be seen distinctly on a fitted spectrum shown in Figure 4.9 (c). Although the exact origin of this peak has been disputed, it is often attributed to the surface oxygen and linked to the outstanding oxidative catalysis demonstrated by CeO_2-based formulations [12, 79-81].

4.3.4 Catalytic studies

4.3.4.1 Total and preferential CO oxidation over $Ce_{0.9}Co_{0.1}O_{2-\delta}$

The catalytic activity of the catalysts was investigated in total CO oxidation in the temperature range of 25 °C - 200 °C, employing different feed-stream compositions (1 – 5). Bare ceria was also studied in order to emphasize the effect of incorporating cobalt ions into the ceria lattice. As can be seen from Table 3, only the oxygen content was varied in the gas composition. The GHSV was varied from 12 000 to 48 000 h^{-1} by changing the weight of the catalyst from 0.3 to 1.2 g, while keeping the total flow rate constant at 140 mL/min. Figure 4.10 (a) shows the typical light-off curves of the total CO oxidation reaction over non-substituted CeO_2, $Ce_{0.90}Co_{0.10}O_{2-\delta}$ and 10 wt% Co_3O_4/CeO_2. As seen for the Co-containing solid-solution catalyst, CO conversion increases with temperature until complete conversion is reached at temperatures above 150 °C (depending on the O_2/CO ratio and/or GHSV used). The temperatures for a CO conversion of 50% are marked with a dotted line on the graph. It is observed that neat ceria shows no significant CO conversion until higher temperatures are reached (150 - 200 °C). Since pure CeO_2 and $Ce_{0.90}Co_{0.10}O_{2-\delta}$ were prepared under the same combustion conditions, the outstanding catalytic performance demonstrated by cobalt substituted ceria suggests that the Co ions in the ceria lattice are involved in the promotion of CO activation during the TOX reaction. Moreover, the solid solution catalyst displays

superior activity to the physical mixture material (10 wt% Co_3O_4/CeO_2). The promising catalytic behaviour displayed by solid-solution catalysts has been generally associated with strong interaction between the components involved [16]. In the present case, the improved activity may be related to the enhanced Ce-Co interaction in $Ce_{0.90}Co_{0.10}O_{2-\delta}$. It is envisaged that such synergism is limited in 10 wt% Co_3O_4/CeO_2. The catalytic profile of $Ce_{0.90}Co_{0.10}O_{2-\delta}$ also appears to be outperforming some of the results reported for 10 wt% Co_3O_4/CeO_2 [23] and $Ce_{0.90}Mno_{0.10}O_2$ [46] composites, which showed complete CO conversion at 420 °C and the maximum of 90% CO conversion at 225 °C, respectively. However, the activity is comparable with that demonstrated by 10 wt% $Co_3O_4/Ce0_{.90}Mno_{0.10}O_2$, which gave complete CO conversion at 150 °C under similar conditions [46].

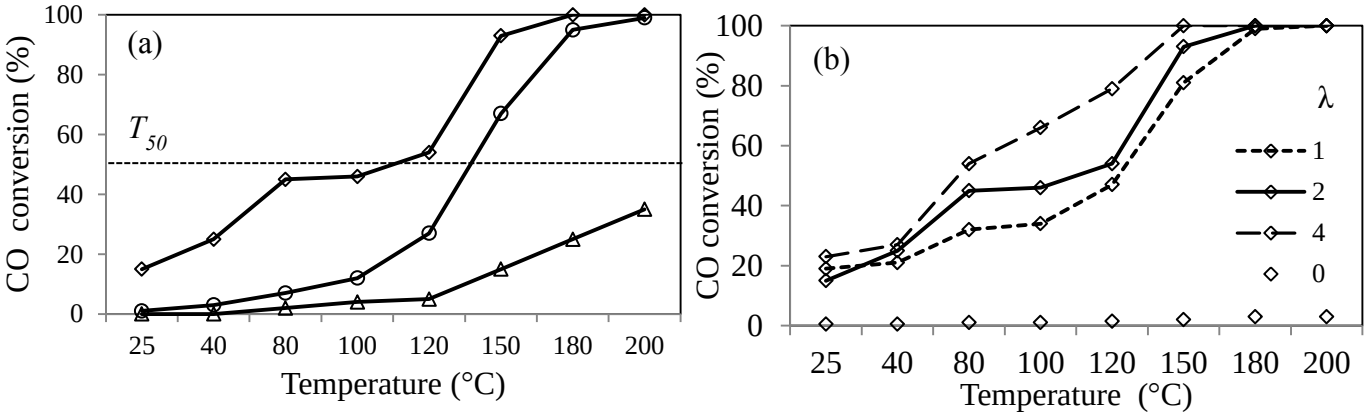

Figure 4.10 *(a) CO conversion as a function of temperature over Δ CeO_2, ○ 10%Co_3O_4/CeO_2 and ◊ $Ce_{0.90}Co_{0.10}O_{2-\delta}$ in TOX reaction (Conditions: λ = 2, GHSV = 12 000 h^{-1}). (b) CO conversion at different O_2/CO ratios over $Ce_{0.90}Co_{0.10}O_{2-\delta}$ in TOX reaction.*

In the feed composition with the O_2 proportion (λ=1) corresponding to the stoichiometric amount needed to convert all the CO (1 vol%), it would be expected that O_2 gets depleted at the point of complete CO oxidation. Notably, although the O_2 conversion is proportional to CO conversion, it is always in the range of 91- 93 % at the point of complete CO conversion. With this in mind, TOX experiments were also conducted in the absence of feed O_2 (λ = 0) to examine the possibility of the involvement of the lattice oxygen in CO oxidation. In the absence of feed oxygen, CO does get converted to CO_2 although the CO conversions are low (Figure 4.10 (b)). This observation suggests that CO gets oxidized through direct reaction

with the activated lattice oxygen. Such a catalytic property is consistent with a dual site mechanism that has been proposed for the oxidation of *n*-octane over the same catalyst [53]. A proposed mechanism of CO oxidation on the structure of $Ce_{0.90}Co_{0.10}O_{2-\delta}$ is adopted from the mechanism of CO oxidation over $Ce_{1-x}Pt_xO_{2-\delta}$ [50, 82] and that of *n*-octane on $Ce_{0.90}Co_{0.10}O_{2-\delta}$ [53], which is depicted in Figure 4.11. The high activity of the cobalt substituted ceria catalyst in CO oxidation can be explained based on a well-known phenomenon of the development of oxide ion vacancies when transition metals are incorporated into a ceria or titania matrix [16]. During CO oxidation over $Ce_{0.90}Co_{0.10}O_{2-\delta}$, CO adsorbs on Co ions and O_2 occupies oxide ion vacant sites generated upon the formation of a solid-solution. The mobility of activated lattice oxygen is assisted by the strong electronic interaction between cobalt and cerium. After the formation of CO_2, the feed oxygen fills the vacant sites for the next catalytic cycle. Therefore, CO oxidation over cobalt substituted ceria catalyst follows a Mars-van Krevelen (MvK) type mechanism, which is a widely accepted pathway for ceria-based oxide catalysts [20]. The reaction progression relies on a continuous supply of feed O_2 as inherent oxygen contributes marginally and would eventually get depleted.

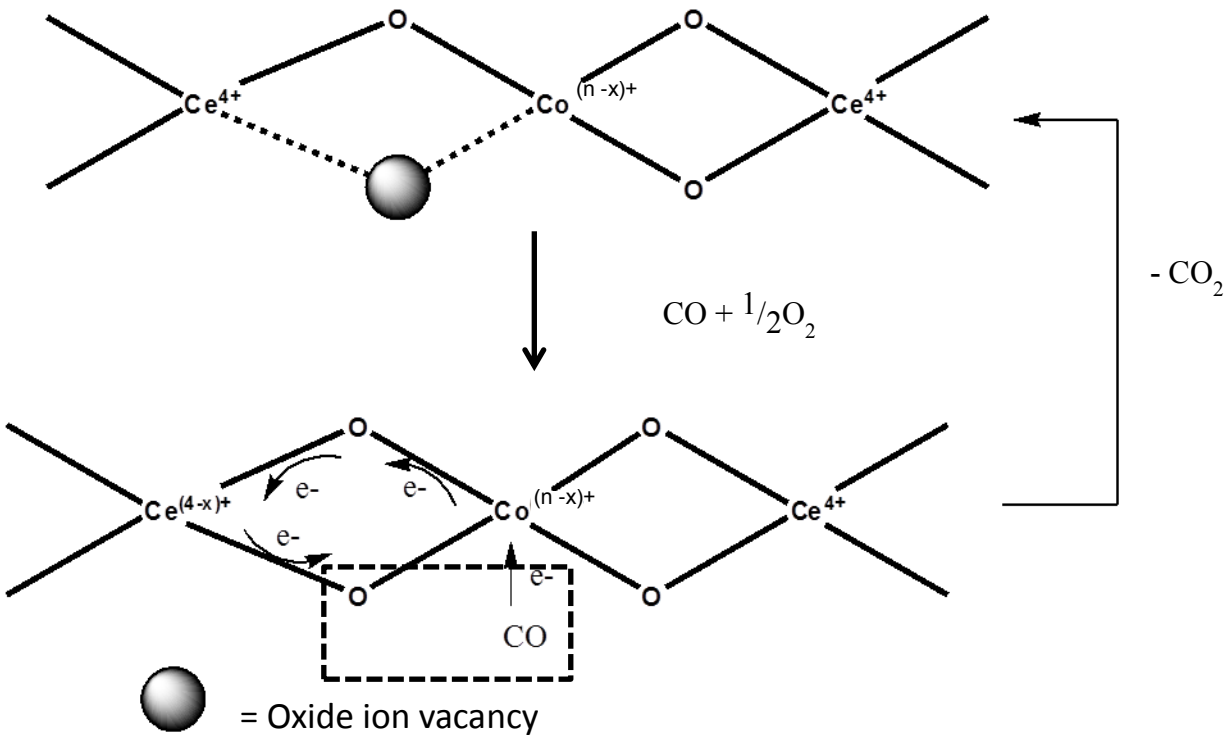

Figure 4.11 *Schematic/ mechanistic representation of CO oxidation over $Ce_{0.9}Co_{0.1}0O_{2-\delta}$. n = 3 or 2.*

As shown in Figure 4.10 (b), the minimum temperature for complete CO oxidation decreases with increasing the proportion of O_2 in the feed: 180 °C for λ=1 or 2 and 150 °C for λ= 4. At reaction temperatures below 30 °C, the performance of the catalyst is similar regardless of the O_2/CO ratio. Under such conditions, adsorbed surface oxygen species act as the main oxidants [83]. When the GHSV is lowered, complete CO oxidation is reached at even lower temperatures: 150 °C for 12 000 h^{-1}, 180 °C for 24 000 h^{-1} and 48 000 h^{-1}, if the λ factor is kept at 4 (Figure 4.12). This trend can be attributed to the different residence times of the reactants.

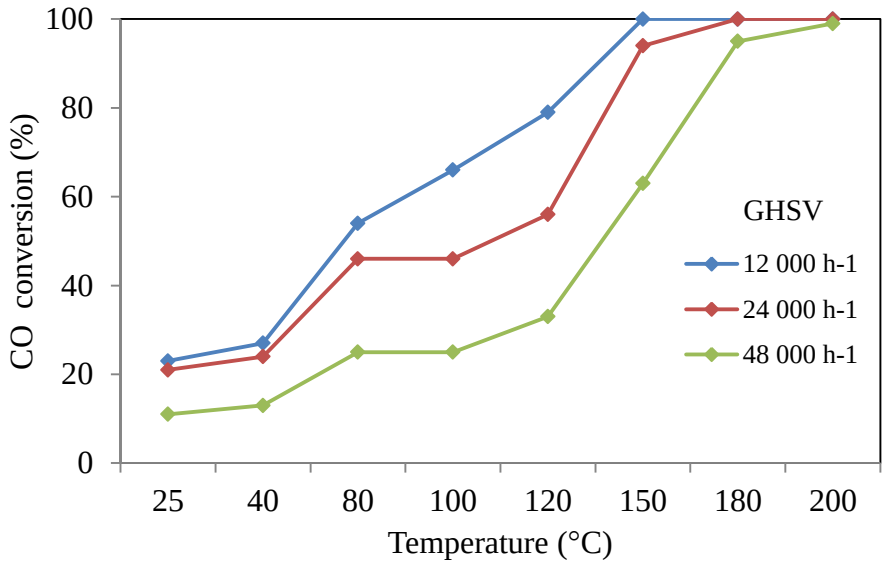

Figure 4.12 *CO conversion as a function of temperature at different gas hourly space velocities (12 000-48 000 h^{-1}). Gas composition: λ = 4.*

Preferential CO oxidation was studied under the same conditions as those employed for total CO oxidation, but with high hydrogen content (50 vol%). Similarly to total CO oxidation, CO conversion increases with increasing temperature (Figure 4.13). It must be underlined that no significant CO and O_2 conversions (≤ 10%) can be observed until 80 °C, regardless of the GHSV and/or O_2/CO ratio used. As observed for other reported PROX catalysts [84], the CO conversion in the presence of H_2 decreases in comparison with the CO conversion in the absence of H_2, under the same conditions. In the temperature range studied (25-250 °C), complete CO conversion is reached at ~200 °C, when a combination of excess oxygen content (λ = 4) and low GHSV (12 000 h^{-1}) is used. Under these experimental conditions, the

catalyst can maintain full CO conversion for a wider temperature window. However, this comes at an expense of compromising the selectivity (58%).

Regardless of the O_2/CO ratio and/or GHSV employed, the catalyst shows a stable selectivity, between 98 and 100 %, at reaction temperatures below 150 °C. This, however, does not suggest that the catalyst selectively adsorbs CO in a low temperature region. Unlike noble metal catalytic systems [11], most transition metal oxides are known to adsorb both CO and H_2 non-competitively [31]. Nonetheless, H_2 oxidation can only happen at high temperatures due to the higher required activation energy for this reaction [42]. Consequently, Figure 4.13 (b) confirms that the selectivity is not sensitive to the O_2/CO ratio at temperatures below 200 °C, even in the presence of excess O_2. For metal oxide catalysed PROX reactions, such a reaction profile is consistent with the operation of the Mars-van Krevelen pathway [35]. Although supported Co_3O_4 catalysts [85, 86] and other analogous catalysts [33, 34] have been reported to selectively oxidize CO to CO_2 in the presence of H_2, the maximum selectivity is not maintained for a wide temperature window. It is worth mentioning that well-known PROX catalysts start to experience a drop in selectivity at temperatures as low as 30 °C (for Au) and 100 °C (for Cu) [87].

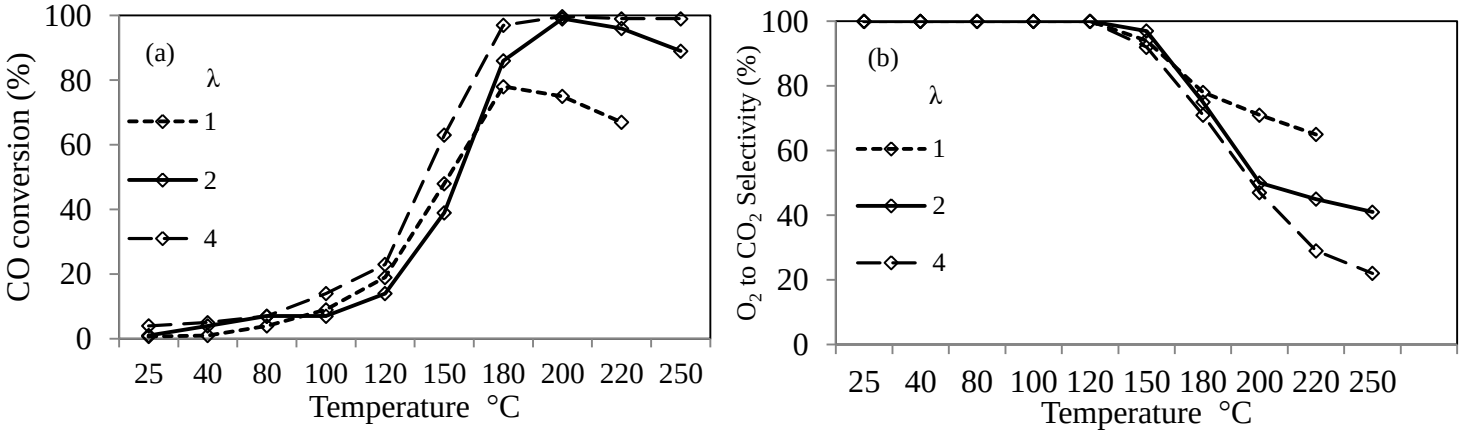

Figure 4.13 *(a) CO conversion and (b) selectivity as a function of temperature at different O_2/CO ratios over $Ce_{0.90}Co_{0.10}O_{2-\delta}$ in PROX reaction. Experimental conditions: λ = 1-4, GHSV = 12 000 h^{-1}.*

In summary, at temperatures above 100 °C, the conversion increases at the given temperature with the decrease in GHSV: 12 000 (97%) > 24 000 (85%) > 48 000 h^{-1} (63%) at 180 °C. On the other hand, at temperatures beyond 150 °C, selectivity at given temperatures can be

improved by increasing GHSV: 12 000 (71%) < 24 000 (76%) < 48 000 h^{-1} (84%) at 180 °C (Figure 4.14). Complete CO conversion and high selectivity by the studied catalyst, in PROX, can be achieved by manipulating GHSV and O_2 concentration.

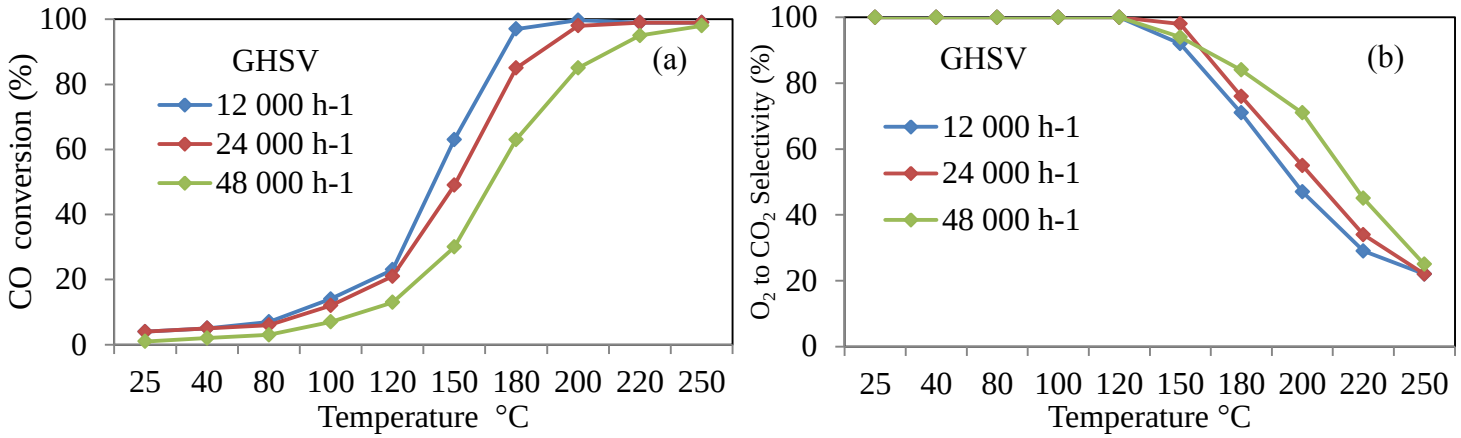

Figure 4.14 *(a) CO conversion and (b) selectivity as a function of temperature at different GHSV (12 000 – 48 000 h^{-1}) over $Ce_{0.90}Co_{0.10}O_{2-\delta}$ in PROX reaction. Experimental conditions: $\lambda = 4$.*

4.3.4.2 The promotional effect of Cu on the TOX and PROX activity of $Ce_{0.90}Co_{0.10}O_{2-\delta}$

The CuO/CeO_2 catalyst formulations are generally associated with improved oxygen mobility and optimized redox properties, which in turn promote oxidative catalysis [88]. In an attempt to improve the activity of $Ce_{0.90}Co_{0.10}O_{2-\delta}$ by possibly harnessing Ce-Co and Ce-Cu synergetic effects, Cu ion additives were incorporated to form bimetallic solid-solution catalysts, $Ce_{0.90-x}Cu_xCo_{0.10}O_{2-\delta}$ (where x = 0, 0.01, 0.03 and 0.05). Figure 4.15 shows the CO conversion during the TOX reaction over $Ce_{0.90-x}Cu_xCo_{0.10}O_{2-\delta}$ catalysts with varied Cu content. From this profile, as the Cu atomic loading increases from 0 to 3 at%, no significant improvement is observed. The temperatures for CO conversion of 50% are almost the same for $Ce_{0.90}Co_{0.10}O_{2-\delta}$ and $Ce_{0.87}Cu_{0.03}Co_{0.10}O_{2-\delta}$. Notably, $Ce_{0.85}Cu_{0.05}Co_{0.10}O_{2-\delta}$ displays the best catalytic performance among the bimetallic systems, with the lowest temperatures for 50% and complete CO conversion. It is noteworthy that the activity of this catalyst has a parallel relationship with its H_2-TPR profile, which shows low temperature reduction peaks as a result of easy reducibility. For a holistic evaluation, the catalytic activity of the catalyst that contains no cobalt ions, $Ce_{0.95}Cu_{0.05}O_{2-\delta}$, was also studied. Interestingly, this catalyst shows superior performance among all studied catalysts. This suggests that there is a close contact between Ce and Cu in the absence of cobalt. Since the XRD data confirmed the formation of a homogeneous solid-solution, it can be concluded that the interaction between

the two ions is enhanced, as revealed by easy reducibility. Based on the temperature values corresponding to 50 and 100% CO conversions (T_{50} and T_{100}), the activity follows the order: $Ce_{0.95}Cu_{0.05}O_{2-\delta}$ > $Ce_{0.85}Cu_{0.05}Co_{0.10}O_{2-\delta}$ > $Ce_{0.9}Co_{0.10}O_{2-\delta}$ ≈ $Ce_{0.87}Cu_{0.03}Co_{0.10}O_{2-\delta}$ > $Ce_{0.89}Cu_{0.01}Co_{0.10}O_{2-\delta}$.

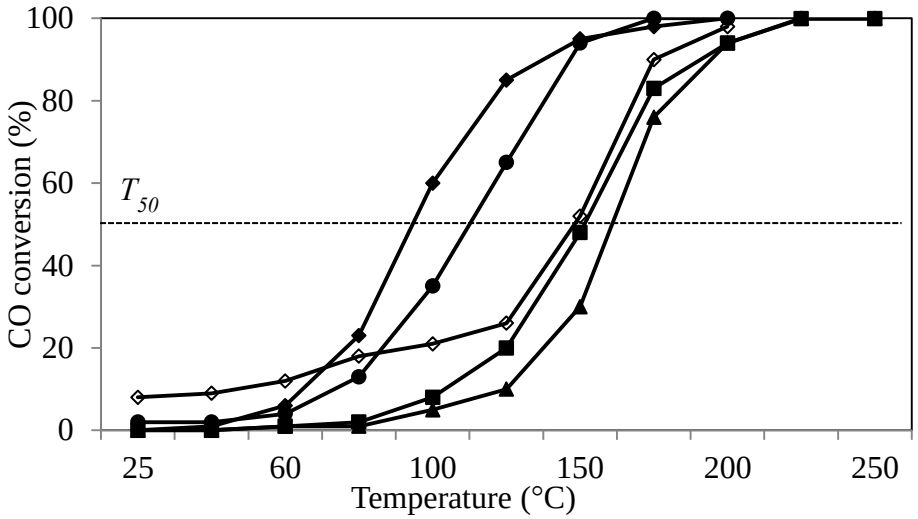

Figure 4.15 *CO conversion as a function of temperature over ceria-based catalysts in TOX reaction.* ◊ = $Ce_{0.9}Co_{0.10}O_{2-\delta}$, ▲ = $Ce_{0.89}Cu_{0.01}Co_{0.10}O_{2-\delta}$, ■ = $Ce_{0.87}Cu_{0.03}Co_{0.10}O_{2-\delta}$, ● = $Ce_{0.85}Cu_{0.05}Co_{0.10}O_{2-\delta}$ *and* ♦ = $Ce_{0.95}Cu_{0.05}O_{2-\delta}$*.Conditions:* $\lambda = 2$, *GHSV = 48 000* h^{-1}.

The catalytic performance of the bimetallic materials and their respective monometallic catalysts was also studied under PROX reaction conditions. CO conversion and O_2 selectivity, as a function of temperature, are shown in Figure 4.16. As depicted in Figure 4.16 (a), $Ce_{0.90}Co_{0.10}O_{2-\delta}$ displays the lowest catalytic activity and has a T_{50} value that is higher than 150 °C. Incorporating Cu ion additives results in bimetallic catalysts with improved catalytic activity. The CO conversion increases substantially with Cu loading increments, from 0 to 5 at%, which is indicative of the promotional effect by Cu ions. Similarly to total CO oxidation, $Ce_{0.85}Cu_{0.05}Co_{0.10}O_{2-\delta}$ displays superior catalytic performance relative to the other bimetallic analogues. For this catalyst, T_{50} and T_{100} temperatures are lower than those of other $Ce_{0.90-x}Cu_xCo_{0.10}O_{2-\delta}$ catalysts and very close to the values observed for $Ce_{0.95}Cu_{0.05}O_{2-\delta}$. As it can be seen from Figure 4.16(b), all studied catalysts are highly selective for CO oxidation, showing no sign of H_2 oxidation at temperatures below 150 °C.

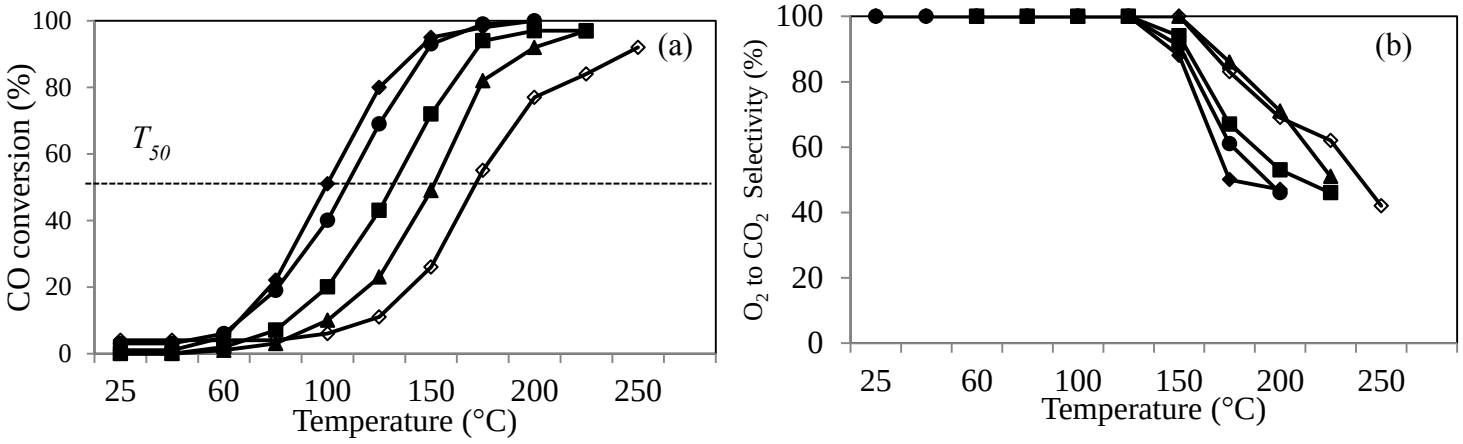

Figure 4.16 *(a) CO conversion and (b) selectivity as a function of temperature over ceria-based catalysts in PROX reaction. ◊ = $Ce_{0.9}Co_{0.10}O_{2-\delta}$, ▲ = $Ce_{0.89}Cu_{0.01}Co_{0.10}O_{2-\delta}$, ■ = $Ce_{0.87}Cu_{0.03}Co_{0.10}O_{2-\delta}$, ● = $Ce_{0.85}Cu_{0.05}Co_{0.10}O_{2-\delta}$ and ♦ = $Ce_{0.95}Cu_{0.05}O_{2-\delta}$. Experimental conditions: $\lambda = 2$, GHSV = 48 000 h^{-1}.*

Interestingly, the activity order of the catalysts in the H_2-rich environment ($Ce_{0.95}Cu_{0.05}O_{2-\delta} \approx Ce_{0.85}Cu_{0.05}Co_{0.10}O_{2-\delta} > Ce_{0.87}Cu_{0.03}Co_{0.10}O_{2-\delta} > Ce_{0.89}Cu_{0.01}Co_{0.10}O_{2-\delta} > Ce_{0.90}Co_{0.10}O_{2-\delta}$) is not similar to the trend observed for H_2-free experiments. To gain more understanding on the catalytic performance of the catalysts, the specific reaction rates were calculated at a reaction temperature of 150 °C, according to a reported method [8]. This reaction temperature is high enough to gain insight into the PROX reaction network. Since pure CeO_2 shows some minor activity at this temperature and above, the specific reaction rates are expressed as moles of CO converted per gram of the catalyst (not Co and/or Cu) and per second. Furthermore, the plots of specific rates with temperature were drawn using data points where CO conversion is below 30% (Figures 4.17(a) and 4.18(a)). The corresponding Arrhenius plots for CO oxidation are shown in Figure 4.17(b) and 4.18(b) and the activation energy values are summarized in Table 4.4.

For both TOX and PROX studies, all Cu-containing catalysts clearly do not show a decline in CO conversion in the presence of H_2, while the opposite is true for $Ce_{0.90}Co_{0.10}O_{2-\delta}$. Considering the 150 °C points, it is seen in Figure 4.19 that the activity of $Ce_{0.89}Cu_{0.01}Co_{0.10}O_{2-\delta}$ and $Ce_{0.87}Cu_{0.03}Co_{0.10}O_{2-\delta}$ is improved upon introducing H_2, with CO conversions increased from 30% to 49% and 48% to 72%, respectively. Accordingly, the specific reaction rates of these catalysts increase from 1.04×10^{-4} to 1.70×10^{-4} $mol.g^{-1}.s^{-1}$ for the former and from 1.67×10^{-4} to 2.50×10^{-4} $mol.g^{-1}.s^{-1}$ for the latter. In contrast, CO

conversion over $Ce_{0.90}Co_{0.10}O_{2-\delta}$ decreases by half in the H_2-rich stream, with respective specific rates of 1.81 x 10^{-4} and 9.03 x 10^{-5} $mol.g^{-1}.s^{-1}$ in TOX and PROX experiments. The performance of $Ce_{0.85}Cu_{0.05}Co_{0.10}O_{2-\delta}$ and $Ce_{0.95}Cu_{0.05}O_{2-\delta}$ appears comparable and unaffected by the absence or presence of H_2.

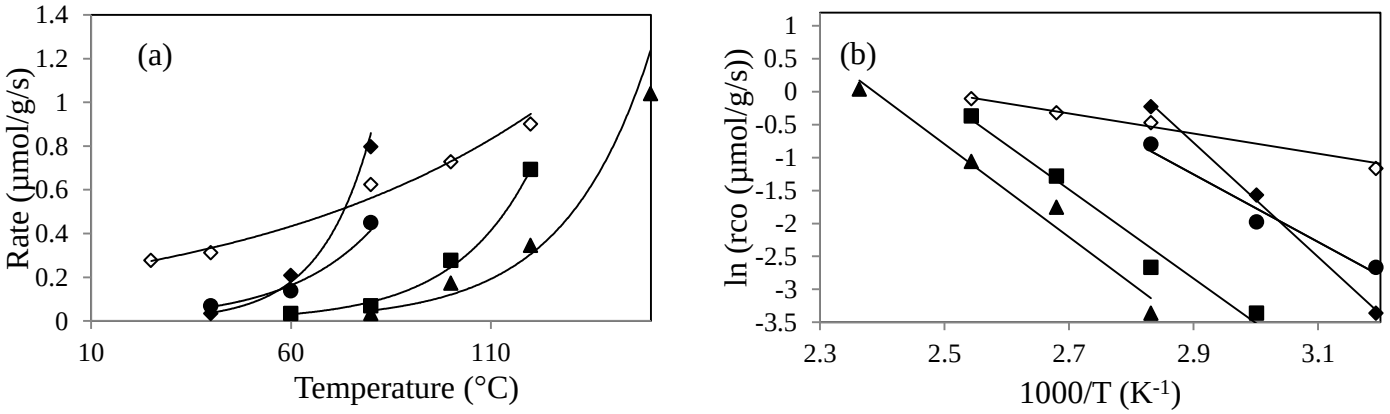

Figure 4.17 *(a) Rate of the reaction as a function of temperature and (b) Arrhenius plots for TOX studies.* ◊ = $Ce_{0.9}Co_{0.10}O_{2-\delta}$, ▲ = $Ce_{0.89}Cu_{0.01}Co_{0.10}O_{2-\delta}$, ■ = $Ce_{0.87}Cu_{0.03}Co_{0.10}O_{2-\delta}$, ● = $Ce_{0.85}Cu_{0.05}Co_{0.10}O_{2-\delta}$ *and* ♦ = $Ce_{0.95}Cu_{0.05}O_{2-\delta}$.

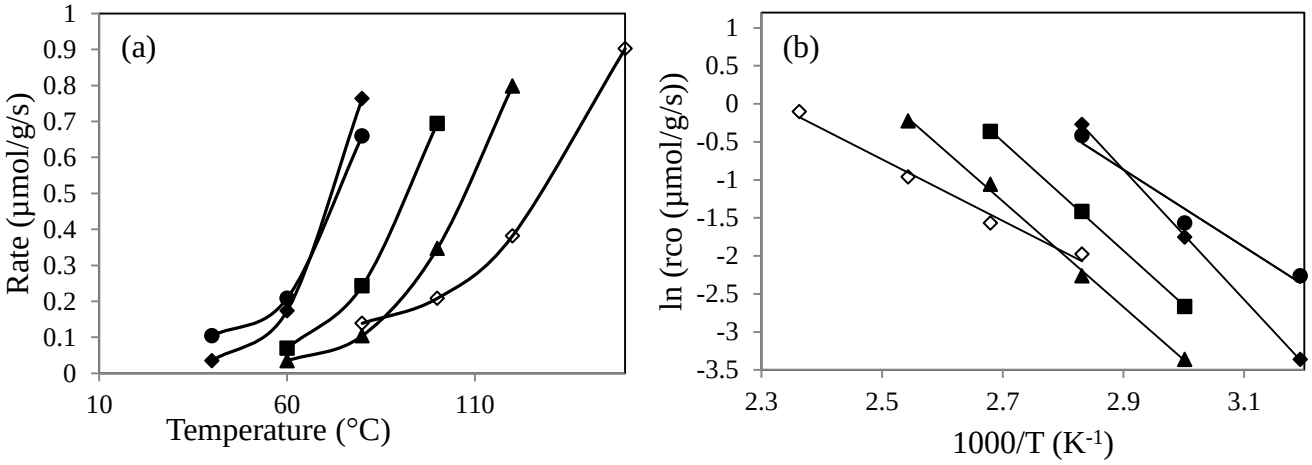

Figure 4.18 *(a) Rate of the reaction as a function of temperature and (b) Arrhenius plots for CO-PROX studies.* ◊ = $Ce_{0.9}Co_{0.10}O_{2-\delta}$, ▲ = $Ce_{0.89}Cu_{0.01}Co_{0.10}O_{2-\delta}$, ■ = $Ce_{0.87}Cu_{0.03}Co_{0.10}O_{2-\delta}$, ● = $Ce_{0.85}Cu_{0.05}Co_{0.10}O_{2-\delta}$ *and* ♦ = $Ce_{0.95}Cu_{0.05}O_{2-\delta}$.

It is shown in Figure 4.19 that $Ce_{0.90}Co_{0.10}O_{2-\delta}$ maintains its oxygen selectivity to CO_2 at 100 % and the O_2 consumption does not increase in the presence of H_2. Instead the O_2 conversion decreases, which indicates that the decrease in CO conversion is not associated with O_2 consumption by the undesirable H_2 oxidation reaction. These results suggest that, over $Ce_{0.90}Co_{0.10}O_{2-\delta}$, the H_2 interacts with the same active sites where CO oxidation occurs,

leading to a decrease in CO conversion [43]. This is reflected in the increase in activation energy for CO oxidation in the presence of H_2, from 13 to 34 kJ/mol. Similar results have been reported for CO oxidation over bulk Co_3O_4 [89]. The fact that the CO oxidation over Cu-containing catalysts is not adversely affected by the presence of H_2 supports the proposition that H_2 and CO oxidation reactions occur on independent sites on such catalysts [9, 90]. Consequently, the calculated activation energies of these catalysts are almost the same for both TOX and PROX (Table 4.4). In the case of $Ce_{0.89}Cu_{0.01}Co_{0.10}O_{2-\delta}$ and $Ce_{0.87}Cu_{0.03}Co_{0.10}O_{2-\delta}$, the improved CO conversion under reducing conditions may be due to the existence of reduced Ce and Cu species (Ce^{3+}, Cu^{+}) which have been reported to facilitate CO oxidation [7, 91]. The presence of Ce^{3+} species is evident from the Ce(3d) XPS of the pre-reduced sample. The reaction profiles show that most of the O_2 consumption over Cu-containing catalysts is associated with the CO oxidation reaction and a minimal portion is consumed through the H_2 oxidation reaction, as revealed by high O_2 to CO_2 selectivity. However, H_2O formation becomes more pronounced at temperatures exceeding 180 °C, leading to high O_2 conversion. The superior catalytic behaviour of Cu-containing samples in PROX correlate well with the H_2-TPR profiles. The reducibility of the catalysts is improved as the Cu loading is increased, suggesting the possible strong interaction between Cu and Ce which in turn promotes oxygen mobility in the catalysts.

Table 4.4 *Comparison of specific rates and activation energies under TOX and PROX*

Catalyst	Specific rate at 150 °C ($mol.g^{-1}.s^{-1}$) $x10^{-4}$		Activation energy (kJ/mol)	
	TOX	PROX	TOX	PROX
$Ce_{0.90}Co_{0.10}O_{2-\delta}$	1.81	0.90	13	34
$Ce_{0.89}Co_{0.10}\ Cu_{0.01}O_{2-\delta}$	1.04	1.70	59	58
$Ce_{0.87}Co_{0.10}\ Cu_{0.03}O_{2-\delta}$	1.67	2.50	56	60
$Ce_{0.85}Co_{0.10}\ Cu_{0.05}O_{2-\delta}$	3.26	3.23	43	42
$Ce_{0.95}Cu_{0.05}O_{2-\delta}$	3.30	3.30	72	71

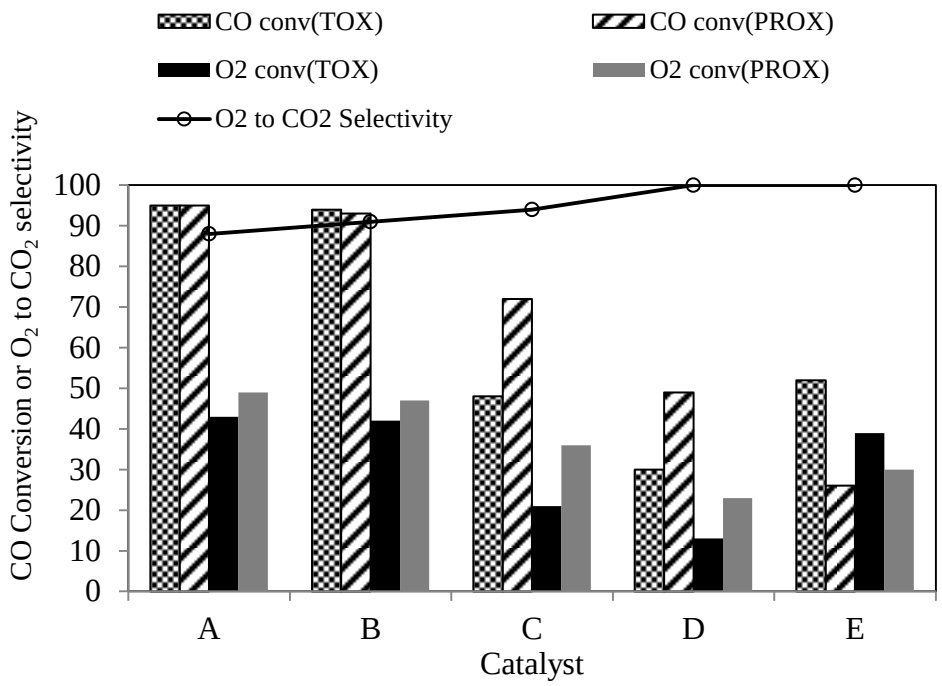

Figure 4.19 *Comparison of catalytic activities of A: $Ce_{0.95}Cu_{0.05}O_{2-\delta}$, B: $Ce_{0.85}Cu_{0.05}Co_{0.10}O_{2-\delta}$, C: $Ce_{0.87}Cu_{0.03}Co_{0.10}O_{2-\delta}$, D: $Ce_{0.89}Cu_{0.01}Co_{0.10}O_{2-\delta}$ and E: $Ce_{0.9}Co_{0.10}O_{2-\delta}$. Conditions: temperature = 150 °C, 48 000 h^{-1}, λ = 2.*

4.3.4.3 Stability of the prepared catalysts and the effect of H_2O and CO_2

The stability of the Co-based catalysts in a reducing environment has been cited as a concern due to reduction of Co to a lower valence state which is not active for CO oxidation [30, 92]. Taking this into account, the stability of the catalysts was evaluated in the presence and absence of CO_2 and/or H_2O. Figure 4.20 shows that all catalysts are quite stable under PROX conditions, showing no significant loss in activity and unchanged selectivity (≥ 50%) within the studied time-on-stream (24 h). This suggests that the active components of the catalysts do not get transformed to inactive species under present experimental conditions. Interestingly, at the reaction temperature of 180 °C, where time-on-stream experiments were conducted, selectivity values of $Ce_{0.95}Cu_{0.05}O_{2-\delta}$ (50%), $Ce_{0.85}Cu_{0.05}Co_{0.10}O_{2-\delta}$ (63%) and $Ce_{0.87}Cu_{0.03}Co_{0.10}O_{2-\delta}$ (72%) are not comparable, although their CO conversion values are within ±5%. The exact CO conversions observed over these respective catalysts are 96, 95 and 92%. This possibly signals the involvement of different active sites over Cu and Co-Cu catalysts.

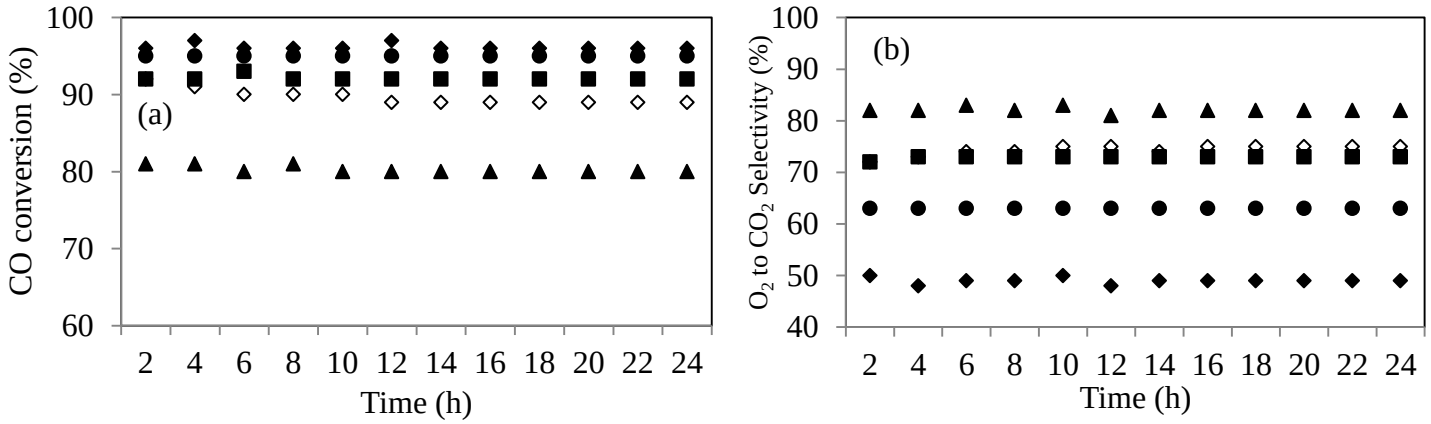

Figure 4.20 *Time-on-stream (a) CO conversion and (b) selectivity on ceria-based catalysts at 180 °C in dry PROX reaction. ◊ = $Ce_{0.9}Co_{0.10}O_{2-\delta}$, ▲ = $Ce_{0.89}Cu_{0.01}Co_{0.10}O_{2-\delta}$, ■ = $Ce_{0.87}Cu_{0.03}Co_{0.10}O_{2-\delta}$, ● = $Ce_{0.85}Cu_{0.05}Co_{0.10}O_{2-\delta}$ and ♦ = $Ce_{0.95}Cu_{0.05}O_{2-\delta}$. Experimental conditions: λ = 2, GHSV = 12 000 h^{-1} for $Ce_{0.9}Co_{0.10}O_{2-\delta}$ and 48 000 h^{-1} for all other catalysts.*

Although the PROX studies conducted with only CO, H_2 and O_2 provide valuable understanding of the catalyst performance, it is necessary to evaluate catalytic behaviour in the presence of H_2O and CO_2, since these components are contained in H_2-rich gas obtained from steam reforming. Hence, the stability of the catalysts was also investigated in the presence of 7 vol% H_2O and 15 vol% CO_2, using the aforementioned conditions, with varied N_2 levels to compensate for the introduction of H_2O and CO_2.

As shown in Figures 4.21 and 4.22, the introduction of H_2O and/or CO_2 has a negative effect in the catalytic activity of the Co-based and bimetallic catalysts. The extent of deactivation in the presence of CO_2 appears to be higher for the $Ce_{0.9}Co_{0.10}O_{2-\delta}$ catalyst compared to its bimetallic analogues. In the presence of 15 vol% CO_2, CO conversion over $Ce_{0.90}Co_{0.10}O_{2-\delta}$ decreases from 90% to 32%, although the selectivity is slightly improved from 72% to 80%. Under the same reaction conditions, CO conversion drops from 81 to 62%, 92 to 79% and 95 to 90% over $Ce_{0.89}Cu_{0.01}Co_{0.10}O_{2-\delta}$, $Ce_{0.87}Cu_{0.03}Co_{0.10}O_{2-\delta}$ and $Ce_{0.85}Cu_{0.05}Co_{0.10}O_{2-\delta}$, respectively. Notably, the negative effect associated with the presence of CO_2 is moderate for Co-Cu catalysts and becomes less as Cu content is increased. However, the deactivation related to the introduction of 7 vol% H_2O (in the absence of CO_2) is more pronounced relative to that induced by CO_2 on the Co-Cu catalysts. In contrast, water is less detrimental, compared to CO_2, on the activity of $Ce_{0.9}Co_{0.10}O_{2-\delta}$. The PROX activity and corresponding selectivity of the investigated catalysts under the different gas compositions are summarized in Table 4.5.

Table 4.5 *PROX activity and selectivity of investigated catalysts under different gas mixtures.*

Catalyst	CO conversion and selectivity at 180 °C [a]			
	H_2O/CO_2-free	15 vol% CO_2	7 vol% H_2O	15 vol% CO_2 and 7 vol% H_2O
$Ce_{0.90}Co_{0.10}O_{2-\delta}$	90 (72)	32 (80)	50 (85)	13 (77)
$Ce_{0.89}Co_{0.10}Cu_{0.01}O_{2-\delta}$	81 (82)	62 (86)	43 (95)	18 (96)
$Ce_{0.87}Co_{0.10}Cu_{0.03}O_{2-\delta}$	92 (72)	79 (80)	52 (83)	31 (92)
$Ce_{0.85}Co_{0.10}Cu_{0.05}O_{2-\delta}$	95 (63)	90 (72)	79 (80)	36 (86)
$Ce_{0.95}Cu_{0.05}O_{2-\delta}$	96 (50)	93 (56)	95 (65)	86 (75)

[a] The values outside and inside brackets represent conversion and selectivity, respectively.

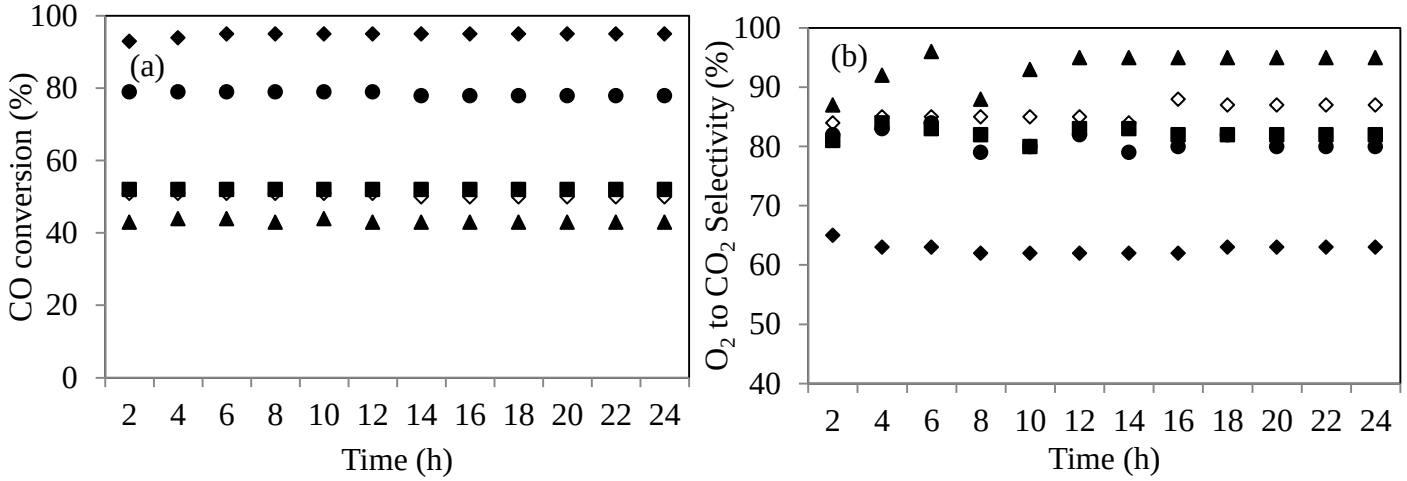

Figure 4.21 *Time-on-stream (a) CO conversion and (b) selectivity on ceria-based catalysts at 180 °C in the presence of 7 vol% H_2O. ◊ = $Ce_{0.9}Co_{0.10}O_{2-\delta}$, ▲ = $Ce_{0.89}Cu_{0.01}Co_{0.10}O_{2-\delta}$, ■ = $Ce_{0.87}Cu_{0.03}Co_{0.10}O_{2-\delta}$, ● = $Ce_{0.85}Cu_{0.05}Co_{0.10}O_{2-\delta}$ and ♦ = $Ce_{0.95}Cu_{0.05}O_{2-\delta}$. Experimental conditions: λ = 2, GHSV = 12 000 h^{-1} for $Ce_{0.9}Co_{0.10}O_{2-\delta}$ and 48 000 h^{-1} for all the other catalysts.*

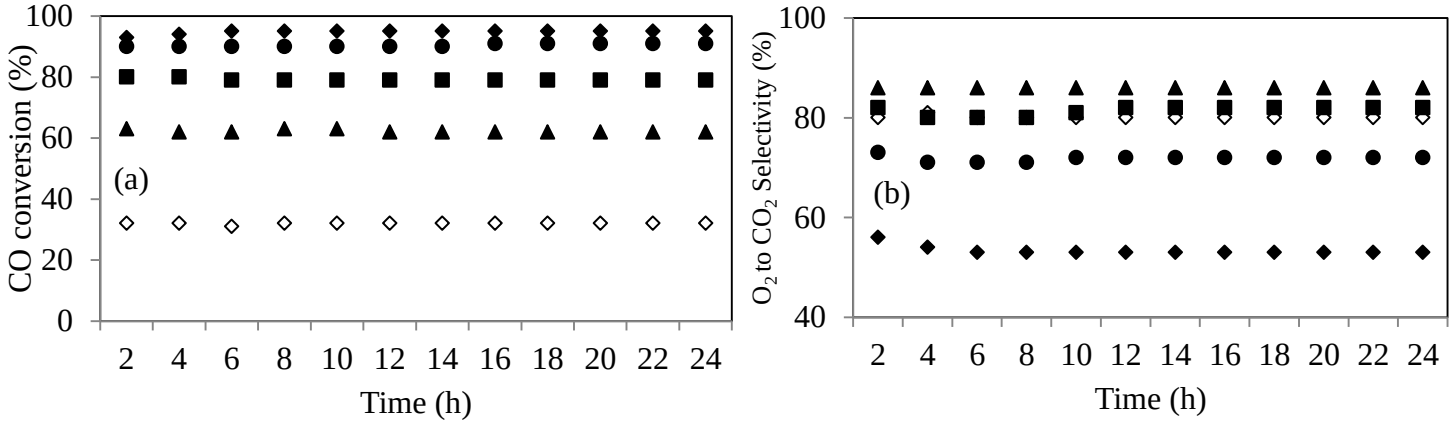

Figure 4.22 *Time-on-stream (a) CO conversion and (b) selectivity on ceria-based catalysts at 180 °C in the presence of 15 vol% CO_2. ◊ = $Ce_{0.9}Co_{0.10}O_{2-\delta}$, ▲ = $Ce_{0.89}Cu_{0.01}Co_{0.10}O_{2-\delta}$, ■ = $Ce_{0.87}Cu_{0.03}Co_{0.10}O_{2-\delta}$, ● = $Ce_{0.85}Cu_{0.05}Co_{0.10}O_{2-\delta}$ and ♦ = $Ce_{0.95}Cu_{0.05}O_{2-\delta}$. Experimental conditions: λ = 2, GHSV = 12 000 h^{-1} for $Ce_{0.9}Co_{0.10}O_{2-\delta}$ and 48 000 h^{-1} for all the other catalysts.*

The addition of both CO_2 and H_2O result in degeneration of the catalytic performance of these catalysts (Figure 4.23). From Figures 4.21, 4.22 and 4.23, it is clear that the degree of deactivation is reduced as the amount of Cu present in the catalyst is increased. Under these reaction conditions, $Ce_{0.9}Co_{0.10}O_{2-\delta}$ only reached CO conversion of 13%. As Cu content of 1, 3 and 5 at% is incorporated, the CO conversion is improved to 18, 31 and 36%. This suggests that the Cu active sites do not greatly change in the presence of either H_2O and/or CO_2. Accordingly, the activity of $Ce_{0.95}Cu_{0.05}O_{2-\delta}$ is not significantly affected by the presence of H_2O and/or CO_2. In the presence of both 7 vol% H_2O and 15 vol% CO_2, this catalyst achieved 86% CO conversion and 75% selectivity. It is noteworthy that all the catalysts can fully retain their performance by switching to a H_2O/CO_2-free feed, which shows that the deactivation is reversible.

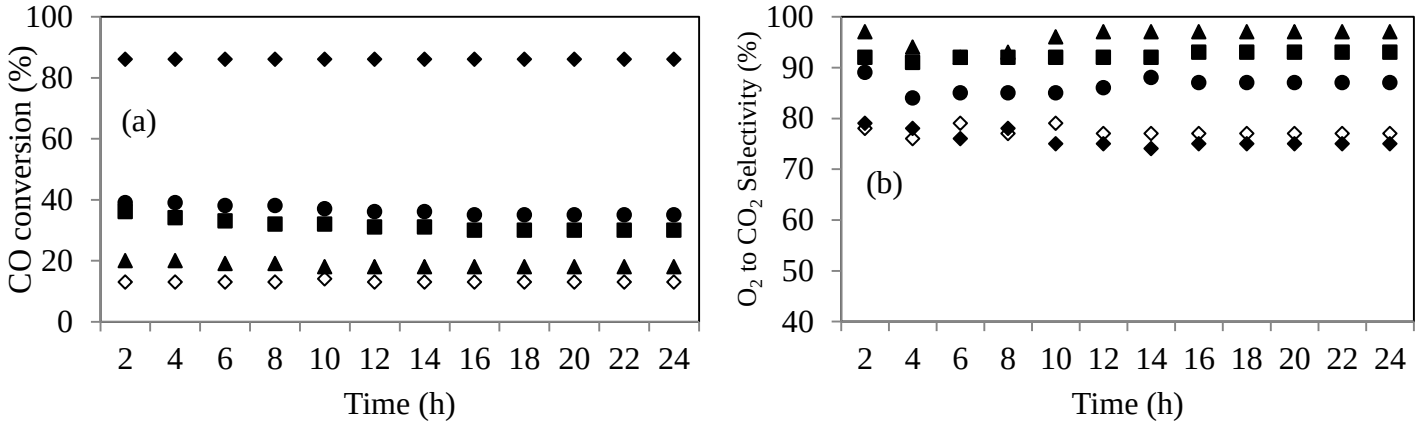

Figure 4.23 *Time-on-stream (a) CO conversion and (b) selectivity on ceria-based catalysts at 180 °C in the presence of 7 vol% H_2O and 15 vol% CO_2. ◊ = $Ce_{0.9}Co_{0.10}O_{2-\delta}$, ▲ = $Ce_{0.89}Cu_{0.01}Co_{0.10}O_{2-\delta}$, ■ = $Ce_{0.87}Cu_{0.03}Co_{0.10}O_{2-\delta}$, ● = $Ce_{0.85}Cu_{0.05}Co_{0.10}O_{2-\delta}$ and ♦ = $Ce_{0.95}Cu_{0.05}O_{2-\delta}$. Experimental conditions: λ = 2, GHSV = 12 000 h^{-1} for $Ce_{0.9}Co_{0.10}O_{2-\delta}$ and 48 000 h^{-1} for all other catalysts.*

In the presence of CO_2 and/or H_2O, the selectivity of O_2 to CO_2 is improved for all studied materials, monometallic and bimetallic catalysts. This observation is accompanied by a decrease in H_2 consumption. Such results confirm that a decrease in CO conversion under these conditions is not caused by the reverse water gas shit reaction (RWG: $CO_2 + H_2 \rightarrow CO + H_2O$). Consistently, the reactions performed using a feed of 15 vol% CO_2 and 50 vol% H_2 showed neither H_2 nor CO_2 conversion, ruling out the occurrence of a reverse water gas shift or methanation reactions. The deactivation behaviour brought about the presence of H_2O can be ascribed to the adsorption of water on the catalyst surface, leading to a blockage of the active sites. The formation of a CO-H_2O complex has also been suggested as the possible

explanation for deterred activity of such catalysts under similar conditions [93, 94]. The negative effect of introducing CO_2 into the feed can be attributed to the competitive adsorption, between CO and CO_2, at the active sites. Since the only active sites for CO oxidation appear to be Co^{2+} ions in $Ce_{0.90}Co_{0.10}O_{2-\delta}$, the effect of CO_2 and/or H_2O is more pronounced due to the disturbance of the redox circle depicted in the proposed mechanism (Figure 4.11) [93, 94].

4.4 Conclusion

In this work, $Ce_{0.90}Co_{0.10}O_{2-\delta}$ and $Ce_{0.90-x}Cu_xCo_{0.10}O_{2-\delta}$ (x = 0.01, 0.03 and 0.05) catalysts were synthesized using a urea-assisted combustion method and evaluated for total and preferential CO oxidation. Based on characterization results, the resulting catalysts are single-phase nanocrystalline materials with a fluorite structure. Minor oxide segregation was only detected when the metal ion content exceeded 13% atomic loading. The results showed that the activity of $Ce_{0.90}Co_{0.10}O_{2-\delta}$ could be significantly enhanced by the addition of Cu, for TOX and PROX. The improvement in the activity has a direct relationship with the boosted reducibility, which could be linked to better oxygen mobility due to Ce-Cu interactions. All catalysts are stable, highly selective and able to achieve complete CO conversion under different reaction conditions, depending on O_2/CO ratio and GHSV.

The presence of H_2 appears to have a negative effect on the CO conversion over $Ce_{0.90}Co_{0.10}O_{2-\delta}$, suggesting that CO and H_2 oxidation reactions may be occurring at the same active sites. On the other hand, Cu-containing catalysts do not experience a drop in CO conversion in the presence of H_2, signalling that H_2 and CO conversion may be taking place at independent sites. For bimetallic, Co-Cu, catalysts it is assumed that CO oxidation predominantly takes place on the Cu site, while H_2 oxidation mainly occurs on the Co site. Co-containing catalysts were found to have a low tolerance for CO_2 and H_2O due to competitive adsorption and blockage of the active sites. However, the CO_2/H_2O tolerance improves with increasing Cu loading.

4.5 Acknowledgements

The authors gratefully acknowledge the Department of Science and Technology (DST) and Mintek (Advanced Metals Initiative Program) for financial support. Thanks are also due to the Catalysis Research Group members for valuable discussions.

References

[1] Y. Wang, K.S. Chen, J. Mishler, S.C. Cho, X.C. Adroher, Appl. Energy 88 (2011) 981-1007.

[2] G. Hoogers, Fuel Cell Technology Handbook, CRC Press LLC, Boca Raton, Florida, 2003.

[3] G. Hoogers, in: G. Hoogers (Ed.), Fuel Cell Technology Handbook, CRC Press LLC, Boca Raton, Florida, 2003, pp. 5/1-5/23.

[4] D. Thompsett, in: G. Hoogers (Ed.), Fuel Cell Technology Handbook, CRC Press LLC, Boca Raton, Florida, 2003, pp. 6/1- 6/22.

[5] A. Mishra, R. Prasad, Bull. Chem. React. Eng. Catal. 6 (2011) 1-14.

[6] G. Avgouropoulos, T. Ioannides, Appl. Catal., A 244 (2003) 155-167.

[7] Z. Zhao, X. Lin, R. Jin, Y. Dai, G. Wang, Catal. Sci. Technol. 2 (2012) 554-563.

[8] T.A. Zepeda, A. Martinez-Hernandez, R. Guil-Lopez, B. Pawelec, Appl. Catal., B 100 (2010) 450-462.

[9] M.M. Schubert, M.J. Kahlich, H.A. Gasteiger, R.J. Behm, J. Power Sources 84 (1999) 175-182.

[10] J.G.E. Cohn, Carbon monoxide removal from hydrogen-containing gases, Engelhard Industries, Inc. . 1965, p. 3 pp.

[11] K. Liu, A. Wang, T. Zhang, ACS Catalysis 2 (2012) 1165-1178.

[12] A. Trovarelli, P. Fornasiero, Editors, Catalysis by Ceria and Related Materials, 2nd Edition, Imperial College Press ; Distributed by World Scientific, London, 2013.

[13] D. Duprez, C. Descorme, in: A. Trovarelli (Ed.), Catalysis by Ceria and Related Materials, 2nd ed., Imperial College Press ; Distributed by World Scientific, London, 2013, pp. 243-280.

[14] M. Shelef, G.W. Graham, R.W. McCabe, in: A. Trovarelli (Ed.), Catalysis by Ceria and Related Materials, Imperial College Press ; Distributed by World Scientific, Landon, 2013, pp. 343-375.

[15] R.J. Gorte, AlChE J. 56 1126-1135.

[16] M.S. Hegde, G. Madras, K.C. Patil, Acc. Chem. Res. 42 (2009) 704-712.

[17] M. Primet, E. Garbowski, in: A. Trovarelli (Ed.), Catalysis by Ceria and Related Materials, 2nd ed., Imperial College Press ; Distributed by World Scientific, London, 2013, pp. 407-429.

[18] S. Imamura, in: A. Trovarelli (Ed.), Catalysis by Ceria and Related Materials, 2nd ed., Imperial College Press ; Distributed by World Scientific, London, 2013, pp. 431-452.
[19] K.C. Patil, M.S. Hegde, T. Rattan, S.T. Aruna, Chemistry of Nanocrystalline Oxide Materials, World Scientific Publishing, Singapore, 2008, pp. 117-153.
[20] J. Beckers, G. Rothenberg, Green Chem. 12 (2010) 939-948.
[21] A. Martínez-Arias, A.B. Hungría, G. Munuera, D. Gamarra, Appl. Catal., B 65 (2006) 207-216.
[22] A. Gómez-Cortés, Y. Márquez, J. Arenas-Alatorre, G. Díaz, Catal. Today 133–135 (2008) 743-749.
[23] M. Kang, M. Song, K. Kim, React. Kinet. Catal. Lett. 79 (2003) 3-10.
[24] T. Tabakova, M. Manzoli, F. Vindigni, V. Idakiev, F. Boccuzzi, J. Phys. Chem. A 114 (2009) 3909-3915.
[25] M. Han, X. Wang, Y. Shen, C. Tang, G. Li, R.L. Smith, J. Phys. Chem. C 114 (2009) 793-798.
[26] S.K. Meher, M. Cargnello, H. Troiani, T. Montini, G.R. Rao, P. Fornasiero, Appl. Catal., B 130–131 (2013) 121-131.
[27] R.V. Gulyaev, A.I. Stadnichenko, E.M. Slavinskaya, A.S. Ivanova, S.V. Koscheev, A.I. Boronin, Appl. Catal., A 439–440 (2012) 41-50.
[28] W. Liu, M. Flytzanistephanopoulos, J. Catal. 153 (1995) 304-316.
[29] W. Liu, M. Flytzanistephanopoulos, J. Catal. 153 (1995) 317-332.
[30] Y. Teng, H. Sakurai, A. Ueda, T. Kobayashi, Int. J. Hydrogen Energy 24 (1999) 355-358.
[31] S. Royer, D. Duprez, ChemCatChem 3 (2011) 24-65.
[32] H.-K. Lin, H.-C. Chiu, H.-C. Tsai, S.-H. Chien, C.-B. Wang, Catal. Lett. 88 (2003) 169-174.
[33] A.A. Firsova, A.N. Il'ichev, T.I. Khomenko, L.V. Gorobinskii, Y.V. Maksimov, I.P. Suzdalev, V.N. Korchak, Kinet. Catal. 48 (2007) 282-291.
[34] A.A. Firsova, T.I. Khomenko, A.N. Il'ichev, V.N. Korchak, Kinet. Catal. 49 (2008) 682-691.
[35] G. Sedmak, S. Hočevar, J. Levec, J. Catal. 222 (2004) 87-99.
[36] G.G. Jernigan, G.A. Somorjai, J. Catal. 147 (1994) 567-577.
[37] Y.-F.Y. Yao, J. Catal. 33 (1974) 108-122.
[38] K. Omata, Y. Kobayashi, M. Yamada, Catal. Commun. 6 (2005) 563-567.
[39] W.-H. Yang, M.H. Kim, S.-W. Ham, Catal. Today 123 (2007) 94-103.

[40] T. Bao, Z. Zhao, Y. Dai, X. Lin, R. Jin, G. Wang, T. Muhammad, Appl. Catal., B 119–120 (2012) 62-73.

[41] D. Perti, R.L. Kabel, AlChE J. 31 (1985) 1420-1426.

[42] P. Gawade, B. Bayram, A.-M.C. Alexander, U.S. Ozkan, Appl. Catal., B 128 (2012) 21-30.

[43] M.P. Woods, P. Gawade, B. Tan, U.S. Ozkan, Appl. Catal., B 97 (2010) 28-35.

[44] L.F. Liotta, G. Di Carlo, G. Pantaleo, A.M. Venezia, G. Deganello, Appl. Catal., B 66 (2006) 217-227.

[45] J. Jansson, A.E.C. Palmqvist, E. Fridell, M. Skoglundh, L. Österlund, P. Thormählen, V. Langer, J. Catal. 211 (2002) 387-397.

[46] Z. Zhao, R. Jin, T. Bao, H. Yang, X. Lin, G. Wang, Int. J. Hydrogen Energy 37 (2012) 4774-4786.

[47] M.S.M. Hegde, GiridharI; Patil, K. C. , Acc. Chem. Res. 42 (2008) 704-712.

[48] L.F. Liotta, G. Di Carlo, G. Pantaleo, G. Deganello, Appl. Catal., B 70 (2007) 314-322.

[49] L.F. Liotta, G. Di Carlo, G. Pantaleo, G. Deganello, Catal. Commun. 6 (2005) 329-336.

[50] P. Bera, A. Gayen, M.S. Hegde, N.P. Lalla, L. Spadaro, F. Frusteri, F. Arena, J. Phys. Chem. B 107 (2003) 6122-6130.

[51] T. Baidya, A. Gayen, M.S. Hegde, N. Ravishankar, L. Dupont, J. Phys. Chem. B 110 (2006) 5262-5272.

[52] T. Baidya, A. Marimuthu, M.S. Hegde, N. Ravishankar, G. Madras, J. Phys. Chem. C 111 (2007) 830-839.

[53] M. Narayanappa, V.D.B.C. Dasireddy, H.B. Friedrich, Appl. Catal., A 447–448 (2012) 135-143.

[54] C. Liu, Q. Liu, L. Bai, A. Dong, G. Liu, S. Wen, J. Mol. Catal. A: Chem. 370 (2013) 1-6.

[55] J. Jiang, L. Li, Mater. Lett. 61 (2007) 4894-4896.

[56] M. Fernandez-Garcia, A. Martinez-Arias, J.C. Hanson, J.A. Rodriguez, Chem. Rev. (Washington, DC, U. S.) 104 (2004) 4063-4104.

[57] F. Zhang, S.-W. Chan, J.E. Spanier, E. Apak, Q. Jin, R.D. Robinson, I.P. Herman, Appl. Phys. Lett. 80 (2002) 127-129.

[58] X.D. Zhou, W. Huebner, Appl. Phys. Lett. 79 (2001) 3512-3514.

[59] S. Tsunekawa, K. Ishikawa, Z.Q. Li, Y. Kawazoe, A. Kasuya, Phys. Rev. Lett. 85 (2000) 3440-3443.

[60] A. Gupta, A. Kumar, U.V. Waghmare, M.S. Hegde, Chem. Mater. 21 (2009) 4880-4891.

[61] A. Gupta, U.V. Waghmare, M.S. Hegde, Chem. Mater. 22 (2010) 5184-5198.

[62] P. Sudarsanam, B. Mallesham, P.S. Reddy, D. Großmann, W. Grünert, B.M. Reddy, Appl. Catal., B 144 (2014) 900-908.

[63] D.H. Prasad, S.Y. Park, H.I. Ji, H.R. Kim, J.W. Son, B.K. Kim, H.W. Lee, J.H. Lee, J. Phys. Chem. C 116 (2012) 3467-3476.

[64] L. Li, G. Li, Y. Che, W. Su, Chem. Mater. 12 (2000) 2567-2574.

[65] J.E. Spanier, R.D. Robinson, F. Zhang, S.W. Chan, I.P. Herman, Phys. Rev. B 64 (2001) 245407.

[66] M. Fernandez-Garcia, A. Martinez-Arias, J.C. Hanson, J.A. Rodriguez, Chem. Rev. (Washington, DC, U. S.) 104 (2004) 4063-4104.

[67] D. Gamarra, G. Munuera, A.B. Hungría, M. Fernández-García, J.C. Conesa, P.A. Midgley, X.Q. Wang, J.C. Hanson, J.A. Rodríguez, A. Martínez-Arias, J. Phys. Chem. C 111 (2007) 11026-11038.

[68] K.S.W. Sing, D.H. Everett, R.A.W. Haul, L. Moscou, R.A. Pierotti, J. Rouquerol, T. Siemieniewska, in: G. Ertl, H. Knözinger, F. Schüth, J. Weitkamp (Eds.), Handbook of Heterogeneous Catalysis, 2nd ed., Wiley-VCH Verlag GmbH & Co. KGaA, Weinheim, Germany, 2008, pp. 1217-1230.

[69] B. Holland, J. Porous Mater. 10 (2003) 17-22.

[70] T. Caputo, L. Lisi, R. Pirone, G. Russo, Appl. Catal., A 348 (2008) 42-53.

[71] D. Gamarra, A. Hornes, Z. Koppany, Z. Schay, G. Munuera, J. Soria, A. Martinez-Arias, J. Power Sources 169 (2007) 110-116.

[72] M.-F. Luo, Y.-J. Zhong, X.-X. Yuan, X.-M. Zheng, Appl. Catal., A 162 (1997) 121-131.

[73] D. Gamarra, A.L. Cámara, M. Monte, S.B. Rasmussen, L.E. Chinchilla, A.B. Hungría, G. Munuera, N. Gyorffy, Z. Schay, V.C. Corberán, J.C. Conesa, A. Martínez-Arias, Appl. Catal., B 130–131 (2013) 224-238.

[74] T. Baidya, M.S. Hegde, J. Gopalakrishnan, J. Phys. Chem. B 111 (2007) 5149-5154.

[75] Y. Nagai, T. Yamamoto, T. Tanaka, S. Yoshida, T. Nonaka, T. Okamoto, A. Suda, M. Sugiura, Catal. Today 74 (2002) 225-234.

[76] S. Sun, X. Zhao, H. Lu, Z. Zhang, J. Wei, Y. Yang, CrystEngComm 15 (2013) 1370-1376.

[77] B.B. Tope, R.J. Balasamy, A. Khurshid, L.A. Atanda, H. Yahiro, T. Shishido, K. Takehira, S.S. Al-Khattaf, Appl. Catal., A 407 (2011) 118-126.

[78] P. Burroughs, A. Hamnett, A.F. Orchard, G. Thornton, J. Chem. Soc., Dalton Trans. (1976) 1686-1698.

[79] D.R. Mullins, S.H. Overbury, D.R. Huntley, Surf. Sci. 409 (1998) 307-319.

[80] J. Xu, J. Harmer, G. Li, T. Chapman, P. Collier, S. Longworth, S.C. Tsang, Chem. Commun. 46 (2010) 1887-1889.

[81] F. Yang, J. Wei, W. Liu, J. Guo, Y. Yang, J. Mater. Chem. A 2 (2014) 5662-5667.

[82] A. Gayen, T. Baidya, G.S. Ramesh, R. Srihari, M.S. Hegde, J. Chem. Sci. 118 (2006) 47-55.

[83] Z. Guo, B. Liu, Q. Zhang, W. Deng, Y. Wang, Y. Yang, Chem. Soc. Rev. 43 (2014) 3480-3524.

[84] R.J.H. Grisel, C.J. Weststrate, A. Goossens, M.W.J. Crajé, A.M. van der Kraan, B.E. Nieuwenhuys, Catal. Today 72 (2002) 123-132.

[85] Z. Zhao, X. Lin, R. Jin, G. Wang, T. Muhammad, Appl. Catal., B 115–116 (2012) 53-62.

[86] Z. Zhao, X. Lin, R. Jin, Y. Dai, G. Wang, Catal. Commun. 12 (2011) 1448-1451.

[87] S. Scirè, C. Crisafulli, P.M. Riccobene, G. Patanè, A. Pistone, Appl. Catal., A 417–418 (2012) 66-75.

[88] R. Prasad, G. Rattan, Bull. Chem. React. Eng. Catal. 5 (2010) 7-30.

[89] Y.-J. Chen, D.-e. Wu, C.-t. Yeh, Rev. Adv. Mater. Sci. 5 (2003) 41-46.

[90] H.C. Lee, D.H. Kim, Catal. Today 132 (2008) 109-116.

[91] A. Martínez-Arias, D. Gamarra, M. Fernández-García, A. Hornés, C. Belver, Top. Catal. 52 (2009) 1425-1432.

[92] M.M. Yung, Z. Zhao, M.P. Woods, U.S. Ozkan, J. Mol. Catal. A: Chem. 279 (2008) 1-9.

[93] Q. Guo, S. Chen, Y. Liu, Y. Wang, Chem. Eng. J. 165 (2010) 846-850.

[94] D. Gamarra, A. Martínez-Arias, J. Catal. 263 (2009) 189-195.

CHAPTER 5

Au supported on substituted titania catalysts for CO oxidation and preferential CO oxidation in H_2-rich stream: Effect of the support, H_2O and CO_2

Keywords: PROX, CO oxidation, gold, $Au/Ti_{0.90}Co_{0.10}O_{2-\delta}$ and $Au/Ti_{0.9}Fe_{0.1}O_{2-\delta}$

Abstract

Cobalt- and iron-substituted titania supports were prepared by a solution combustion method. Gold deposition onto these supports and pure TiO_2 was achieved by a deposition-precipitation method. The catalysts were characterised by HR-TEM, XRD, Raman spectroscopy, XPS, TPR and BET surface area. The formation of a single-phase solid-solution for the supports was confirmed by HR-TEM, XRD and Raman spectroscopy. The performance of the gold catalysts was evaluated for total and preferential CO oxidation (TOX and PROX) and compared with those of their respective supports. The catalytic activity of the Co-substituted support was found to be higher than that of Fe-substituted support in TOX and PROX reactions. Although effective in TOX, neither support was found to be a promising candidate for PROX applications. Regarding TOX, the activity of the gold catalysts followed the trend $Au/Ti_{0.90}Co_{0.10}O_{2-\delta}$ > $Au/Ti_{0.9}Fe_{0.1}O_{2-\delta}$ > Au/TiO_2. The performance of the three catalysts improved in the presence of excess H_2, all reaching complete CO removal between 60-100 °C. The effects of H_2O and CO_2 on the PROX activity and stability of the gold catalysts were evaluated at 100 °C. In the presence of both H_2O and CO_2, CO conversions over Au/TiO_2 and $Au/Ti_{0.90}Co_{0.10}O_{2-\delta}$ catalysts decreased by nearly 20%. $Au/Ti_{0.9}Fe_{0.1}O_{2-\delta}$, however, showed no loss in activity in the presence of H_2O and/or CO_2 or one of these co-reactants. The catalyst sustained its remarkable activity and stability during the time-on-line study (24 h).

5.1 Introduction

In the context of growing environmental concerns and interest on the development of clean energy alternative technologies, polymer electrolyte membrane fuel cells (PEMFCs) have become an important subject of research aimed at addressing energy-related concerns. Amongst other types of fuel cells, PEMFCs are the most pursued by researchers and companies because of their response to transients, low operating temperature, compactness and zero emissions [1]. Therefore, PEMFCs are considered as the most versatile and promising fuel cell systems, with a technology suitable for power generation for transportation, residential and portable device applications [2]. Although significant progress is being made in developing different hydrogen production processes, almost all the hydrogen used as fuel in PEMFCs is produced via steam reforming of hydrocarbons [3]. This process is normally followed by the water gas shift (WGS) reaction in order to concurrently improve hydrogen yield and reduce residual carbon monoxide (CO) in the reformate. After WGS, the concentration level of CO is usually ≈ 1%, which is still high enough to poison the Pt anode in the PEMFC [4]. This problem could be addressed by developing a catalyst that is capable of converting residual CO, with minimal H_2 consumption [5]. Alternatively, CO-tolerant anodes can be developed to replace Pt analogues [6]. Selective reactions, such as selective methanation and preferential CO oxidation (PROX), have been extensively studied and continue to receive tremendous interest as promising ways to achieve reformate clean-up. Since CO methanation consumes rather higher amounts of H_2, an oxidative removal of CO is regarded as the most effective and cost-efficient process for CO cleanup in fuel cells [7]. The technological importance of catalytic CO oxidation goes beyond the fuel cells applications. As one of the health-threatening pollutants from automobile exhaust, CO needs to be completely converted to the less-harmful CO_2.

Metal oxide-supported Pt, Pd and Rh catalysts are conventionally used as exhaust and PROX catalysts. Generally, these catalysts are effective at temperatures above 150 °C, which is high enough to trigger undesirable H_2 oxidation. Notably, this temperature is higher than the PEMFC operating temperature (~ 80 °C). Until Haruta and co-workers first demonstrated that supported gold nanoparticles are catalytically highly active for CO oxidation at much lower temperatures, gold was regarded as inert and overlooked as an important component of catalyst formulations [8]. It has been shown that the dispersion of gold nanoparticles on reducible oxides provides

catalyst formulations that are more active than gold on non-reducible oxides. It is a widely-held view that the superior catalytic performance demonstrated by these systems is mainly due to the ability of reducible oxides to provide active oxygen species needed for CO oxidation [9]. Reducible oxides such as TiO_2 [10-15], α-Fe_2O_3 [10, 16-18], Co_3O_4 [10, 11], CeO_2 and MnOx [19-21] have been found to demonstrate promising catalytic activity for CO oxidation and PROX. The studies reported by Haruta *et al*. [10], Hutchings's group [17] and Schubert *et al*. [16] have revealed that Au/α-Fe_2O_3 catalysts, prepared by co-precipitation, are amongst the most active and robust catalysts for CO oxidation and PROX, surpassing the intensively studied Au/TiO_2 system. The superiority of these catalysts has been associated with the fact that α-Fe_2O_3 is a more reducible support and the presence of anion vacancies near gold nanoparticles [22]. Other authors have reported outstanding catalytic activity for Au/Co_3O_4 catalysts, comparable to that of Au/α-Fe_2O_3.

Recently, it has been reported that the catalytic activity of Au/TiO_2 catalysts can be enhanced by adding Co_3O_4 [23] and Fe_2O_3 [22, 24] as additives on the TiO_2 support. There is a consensus amongst researchers that supports such as TiO_2-Fe_2O_3 and TiO_2-Co_3O_4 have higher proportions of oxygen defect sites, which act as local sites for active oxygen needed during catalytic progression [24-26]. Moreover, supporting gold on such materials has been reported to produce stable catalysts, with strong metal-support interaction. In the present work, we report the incorporation of cobalt and iron ions into the TiO_2 matrix, *via* the solution combustion method. The intention was to prepare supports with improved redox properties, wherein Co and Fe ions are fully dispersed as ions within the $Ti_{1-x}M_xO_{2-\delta}$ single-phase material. These solid-solution materials were used as supports for Au nanoparticles and the catalytic behaviour of Au/metal-doped TiO_2 catalysts was compared with that of Au/TiO_2.

5.2 Experimental

5.2.1 Catalyst synthesis

Cobalt and iron substituted titania materials were prepared by the solution combustion method, using titanium tetra-isopropoxide ($[Ti(OCH(CH_3)_2)_4]$, Sigma-Aldrich), ferric nitrate ($[Fe(NO_3)_3.9H_2O]$, Sigma-Aldrich) and cobalt nitrate ($[Co(NO_3)_2.5H_2O]$, Sigma-Aldrich) as the starting precursors. Prior to synthesis, titanium tetra-isopropoxide was converted to titanyl nitrate ($[TiO(NO_3)_2]$) by dissolving the precipitated titanyl hydroxide in nitric acid. A typical redox combustion mixture was made by dissolving stoichiometric amounts of $TiO(NO_3)_2$, $Co(NO_3)_2.5H_2O$ or $Fe(NO_3)_3.9H_2O$ and urea fuel in the ratio of 0.90: 0.1: 1.67 respectively. For example, for the preparation of $Ti_{0.9}Co_{0.1}O_{2-\delta}$, 8.8 mL of titanyl nitrate, 0.0.970 g of cobalt nitrate and 3.337 g of urea were dissolved in 50 mL of water in a borosilicate dish. The solution was mixed and reduced to a volume 20 ml at 150 °C on a hotplate. A boiling solution was then transferred into a muffle furnace which was preheated to 400 °C. After a nearly complete dehydration, the solution boiled with foaming and dried up before burning in flame. The resulting material was kept in the furnace overnight at 400 °C. Pure TiO_2 and $Ti_{0.9}Fe_{0.1}O_{2-\delta}$ analogues were prepared by a similar combustion method.

Gold (~0.5 wt%) catalysts were prepared by a deposition-precipitation method [13-15]. The pH of the required amount of dilute $HAuCl_4$ (0.01 $mol.dm^{-3}$) was adjusted to 8 by adding 0.1 $mol.dm^{-3}$ of NaOH. The support was suspended and the resulting suspension was heated to 70 °C, while continuously stirring. After aging for 1 h, the reaction mixture was cooled, filtered and washed with warm deionized water repeatedly. The samples were dried overnight at 100 °C and calcined at 300 °C in air for 4 h. The respective samples were named as Au/TiO_2, $Au/Ti_{0.9}Fe_{0.1}O_{2-\delta}$ and $Au/Ti_{0.9}Co_{0.1}O_{2-\delta}$.

5.2.2 Catalyst characterization

Metal contents in the catalysts were determined by an inductively coupled plasma-optical emission spectrometer (ICP-OES, Perkin Elmer Optima 5,300 DV) and the standards (1,000 ppm Fe, Co and Au) were obtained from Fluka. Specific surface areas (BET), total pore volume and pore size of the catalysts were determined from the adsorption and desorption isotherms of

nitrogen at -196 °C using a micromeritics TriStar 3000 multipoint analyser. Prior to the analysis, the samples were degassed overnight at 200 °C under nitrogen flow. The linear part of the adsorption curve was used to determine the specific surface area (S_{BET}) and the pore size distribution was determined from the desorption curve applying the Barret-Joyner-Halenda (BJH) theory. X-ray powder diffraction (XRD) experiments were conducted on a Bruker D8 Advance diffractometer equipped with an Anton Paar XRK900 *in situ* cell and a Cu Kα source (λ = 1.5406 Å). The XRD patterns were recorded in the 2θ range of 10–90 ^{o} at a scan rate of 0.5°/min, with a step width of 0.02 °. The average crystallite size (*D*) values of metal-substituted titania materials were estimated by applying the Scherrer equation (5.1) at the [101] peak. Structural properties of the catalysts were further studied by Raman spectroscopy, using an Advantage 532 series spectrometer and employing the visible laser line of 514 nm in the spectral range of 200 cm^{-1} to 3400 cm^{-1}.

$$D=\frac{K\lambda}{\beta_{hkl}\cos\theta} \qquad (5.1)$$

Transmission electron microscopy (TEM) and high resolution TEM (HR-TEM) analyses were performed on Jeol JEM-1010 and JEM-2100 electron microscopes, respectively. The images were further analyzed using ImageJ software. Samples were prepared by dispersing them in ethanol before they were deposited onto the holey carbon-coated grids. The field emission scanning electron microscope (FEG-SEM) images were obtained from a ZEISS FEG-SEM Ultra Plus instrument. X-ray photoelectron spectra (XPS) were collected with a Thermo Scientific Multilab 2000 apparatus, using the Al Kα radiation (1486.6 eV) and the C (1s) spectra as the reference (284.5 eV) for all binding energies. Hydrogen temperature-programmed reduction (H_2-TPR) measurements were carried on a Micromeritics AutoChem II 2920 Chemisorption analyzer equipped with a thermal conductivity detector (TCD) to measure H_2 consumption. Prior to data collection, the sample (~30 mg) was pretreated under an argon flow at 400 °C for 30 minutes and then cooled to room temperature.

5.2.3 Catalytic activity measurements

Both TOX and PROX activity measurements were performed in the gas phase at atmospheric pressure and different temperatures (ambient temperature to 250 °C) under steady-state conditions. Experiments were conducted in a continuous flow fixed-bed reactor whose temperature was controlled by an insulated *unitemp* thermocouple wire. Feed and effluent gases were analysed online with a three-channel Agilent CP-4900 micro gas chromatograph, each channel equipped with a TCD and column. The GC is fitted with Molsieve 5Å and CP-Sil5 CB columns, with 1.0 µL back-flushing to discharge residual components after analysis. All gases used were analytical grade and were received from Afrox or Air Products. The powder catalysts were pelletized and sieved into a 300-600 µm mesh. The catalyst granules were diluted with inert carborundum beads (24-grit, ~ 600 µm) to a volume of 3 mL and loaded at the centre of a tubular reactor with an inner diameter of 18 mm and length of 500 mm. The catalyst bed was held by glass wool and carborundum on either side of the reactor tube. Prior to each experiment, the catalyst was pre-treated *in situ* for 4 h at 150 °C with air and then cooled down to room temperature under nitrogen flow.

All experiments were performed at a gas hourly space velocity (GHSV) of 48000 h^{-1}. The aforementioned GHSV figure was calculated based on the catalyst bed volume of 0.1 mL for a corresponding catalyst weight of 0.095 g and the total reactant flow rate of 80 mL/min. For total CO oxidation, the reactant gas composition contained 1 vol% CO, 1 vol% O_2 and the balance was nitrogen. In PROX experiments, the following feed composition was used: 1 vol% CO, 2 vol% O_2, 50 vol% H_2 and 47 vol% N_2. The catalytic behaviour of the catalysts was evaluated in the presence of water and 15 vol% CO_2 and 7 vol% H_2O. Water was introduced by passing the dry gas composition through a bubbler maintained at 38 °C. CO conversions and O_2 selectivity values were calculated based on Equations 5.2 and 5.3, respectively. Data points were collected within 30 minutes in triplicates at steady state and all carbon and oxygen balances were within ± 5%.

$$\text{CO conversion } (X_{co}) = \frac{([CO]_{in} - [CO]_{out})}{[CO]_{in}} \times 100 \qquad (5.2)$$

$$\text{Selectivity to } CO_2 \left(S_{CO_2}\right) = \frac{([CO]_{in} - [CO]_{out})}{2([O_2]_{in} - [O_2]_{out})} \times 100 \qquad (5.3)$$

5.3 Results and discussion

5.3.1 Composition, structural and morphology studies

The XRD patterns of all the catalysts, as shown in Figure 5.1, can be indexed to the tetragonal anatase structure of TiO2 with a D4h space group (I41/amd, JCPDS no.21-1272). The diffraction peaks observed at 25.68°, 36.24°, 48.45°, 54.75°, 63.18° correspond to the [101], [004], [200], [105] and [204] planes, respectively. Notably, the XRD profiles of $Ti_{0.9}Fe_{0.1}O_{2-\delta}$ and $Ti_{0.9}Co_{0.1}O_{2-\delta}$ did not show any measurable diffraction peaks corresponding to pure oxides, Co_3O_4 and Fe_2O_3. The absence of pure oxide peaks indicates that the foreign metal ions (Fe^{3+} and Co^{2+}) were successfully incorporated into the lattice of the anatase structure. In the present study, 10% Co_3O_4/commercial-TiO_2 was also prepared by an impregnation method and its XRD was studied in order to examine the expected Co_3O_4 peak intensity and structural distortion. As anticipated, the XRD pattern of this sample showed small peaks at $2\theta = 31°$ and 37.5° which are associated with Co_3O_4 [220] and [311] respectively. This observation further confirms that 10% of Co_3O_4 species can be detected by XRD.

The diffraction lines of the samples that were prepared by solution combustion had broader full width half maximum (FWHM) values compared to those of the reference, commercial TiO_2. Such broad peaks suggest that these materials are comprised of nano-crystallites. Accordingly, the average crystallite sizes, estimated by the Scherrer equation, were found to be 17, 8.5, 6 and 6.4 nm for commercial TiO_2, prepared TiO_2, $Ti_{0.9}Fe_{0.1}O_{2-\delta}$ and $Ti_{0.9}Co_{0.1}O_{2-\delta}$, respectively. The enlarged XRD peaks for the [101] plane of all catalysts are shown as an insert in Figure 5.1. The diffraction peaks of prepared TiO_2 and metal ion substituted TiO_2 are slightly shifted to higher 2θ values, which is indicative of lattice distortion. Such structural changes may arise as a result of intrinsic defects induced during the preparation or extrinsic defects due to substituting Ti^{4+} (0.605 Å), in the TiO_2 framework, with foreign metal ions that have different ionic radii and valence (Fe^{3+} = 0.55 Å and Co^{2+} = 0.74 Å). Gold deposition on the titania-based supports did not result in further changes in the XRD patterns. The reflections for metallic gold (2θ = 38.2° [111], 44.5° [200] and 64.5° [220]) were not observed, suggesting the presence of small and highly dispersed gold particles.

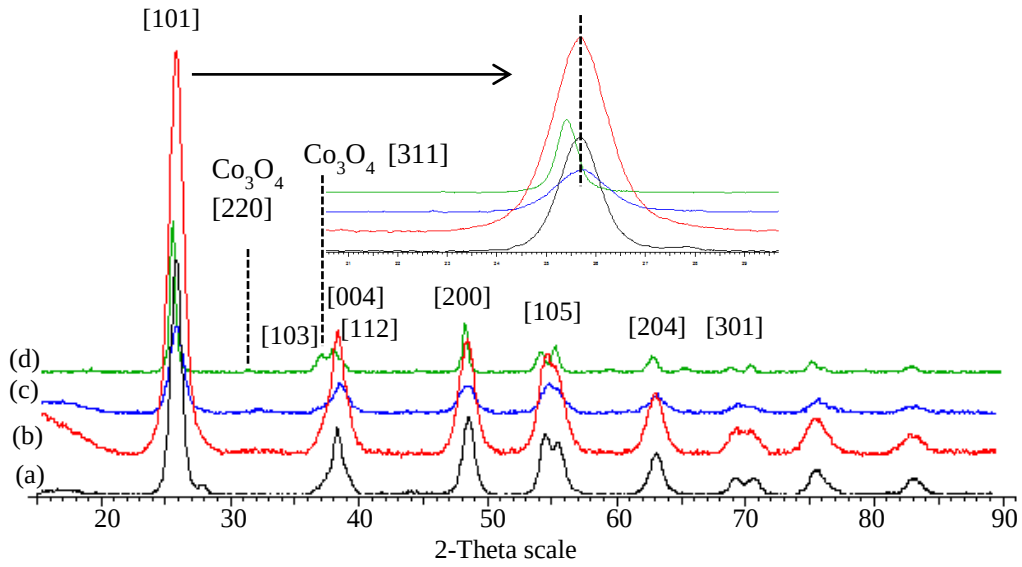

Figure 5.1 *XRD profiles of (a) Au/TiO_2, (b) $Au/Ti_{0.9}Fe_{0.1}O_{2-\delta}$, (c) $Au/Ti_{0.9}Co_{0.1}O_{2-\delta}$ and (d) $10\%Co_3O_4/TiO_2$*

Rietveld analysis of the substituted titania materials was performed, substituting Ti^{4+} with Fe^{3+} or Co^{2+} ions. The Rietveld-refined XRD patterns of $Ti_{0.9}Fe_{0.1}O_{2-\delta}$ and $Ti_{0.9}Co_{0.1}O_{2-\delta}$ are shown in Figure 5.2 and the lattice parameters obtained from the analysis are given in Table 5.1. The observed, modelled and the difference (between observed and modelled) XRD patterns are represented in red, black and blue in Figure 5.2, respectively. The difference plots from the refined patterns show a good fit, with no oxide or metallic peaks relate to Co_3O_4 and Fe_2O_3 or Co and Fe. This further suggests that Fe^{3+} and Co^{2+} ions are incorporated into the lattice structure of anatase TiO_2. The goodness-of-fit and *R* factor for the profile fitting of $Ti_{0.9}Fe_{0.1}O_{2-\delta}$ are 1.30 and 1.94, respectively. For $Ti_{0.9}Co_{0.1}O_{2-\delta}$, the respective values are 1.18 and 2.63. According to Rietveld analysis reliability standards, these results confirm a good agreement between the observed and modelled data [27]. The lattice parameters of TiO_2, a = b and c, decrease slightly upon incorporating cobalt and iron ions into the lattice. This is indicative of the possible formation of a solid-solution wherein some of the Ti^{4+} host ions are substituted by foreign metal ions with different valence and ionic radii. The overall effect of these two factors is the contraction of the lattice.

Table 5.1 *Structural parameters of titania-based materials.*

Catalyst	Lattice parameter a = b (Å)	Lattice parameter c (Å)	Structure factor (R_f)	Bragg factor (R_B)	χ^2	Crystallite size (nm)	d-spacing (nm)[a]
TiO_2	3.7794	9.4908	4.77	5.88	1.65	8.5	0.347 (0.350)
$Ti_{0.9}Fe_{0.1}O_{2-\delta}$	3.7784	9.4747	1.94	1.54	1.30	6	0.346 (0.358)
$Ti_{0.90}Co_{0.10}O_{2-\delta}$	3.7761	9.4380	2.63	3.09	1.18	6	0.346 (0.355)

[a] Values show in parentheses were estimated from HR-TEM

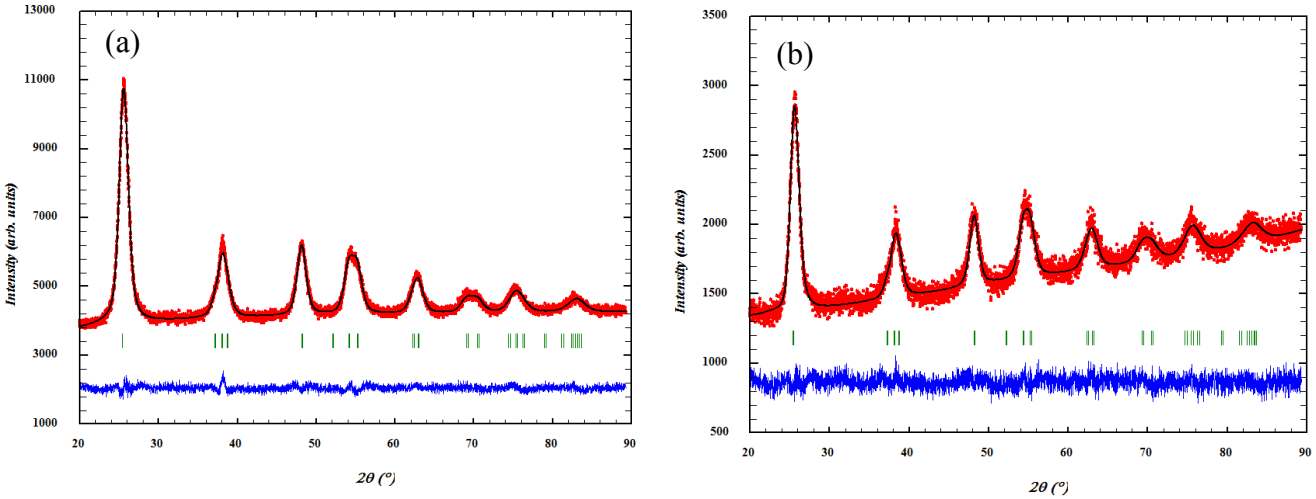

Figure 5.2 *Rietveld-refined XRD profiles of (a) $Ti_{0.9}Fe_{0.1}O_{2-\delta}$ and (b) $Ti_{0.9}Co_{0.1}O_{2-\delta}$*

Raman spectroscopy was used to further study structural properties and phases of titania-based materials and the spectra of the prepared samples are depicted in Figure 5.3. The Raman spectra of all samples show characteristic bands at 400, 520 and 635 cm^{-1}, which are associated with B_{1g}, A_{1g} & B_{1g} and E_g Raman-active modes of the anatase-structured TiO_2 material [26]. The presence or absence of pure Co_3O_4 species may not be conclusively ascertained by Raman spectroscopy since Raman-active modes of Co_3O_4 are in close proximity with those of anatase TiO_2. In the case of Fe_2O_3 species, the strongest band at 1300 cm^{-1}, which is a prominent signature of even low loadings of crystalline Fe_2O_3, can be used as a detector of the presence or absence of surface species. This band is attributed to the second harmonic vibrations of hematite

[25]. Its absence from the spectrum of $Ti_{0.9}Fe_{0.1}O_{2-\delta}$ suggests that Fe^{3+} ions are substitutionally incorporated in the anatase matrix, replacing some of the Ti^{4+} ions. The incorporation of foreign metal ions into the TiO_2 framework is accompanied by the broadening of the peaks. In addition, the peaks are marginally shifted to lower wavenumbers. The broadening and blue shift of the Raman bands (Figure 5.3) can be interpreted as a reflection of distortion induced by defects created upon the incorporation of foreign metal ions with different ionic radii and valences. Wang *et al*. have associated such phenomena with the existence of possible oxygen vacancies in TiO_2 nanostructures [28]. Since the average crystallite sizes of the prepared materials are below 10 nm, line broadening was expected. Summarily, Raman results are in agreement with the XRD data and suggest successful formation of the single-phase solid-solution materials.

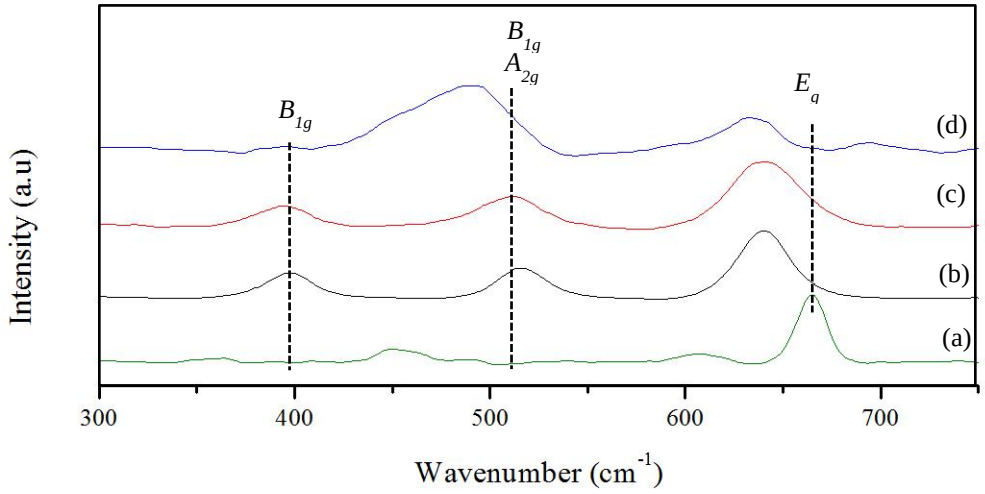

Figure 5.3 *Raman spectra of (a) 10% Co_3O_4/TiO_2, (b) Au/TiO_2, (c) $Au/Ti_{0.9}Fe_{0.1}O_{2-\delta}$ and (d) $Au/Ti_{0.9}Co_{0.1}O_{2-\delta}$*

HR-TEM images of Au/TiO_2, $Au/Ti_{0.9}Fe_{0.1}O_{2-\delta}$ and $Au/Ti_{0.9}Co_{0.1}O_{2-\delta}$ are shown in Figure 5.4. High-resolution images of the samples show that the lattice fringes of individual small crystallites are 0.350, 0.358 and 0.355 nm for Au/TiO_2, $Au/Ti_{0.9}Fe_{0.1}O_{2-\delta}$ and $Au/Ti_{0.9}Co_{0.1}O_{2-\delta}$, respectively. These interplanar distances correspond to the anatase [101] lattice spacing and are in good agreement with the *d* spacings obtained from XRD profiles. The lattice fringes corresponding to Co_3O_4 or Fe_2O_3 were not observed, again suggesting the incorporation of the metal ions into the anatase matrix. The average particle sizes of the combustion synthesized

titania materials are comparable and around 10 nm, which is slightly higher than the values calculated from the Scherrer equation.

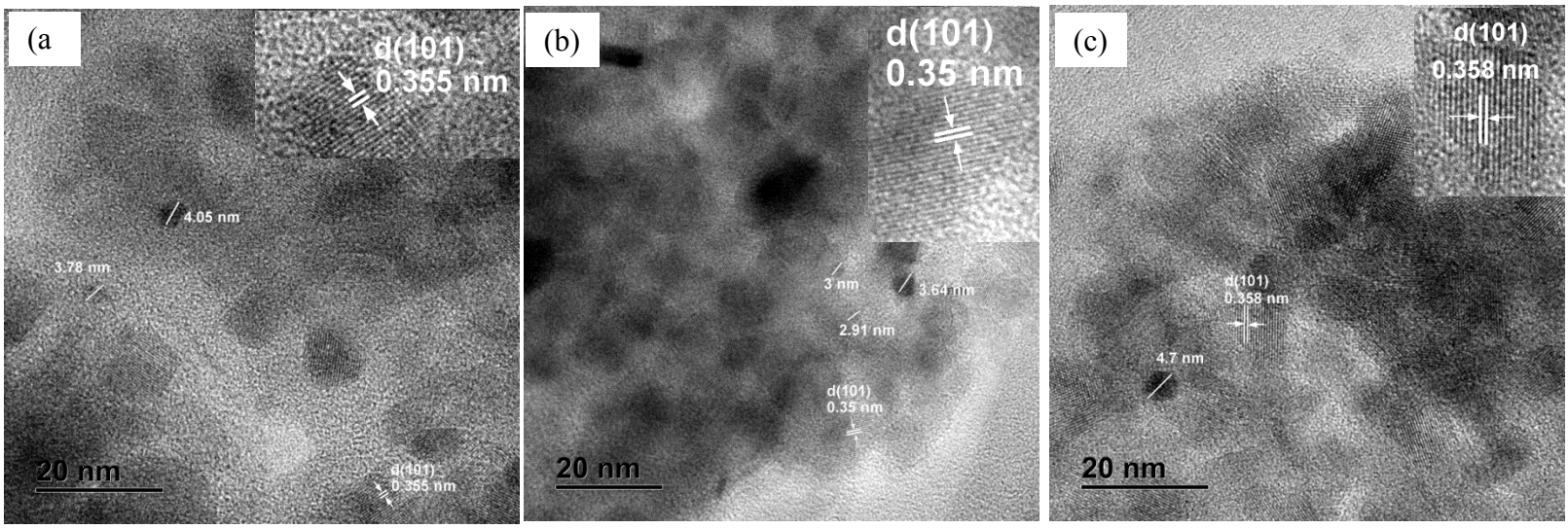

Figure 5.4 *HR-TEM images of (a) Au/TiO_2, (b) Au/ $Ti_{0.9}Co_{0.1}O_{2-\delta}$ and (c) Au/$Ti_{0.9}Fe_{0.1}O_{2-\delta}$*

ICP-OES results presented in Table 5.2 show the precise atomic percent of Fe and Co on the support and the Au weight loading. The results reveal that metal ion substituted TiO_2 supports have Ti:Fe and Ti:Co atomic ratios of 90.5:9.5 and 92:8. Therefore the chemical formulations of these supports are based on the ICP results. The exact content of gold deposited on the supports differs only by 0.13 wt%, which allows assessing the effect of modifying the TiO_2 support.

The nitrogen adsorption/desorption isotherms and the corresponding pore size distribution plots of all the catalysts are shown in Figure 5.5 (a) and (b), respectively. The isotherms of all the samples are of type IV and their corresponding hysteresis loops belong to the H2 type, which is characteristic of mesoporous materials with good structural homogeneity [29, 30]. Accordingly, the pore diameters are within the narrow range of 20 to 70 Å, confirming the presence of uniform mesopores. The BET surface area increased from 120 to 129 and 137 $m^2.g^{-1}$ upon the incorporation of cobalt and iron ions, respectively. An increase in surface area may be linked to reduced crystallite size due to the presence of foreign metal ions [31]. The BET results collate well with crystallite sizes estimated from the XRD profiles. Textural properties of the catalysts are surmised in Table 5.2.

Table 5.2 *Chemical composition and surface properties of prepared catalysts*

Catalyst	Ti (at%)	M (at%)	Au (wt%)	Au particle size (nm)[c]	S_{BET} (m^2/g)	Average pore size (Å)	Pore volume (cm^3/g)
Au/TiO_2	100	-	0.48	4	120	51	0.22
$Au/Ti_{0.9}Fe_{0.1}O_{2-\delta}$	90.5	9.5[a]	0.50	4.7	137	45	0.23
$Au/Ti_{0.90}Co_{0.10}O_{2-\delta}$	92	8[b]	0.49	3.2	129	50	0.23

[a] M = Fe, [b] M = Co, [c] the particle size is based on few Au particles that could be accurately measured.

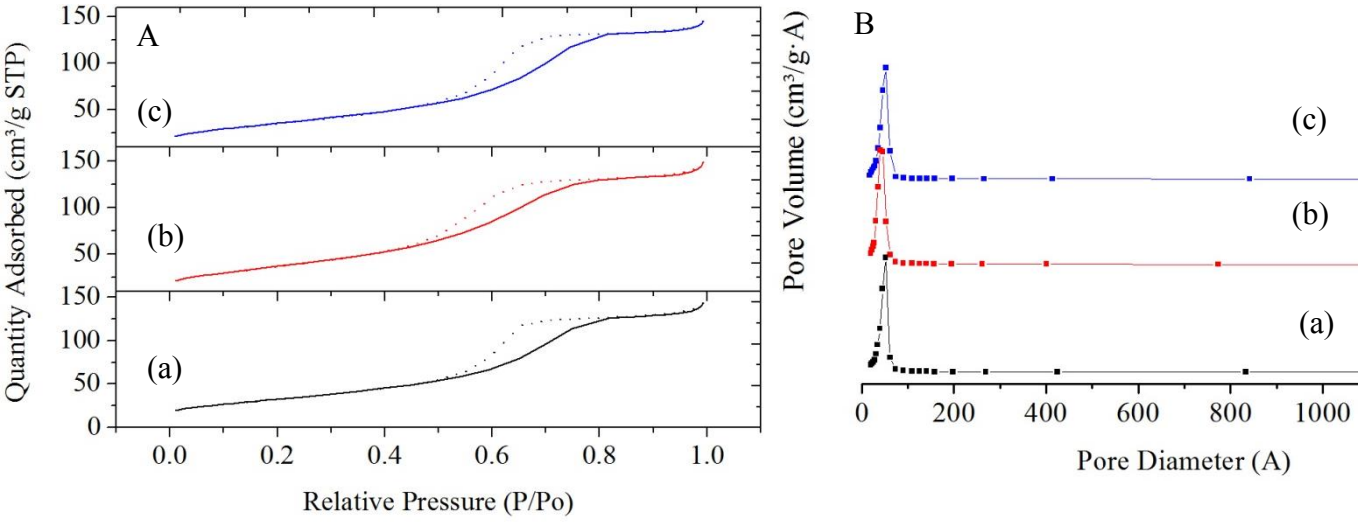

Figure 5.5 *A Nitrogen adsorption/desorption isotherms and B: pore size distribution curves of ((a) Au/TiO_2, (b) $Au/Ti_{0.9}Fe_{0.1}O_{2-\delta}$ and (c) $Au/Ti_{0.90}Co_{0.10}O_{2-\delta}$*

5.3.2 Electronic and redox studies

Ti 2p core level X-ray photoelectron spectra (XPS) of the supported gold catalysts are shown in Figure 5.4. The binding energies of Ti($2p_{3/2}$) and Ti($2p_{1/2}$) are located at around 460 and 466 eV, respectively, for all the catalysts. This confirms that Ti is present in the +4 oxidation state in all metal ion substituted titania materials. In addition, the Ti 2p peaks are marginally shifted to lower energies for Fe and Co-containing samples. Such changes can be attributed to the formation of oxygen vacancies upon the incorporation of foreign metal ions into the TiO_2 matrix [32]. The Au 4f core level spectra of all supported gold catalysts are characterized by the doublet of two spin orbits, located at 83.5 and 89 eV. The two peaks are due to the respective Au 4($f_{7/2}$) and 4($f_{5/2}$) components of the metallic gold. The presence of a small percentage of positively charged gold, Au^{3+}, cannot be ruled out completely, as its reported binding energy of

89.6 eV may overlap with that of the metallic state [22]. The core level Fe(2p) spectrum of $Au/Ti_{0.9}Fe_{0.1}O_{2-\delta}$ is depicted in Figure 5.4 B. The binding energy of Fe($2p_{3/2}$) is located at 711.0 eV and that of the Fe($2p_{1/2}$) component appears at 725.9 eV. In addition, a weak satellite positioned at 8 eV from the main peak confirms that Fe exists as Fe^{3+} in $Au/Ti_{0.9}Fe_{0.1}O_{2-\delta}$ [22]. Figure 5.4 C shows the core level Co(2p) XP spectrum of $Au/Ti_{0.90}Co_{0.10}O_{2-\delta}$. The peaks positioned at the binding energy of 794 and 779 eV are attributed to Co ($2p_{1/2}$) and Co ($2p_{3/2}$) orbit components, respectively. The peaks are characteristic of the Co^{2+} state [33].

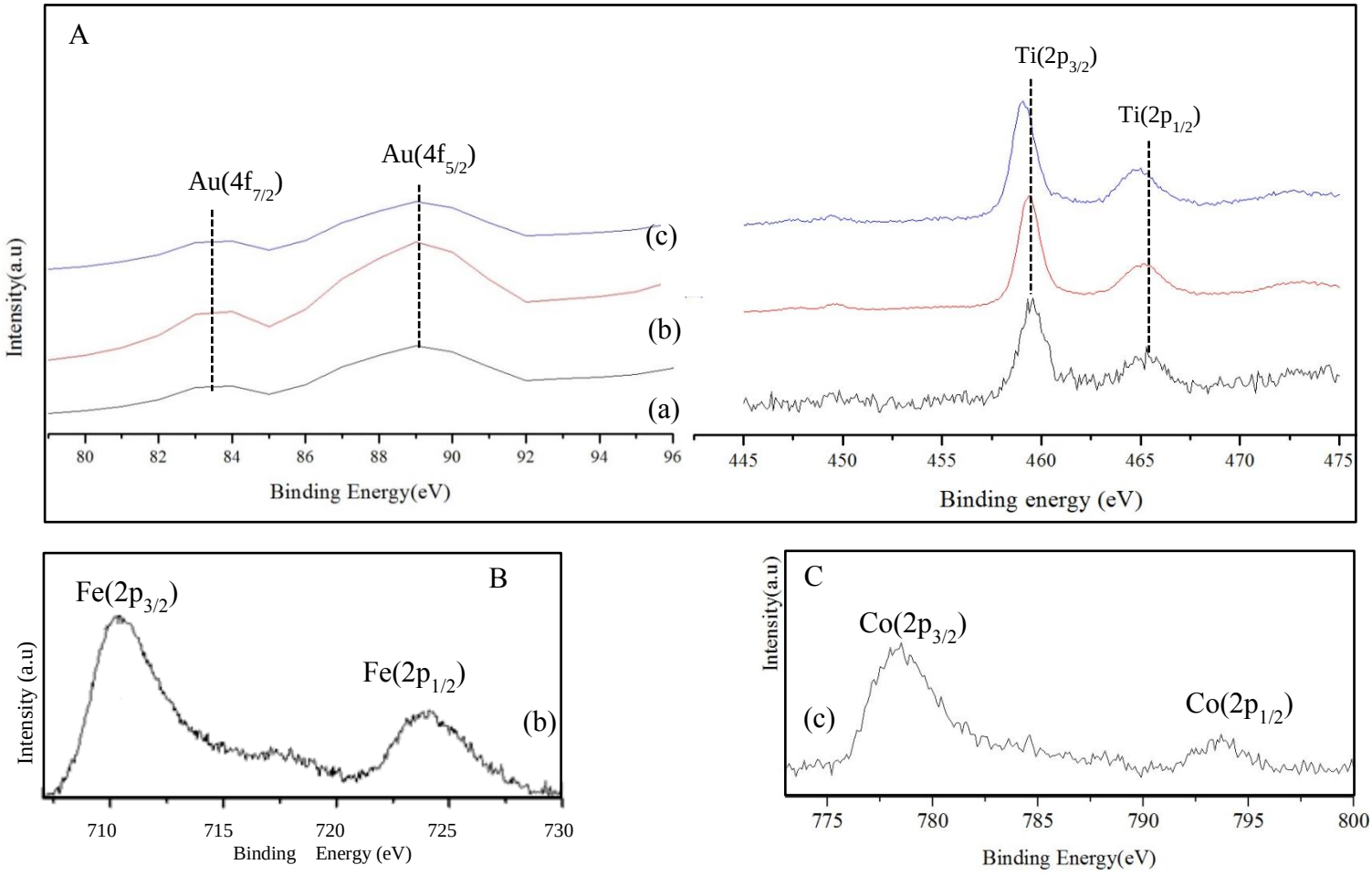

Figure 5.6 *A: Au(4f) and Ti(2p), B: Co(2p) and C: Fe(2p) XP spectra of (a) Au/TiO_2, (b) $Au/Ti_{0.9}Fe_{0.1}O_{2-\delta}$ and (c) $Au/Ti_{0.90}Co_{0.10}O_{2-\delta}$ catalysts*

5.3.3 Catalytic studies

5.3.3.1 Total CO oxidation

The catalytic activity profiles of pure TiO_2 and metal ion substituted titania for total CO oxidation are presented in Figure 5.7. Based on the respective temperatures of CO conversion of 50 and 100%, T_{50} and T_{100}, the activities are in the order of $Ti_{0.90}Co_{0.10}O_{2-\delta}$ > $Ti_{0.9}Fe_{0.1}O_{2-\delta}$ > TiO_2. Complete CO oxidation was achieved at 220 °C over $Ti_{0.90}Co_{0.10}O_{2-\delta}$, while a maximum of 68% CO conversion was reached at 300 °C for $Ti_{0.9}Fe_{0.1}O_{2-\delta}$. As anticipated and reported elsewhere [34], no substantial conversion was observed over pure TiO_2, even at reaction temperatures above 200 °C. Since all the three oxide materials were prepared under the same combustion conditions, the observed catalytic performance demonstrated by Co- and Fe-substituted TiO_2 suggests that the incorporated foreign metal ions are involved in the promotion of CO activation during the TOX reaction.

As shown in Figure 5.7, depositing minimal content of gold onto these oxides considerably improves the activity. The order of the activities for TOX increases in the following trend: $Au/Ti_{0.90}Co_{0.10}O_{2-\delta}$ > $Au/Ti_{0.9}Fe_{0.1}O_{2-\delta}$ > Au/TiO_2, with respective T_{100} values of 100, 120 and 180 °C. Since TiO_2 on its own is inactive, CO oxidation over a Au/TiO_2 catalyst is envisaged to proceed via the adsorption of CO on Au, followed by oxidation by an oxygen atom released from the support, as widely reported in literature [9, 35, 36]. Therefore, the superior performance showed by $Au/Ti_{0.90}Co_{0.10}O_{2-\delta}$ and $Au/Ti_{0.9}Fe_{0.1}O_{2-\delta}$ can be associated with the presence of oxygen vacancies in these *active* supports, as verified by Raman and XPS analysis. Thus, the incorporation of Fe and Co into the TiO_2 structure yields support materials that can readily uptake and release oxygen required for CO oxidation, compared to pure TiO_2.

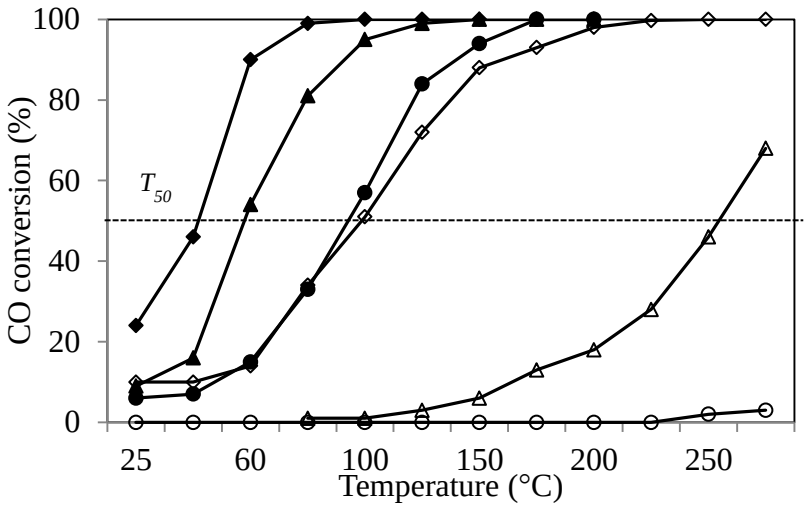

Figure 5.7 *CO conversion as a function of temperature over (a) titania-based materials(○ TiO_2, Δ$Ti_{0.9}Fe_{0.1}O_{2-\delta}$ and ◊ $Ti_{0.90}Co_{0.10}O_{2-\delta}$) and (b) supported gold catalysts (● Au/TiO_2, ▲$Au/Ti_{0.9}Fe_{0.1}O_{2-\delta}$ and ♦$Au/Ti_{0.90}Co_{0.10}O_{2-\delta}$) in TOX reaction*

5.3.3.2 Preferential CO oxidation

Figure 5.8(a) shows the CO conversions as a function of temperature during preferential CO oxidation experiments. In comparison with TOX, CO conversions over $Ti_{0.9}Fe_{0.1}O_{2-\delta}$ and $Ti_{0.90}Co_{0.10}O_{2-\delta}$ decreased under PROX conditions. In a H_2-rich stream, no substantial CO conversions were observed at reaction temperatures below 150 °C over these materials. The decrease in conversion was more pronounced for the Co-containing support, from 98 to 42% at 200 °C. This can be associated with the reduction of cobalt species to a lower valence, which is known to be inactive for CO oxidation [37, 38]. In the case of $Ti_{0.9}Fe_{0.1}O_{2-\delta}$, the CO conversions under TOX and PROX are almost the same at reaction temperatures below 220 °C. This possibly suggests that the active species remain mostly unchanged, especially at lower temperatures, in the presence of H_2. Above 250 °C, CO conversion decreased due to competing H_2 oxidation, which leads to O_2 starvation. The difference in the activity of the two supports cannot be justified based on surface area differences since the less active support had a higher surface area. These results indicate that the more readily reducible cobalt species, compared to their iron counterparts, may facilitate CO oxidation reaction.

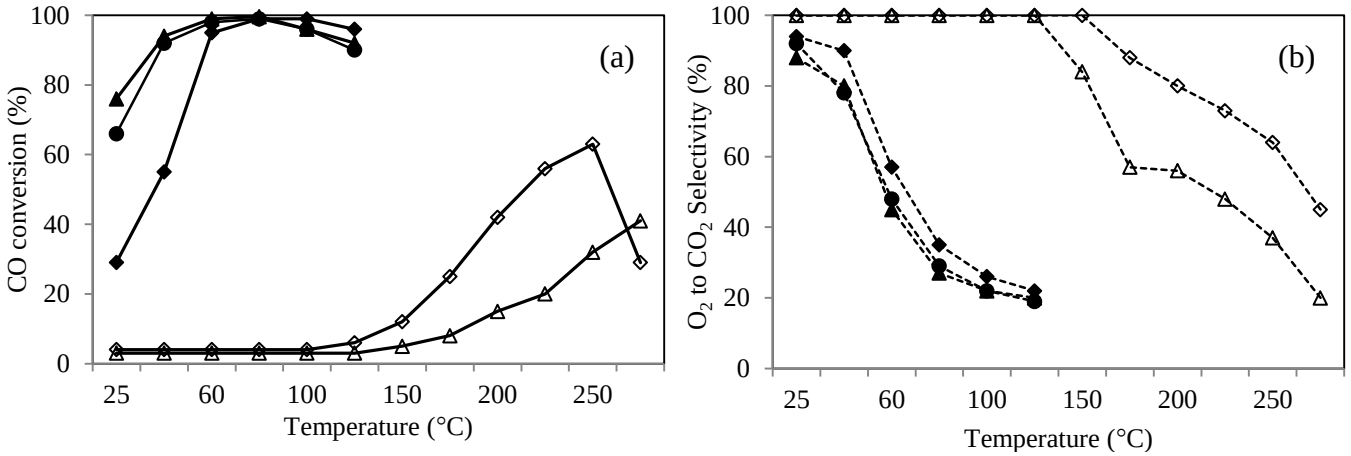

Figure 5.8 *(a) CO conversion and (b) selectivity as a function of temperature over* $\Delta Ti_{0.9}Fe_{0.1}O_{2-\delta}$, $\lozenge$ $Ti_{0.90}Co_{0.10}O_{2-\delta}$, ● Au/TiO_2, ▲ $Au/Ti_{0.9}Fe_{0.1}O_{2-\delta}$ *and* ♦ $Au/Ti_{0.90}Co_{0.10}O_{2-\delta}$

In Figure 5.8(a), the catalytic performance of gold catalysts for the PROX reaction is compared with those of their respective supports. Contrary to the catalytic behaviour of the supports, CO conversions over gold catalysts are evidently improved in the presence of H_2, compared to values obtained under TOX conditions. Considering a reaction temperature of 25 °C, CO conversion is improved from 6 to 66, 24 to 29 and 9 to 76% for Au/TiO_2, $Au/Ti_{0.90}Co_{0.10}O_{2-\delta}$ and $Au/Ti_{0.9}Fe_{0.1}O_{2-\delta}$, respectively. Below 60 °C, PROX activities are in the order of $Au/Ti_{0.9}Fe_{0.1}O_{2-\delta}$ $\approx$ Au/TiO_2 > $Au/Ti_{0.90}Co_{0.10}O_{2-\delta}$. The performance of all gold catalysts is comparable from 60 °C onwards, reaching complete CO oxidation between 60 – 80 °C. A further increase in temperature leads to a decrease in CO conversion due to H_2 oxidation, which uses O_2 required for CO transformation. Since the active components in $Ti_{0.9}Fe_{0.1}O_{2-\delta}$ appear to be mostly unchanged, as evident from the light-off cures of this support for TOX and PROX, the release and uptake of oxygen atoms by this material is believed to be uninterrupted [26]. Thus, this redox phenomenon allows the support to act as the local site for active oxygen, which leads to a superior PROX performance by $Au/Ti_{0.9}Fe_{0.1}O_{2-\delta}$ (Figure 5.9). In the case of $Au/Ti_{0.90}Co_{0.10}O_{2-\delta}$, this cobalt species are readily transformed under a reducing environment, depriving the support from playing a measure role during oxygen activation for CO oxidation [23, 25].

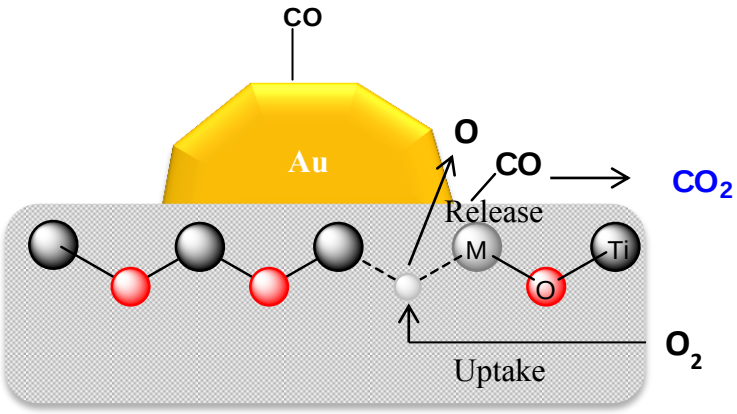

Figure 5.9 *Schematic representation of CO oxidation over Au/$Ti_{0.9}Fe_{0.1}O_{2-\delta}$*

Figure 5.8(b) shows the O_2 selectivity to CO_2 during PROX experiments. For modified titania supports, meaningful selectivity values can be restricted to temperatures above 150 °C, where substantial CO conversion starts. As the reaction temperature is increased beyond 150 °C, the selectivity decreases until it reaches 37 and 45% for $Ti_{0.9}Fe_{0.1}O_{2-\delta}$ and $Ti_{0.90}Co_{0.10}O_{2-\delta}$, respectively. All gold catalysts show a decrease in selectivity as the temperature is increased. The decrease in the selectivity is accompanied with a significant H_2 conversion at higher temperatures, which is a similar trend found in other reports [17, 22, 23]. The O_2 to CO_2 selectivity values of Au/$Ti_{0.9}Fe_{0.1}O_{2-\delta}$ and Au/TiO_2 are comparable at all reaction temperatures, whereas those of Au/$Ti_{0.90}Co_{0.10}O_{2-\delta}$ are slightly higher. At 80 °C, the fuel cell operation temperature and the temperature where all the gold catalysts show complete CO conversion, the O_2 to CO_2 selectivity is 35, 29 and 27% for Au/$Ti_{0.90}Co_{0.10}O_{2-\delta}$, Au/$TiO_2$ and Au/$Ti_{0.9}Fe_{0.1}O_{2-\delta}$, respectively.

5.3.3.3 Catalyst stability and the effect of CO_2 and H_2O

Although metal oxide supported gold catalysts are known for their high activity for CO oxidation at low temperatures, deactivation is a general drawback of Au catalysts [39, 40]. Typical streams for PROX are in the temperature range of 80 – 120 °C. Therefore, the stability studies of the gold catalysts were performed at a representative reaction temperature of 100 °C. The time-on-line activity and selectivity results are reported in Figure 5.10. It can be seen that all catalysts show stable activities for PROX, with Au/TiO_2 showing only a 3% decline in CO conversion. These

catalyst performances were consistently observed during the 24 h of catalyst testing. In addition, the selectivity didn't change for all catalysts, maintained at 30, 22 and 22% for $Au/Ti_{0.90}Co_{0.10}O_{2-\delta}$, Au/TiO_2 and $Au/Ti_{0.9}Fe_{0.1}O_{2-\delta}$, respectively. The results suggest that the active sites remain mostly unmodified during the reaction. It has been suggested that the presence of Co_3O_4 in Au/Co_3O_4-TiO_2 can suppress H_2 oxidation, which was linked to the presence of stabilized Au^+ species [23]. In the present study, $Au/Ti_{0.90}Co_{0.10}O_{2-\delta}$ also shows better O_2 to CO_2 selectivity, compared to other two catalysts.

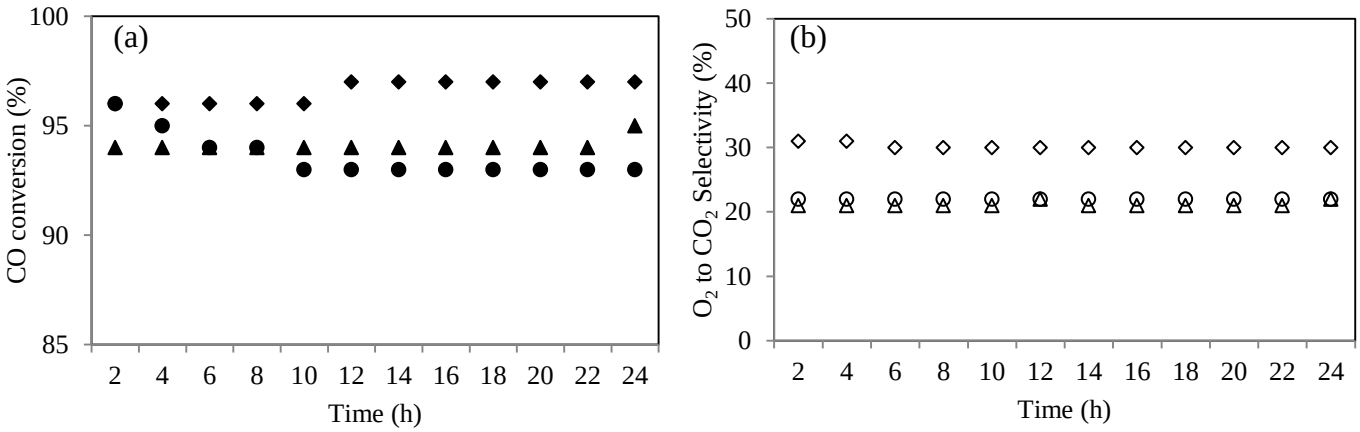

Figure 5.10 *(a) CO conversion and (b) selectivity as a function of time-on-stream on gold catalysts in dry PROX reaction at 100 °C. ●Au/TiO_2, ▲$Au/Ti_{0.9}Fe_{0.1}O_{2-\delta}$ and ♦$Au/Ti_{0.90}Co_{0.10}O_{2-\delta}$*

Taking into account that the realistic PROX feed is generated from steam reforming and, hence, contains CO_2 and H_2O, it is necessary to ascertain if the high activity and selectivity obtained under idealized PROX conditions can be maintained in the presence of CO_2 and H_2O . In the present work, the effects of 15% CO_2, 7% H_2O and 15% CO_2 + 7% H_2O on the stability of gold catalysts were evaluated. Figures 5.11(a) and 5.11(b) show respective CO conversions and selectivity plots in CO_2-containing reformate. For $Au/Ti_{0.9}Fe_{0.1}O_{2-\delta}$, both CO conversion and selectivity are maintained at 95 and 22%, respectively, in the presence of CO_2. In the case of $Au/Ti_{0.90}Co_{0.10}O_{2-\delta}$, the CO conversion decreases from 97% under CO_2-free conditions to 93% in the presence of CO_2. Addition of CO_2 leads to a decline in CO conversion over Au/TiO_2, from 93 to 89%. For all catalysts, the O_2 to CO_2 selectivity is hardly affected by the presence of CO_2, comparable to the values obtained under CO_2-free conditions. The presence of H_2O, in the

absence of CO_2, clearly has no negative or beneficial effect on the performance and stability of Au/TiO_2 and $Au/Ti_{0.9}Fe_{0.1}O_{2-\delta}$, except that the selectivity of the former catalyst is improved by 12% (Figures 5.11 (c) and (d)). Under the same conditions, CO conversion over gold on Co-substituted TiO_2 decreases from 97 to 89%, which is probably due to the accumulation of water on the surface as Co-containing catalysts are known to have low tolerance for H_2O [41, 42]. This in turn affects the oxygen release and uptake by the support.

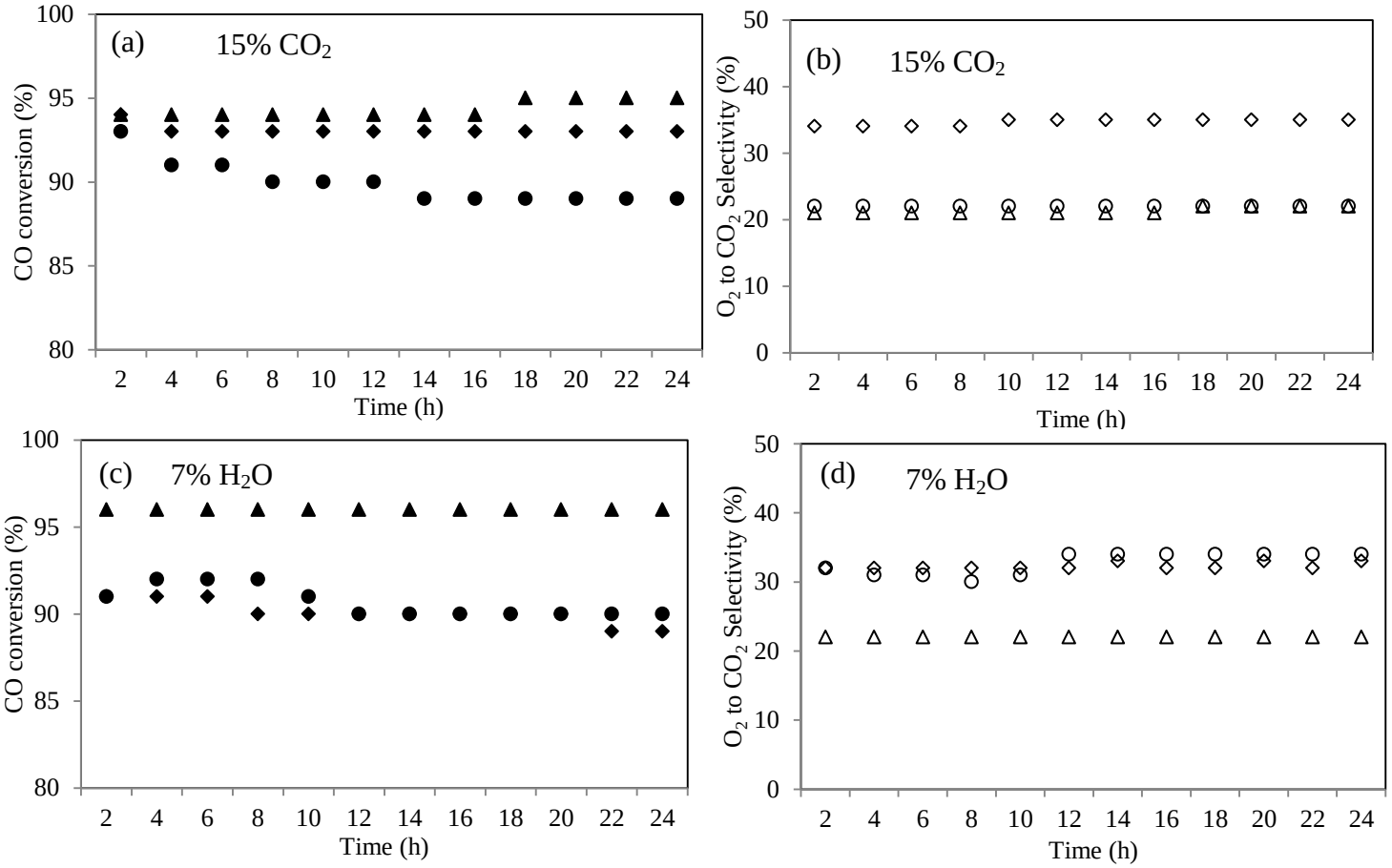

Figure 5.11 *(a) & (c) CO conversion and (b) & (d) selectivity as a function of time-on-stream on gold catalysts (● Au/TiO_2, ▲$Au/Ti_{0.9}Fe_{0.1}O_{2-\delta}$ and ♦$Au/Ti_{0.90}Co_{0.10}O_{2-\delta}$) in PROX in the presence of 15 vol% CO_2 and 7 vol% H_2O(reaction temperature 100 °C)*

Different authors have reported that the presence of CO_2 and H_2O leads to the deactivation of Au/TiO_2 and Au/Fe_2O_3 catalysts, due to carbonate formation, surface hydration and/or the modification of the catalytic properties, particularly the Au^0/Au^{x+} balance [39, 43]. In contrast, in the present work, it is observed that supporting gold on Fe-substituted titania produces a stable

catalyst. The $Au/Ti_{0.9}Fe_{0.1}O_{2-\delta}$ catalyst maintained its activity and selectivity even in the presence of both H_2O and CO_2. The beneficial effect of iron on the stability and activity of this catalyst can be linked to the formation of oxygen vacancies, which can act as local sites for oxygen chemisorption and activation [24, 25]. Under similar conditions, Au/TiO_2 and $Au/Ti_{0.90}Co_{0.10}O_{2-\delta}$ lose their activities by almost 20%. The activities of these catalysts could be restored by calcining them in air at 200 °C. Therefore, it is highly unlikely that the sintering of gold particles plays a major role in the deactivation mechanism. Based on this, it can be inferred that the deactivation is most likely due to the distortion of the proposed balance between metallic and ionic gold species. The PROX activity and corresponding selectivity of the investigated catalysts under different gas compositions are summarized in Table 5.3.

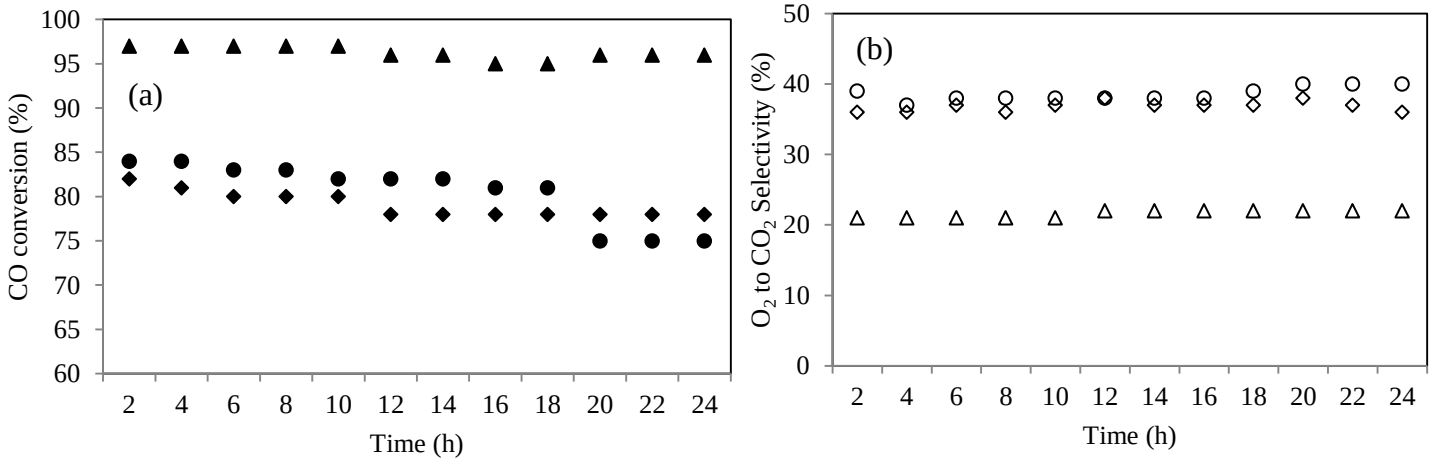

Figure 5.12 *(a) CO conversion and (b) selectivity as a function of time-on-stream on gold catalysts(● Au/TiO_2, ▲$Au/Ti_{0.9}Fe_{0.1}O_{2-\delta}$ and ♦$Au/Ti_{0.90}Co_{0.10}O_{2-\delta}$) in PROX in the presence of 15 vol% CO_2 +7 vol% H_2O (reaction temperature 100 °C)*

Table 5.3 *PROX activity and selectivity of investigated catalysts under different gas mixtures.*

Catalyst	CO conversion and selectivity [a]			
	H_2O/CO_2-free	15 % CO_2	7 % H_2O	15 % CO_2 and 7 % H_2O
Au/TiO_2	93 (22)	89 (22)	90 (34)	75 (40)
$Au/Ti_{0.90}Co_{0.10}O_{2-\delta}$	97 (30)	89 (33)	93 (35)	78 (36)
$Au/Ti_{0.9}Fe_{0.1}O_{2-\delta}$	95 (22)	96 (22)	95 (22)	96 (22)

[a] The values outside and inside brackets represent conversion and selectivity, respectively.

5.4 Conclusions

The results reported here suggest that the introduction of Co and Fe into the TiO_2 matrix results in the formation of single-phase solid-solutions, viz. $Ti_{0.90}Co_{0.10}O_{2-\delta}$ and $Ti_{0.9}Fe_{0.1}O_{2-\delta}$. Three different catalysts were prepared by depositing gold on these materials and TiO_2. Under TOX conditions, $Au/Ti_{0.90}Co_{0.10}O_{2-\delta}$ is the most active catalyst, followed by $Au/Ti_{0.9}Fe_{0.1}O_{2-\delta}$ and then Au/TiO_2. The presence of excess H_2, in the PROX reaction, improved the activity of all studied gold catalysts, with $Au/Ti_{0.9}Fe_{0.1}O_{2-\delta}$ displaying superior performance. The catalytic behaviour of gold on Fe-doped TiO_2 could be ascribed to the redox properties of the support, viz. oxygen release and uptake on the oxygen vacancies. The effects of CO_2 and H_2O on the activity and the stability of the catalysts were investigated. It was found that the presence of CO_2 or H_2O, in the absence of the other, led to slight decrease (less than 9%) on the activity of $Au/Ti_{0.90}Co_{0.10}O_{2-\delta}$ and Au/TiO_2. The presence of both co-reactants, CO_2 and H_2O, resulted in a significant decrease (19%) in the activity of the two catalysts. In contrast, the high activity displayed by $Au/Ti_{0.9}Fe_{0.1}O_{2-\delta}$ remained unchanged in the presence of both CO_2 and H_2O. No loss of activity or selectivity was observed over a period on 24 h. The above results suggest that gold on Fe-substituted TiO_2 is a promising catalyst formulation for the removal of CO from steam reformate for PEMFCs. Full optimization of the formulation may lead to their practical application.

5.5 Acknowledgements

The authors gratefully acknowledge the Department of Science and Technology and Mintek (Advanced Metals Initiative Program) for financial support. Thanks are also due to the Catalysis Research Group members for valuable discussions.

References

[1] F. Barbir, in: F. Barbir (Ed.), PEM Fuel Cells (Second Edition), Academic Press, Boston, 2013, pp. 1-16.

[2] D. Shekhawat, D.A. Berry, J.J. Spivey, Fuel Cells: Technologies for Fuel Processing, 1st ed., Elsevier Ltd., Amsterdam, Netherlands 2011, pp. 1-9.

[3] L. Barreto, A. Makihira, K. Riahi, Int. J. Hydrogen Energy 28 (2003) 267-284.

[4] C. Ratnasamy, J.P. Wagner, Catalysis Reviews 51 (2009) 325-440.

[5] T. Kaltschmitt, O. Deutschmann, in: S. Kai (Ed.), Advances in Chemical Engineering, Academic Press, 2012, pp. 1-64.

[6] J.-H. Wee, K.-Y. Lee, J. Power Sources 157 (2006) 128-135.

[7] A. Mishra, R. Prasad, Bull. Chem. React. Eng. Catal. 6 (2011) 1-14.

[8] M. Haruta, T. Kobayashi, H. Sano, N. Yamada, Chem. Lett. 16 (1987) 405-408.

[9] M. Haruta, The Chemical Record 3 (2003) 75-87.

[10] M. Haruta, Catal. Today 36 (1997) 153-166.

[11] M. Haruta, S. Tsubota, T. Kobayashi, H. Kageyama, M.J. Genet, B. Delmon, J. Catal. 144 (1993) 175-192.

[12] K.M. Parida, P. Mohapatra, J. Moma, W.A. Jordaan, M.S. Scurrell, J. Mol. Catal. A: Chem. 288 (2008) 125-130.

[13] F. Moreau, G.C. Bond, Appl. Catal., A 302 (2006) 110-117.

[14] F. Moreau, G.C. Bond, Catal. Today 122 (2007) 260-265.

[15] F. Moreau, G.C. Bond, A.O. Taylor, J. Catal. 231 (2005) 105-114.

[16] M.M. Schubert, M.J. Kahlich, H.A. Gasteiger, R.J. Behm, J. Power Sources 84 (1999) 175-182.

[17] P. Landon, J. Ferguson, B.E. Solsona, T. Garcia, S. Al-Sayari, A.F. Carley, A.A. Herzing, C.J. Kiely, M. Makkee, J.A. Moulijn, A. Overweg, S.E. Golunski, G.J. Hutchings, J. Mater. Chem. 16 (2006) 199-208.

[18] M.J. Kahlich, H.A. Gasteiger, R.J. Behm, J. Catal. 182 (1999) 430-440.

[19] L.H. Chang, N. Sasirekha, Y.-W. Chen, W.-J. Wang, Ind. Eng. Chem. Res. 45 (2006) 4927-4935.

[20] E.O. Jardim, S. Rico-Francés, F. Coloma, E.V. Ramos-Fernández, J. Silvestre-Albero, A. Sepúlveda-Escribano, Appl. Catal., A 487 (2014) 119-129.
[21] Z. Ma, C. Liang, S.H. Overbury, S. Dai, J. Catal. 252 (2007) 119-126.
[22] Y.-F. Yang, P. Sangeetha, Y.-W. Chen, Ind. Eng. Chem. Res. 48 (2009) 10402-10407.
[23] Y.-W. Chen, H.-J. Chen, D.-S. Lee, J. Mol. Catal. A: Chem. 363–364 (2012) 470-480.
[24] K.M. Parida, N. Sahu, P. Mohapatra, M.S. Scurrell, J. Mol. Catal. A: Chem. 319 (2010) 92-97.
[25] S. Carrettin, Y. Hao, V. Aguilar-Guerrero, B.C. Gates, S. Trasobares, J.J. Calvino, A. Corma, Chemistry – A European Journal 13 (2007) 7771-7779.
[26] S. Yu, H.J. Yun, D.M. Lee, J. Yi, J. Mater. Chem. 22 (2012) 12629-12635.
[27] B.H. Toby, Powder Diffr. 21 (2006) 67-70.
[28] D. Wang, J. Zhao, B. Chen, C. Zhu, J. Phys.: Condens. Matter 20 (2008) 085212.
[29] K.S.W. Sing, D.H. Everett, R.A.W. Haul, L. Moscou, R.A. Pierotti, J. Rouquerol, T. Siemieniewska, in: G. Ertl, H. Knözinger, F. Schüth, J. Weitkamp (Eds.), Handbook of Heterogeneous Catalysis, 2nd ed., Wiley-VCH Verlag GmbH & Co. KGaA, Weinheim, Germany, 2008, pp. 1217-1230.
[30] J.-Y. Luo, M. Meng, J.-S. Yao, X.-G. Li, Y.-Q. Zha, X. Wang, T.-Y. Zhang, Appl. Catal., B 87 (2009) 92-103.
[31] M.H. Razali, M.N. Ahmad-Fauzi, A.R. Mohamed, S. Sreekantan, Int. J. Mater., Mech. Manuf. 1 (2013) 314-318.
[32] K. Das, S.N. Sharma, M. Kumar, S.K. De, J. Phys. Chem. C 113 (2009) 14783-14792.
[33] S. Sun, X. Zhao, H. Lu, Z. Zhang, J. Wei, Y. Yang, CrystEngComm 15 (2013) 1370-1376.
[34] S. Roy, A. Marimuthu, M.S. Hegde, G. Madras, Appl. Catal., B 73 (2007) 300-310.
[35] H. Liu, A.I. Kozlov, A.P. Kozlova, T. Shido, K. Asakura, Y. Iwasawa, J. Catal. 185 (1999) 252-264.
[36] M.M. Schubert, S. Hackenberg, A.C. van Veen, M. Muhler, V. Plzak, R.J. Behm, J. Catal. 197 (2001) 113-122.
[37] Z. Zhao, M.M. Yung, U.S. Ozkan, Catal. Commun. 9 (2008) 1465-1471.
[38] W.-H. Yang, M.H. Kim, S.-W. Ham, Catal. Today 123 (2007) 94-103.
[39] J. Steyn, G. Pattrick, M.S. Scurrell, D. Hildebrandt, M.C. Raphulu, E. van der Lingen, Catal. Today 122 (2007) 254-259.

[40] Y. Denkwitz, B. Schumacher, G. Kučerová, R.J. Behm, J. Catal. 267 (2009) 78-88.

[41] M. Date, M. Okumura, S. Tsubota, M. Haruta, Angew. Chem., Int. Ed. 43 (2004) 2129-2132.

[42] J. Jansson, A.E.C. Palmqvist, E. Fridell, M. Skoglundh, L. Österlund, P. Thormählen, V. Langer, J. Catal. 211 (2002) 387-397.

[43] M.M. Schubert, A. Venugopal, M.J. Kahlich, V. Plzak, R.J. Behm, J. Catal. 222 (2004) 32-40.

CHAPTER 6

Summary and conclusion

In view of its relevance in pollution control and fuel cell applications, catalytic CO oxidation continues to receive research interest. Hence, the purpose of the current study was to develop active catalysts for total and preferential CO oxidation. Solid-solution ceria-based and supported gold catalysts were synthesized, characterized and tested for total and preferential CO oxidation. A continuous flow fixed-bed reactor was used for catalytic measurements.

The combined effect of Cu^{2+} and Pd^{2+} ions within the ceria lattice was investigated. This was assessed by synthesizing and comparing the catalytic properties and behaviour of mono-metallic ($Ce_{0.98}Pd_{0.02}O_{2-\delta}$ and $Ce_{0.95}Cu_{0.05}O_{2-\delta}$) and bimetallic catalysts ($Ce_{0.93}Pd_{0.02}Cu_{0.05}O_{2-\delta}$). Total CO oxidation was used as a model reaction. Based on XRD, Raman spectroscopy and HRTEM, it was concluded that these catalysts, synthesized by a single-step solution combustion method, were fluorite structured single-phase solid-solution oxides. The CO oxidation activity of $Ce_{0.93}Pd_{0.02}Cu_{0.05}O_{2-\delta}$ was found to be higher than that of the corresponding mono-metallic analogues. It was established that the synergetic effect between palladium, copper and cerium ions in the $Ce_{0.93}Pd_{0.02}Cu0_{.05}O_{2-\delta}$ catalyst resulted in improved reducibility and superior catalytic performance. The activation energy for CO oxidation over $Ce_{0.93}Pd_{0.02}Cu_{0.05}O_{2-\delta}$ was 26.4 kJ/mol less than that over $Ce_{0.95}Cu_{0.05}O_{2-\delta}$. This bimetallic catalyst formulation may be a promising candidate for future applications in auto-emission control, although further investigation and optimization of this catalyst formulation is still required.

Another series of metal ion substituted ceria catalysts, $Ce_{0.90}Co_{0.10}O_{2-\delta}$ and $Ce_{0.90-x}Cu_xCo_{0.10}O_{2-\delta}$ (x = 0.01, 0.03 and 0.05) were synthesized, with the view to improve the catalytic performance of the developed $Ce_{0.90}Co_{0.10}O_{2-\delta}$ catalyst. In this study, it has been shown that the activity of $Ce_{0.90}Co_{0.10}O_{2-\delta}$ for TOX and PROX could be significantly enhanced by the addition of Cu. The improvement in the activity could be linked to improved reducibility, which was associated with better oxygen mobility due to Ce-Cu interactions.

Amongst the studied bimetallic Cu-Co catalysts, the $Ce_{0.85}Cu_{0.05}Co_{0.10}O_{2-\delta}$ catalyst showed superior catalytic performance compared to the other bimetallic catalysts. This catalyst could achieve complete CO conversion below 200 °C under both TOX and PROX conditions, even at a higher GHSV of 48000 h^{-1}.

In the presence of excess H_2, the $Ce_{0.90}Co_{0.10}O_{2-\delta}$ and $Ce_{0.90-x}Cu_xCo_{0.10}O_{2-\delta}$ catalysts proved to be highly selective for CO oxidation. Regardless of the O_2/CO ratio and/or GHSV employed, the O_2 to CO_2 selectivity was maintained between 98 and 100 %, for reaction temperatures not exceeding 150 °C. Such PROX reaction profiles are consistent with the operation of the Mars-van Krevelen pathway. The rate of CO oxidation over $Ce_{0.90}Co_{0.10}O_{2-\delta}$ decreased in a H_2-rich stream. However, for $Ce_{0.90-x}Cu_xCo_{0.10}O_{2-\delta}$ and $Ce_{0.95}Cu_{0.05}O_{2-\delta}$ catalysts, the CO oxidation rate was not adversely affected by the presence of excess H_2. Based on these results, it has been suggested that H_2 and CO oxidation over $Ce_{0.90}Co_{0.10}O_{2-\delta}$ may be occurring on the same active sites while the two reactions seem to be taking place on independent sites over Cu-containing catalysts.

The effects of H_2O and CO_2 on the PROX activity and stability of the $Ce_{0.90}Co_{0.10}O_{2-\delta}$ and $Ce_{0.90-x}Cu_xCo_{0.10}O_{2-\delta}$ catalysts were evaluated at 180 °C. In the absence of H_2O and CO_2, the catalysts were highly active, selective and stable under PROX conditions. It was shown that both H_2O and CO_2 have detrimental effects on the PROX performance of the $Ce_{0.90}Co_{0.10}O_{2-\delta}$ and $Ce_{0.90-x}Cu_xCo_{0.10}O_{2-\delta}$ catalysts. The extent of deactivation was more pronounced for $Ce_{0.90}Co_{0.10}O_{2-\delta}$. However, the CO_2/H_2O tolerance improved with increasing Cu loading in the $Ce_{0.90-x}Cu_xCo_{0.10}O_{2-\delta}$ catalysts. The activities of these catalysts could be restored by calcining them in air at 200 °C, which is indicative of a reversible deactivation. The $Ce_{0.95}Cu_{0.05}O_{2-\delta}$ catalyst proved to be the most robust catalyst, achieving CO conversion and selectivity of 86 and 75%, respectively, in the presence of 7% H_2O + 15% CO_2. This remarkable activity was consistently maintained during the time-on-line study (24 h). The results showed no evidence of the reverse water gas shift reaction.

TOX activity of gold catalysts prepared with TiO_2, cobalt- and iron-substituted titania supports followed the trend: $Au/Ti_{0.90}Co_{0.10}O_{2-\delta}$ > $Au/Ti_{0.9}Fe_{0.1}O_{2-\delta}$ > Au/TiO_2. Under PROX

conditions, the catalytic performance of the three catalysts improved, with all achieving complete CO removal between 60-100 ° C. In a simulated reformate, containing 7 vol% H_2O and 15 vol% CO_2, $Au/Ti_{0.9}Fe_{0.1}O_{2-\delta}$ maintained its activity and stability during the time-on-line test (24 h). On the other hand, CO conversion over Au/TiO_2 and $Au/Ti_{0.90}Co_{0.10}O_{2-\delta}$ catalysts decreased by nearly 20% in the presence of 7 vol% H_2O and 15 vol% CO_2. However, these catalysts regained their activity after calcining them in air at 200 °C. The deactivation could not be traced to the sintering of gold particles, but perhaps due to the distortion of the proposed balance between metallic and ionic gold species. The results suggest that gold supported on Fe-substituted TiO_2 is a promising catalyst formulation for the removal of CO from steam reformate for PEMFCs. Full optimization of the formulation may lead to their practical application.

APPENDIX 1

Additional characterization data

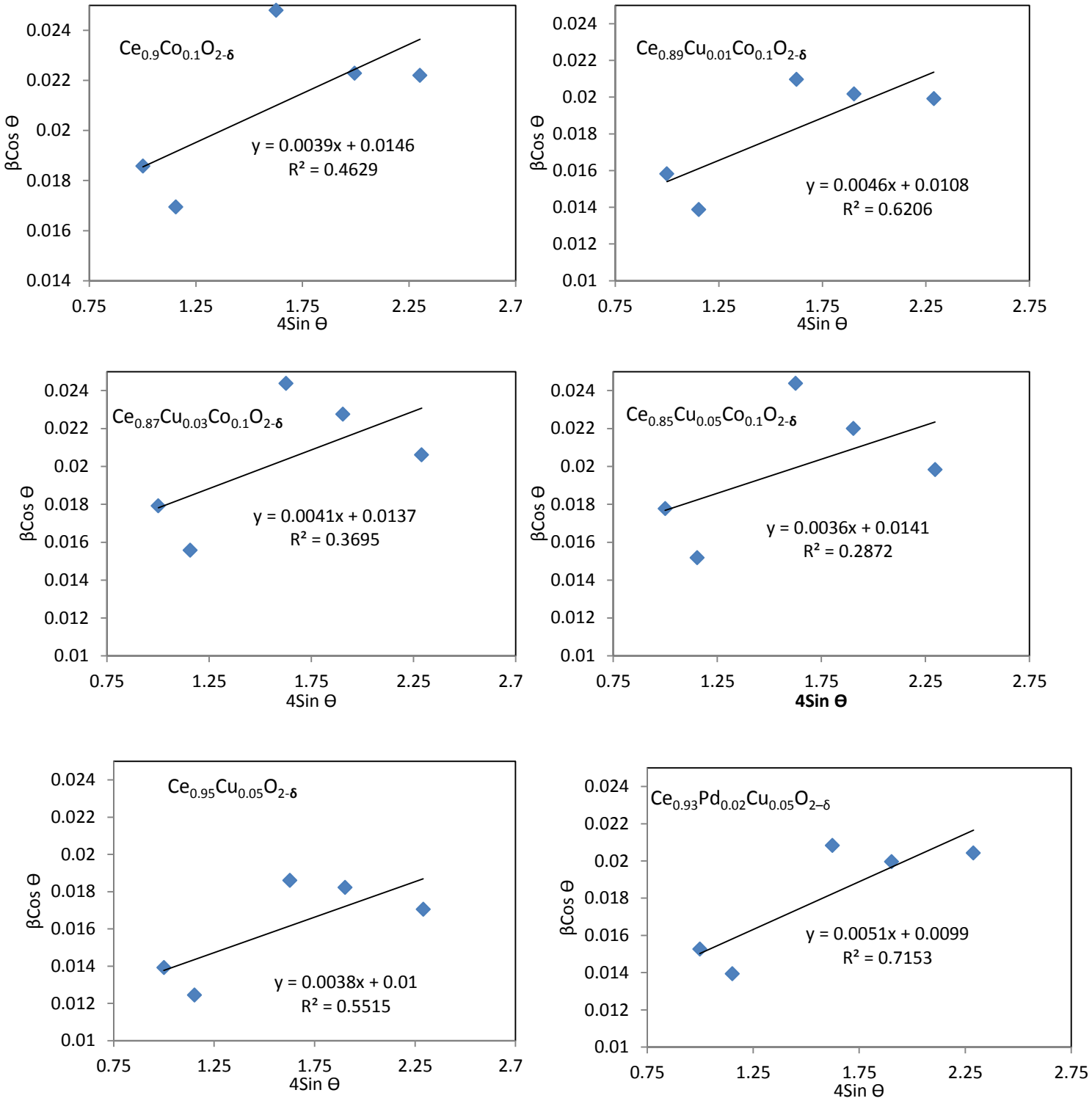

Figure A-1 *Classical Williamson-Hall plots used to determine the lattice strain and crystallite sizes*

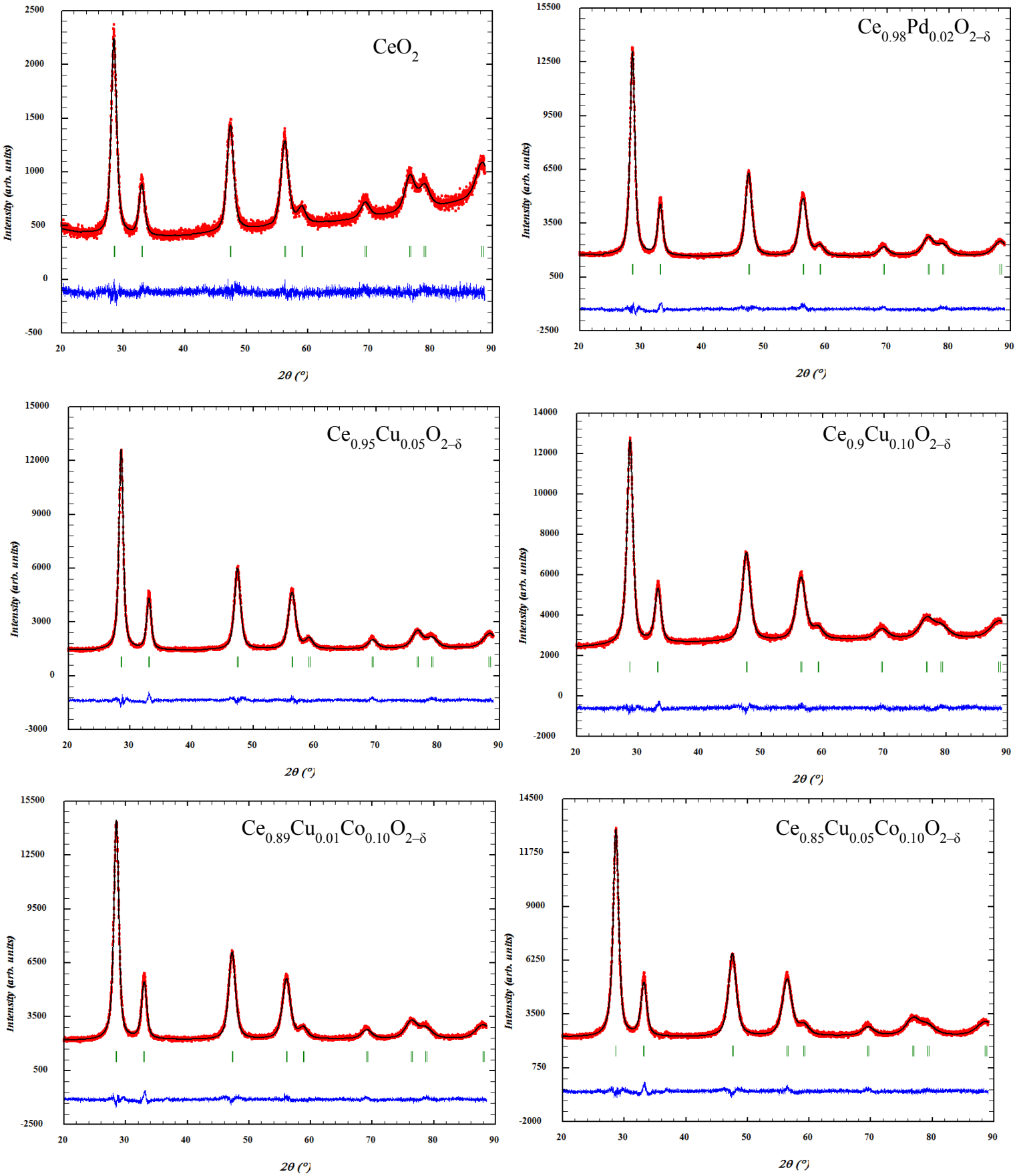

Figure A-2 *Rietveld refined XRD pattern of substituted ceria materials*

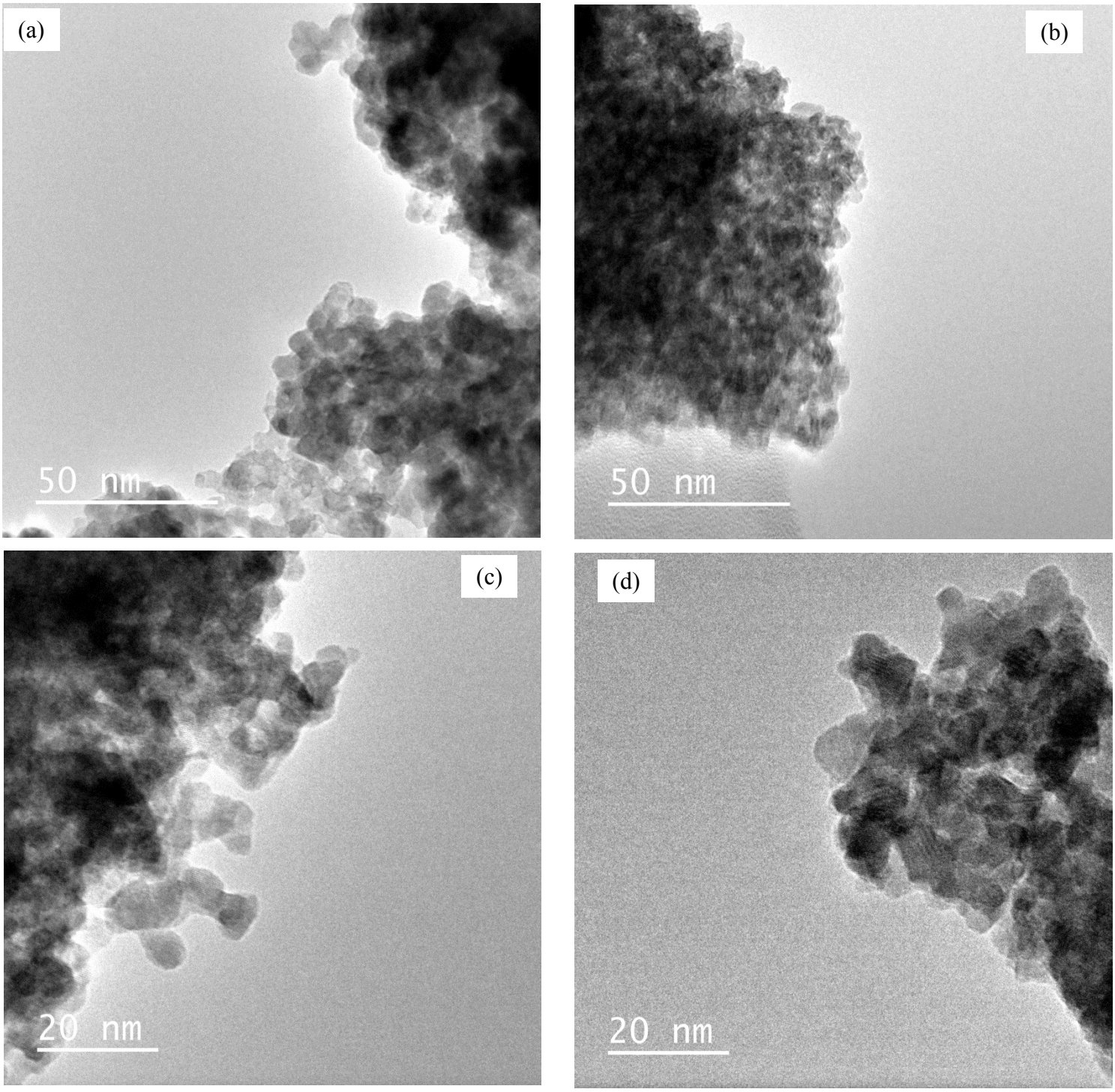

Figure A- 3 *TEM images of (a) $Ce_{0.95}Cu_{0.05}O_{2-\delta}$, (b) CeO_2, (c)$Ce_{0.98}Pd_{0.02}O_{2-\delta}$ and (d) $Ce_{0.93}Cu_{0.05}Pd_{0.02}O_{2-\delta}$ catalysts*

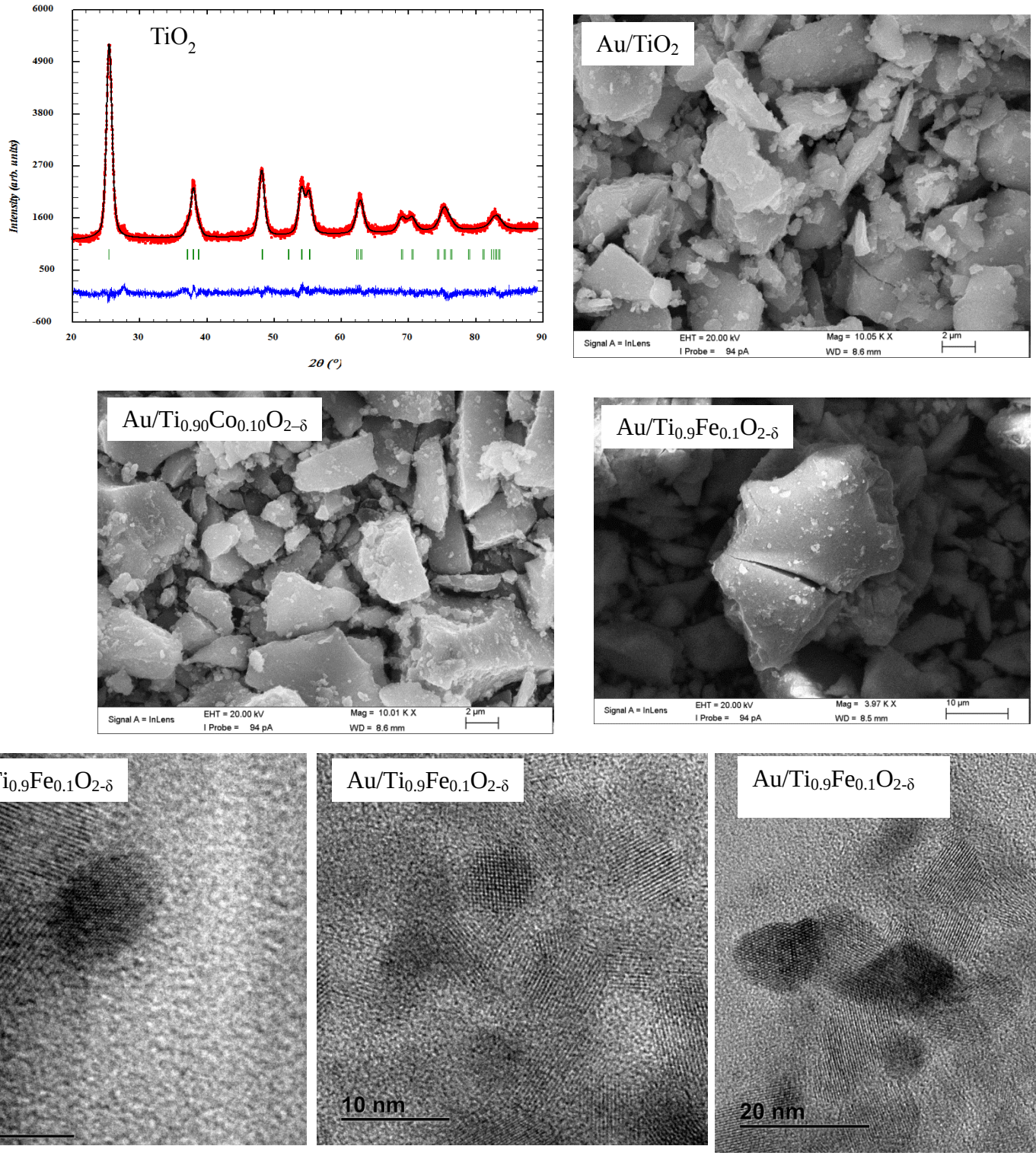

Figure A-4 *Rietveld refined XRD pattern of TiO2. SEM images of Au/TiO2, Au/$Ti_{0.9}Co_{0.1}O_{2-\delta}$ and Au/$Ti_{0.9}Fe_{0.1}O_{2-\delta}$. HR-TEM images of Au/$Ti_{0.9}Fe_{0.1}O_{2-\delta}$.*

GC specifications and calibration

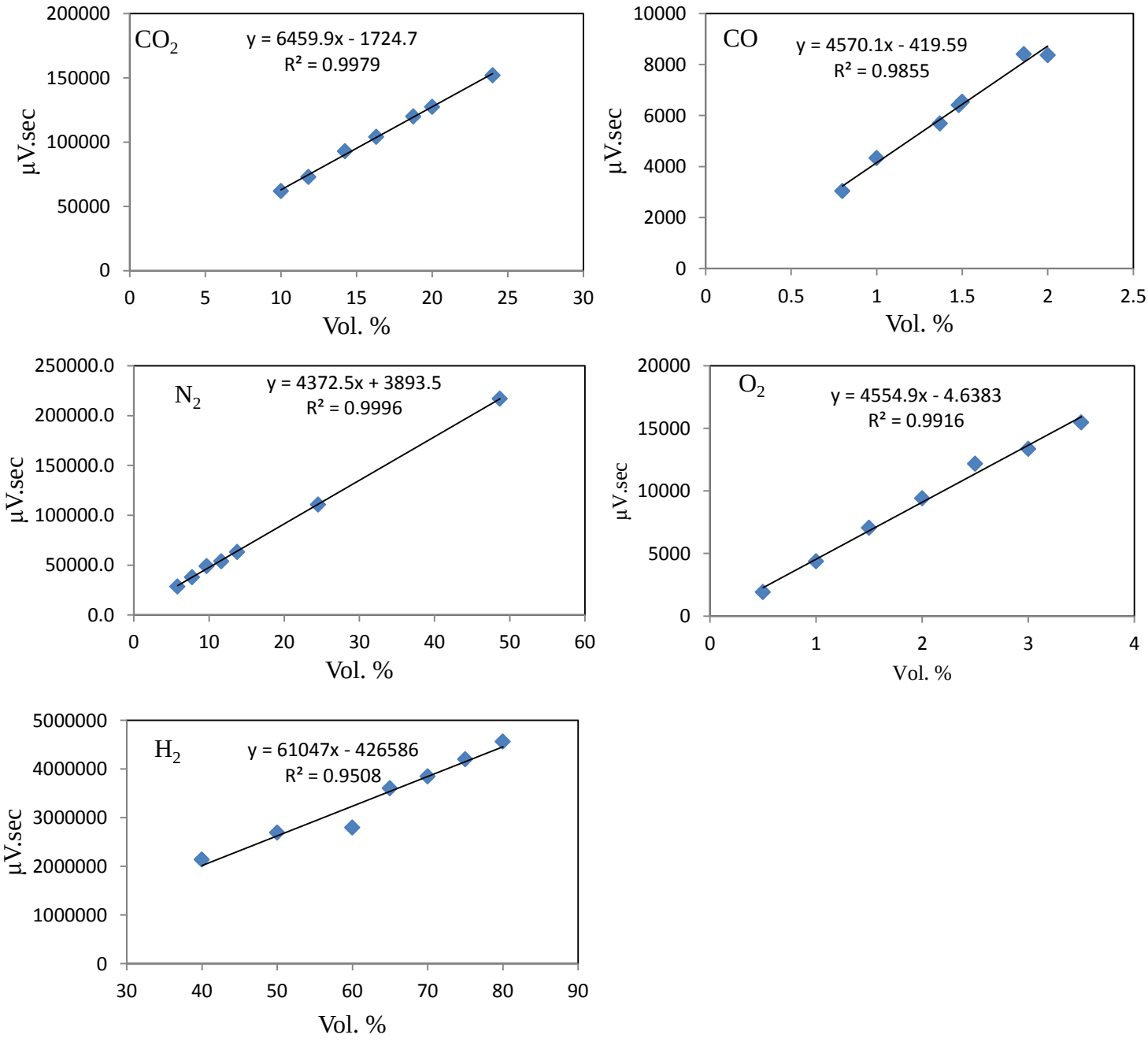

Figure A- 5 *Gas calibration curves*

Table A-1 *Details of the Varian Micro GC-4900 used in this study.*

Channel	**1st**	**2nd**	**3rd**
Column type	Molsieve 5Å	Molsieve 5Å	CP-Sil5 CB
Column length (m)	10	10	10
Column temperature (°C)	50	50	50
Column Pressure (kPa)	150	150	70
Carrier gas	Ar	H_2	H_2
Sample line and injector temperature (°C)	50	50	50
Product analysis	H_2	O_2, CO and N_2	CO_2 and H_2O

APPENDIX 2

Additional experimental details

A2.1 Calculations and thermodynamic considerations during the synthesis of solid-solution

The amounts of the starting materials contained in the redox mixture were determined according to the method reported by Jain et al. [1]. Generally, the redox mixture is a saturated aqueous solution of urea fuel, as the reducing agent, and the required metal precursor as the oxidizing agent. Upon heating the redox mixture ignites, all the organic material decomposes and large amounts of gases are evolved. The reaction is exothermic and the heat required for the synthesis comes from the resulting redox after ignition. The main gaseous products produced during combustion synthesis are CO_2, H_2O and N_2.

According to Jain's method, the molar ratio of the precursors is determined by calculating the oxidising/reducing or oxidizer/fuel valencies (ϕ) of the redox mixture. In solution combustion calculations, reducing elements are considered as positive, the oxidizing elements as negative and neutral nitrogen is considered to be zero. Hydration water is not included in the overall valence. Using these rules, the respective reducing valence of urea fuel and the oxidizing valence of $(NH_4)_2Ce(NO_3)_6$ are +6 and -24. Therefore, an optimal cerium ammonium nitrate/ urea molar ratio for the combustion synthesis of CeO_2 becomes 24/6 = 4. Detailed calculations are shown below, with CeO_2 and $Ce_{0.9}Co_{0.1}O_{2-\delta}$ as examples. The concept described above and detailed in Table A-3 was followed to calculate the stoichiometric proportion of metal salts and urea fuel for the preparation of other ceria and titania-based materials.

Table A- 2 *Detailed calculations for the preparation of solid solution materials* [a]

	CeO_2		
	Fuel	Ce precursor	
	$CO(NH_2)_2$ (60.06)	$(NH_4)_2Ce(NO_3)_6$ (548.26)	
Valence	C = +4	Ce = +4	
	2N = 0	8N = 0	
	4H = (+1 x 4) = +4	8H = (+1 x 8) = +8	
	O = -2	18O = (-2 x 18) = -36	
Overall valence	+6	-24	
Φ	4		
Mass used (g)	4.8048	10.9652	
Moles (mol)	0.08	0.02	
	$Ce_{0.90}Co_{0.10}O_{2-\delta}$		
	Fuel	Ce precursor	Foreign metal precursor
	$CO(NH_2)_2$ (60.06)	$(NH_4)_2Ce(NO_3)_6$ (548.26)	$Co(NO_3)_2.6H_2O$ (291.03)
Valence	C = +4	Ce = +4	Co = +2
	2N = 0	8N = 0	2N = 0
	4H = (+1 x 4) = +4	8H = (+1 x 8) = +8	6O = (-2 x 6) = -12
	O = -2	18O = (-2 x 18) = -36	
Overall valence	+6	(0.9 x -24) + (0.1 x -10) = -22.6	
Φ		3.77	
Mass used (g)	4.529	9.869	0.582
Moles (mol)	0.0754	0.018	0.002

[a] Values in brackets represent molecular weights in g/mol

A2.2 Bubbler system

Water delivery was carried out by the use of a traditional bubbler system. A bubbler unit was introduced in the reactor system, as seen in Figure 2.15, by attaching a water reservoir between the reactor mass flow controller and the reactor tube. A schematic representation of the bubbler system is shown in Figure A-5. The temperature of the water reservoir was kept constant at 38 °C, while a dry gas composition was passed through the bubbler.

The interaction between the liquid and the gas mixture depends on the relative size of bubbles, the residence time of the carrier gas in the liquid, the temperature of water, and the

stability of the gas flow into the reservoir. The relationship between these factors is expressed in equation A-1[2].

$$\dot{m} = F_c \left(\frac{\alpha \dot{p}}{P_h - \dot{p}}\right) f_\alpha(F_c, T, L) \quad \text{(A-1)}$$

In the above equation, $\dot{m}$ stands for the water vapour carry-over, F_c is the flow rate of the dry gas, P_h is the pressure at the headspace of the water, $\dot{p}$ represents water vapour pressure, α is a constant of the liquid and f_α stands for an imperial correction factor. The correction factor is a function of water temperature (T), the water level in the bubbler (L), and F_c. The dependence between F_c and $\dot{m}$ is known to follow a linear trend for experiments conducted under isothermal conditions, provided the gas flow rate is below 300 mL/min [3, 4]. Therefore, an imperial correction factor, f_α, in equation A-1 can be ignored as it caters for non-linear behaviour due to temperature changes. It is then assumed that there is enough residence time and the water level is kept high. Summarily, equation A-1 is reduced to equation A-2.

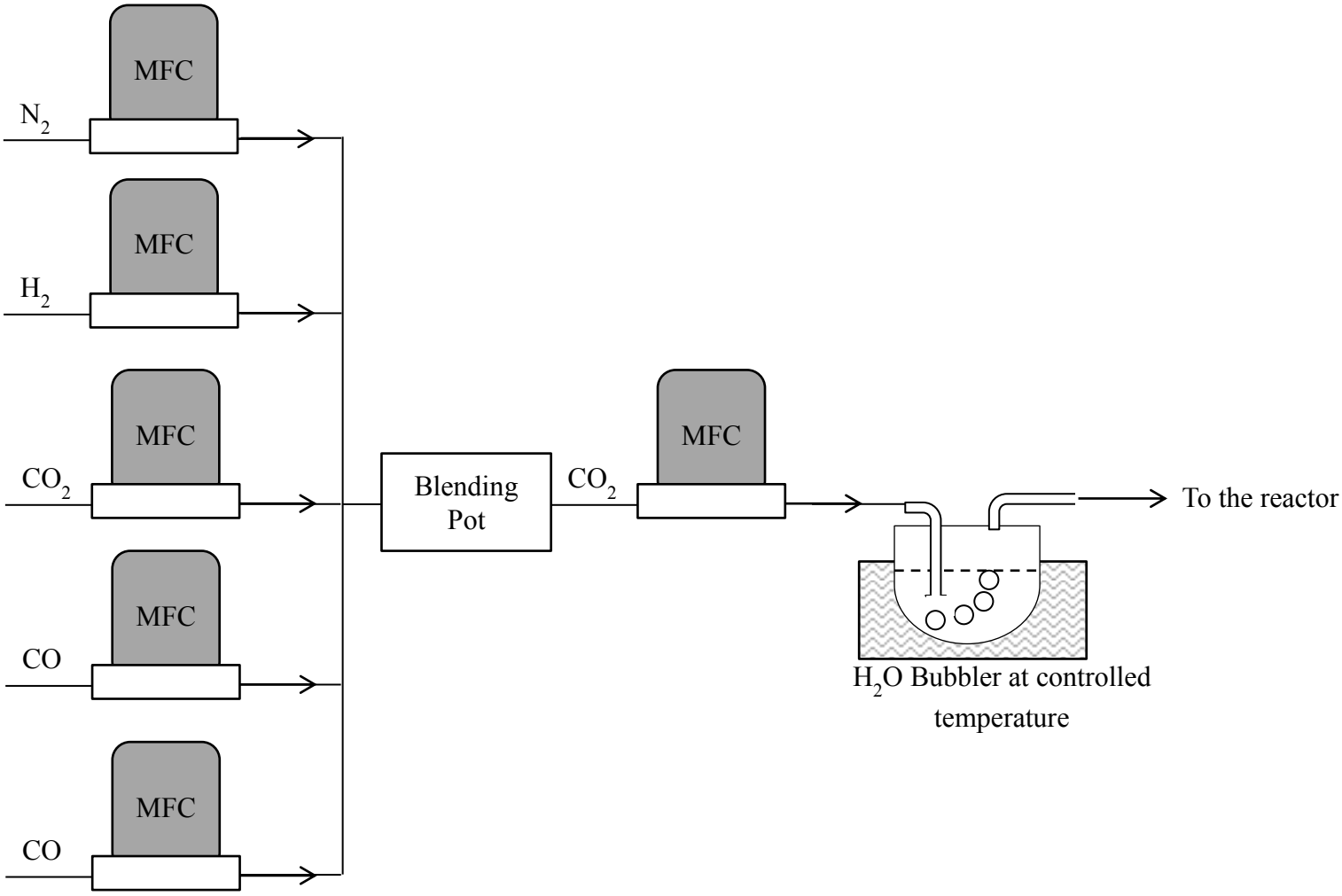

Figure A- 6 *Schematic representation of the bubbler system used for vapour delivery*

$$\dot{m} = F_c \left(\frac{\alpha \dot{p}}{P_h - \dot{p}}\right) \quad \text{(A-2)}$$

Because the bubbler was operated at atmospheric pressure, with the temperature of the reservoir kept constant, the vapour delivery was controlled by varying the flow rate of the gas (but not exceeding 300 mL/min). Water vapour ($\dot{p}$) was calculated using the Antoine equation.

$$\log \dot{p} = A - \frac{B}{T + C} \quad \text{(A-3)}$$

In equation A-3, A (8.07131), B (1730.63) and C (233.426) are component specific thermodynamic constants of water.

A2.3 Temperature profiles

Using temperature controls and thermocouples installed in the reactor unit, the catalyst bed was placed in the isothermal zone of the reactor tube (200-250 mm) as shown in Figure A-6. For all catalyst testing experiments, typical temperature profiles showed constant temperature, within ±5 °C to the desired reaction temperature (Figure A-6).

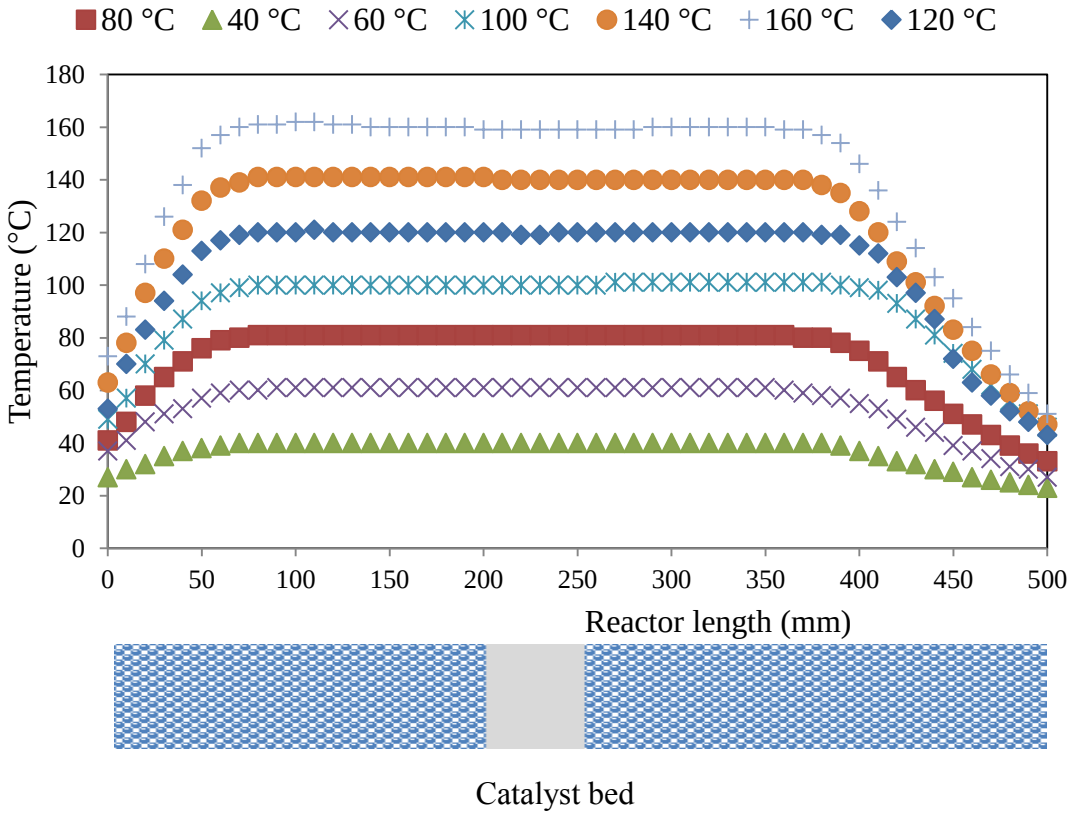

Figure A- 7 *Temperature profiles, from 40 to 160 °C*

References

[1] S.R. Jain, K.C. Adiga, V.R. Pai Verneker, Combust. Flame 40 (1981) 71-79.

[2] J.C. McMenamin, Vapor mass flow control system, J.C. Schumacher Co., US4436674 A, 1984, p. 4.

[3] A. Love, S. Middleman, A.K. Hochberg, J. Cryst. Growth 129 (1993) 119-133.

[4] S.S. Araya, S.K. Kaer, S.J. Andreasen, J. Fuel Cell Sci. Technol. 9 (2012) 015001/015001-015001/015006.